0-315-17508-9

65417

NAME OF AUTHOR/*NOM DE L'AUTEUR*___Didier P. Teirlinck_____

TITLE OF THESIS/*TITRE DE LA THÈSE*___"Influence of the Stress State on a Variety of___

_____Fracture Modes".___

UNIVERSITY/*UNIVERSITÉ*___McMaster_____

DEGREE FOR WHICH THESIS WAS PRESENTED/
*GRADE POUR LEQUEL CETTE THÈSE FUT PRÉSENTÉE*___Ph.D.___

YEAR THIS DEGREE CONFERRED/*ANNÉE D'OBTENTION DE CE DEGRÉ*___1984___

NAME OF SUPERVISOR/*NOM DU DIRECTEUR DE THÈSE*___Dr. J.D. Embury___

DATED/*DATÉ*___December 9, 1983.___ SIGNED/*SIGNÉ*___Teirlinck___

PERMANENT ADDRESS/*RÉSIDENCE FIXÉ*___8 ~~rue~~ Boulevard du

Colonel Driant

38000 - GRENOBLE - FRANCE

INFLUENCE OF THE STRESS STATE

ON VARIOUS FRACTURE MODES

by

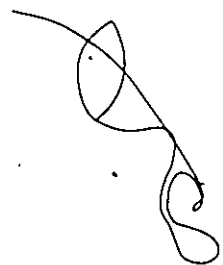DIDIER TEIRLINCK

A Thesis

Submitted to the School of Graduate Studies

in Partial Fulfilment of the Requirements

For the Degree

Doctor of Philosophy

McMaster University

© November 1983

INFLUENCE OF THE STRESS STATE

ON VARIOUS FRACTURE MODES

DOCTOR OF PHILOSOPHY
(Metallurgy and Materials Science)

McMASTER UNIVERSITY
Hamilton, Ontario

TITLE: Influence of the Stress State on
             Various Fracture Modes

AUTHOR: Didier Teirlinck, ingénieur civil des Mines
                          Docteur-Ingénieur (Université de Nancy)

SUPERVISOR: J.D. Embury

NUMBER OF PAGES: xviii, 264

ABSTRACT

The influence of superimposed pressure on the damage accumulation

processes leading to various tensile fracture modes has been studied on

axisymmetric samples of different materials.

. For ductile fracture, damage accumulated in both smooth and

notched tensile samples has been characterized in a variety of spheroi-

dized steels tested under superimposed pressures ranging from 0.1 MPa

to 1100 MPa by counting the number of voids existing at the cementite-

iron interfaces and measuring their area fraction. A quantitative

model accounting for the size dependence of void nucleation has been

developed to describe these results.

The shear fracture mode has been investigated by performing

tensile tests on an Al - Zn - Mg alloy under superimposed pressures

up to 1100 MPa. The pressure does not affect the onset of shear bands,

but changes their growth as it opposes any dilational damage created in

the bands. This allows the occurrence of the further plastic deformation

process to take place. The microscopic observation of the shear bands

has revealed that they are created by structural softening events, and

that they involve a complex spatial correlation of crystallographic

slip events over the entire cross-section.

Brittle fracture has been studied in both Al-Cu and Fe-P alloys,

displaying intergranular fracture and transgranular cleavage. The pattern

of microcrack development and the changes in fracture modes have been

characterized for these two alloys.

(iii)

Finally, two types of fracture maps in stress space are presented, where the various fracture mechanisms are represented by lines, and which can also be used as damage contour maps. These maps are constructed either by considering a complete model of damage accumulation and fracture criterion, or simplified analytical relationships to express damage development and occurrence of failure.

à Claire

à mes Parents

ACKNOWLEDGEMENTS

TABLE OF CONTENT

LIST OF FIGURES

LIST OF TABLES

CHAPTER 1

INTRODUCTION

When reviewing the different modes of failure occurring
in a wide range of materials including metals, alloys, rocks and
some polymers, it appears that a common feature of all these modes
is the accumulation of some form of microstructural damage in the
material, prior to the occurrence of failure. This damage develops
during the deformation of the material at a rate which is related
to the stress state and the strain history. Damage can be charac-
terized at a macroscopic level, for example as cracks, or at a micro-
scopic level, related to the microstructure of the material. More
precisely, damage can be defined as any kind of change in the structure
of a material, or in its mechanical properties, which leads to a
decrease of its load-bearing capacity. This definition includes the
variation in the volume of a material when voids are opened due to
the presence of hard second phase particles which do not deform like
the matrix material. It also accounts for the occurrence of micro-
cracks in brittle metals, either within a grain or at grain boundaries,
and in rocks. It also can be extended to the occurrence of localization
of the deformation into a narrow band, as this event is very often
associated with the presence of voids or microcracks. It should be
noticed, however, that it is not obvious to know what is the critical

event, that is to say whether the existence of voids triggers the localization, or the reverse process.

To summarize, it appears that damage is in general associated with a change in the volume of a material.

As long as the material is incompressible, the plasticity theory applies to describe its behaviour. The material deforms by shear under the action of the deviatoric part of the stress tensor. If a change in the volume occurs, the yield criterion has to be modified to take into account this porosity (Gurson, 1977a). In this case, the work done to break a specimen has two components: one is the plastic work term, the other is associated with the variation in volume dV and the "hydrostatic" stress, or more exactly the mean stress component of the stress tensor, σ_m. It appears then that this last component is a very important parameter in the fracture behaviour of dilatant materials (Oyane, 1972).

To examine the influence of the mean stress component, it is necessary to be able to vary its value over a wide range. This can be done in two different ways. The first one is related to the occurrence of a neck during the tensile deformation of ductile materials. This neck creates a triaxial state of stress, and the value of σ_m is altered. The second possibility is to superimpose either an hydrostatic pressure or an hydrostatic tension. The first case is realized when the material is tested in a container filled with a fluid at a certain pressure, and it has been applied to a number of materials following the work of Bridgman in 1945. The second case involves the machining of a notch of a certain geometry before testing the material.

Using these two alternatives, it is possible to look at a wide range
of fracture strains and mean stress values σ_m, and, therefore, to
study quantitatively the development of damage prior to failure.

In this study, two types of fracture have been investigated
with relation to damage: ductile fracture and brittle fracture.
The fibrous mode of ductile fracture has been studied in the iron-
cementite system, and the shear mode in an heat-treatable, high-
strength aluminum alloy. Brittle fracture has been investigated in
two experimental alloys, an iron-phosphorus alloy giving both trans-
granular cleavage and intergranular failure, and an aluminum-copper
alloy giving only intergranular failure.

Throughout the study, and for all the materials investigated,
the procedure has been the following:

- to determine the fracture characteristics of a given material
  at atmospheric pressure.
- to examine the changes in fracture mode when the stress state
  is changed by superimposing an hydrostatic pressure, or machining
  a notch.
- to perform a metallographic examination of the samples to
  characterize quantitatively the damage and to relate it to the
  corresponding stress state and strain level.
- to determine, if necessary and if possible, a quantitative
  fracture criterion and, if possible, to determine a model
  describing the effect of stress state on damage accumulation.

The final stage in this study was to find a convenient way of representing the effect of stress state on the fracture mode. The concept of fracture surface or limiting surface of rupture (McAdam, 1945), plotted in a stress space, appears to be the easiest way to represent on a map or a diagram the different regions where a fracture mode is dominant. The choice of the coordinates depends on the variables needed in the model of the fracture surfaces. For example, Gandhi and Ashby (1979) have drawn fracture maps with normalized stress-normalized temperature as coordinates. The interests of these maps are multiple. They are first a useful pedagogical help in presenting the different fracture modes occurring in a material with a given microstructure. They also represent and normalize on a unique plot a great deal of data, available in the literature. Further, they may be of engineering utility.

This study is organized as follows. After a general literature review describing the work already done on the influence of stress state on the two fracture modes considered, and describing the work done in the field of mapping different physical events, the following chapters present the results obtained and, if necessary, the models proposed concerning the influence of a superimposed hydrostatic stress on ductile fracture, in both the fibrous mode and the shear mode, and on brittle fracture. The last chapter describes the construction of fracture maps both from the results obtained in this work and, in a more general way, from the existing fracture data in the literature.

CHAPTER II

LITERATURE REVIEW

In this review, the characteristics of each fracture mode
considered are given, together with the quantitative models which
have been proposed to describe it. Then, the previous results
concerning the influence of a superimposed hydrostatic stress on
the behaviour of different materials are reviewed. Finally, a
survey of the mapping of physical events in different coordinates,
is presented.

II - 1 The Ductile Fracture

II-1-1 Introduction

This portion of the review is concerned with the fibrous
mode of ductile fracture, which is observed typically in the center
part of the fracture surface of a broken round tensile specimen.

It is well known (Puttick, 1959; Rogers, 1960) that this
mode occurs by the nucleation, growth and coalescence of voids inside
the material, generally associated with heterogeneities of the micro-
structure (e.g. the presence of second phase particles).

The first two steps generally occur simultaneously, that
is to say some voids are nucleated while previously created ones are
simultaneously growing by plastic deformation of the matrix. The
coalescence step is rather critical, and the strain associated with
it is negligible.

For the sake of clarity, each of these steps is examined separately.

II-1-2 Nucleation of Voids

It has been previously shown (Blum and Morrisey, 1966; Palmer and Smith, 1966) that inclusions and second phase particles are responsible for the occurrence of cavitation. The voids are produced because the particle and the matrix do not deform in the same way during straining of the material. This plastic heterogeneity (Ashby, 1970) leads to the opening of voids in two ways:

- cracking of brittle second phase particles,

- decohesion at the particle-matrix interface.

In general, the first case is associated with irregularly shaped particles or those having large aspects ratios (e.g. manganese sulfides or oxides stringers)., and the second case with approximately spherical particles. Before presenting the models of nucleation, the concept of nucleation strain and some experimental results related to this concept will be introduced.

II - 1 - 2 - 1 Nucleation Strain

Lindley et. al. (1970) have shown that it is not the magnitude of the applied stress which determines cavity initiation, but rather the local state of deformation. This can be characterized by a critical strain at which nucleation occurs. The existence of such a nucleation strain has been experimentally supported and must exist as nucleation is a process involving both stress and strain

energy release, so that there exists a threshold value of the far field strain below which there is either insufficient stress to break the interface (or fracture the particle itself), or insufficient elastic strain energy to create new surfaces.

The experimental determination of the nucleation strain, ϵ_N, can be made using various techniques such as optical microscopy, scanning and transmission electron microscopy, or density measurements. Obviously, the value of ϵ_N will depend upon the sensitivity of the technique used.

The experimental observations found in the literature are as follows:

- the value of ϵ_N depends on the system under consideration, and can take values from 0 to 1.

- Cavity formation by interfacial separation is sensitive to the cohesive energy of the interface. Therefore, ϵ_N is altered by impurity levels or solute additions which can segregate at the interface (Hippsley and Druce, 1983). The addition of solute can also lower the stacking fault energy, producing coarse planar slip, resulting in high local stress concentrations.

- There is a variation of ϵ_N with the particle size. The majority of authors find that larger particles nucleate first (Palmer and Smith, 1966; Leroy, 1978; Fisher and Gurland, 1981). However, there is some conflicting evidence in the literature (Atkinson, 1973; Rogers, 1968).

- The volume fraction f_v of second phase particles has a very small influence on ϵ_N: a slight decrease of ϵ_N with increasing f_v is expected if f_v is high enough.

- A superimposed hydrostatic pressure delays nucleation (French and Weinrich, 1974a; Brownrigg, 1982) and an hydrostatic tension reduces it (Argon and Im, 1975).

- Particle cracking, or cavitation, is related to the attainment of a critical value of local tensile stresses (Gurland, 1972).

II - 1 - 2 - 2   Models

Two conditions have to be fulfilled in order to nucleate a void: the first one is an energy balance condition, the second one is the building of a critical stress at the interface.

The first necessary condition can be expressed as follows: the elastic energy released by removing the stress from the particle must be at least equal to the surface energy created, that is:

$$\Delta E_{el} + \Delta W \leq 0 \qquad (II - 1)$$

where ΔE_{el} is the internal elastic energy in the particle, and ΔW is the energy increase in forming the cavity. Gurland and Plateau (1963) have obtained:

$$\Delta E_{el} = \frac{1}{2} E \epsilon^2 \times \frac{4\pi}{3} R_o^3$$
$$\Delta W = 4\pi R_o^2 \gamma \qquad (II - 2)$$

where E is the elastic modulus, assumed to be the same for the particle and the matrix, R_o is the particle radius and γ is the work of separation of the interface (Rosenfield, 1968).

Equation (II - 1) leads to the value of ε_N:

$$\varepsilon_N \geq \frac{6}{ER_o} \gamma \qquad\qquad (II - 3)$$

Taking some typical values of γ, E and R_o, this relationship gives $\varepsilon_N \simeq 0.05$, which is consistent with most experimental results, although quite low. Brown and Stobbs (1976) have used a combined continuum and microstructural approach, and have obtained:

$$\Delta E_{el} = \frac{4}{3} \pi \mu^* R_o^{3} \varepsilon_p^{*2}$$

$$\Delta W = 4 \pi R_o^{2} \gamma \qquad\qquad (II - 4)$$

Here, ε_p^* is the unrelaxed strain, i.e. a measure of the incompatibility between the matrix and particle deformation; μ^* is the shear modulus of the particle. If there is no plastic relaxation or other stress relief mechanism, then $\varepsilon_p^* = \varepsilon_p$, where ε_p is the symmetrical shear strain producing the shape change. If plastic relaxation occurs, by secondary slip of dislocations, then $\varepsilon_p^* = \left[\frac{b \, \varepsilon_p}{R_o} \right]^{\frac{1}{2}}$, where b is the Burgers vector.

The equation (II - 1) gives then:

$$\varepsilon_N \geq \frac{3\gamma}{\mu^* b} \qquad\qquad (II - 5)$$

This value of ε_N is independent of the particle size. In fact, there must exist a variation with R_o, as secondary slip is more likely to occur when R_o is large. A more detailed calculation in an earlier paper (Brown and Stobbs, 1971) shows that ε_N is proportional to $R_o^{\frac{1}{4}}$, thus the dependence is quite weak. The sense of this dependence

is also contrary to that observed experimentally. Recently, Goods and Brown (1979) have improved this treatment by taking into account the fact that cavities form over small regions of the particle surface, giving "caps" along the tensile axis (fig. II - 1). The energy criterion (II - 1) so corrected gives:

$$\varepsilon_N \; \geq \; \frac{1 - \cos\theta}{4 \, \sin^2\theta} \; \frac{3\gamma}{\mu^* b} \qquad (II - 6)$$

where θ is defined in fig. II - 1.

Tanaka et al. (1970) have also proposed an energy criterion based on a strain energy calculation in and adjacent to the particles. They find that the nucleation strain is of the form:

$$\varepsilon_N \; \geq \; \left[\frac{\beta}{R_o} \right]^{\frac{1}{2}} \qquad (II - 7)$$

where β is a constant depending on the elastic properties of both phases. Equation (II - 7) shows a inverse variation of ε_N with R_o, in accord with most experimental observations.

Fisher and Gurland (1981) have calculated the energy release for the particle, ΔE_{el}, as the sum of three terms:

- the elastic energy release associated with the applied load; it is calculated using linear elastic fracture mechanics.

- the stored energy associated with unrelaxed plastic incompatibility.

- the interaction energy between the stress field of the inclusion and the applied stress field.

They also examine the influence of the grain boundaries, where particles
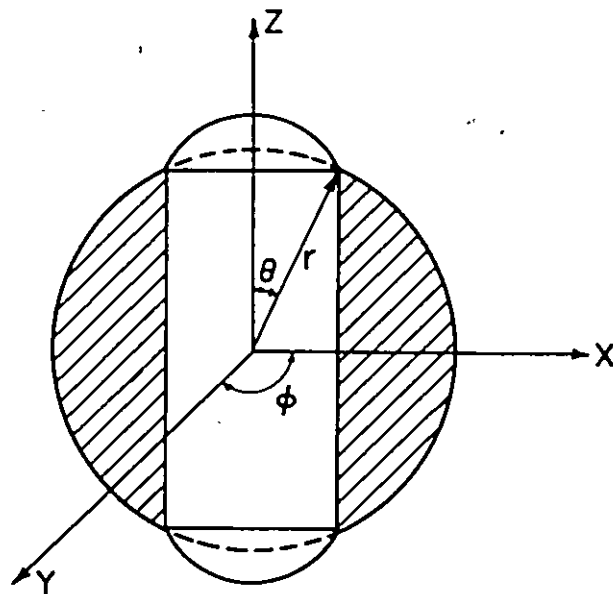
Fig. II-1 : Schematic representation of cavity nucleation. Cavities have formed as "caps" at the particle poles in the direction of the maximum tensile stress (after Goods and Brown, 1979).

are located which cavitate first; in this case, the plastic zone around a particle is affected, then modifying the relaxation process, thus the value of the unrelaxed plastic strain. The condition (II - 1) has to be solved numerically because of the large number of non-analytical equations involved. Finally it must be noted that this energy requirement is only a necessary condition, i.e. the critical stress criterion has to be fulfilled simultaneously to nucleate a void. Tanaka et. al. (1970) have shown that the energy requirement is fulfilled upon yielding for all particles whose radius is larger than 25nm. It appears then that the local stress criterion is the most critical one, as the particle radii considered are generally larger than 25 nm.

The local stress criterion is very simple: the stress at the particle-matrix interface must be at least equal to the interfacial strength σ_I, which is a characteristic of a system particle-matrix in a given condition. The problem is then to calculate the local stress at the interface using realistic models of the plastic zones surrounding the particles.

The first approach to be considered is the continuum plasticity one, proposed by Argon et al. (1975) for large particles. The maximum interfacial stress resulting from a pure shear loading is found to be nearly equal to the strain-dependent flow stress of the matrix in tension. If, however, a hydrostatic stress σ_T is existing in the far deformation field, it has to be included in the calculation of the stress, which becomes:

$$\sigma_{loc} \simeq Y(\bar{\epsilon}^P) + \sigma_m \qquad (II - 8)$$

where $Y(\bar{\epsilon}^P)$ is the flow stress in tension, and σ_m is the hydrostatic
or mean stress component of the stress field, thus including any
superimposed hydrostatic pressure or tension.

The second type of approach deals with a description in
terms of dislocations of the deformation around a particle.
Ashby (1966) considers a model of plastic relaxation by punching out
dislocation loops. These loops form reverse pile-ups and can build
up increasing interfacial stress. The local stress is then:

$$\sigma_{loc} = \alpha \ \frac{\epsilon R_o}{2 \ kb} \qquad (II - 9)$$

where α is a constant and k is the length of the stack of dislocation
loops, i.e. roughly half the interparticle spacing. The nucleation
strain is given by:

$$\epsilon_N \geq \frac{\sigma_I}{R_o} \ \frac{2kb}{\alpha} \qquad (II - 10)$$

This equation gives the right variation of ϵ_N with particle size.
Brown and Stobbs (1976) consider that plastic relaxation occurs by
secondary slip, and is accompanied by strong work hardening around
the particle, making subsequent relaxation more difficult. They
use an extremum analysis to obtain the local stress at the interface
σ_{loc} and the dislocation density ρ_ℓ around the particle. Their results
are:

$$\sigma_{loc} = 4.2\ \sigma_\ell \qquad\qquad (II - 11)$$

where σ_ℓ is the flow stress which is related to the dislocation density by:

$$\sigma_\ell = \alpha\ \mu\ b\ \sqrt{\rho_\ell} \qquad\qquad (II - 12)$$

where α is a constant equal to 1/7 and μ the shear modulus of the matrix. The dislocation density is found to be:

$$\rho_\ell \simeq 1.7\ \frac{\varepsilon}{R_o\ b} \qquad\qquad (II - 13)$$

Using equations (II - 11) to (II - 13), the nucleation strain is:

$$\varepsilon_N \geq \frac{1}{30}\ \left(\frac{\sigma_I}{\alpha\mu}\right)^2\ \frac{R_o}{b} \qquad\qquad (II - 14)$$

Finally, the nucleation strain is sensitive to any hydrostatic stress which is superimposed. In order to take this into account in the microscopic approach, Goods and Brown (1979) determine the relationship between ε_N· and the stress state by considering all the stress terms contributing to the decohesion:

- the flow stress $\bar{\sigma}$

- the local stress σ_{loc}

- any applied hydrostatic stress σ_H

Brown and Stobbs (1976) have expressed $\bar{\sigma}$ as a function of microstructural parameters and of the strain. It is however generally negligible in comparison of the local stress σ_{loc} given by rewriting ·equation (II - 14):

$$\sigma_{loc} = 5.4\ \alpha\ \mu\ \left(\frac{\varepsilon_N\ b}{R_o}\right)^{\frac{1}{2}} \qquad\qquad (II - 15)$$

at the occurrence of nucleation.

The nucleation condition is then:

$$\sigma_I \simeq \sigma_{loc} + \sigma_H \qquad (II - 16)$$

combining equations (II - 15) and (II - 16) leads to the following equation:

$$\sqrt{\epsilon_N} = H (\sigma_I - \sigma_H) \qquad (II - 17)$$

where H can be calculated for a given volume fraction and particle size. It should be noticed that equation (II - 17) differs from equation (II - 8) in the fact that the former does not include the hydrostatic component of the applied tensile stress, i.e. the flow stress itself. This component has however to be considered so that equation (II - 8) is more rigorous. However, Goods and Brown find a good agreement of equation (II - 17) with experimental data. They determine an interfacial strength for the system Fe - Fe_3C of 2000 MPa, which is close to the value of 1700 MPa obtained by Argon and Im (1975). Leroy (1978) has used the more rigorous equation (II - 8) on the same system and found a value of 1200 MPa. These values of interfacial strengths are, however, quite close and it can be concluded that the interface between Fe and Fe_3C breaks at a critical stress of about $\mu/50$.

II - 1 - 2 - 3 Conclusions

To conclude this portion of the review concerning the nucleation of voids, two points need to be emphasized:

- the dependence of ε_N on particle size is not unambiguously given from the experimental evidence. It could vary from one system to another, and should be examined with care. In relation to this, it is worth mentioning that Fisher and Gurland (1981) have proposed to use the particle size distribution to describe the progressive nucleation of voids: every increment of plastic strain corresponds to an increment in the critical radius to cavitate, which can in turn be related to an increase in the percentage of cavitated particles through the particle size distribution.

- the second point is related to the relationship between the nucleation strain and the local stress. When large strains are involved, the relaxation mechanisms around the particles are affected. Some recovery processes can occur and even lead to recrystallization (Humphreys, 1979). Therefore, the relationships between ε_N, ρ_ℓ and σ_{loc} have to be modified.

II - 1 - 3 Growth of Voids

Once the cavities have nucleated, they grow during further plastic deformation of the matrix.

Several experimental methods have been used to determine the growth of damage; they generally involve the observation of longitudinal sections of deformed or broken specimens (Leroy, 1978; Fisher and Gurland, 1981), but other methods such as density measurements are sometimes used (Schmitt and Jalinier, 1982).
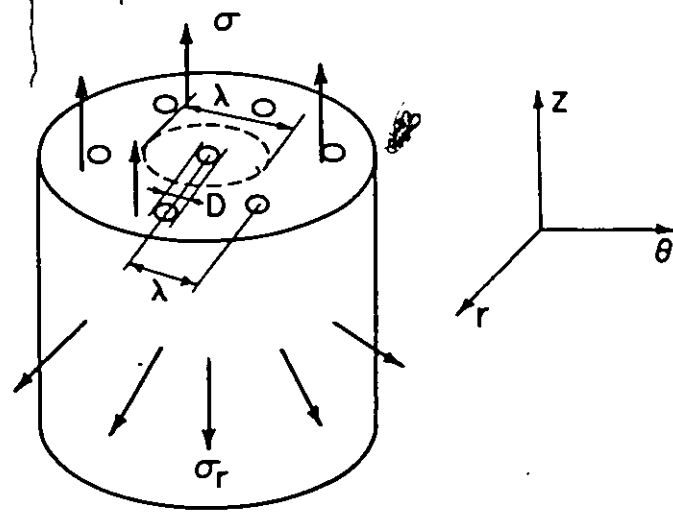
Fig. II-2 : Schematic diagram representing cylindrical holes
(after McClintock, 1968a).

The purpose of these measurements is to produce a relationship between the value of damage, expressed as an area or volume fraction of voids, or a variation in density, and the axial strain. These results are subsequently compared with predictions from theoretical models. Several treatments have been proposed, which are using the methods of continuum plasticity, and are dealing with the expansion of a pre-existing void under a particular state of stress.

The first model has been proposed by McClintock (1968a). He considers the growth of long cylindrical holes parallel to the tensile axis and having an initial spacing λ_o and diameter D_o (fig. II - 2). The integration of the growth law gives for the fracture strain :

$$\epsilon_f = \frac{2}{\sqrt{3}} \quad \frac{\ln F_f}{\sinh (\sqrt{3} \, \sigma_r / (\sigma_z - \sigma_r))} \qquad (II - 18)$$

where F_f is the relative growth factor given by :

$$F = \frac{D}{D_o} \quad \frac{\lambda_o}{\lambda} \qquad (II - 19)$$

at the onset of coalescence.

A modification can be done to consider cylindrical holes with elliptical cross-sections, and to take into account the strain hardening by an extrapolation between two extreme cases (elastic-plastic n = 0, and linear hardening n = 1). The fracture strain is then :

$$\epsilon_f' = \frac{(1 - n) \ln F_f'}{\sinh ((1 - n)(\sigma_1 + \sigma_2) / (2\bar{\sigma} / \sqrt{3}))} \qquad (II - 20)$$

where σ_1 and σ_2 are the two unequal transverse stress components. The ratio $(\sigma_1 + \sigma_2) / \bar{\sigma}$ characterizes triaxiality of the stress state.

The second model was developed by Rice and Tracey (1969). It describes the initial growth of an isolated spherical void of initial radius R_o in a non-hardening material. The analytical solution for the rates of growth is :

$$\dot{R}_i = R_o (\gamma \, \dot{\varepsilon}_i^\infty + (\frac{2}{3} \dot{\varepsilon}_j^\infty \, \dot{\varepsilon}_j^\infty)^{\frac{1}{2}} D) \qquad (II - 21)$$

where :

$\dot{R}_i$ = growth rate in the principal direction i

$\dot{\varepsilon}_i^\infty$ = remote strain rate in that direction

γ = amplification factor, varying between 5/3 for a strong hardening or very low triaxiality in a non-hardening material, and 2 for higher triaxiality in the latter case.

D is given by :

- for a non-hardening material

$$D = 0.56 \sinh (\frac{\sqrt{3}}{2} \frac{\sigma_m^\infty}{\tau_o}) \qquad (II - 22)$$

where :

σ_m^∞ = remote mean stress component

τ_o = shear yield stress

- for a strong linear hardening material

$$D = \frac{\sqrt{3}}{4} \frac{\sigma_m^\infty}{\tau_o} \qquad (II - 23)$$

In the right handside of equation (II - 21), the first term refers to a change in the shape of a void, and the second term to a change in its volume. This model emphasizes then the determining influence of the stress state parameter, i.e. the ratio σ_m / τ_o, on the growth of voids.

Particular cases have been considered for this model :

- if the void remains spherical, the shape change term disappears,

  and equation (II - 21) becomes :

$$\dot{R}_o / R_o = (\frac{2}{3} \dot{\varepsilon}_j^\infty \dot{\varepsilon}_j^\infty)^{\frac{1}{2}} \; D = \dot{\bar{\varepsilon}} \; D \qquad (II - 24)$$

- for an uniaxial tension test, equation (II - 21) takes the simplified

  form (Brown, 1976) :

$$\Delta R_{//} = R_o (2 + 0.56 \sinh (\frac{\sqrt{3}}{2} \frac{\sigma_m}{\tau_o})) \Delta\varepsilon_p$$
$$\Delta R_{\perp} = R_o (-1 + 0.56 \sinh (\frac{\sqrt{3}}{2} \frac{\sigma_m}{\tau_o})) \Delta\varepsilon_p \qquad (II - 25)$$

where $\Delta\varepsilon_p$ is a plastic shear strain increment, and $\Delta R_{//}$ and $\Delta R_{\perp}$
are the parallel and transverse dimensions of the void.

- Leroy (1978) has considered the change in the amplification factor

  γ in equation (II - 21).A spherical void elongates at a rate

which is twice that of the matrix. Therefore, in an axisymmetric

tension test, equation (II - 21) is written as :

$$\dot{R}_1 = R_1 (-\frac{\gamma_a}{2} + 0.56 \sinh (\frac{3}{2} \frac{\sigma_m}{\gamma})) \dot{\varepsilon}_3^\infty$$
$$\dot{R}_3 = R_3 (\gamma_a + 0.56 \sinh (\frac{3}{2} \frac{\sigma_m}{\gamma})) \dot{\varepsilon}_3^\infty \qquad (II - 26)$$

Here the subscript 3 refers to the tensile direction, Y is the flow

stress (constant) of the rigid-plastic material, and γ_a is the

amplification factor, decreasing from 2 for a spherical void, to 1

for a cylindrical void.

Taking :

$$\gamma_a = 1 + \frac{R_1}{R_3} \qquad (II - 27)$$

Leroy et. al. (1981) can integrate equations (II - 26) and they obtain:

$$R_3 = R_o \cdot \exp (D\bar{\epsilon}) \ [2 \exp (\frac{3}{2} \bar{\epsilon}) - 1]^{2/3}$$

$$R_1 = R_o \exp (D\bar{\epsilon}) \ [2 \exp (\frac{3}{2} \bar{\epsilon}) - 1]^{-1/3} \qquad (II - 28)$$

Using the Bridgman's analysis (1952) to calculate the variation of D with $\bar{\epsilon}$, Leroy et. al. (1981) can calculate the evolution of damage with strain from equations (II - 28), and this compares quite well with their experimental results (fig. II - 3).

In conclusion, the models which have been reviewed describe quite accurately the growth of voids as long as these are isolated. They might break down when the voids are too close to each other, i.e. when there is a high volume fraction of voids, or in the late stage of the deformation.

II - 1 - 4 Coalescence of Voids and Models of Ductile Fracture

The coalescence of voids which leads to final rupture is the most difficult step of the ductile fracture process to describe by a model.

From experimental observations, it has been shown that growing cavities can link in two possible ways: the first one is by normal contact, as the growth is limited by the interparticle spacing (Rogers, 1960); the second one is by localization of strain in well-defined shear bands occurring between voids (Palmer and Smith, 1966; Baker and Charles, 1971). If two populations of particles with different sizes exist, localization can take place between voids created at the larger particles, giving rise to the nucleation, growth
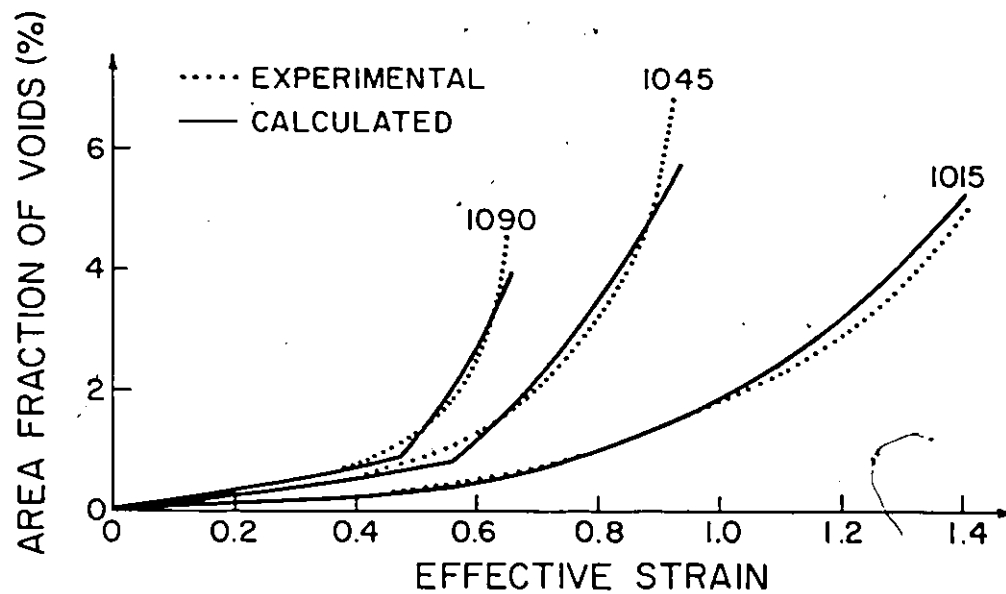
Fig. II-3 : Comparison of the calculated area fraction of voids
vs strain curves with the experimental ones (after
Leroy, 1978)
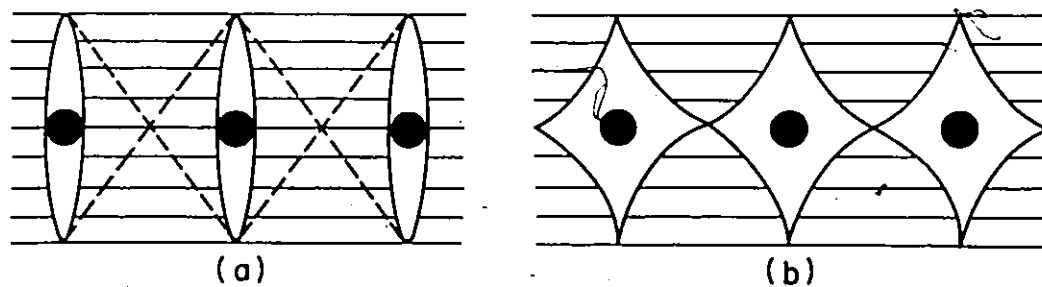
Fig. II-4 : Onset of internal necking after Brown and Embury
(1973). When a slip line field can be drawn between
voids, (a), fracture occurs by local necking (b).

and linkage of voids at the smaller particles within the shear
bands (Cox and Low, 1974).

The criteria and models of ductile fracture are generally
based upon a condition for localization of deformation. This
condition can be a geometric one, an energetic one or even can be
expressed from a bifurcation treatment in continuum mechanics.

II - 1 - 4 - 1 Geometric Models
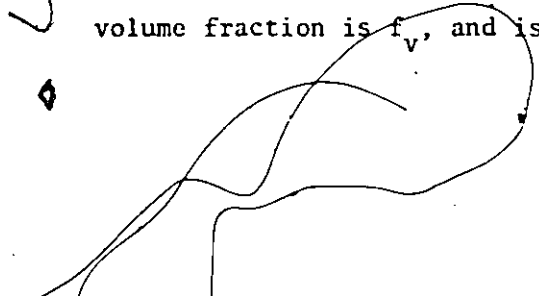
The method followed in these models is to find a critical
dimension of the voids at which several voids can join to form a
microcrack leading to final fracture.

The first model was proposed by McClintock (1968a). The
voids expand until they touch in the transverse direction. However,
this model leads to fracture strains highly over-estimated (Hancock
and MacKenzie, 1976).

Brown and Embury (1973) suggested that when the void length
parallel to the tensile axis is equal to the spacing between voids,
then a 45° slip line field can be drawn between the voids (fig. II - 4),
removing the plastic constraint and allowing internal necking i.e.
linking between voids. If a void is nucleated at a particle of
radius R_o, a further strain ϵ_g produces voids of length 2 R_o (1 + ϵ_g).
The fracture criterion is then:

$$2 R_o (1 + \epsilon_g) = \lambda \qquad (II - 29)$$

where λ is the mean planar spacing of spherical particles whose
volume fraction is f_v, and is given by:

$$\lambda = R_b \left[\sqrt{\frac{2\pi}{3 f_v}} - \sqrt{\frac{8}{3}} \right] \qquad (II - 30)$$

The fracture strain is therefore:

$$\varepsilon_f = \ln \frac{A_o}{A_f} = \ln (1 + \varepsilon_N + \varepsilon_g)$$

i.e. $\varepsilon_f = \ln \left[\sqrt{\frac{\pi}{6 f_v}} - \sqrt{\frac{2}{3}} + \varepsilon_N \right] \qquad (II - 31)$

This equation fits the experimental results quite well using a plot of ε_f vs f_v for different systems, if the nucleation strain ε_N is included.

Thomason (1968, 1971) has used a similar approach in which the material is assumed to deform homogeneously until localized deformation along a fracture path of voids becomes more favourable from an energetic point of view. The material necks down between voids, at such a small increase of the overall strain that fracture strain is equal to the strain at the beginning of this localization. The fracture strain ε_f is found to vary as $f_v^{-\frac{1}{2}}$.

Leroy (1978) used a criterion similar to that of Brown and Embury, to calculate the fracture strain under various stress states. At fracture, the void radius in the tensile direction is given by:

$$2 R_3^f = \phi \lambda$$

where ϕ is a constant which may be a function of the material tested, and was found to be close to unity for different spheroidized steels tested. Using the integrated growth laws (II - 28), the fracture strains can be determined for different stress conditions.

II - 1 - 4 - 2 Other Models

Due to the complication of the various factors governing void coalescence (material properties such as strain hardening rate, or shape and dimension of voids), alternative models to the geometric ones have been proposed more recently.

Melander (1980) considers a material composed of a work-hardening matrix and a three-dimensional regular distribution of voids. This distribution has a softening effect on the material. He assumes that crack initiation and, therefore, fibrous fracture, occurs when deformation becomes unstable, at the strain where the work-hardening ability of the matrix is just counter-balanced by the softening effects of voids (fig. II - 5). This occurs when the energy consumption per unit effective strain no longer increases with effective strain, i.e.:

$$\frac{d^2 W}{d \bar{\epsilon}} = 0 \qquad (II - 32)$$

and: $\qquad dW = \bar{\sigma} \, d \, \bar{\epsilon} - \sigma_m \, d \, \epsilon_{nn} \qquad (II - 33)$

where σ_m is the hydrostatic stress component and ϵ_{nn} the macroscopic dilation or variation of volume. Solving equation (II - 32) for the relevant parameters of a given material leads to an expression of the fracture strain as a function of volume fraction of particles and superimposed hydrostatic stress. According to Melander, the model agrees quite well with experiments done in the wire drawing of a copper bar. However, in regard to the great importance that local events have in the final linkage of voids, a macroscopic criterion such as equation (II - 32) seems to be questionable.
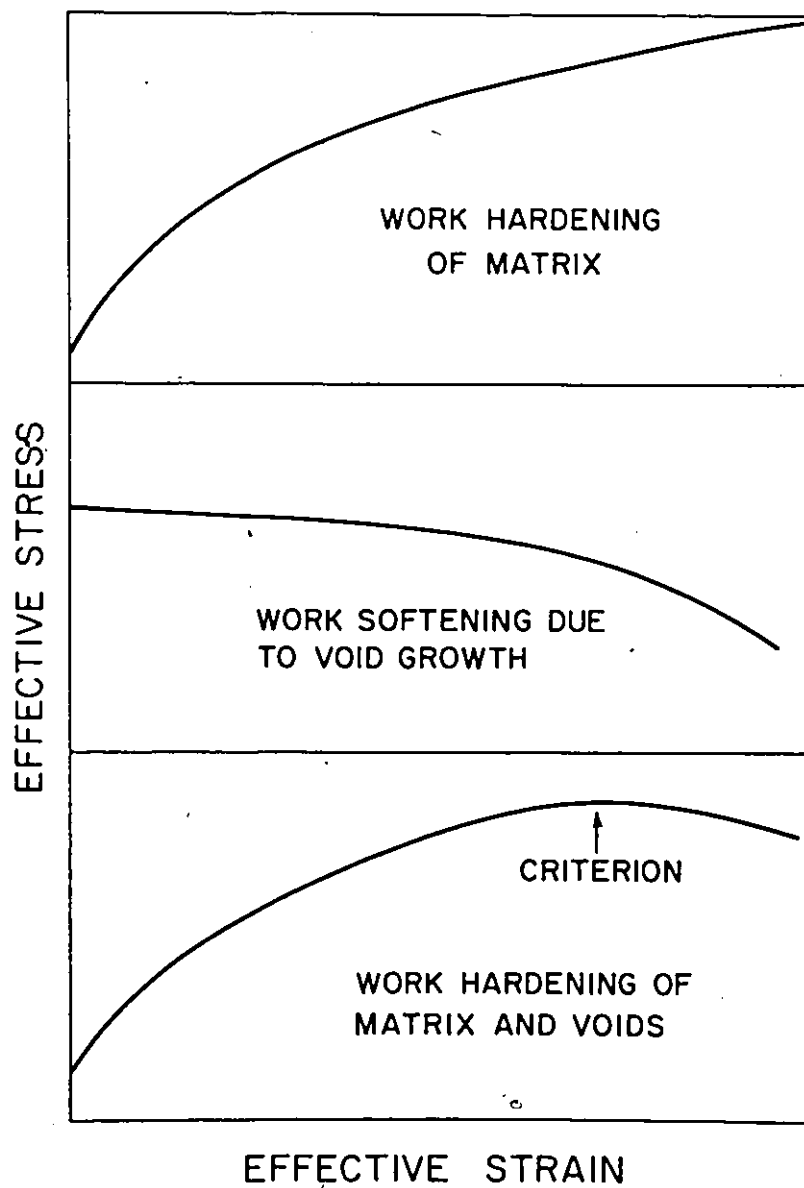
Fig. II-5 : Schematic representation of the criterion for ductile
fracture, after Melander (1980). Fracture occurs when
work hardening of the matrix is balanced by softening
from void growth.

Finally, it is worth considering a recent and attractive approach to the final coalescence of voids. It is, in fact, a part of a more general and extensive study of the conditions under which bifurcation to a localized mode of deformation occurs. Here, damage is involved not in a geometrical way, but as a deviation from normal plastic behaviour. Needleman and Rice (1978) and Yamamoto (1978) have examined the onset of such a localization in a ductile material containing a small initial imperfection. This imperfection is a narrow band of material where the volume fraction of voids is slightly higher than in the outside matrix. Using the constitutive equations for porous materials (Gurson, 1977a, 1977b), they calculate incrementally at what strain the deformation starts to localize within this band. More recently, Saje et al. (1982) have improved this model by introducing the possibility of nucleation and growth of voids. In order to compare their model with experimental results, they identify the strain at which localization occurs with the fracture strain. Doing so, their model compares rather well with the experimental results of Fisher and Gurland (1981), once the relevant nucleation parameters and magnitude of the imperfection have been adjusted.

This approach emphasizes then the importance of damage development on the intrinsic mechanical behaviour of the material, and despite the fact that it does not describe how the localization takes place physically, it represents an alternative to the geometric models.

II - 1 - 5 Conclusions

The three stages involved in the fibrous mode of ductile fracture, viz nucleation, growth and coalescence, have been widely studied, and the existing models give a good description of the different events. However, it is worth making two remarks:

- the drastic influence of the stress state on the nucleation and growth of voids has emerged clearly from this review. As porosity is created, the hydrostatic component of the stress tensor will influence the process of damage accumulation.

- There is still some uncertainty concerning the physical process involved in the coalescence of voids, and an unambiguous quantitative criterion for the onset of fracture is still not available.

II - 2 The Shear Fracture

II - 2 - 1 Introduction

It is a commonly observed fact that in deforming ductile materials up to sufficiently large strains in the plastic range, a smooth and continuously varying deformation pattern turns into a highly localized deformation in the form of a shear band. In such cases, two possibilities are observed: either the shear bands persist and support almost all the subsequent non-uniform deformation, or their formation leads directly to failure, i.e. the onset of localization means the occurrence of fracture.

These phenomena have been observed in a wide range of materials, from single crystals (Price and Kelly, 1964; Chang and Asaro, 1980;

Spitzig, 1981) to polycrystals (Chung et al., 1977; Tanaka and Spretnak, 1973; Anand and Spitzig, 1982), and are very often a problem in rolling processes (Lloyd, 1982; Korbel et al., 1982).

The fracture surfaces obtained after final separation along the shear bands are covered with characteristic shallow elongated dimples. These dimples are associated with the existence of some form of damage within the bands, such as voids opened at second phase particles. The question then arises to know whether localization of deformation is responsible for the creation of voids, due to the large strains reached into the bands, or if localization occurs because of the existence of an array of voids created by prior plastic deformation. Obviously, the latter is happening in the outer part of the "cup and cone" fracture surface, and the former could be happening in the creation of voids at smaller particles within a band of localized flow created between voids opened at larger particles (Cox and Low, 1974).

After a short review of the main characteristics of shear bands, the two attempts made to answer the question previously asked will be presented. The first one deals with structural reasons and parameters, while the second one is based on a continuum mechanics bifurcation analysis.

II - 2 - 2 Characteristics of the Shear Bands

The purpose of this part is to present some common features found experimentally about shear bands. Recently some comprehensive reviews have been published (Hatherly, 1982; Gil-Sevillano et al.,

1980; Chandra-Holm and Embury, 1982; Pierce et al., 1982), from where the following points are taken.

Shear bands are a form of plastic instability. They are initially confined to a single grain or a group of grains, and they become really macroscopic at higher strains, that is to say they spread through the entire specimen, crossing the grain boundaries without deviation.

They have no crystallographic appearance: their shear systems (plane & direction) do not coincide with crystallographic slip systems of the matrix.

Some transmission electron microscopic observations show that inside a shear band, the lattice is rotated with respect to the matrix one.

Shear bands are generally thin and contain elongated sub-grains aligned with the shear plane. Indeed, very large strains can be reached inside shear bands, so that recrystallization can occur.

Inside the shear bands, there is some evidence that deformation occurs by multiple slip, and boundaries between matrix and bands are grain boundaries.

In the case of ductile single crystals, shear bands occur while the material is strain hardening. It appears that in stronger crystals with lower strain hardening rates (or with rates decreasing rapidly with strain), localized shear can be quite abrupt, leading to rapid shear fracture. On the contrary, in higher hardening materials, or in softer ones, necking is more pronounced, and shear bands form gradually with strain.

For rolled products, assuming that the boundary planes of the bands are parallel to the shear plane, then the shear bands are at $\pm 35^\circ$ to the main strain axis. However, some important deviations can occur.

Therefore, it appears that over a wide range of deformation paths and materials, shear bands have some important common characteristics. This leads then to think about a unique mechanism for the creation of these bands, i.e. for the occurrence of localized deformation.

II - 2 - 3   The Classical Approach

This approach emphasizes the structural reasons in the occurrence of localization. The principle of this is the following: strain localization occurs through a local softening process, which can be of two types.

The first type is a geometrical softening, whose structural cause is a rotation of the lattice within a band, leading to a softening which competes with the work hardening of the material to reduce the stiffness of the material. However, the reasons for this softening are not well understood at a microscopic scale. Macroscopically, a model has been proposed by Gil-Sevillano et al. (1980), using the Taylor and Bishop-Hill theories. The condition for localization is the achievement of an ideal plastic state, i.e.:

$$\frac{1}{\bar{\sigma}} \frac{d\bar{\sigma}}{d\bar{\varepsilon}} \leq 0 \qquad\qquad (II - 34)$$

The flow stress $\bar{\sigma}$ is given by:

$$\bar{\sigma} = M \tau_c(\Gamma) \qquad (II - 35)$$

where τ_c is the critical shear stress of a given slip system, and is

depending only on Γ, the total slip accumulated in the grain. M is the

Taylor factor. Therefore :

$$\frac{d\bar{\sigma}}{d\bar{\epsilon}} = \tau_c \cdot \frac{dM}{d\bar{\epsilon}} + M^2 \frac{d\tau_c}{d\Gamma} \qquad (II - 36)$$

Considering a linear hardening law $\tau_c(\Gamma)$ within a small range where $\theta = \frac{d\tau_c}{d\Gamma}$

can be regarded as a material constant, equation (II -36) becomes :

$$\frac{d\bar{\sigma}}{d\bar{\epsilon}} = \tau_c \frac{dM}{d\bar{\epsilon}} + M^2 \theta \qquad (II - 37)$$

$M^2 \theta$ is the contribution of work hardening, $\tau_c \frac{dM}{d\bar{\epsilon}}$ is the contribution of

geometrical softening or hardening. If $dM/d\bar{\epsilon}$ is sufficiently negative, i.e.

if a local softening process occurs, it can overcome the work hardening

term and fulfill equation (II - 34). For a polycrystal, the equations must

be averaged over all the grains, so that the development of a texture is

of great importance in the occurrence of localization.

The second type of softening, is a structural softening, which is

temperature and strain rate dependent. It can take different forms such as

adiabatic shearing (Chin et al., 1964), rapid recovery or in-situ recrystal-

lization. These events are related to the existence of high strain rates

inside the shear bands. Therefore, they may not trigger localization and

shear band formation, but rather be a consequence of the development of a

shear band. It is very difficult to give a definitive answer to this

question. The condition for growth of a band of localized flow can be

macroscopically expressed by the decrease in the load bearing capacity of

the material :

$$dF < 0 \quad \text{and} \quad F = \sigma A \qquad (II - 38)$$

where F is the load and A the cross-sectional area. Using a constitutive relationship for the flow stress of the form :

$$\bar{\sigma} = \bar{\sigma}(\bar{\epsilon}, \dot{\epsilon}, T) \qquad (II - 39)$$

where T is the absolute temperature and $\dot{\epsilon}$ the strain rate, the condition (II - 38) becomes :

$$d\bar{\sigma} = \left(\frac{\partial\bar{\sigma}}{\partial\bar{\epsilon}}\right)_{\dot{\epsilon},T} d\bar{\epsilon} + \left(\frac{\partial\bar{\sigma}}{\partial\dot{\epsilon}}\right)_{\bar{\epsilon},T} d\dot{\epsilon} + \left(\frac{\partial\bar{\sigma}}{\partial T}\right)_{\dot{\epsilon},\bar{\epsilon}} dT \leq 0 \qquad (II - 40)$$

Unfortunately, a constitutive law such as (II - 39) does not exist over a large enough range of conditions to be used in equation (II - 40). Chung et al. (1977) have altered this treatment by expressing the change in elastic energy during straining. They find the following condition :

$$\left(\frac{\partial\bar{\sigma}}{\partial\bar{\epsilon}}\right) d\bar{\epsilon} + \left(\frac{\partial\bar{\sigma}}{\partial\dot{\epsilon}}\right) d\dot{\epsilon} < 0 \qquad (II - 41)$$

i.e. either a strain softening or a negative strain rate sensitivity are required for strain localization.

Therefore, for both these two types of softening, it can be concluded that their microscopic causes are not well established, and that their macroscopic description is not complete.

It is worth now presenting the models which have been proposed to explain the relationship between the existence of voids and the creation of shear bands. Berg (1962) emphasized that localized flow could occur in porous materials. Assuming that a shear band exists prior to the occurrence of any porosity, McClintock et al. (1966) have developed a theory to explain subsequent void growth in the shear band. The voids of initial radius R_o are considered to be located in elements of material of longitudinal dimension L_ℓ and transverse dimension L_t with respect to the

shear band. Fracture is occurring when the voids grow to touch an element boundary. The resulting approximate equation for the ratio of longitudinal cell size to void diameter $L_\ell/2R_o$ in terms of the shear strain γ is :

$$\ell n \frac{L_\ell}{2R_o} = \ell n \sqrt{1 + \gamma^2} + \frac{\gamma}{2(1 - n)} \sinh \frac{(1 - n)\sigma}{\tau} \quad \text{(II - 42)}$$

Similarly, for the transverse dimension, the equation is :

$$\ell n \frac{L_t}{2R_o} = \frac{\gamma}{2(1 - n)} \sinh \frac{(1 - n)\sigma}{\tau} \quad \text{(II - 43)}$$

Here, n is the strain hardening exponent, τ is the principal shear stress and σ the mean normal stress. French and Weinrich (1979) have applied this theory to the shear fracture mode in sheets of spheroidized steels, and found that the model was predicting higher shear strains to fracture than those experimentally measured.

The other possibility is the occurrence of a band of localized flow between adjacent voids. Recently, Dodd and Atkins (1983) have shown that data on shear strains related to flow instabilities, which are considerably overestimated by thermoplastic theory such as equations (II - 40) or (II - 41), are readily explained by isothermal geometric softening due to the presence of voids. McClintock (1968b) has proposed an approximate analysis of the termination of ductile fracture by localized shear. The geometry under consideration is shown in fig. II - 6. The first condition for a shear band to appear is that the load for shearing be less than that for homogeneous deformation. By an upper-bound calculation, McClintock obtains :
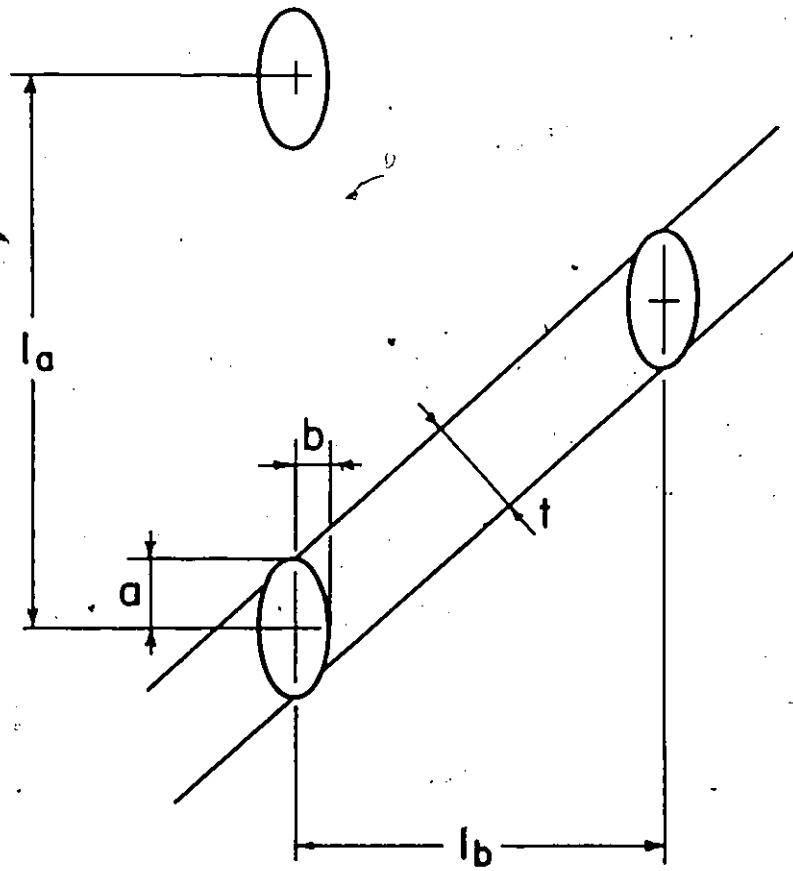
Fig. II-6 : Shear band joining adjacent ellipsoidal holes with
semi-axes a, b, c; the c direction is normal to l_a
and l_b (after McClintock, 1968b).

$$\frac{\sqrt{3}}{2} > [1 - \frac{\pi \; ab}{l_a \; l_b} \; \sqrt{2(1 + a^2/b^2)} \;] / (1 - \frac{4}{3} \pi \frac{a}{l_a} (\frac{b}{l_b})^2) \quad (II - 44)$$

This condition is a function of three independent geometrical ratios
defined in fig. II - 6, but is independent of the strain hardening
rate. The second condition is that the maximum load has been
attained for the localized mode. Considering that the shear band
is thin enough compared to the voids so that it may be considered
to shear them without producing any other deformation, McClintock
gives an upper-bound estimate of the condition. The area of the
voids increases by shearing by:

$$d \; A_v = 2 \; c \; du \quad (II - 45)$$

where du is the displacement and 2c is the void dimension normal
to the plane of fig. II - 6, (b = c). The shear displacement is
given by:

$$du = t \; d\gamma \text{ and } d\gamma = \sqrt{3} \; d\epsilon$$

where t is the thickness of the band.

The net area of an element surrounding a single void, A_n, is the
gross area A_t less the area of the void intercepted by the slip
plane, A_v, and is given by:

$$A_n = \sqrt{2} \; l_b \; l_c - \pi \; bc \; \sqrt{2(a^2/b^2 + 1)} \quad (II - 46)$$

when localization occurs, the load is decreasing, so that:

$$d \; F = \tau \; dA_n + A_n \; d\tau < 0 \quad (II - 47)$$

The final condition is then:

$$\frac{1}{\bar{\sigma}} \frac{d\bar{\sigma}}{d\bar{\epsilon}} < \sqrt{6} \; ct / l_b \; l_c \quad (II - 48)$$

or, taking t of the order of $\sqrt{a^2 + b^2}$,

$$\frac{1}{\bar{\sigma}} \frac{d\bar{\sigma}}{d\bar{\varepsilon}} < \sqrt{6} \quad c\sqrt{a^2 + b^2} \ / \ l_b \ l_c \qquad\qquad (II - 49)$$

This condition then expresses that localization will occur as soon
as the strain hardening rate will fall below a certain value given
by the geometrical distribution of voids in the material. This
will happen if two conditions are met: first, a low strain hard-
ening rate must be reached; this will be the case if large strains
are obtained; secondly, the voids will have to develop enough but not
coalesce or link, which would give a fibrous fracture mode. As it
will be seen later in this review, these two conditions are met
when a sufficiently high hydrostatic pressure is superimposed during
the tensile deformation of a ductile material.

II - 2 - 4   The Continuum Mechanics Approach

This type of model has already been mentioned for the final
coalescence of voids in fibrous ductile fracture. Flow localization
was created in this case due to deviations from the normal plastic
behaviour occurring in the material because of the presence of voids.
The occurrence of shear bands similarly stems from deviations from
normal behaviour in the material. Rice (1976) and Needleman and
Rice (1978) have given the general procedure to be followed:

- first, determine the constitutive equations explaining the
  pre-localization behaviour of the material, taking into account
  any non-normality effects.

- secondly, determine some physical parameters which must reach
  a critical value for the bifurcation to a non-uniform deformation
  pattern to occur.

- finally, compare these predictions with experimental data.

Departures from the classical rate independent Prandtl Reuss equations

have to be considered in the determination of constitutive laws.

A first type of departure is the existence of a vertex on the yield

surface. Fig. II - 7 illustrates the difference between a smooth yield

surface, and a yield surface with a vertex. In the latter case, the

normality rule does not necessarily apply. These vertices are a con-

sequence of the discreteness of slip systems within a grain (Hill, 1967),

or in rocks, they are related to the presence of micro fissures; this

has led Rudnicki and Rice (1975) to propose approximate modified Prandtl-

Reuss equations.

The second type of departure is the existence of non-normality effects,

such as a pressure-sensitive yielding, i.e. the existence of a strength

differential effect in high strength steels (Spitzig et al., 1975, 1976)

having a yield strength in compression different from that in tension.

In single crystals, deviations from the Schmid law can appear due to the

occurrence of cross slip (Asaro and Rice, 1977).

As an example of this type of treatment, the results obtained by Asaro

(1979) and Chang and Asaro (1980) for the occurrence of shear bands in

single crystals of Al - 3% Cu are presented. Their theoretical model

assumes an idealized symmetric double crystalline slip as shown in

fig. II - 8, where $m^{(1,2)}$ are the slip plane normals and $s^{(1,2)}$ the

slip vectors. Assuming that yielding on the slip systems $\alpha = 1, 2$

occurs according to the Schmid law with $(h_{\alpha\beta})$ being the hardening matrix,
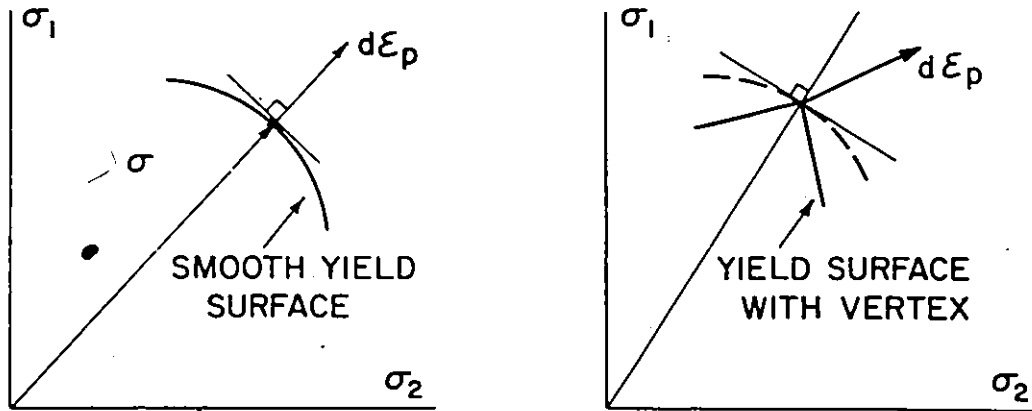
Fig. II-7 : Schematic representation of the difference between a smooth yield surface and a yield surface with a vertex.
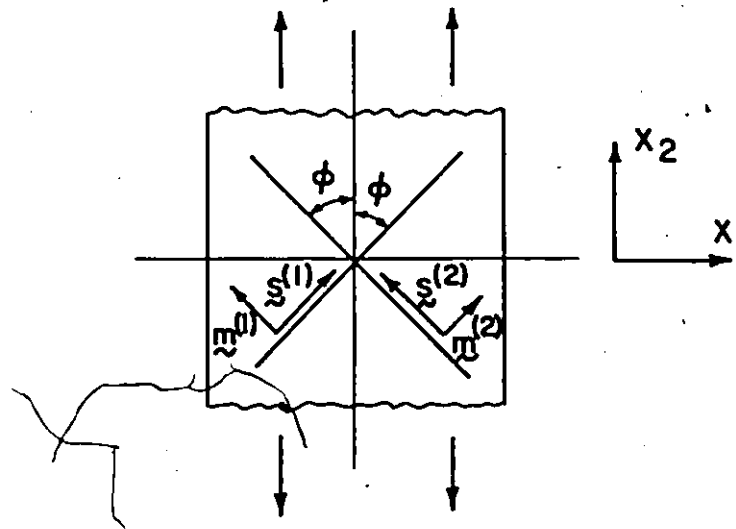
Fig. II-8 : Geometry for idealized symmetric double crystalline slip (after Asaro, 1979).

and taking an orthotropic, incompressible and pressure insensitive material, the constitutive laws can be determined in terms of the Jauman rate of the Cauchy stress defined by:

$$\overset{\nabla}{\underset{\sim}{\sigma}} = \dot{\underset{\sim}{\sigma}} - \underset{\sim}{\Omega} . \underset{\sim}{\sigma} - \underset{\sim}{\sigma} . \underset{\sim}{\Omega}^T , \qquad (II - 50)$$

where $\dot{\underset{\sim}{\sigma}}$ is the material rate of change of the Cauchy stress tensor $\underset{\sim}{\sigma}$, $\underset{\sim}{\Omega}$ is the rate of rotation and $\underset{\sim}{\Omega}^T$ its transpose. Asaro obtains:

$$\overset{\nabla}{\sigma}_{22} - \overset{\nabla}{\sigma}_{11} = \frac{2 \, G \, (h + h_1)}{(h + h_1) \, 2G \, \sin^2 2\phi} \, (D_{22} - D_{11}) \qquad (II - 51)$$

$$\overset{\nabla}{\sigma}_{12} = \frac{2G \, (h - h_1 + \sigma \, \cos 2\phi)}{h - h_1 + 2G \, \cos^2 2\phi} \, D_{12} \qquad (II - 52)$$

$$D_{11} + D_{22} = 0 \qquad (II - 53)$$

$\underset{\sim}{D}$ is the rate of deformation tensor, G the elastic shear modulus and the hardening matrix is taken as:

$$h_{11} = h_{22} = h$$
$$h_{12} = h_{21} = h_1$$

h_1 expresses the existence of latent hardening.

Two remarks can be made about these constitutive laws. First, the term $2G \, \cos^2 2\phi$ in the denominator of equation (II - 52) is in fact a vertex on the yield surface, as the "effective" shear modulus is no more G, but $G \, \cos^2 2\phi$. Secondly the term $\sigma \, \cos^2 2\phi$ in the numerator of equation (II - 52) gives an account of the geometrical softening due to the rotations of the crystal lattice in the stress field.

The next step is to analyze the bifurcation by looking at conditions under which deformation concentrates into a narrow band, which is shown schematically in fig. II - 9. Within this band, incremental field quantities are allowed to take values different from their values outside the band, with an homogeneous deformation state presumed to prevail both inside and outside the band. Then two conditions have to be fulfilled:

- the velocity gradient field $v_{i,j}$ inside the band differs from that outside $v^o_{i,j}$ only by an expression of the form:

$$v_{i,j} - v^o_{i,j} = g_i n_j \qquad (II - 54)$$

- it must have a continuing equilibrium across the band, so that:

$$n_i \dot{\sigma}_{ij} - n_i \dot{\sigma}^o_{ij} = 0 \qquad (II - 55)$$

where $\dot{\sigma}_{ij}$ and $\dot{\sigma}^o_{ij}$ are the stress rates within and outside the band respectively.

Writing the constitutive laws in the form:

$$\dot{\sigma}_{ij} = C_{ijk\ell} v_{k,\ell}$$

and assuming that the coefficients $C_{ijk\ell}$ apply both inside and outside the band, the two requirements (II - 54) and (II - 55) are satisfied simultaneously if:

$$\det (n \cdot C \cdot n) = 0 \qquad (II - 56)$$

From this analysis, Hill and Hutchinson (1975) have shown that a shear band can form on a plane with normal (n_1, n_2) if the following equation has real roots in $(n_2/n_1)^2$:
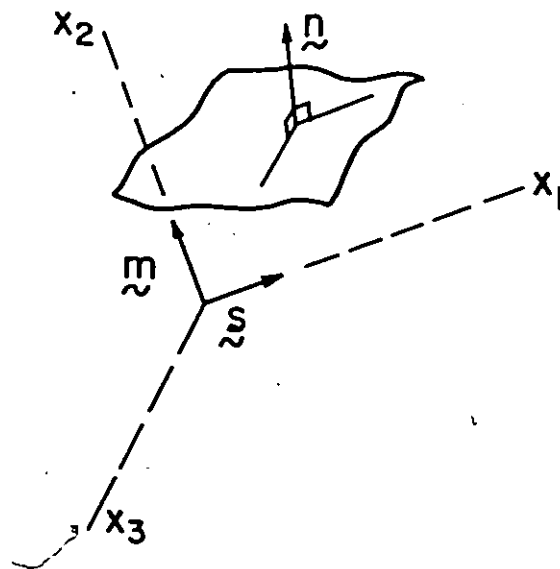
Fig. II-9 : Schematic representation of of the band where
localized deformation takes place.
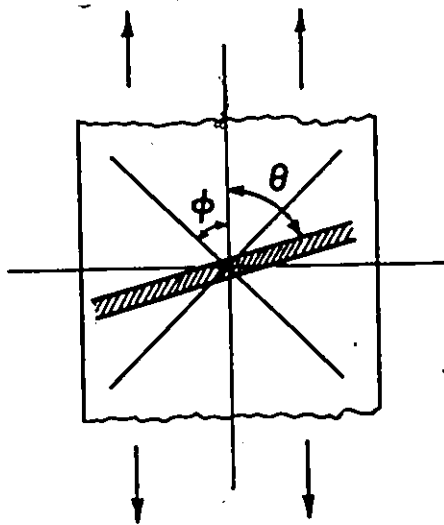
Fig. II-10 : Geometry of the shear band with respect to the
slip planes (after Asaro, 1979).

$$(\mu - \frac{1}{2} \sigma) \, n_1{}^4 + 2 \, (2\mu^* - \mu) \, n_1{}^2 \, n_2{}^2 + (\mu + \frac{1}{2} \sigma) \, n_2{}^4 = 0 \quad (II - 57)$$

where:

$$\mu^* = \frac{2G \, (h + h_1)}{(h + h_1) + 2G \, \sin^2 2\phi}$$

$$\mu = \frac{2G \, (h - h_1 + \sigma \, \cos 2\phi)}{h - h_1 + 2G \, \cos^2 2\phi}$$

Taking $\phi = 35°$, which is commonly found in f.c.c. materials, this gives $\mu > 2\mu^*$, and the roots are positive if the hardening rate is such that:

$$\left(\frac{h}{\sigma} \right) \leq \frac{\cos 2\phi \, \pm \, \dfrac{\sin 4\phi}{\sqrt{2 \, (1 + k)}}}{2 \, (k + \cos 4\phi)} \, \sin^2 2\phi \quad (II - 58)$$

where

$$k = h_1/h$$

This gives:

$$\left(\frac{h}{\sigma} \right)_{crit} = \begin{cases} 0.064 & \text{if } k = 0 \\ 0.040 & \text{if } k = 1 \\ 0.028 & \text{if } k = 2 \end{cases}$$

It is necessary to know the specific orientation of the band; indeed the band can have an orientation θ different from that ϕ of the slip system as shown in fig. II - 10. In this case, the critical hardening rate is:

$$\left(\frac{h}{\sigma} \right)_{crit} = \frac{\cos 2\theta \, \dot{-} \, \cos^2 2\theta' / \cos 2\phi}{(1 - k) \, \cos^2 2\theta / \cos^2 2\phi + (1 + k) \, \sin^2 2\theta / \sin^2 2\phi} \quad (II - 59)$$

Taking $k = 0$ and $\phi = 35°$, the maximum of $(h/\sigma)_{crit}$ is reached for $\theta = 40°$. Therefore, the bands are predicted to rotate from the slip planes by several degrees away from the tensile axis.

The experimental results of Chang and Asaro (1980) are very

consistent with the predictions of the model. For an Al - 3% Cu alloy,

they find that, regardless the microstructure of the initial orientation,

the critical hardening rate is:

$$\left(\frac{h}{\sigma} \right)_{crit} = 0.035$$

The angle between the tensile axis and the slip traces is about 30°, while

that between the macroscopic band and the tensile axis is about 40°.

To conclude this section, the bifurcation analysis seems to provide

a good description of the onset of localized deformation in different

materials. In particular, it shows that shear bands can be formed for a

positive value of the strain hardening rate, i.e. prior to the achievement

of an "ideal" plastic state. However, this analysis does not give answers

about the microstructural events which trigger localization.

II - 2 - 5 Conclusions

The occurrence of localized deformation is a common feature of the

deformation of materials. This phenomenon can be described by a sequence

of nucleation of a shear band and its subsequent growth through the

material. The nucleation event has some microstructural reasons related

to the slip behaviour, the dislocation substructure, and/or the distribution

of damage in the form of voids or microcracks. It can, however, be described

quite accurately by a continuum plasticity model of bifurcation which does

not take into account the physical reasons for bifurcation.

Shear band formation is closely related to damage. In particular, if damage follows the creation of a shear band, any means of delaying damage growth should bring the opportunity of delaying final catastrophic failure and, therefore, the possibility of studying the shear bands in detail.

II - 3   The Brittle Fracture

II - 3 - 1   Introduction

The brittle fracture involves the nucleation and growth of micro-structural damage prior to final failure. In this case, damage takes the form of microcracks which are propagating at very high speed through the material, with little associated plastic deformation.

Brittle fracture is the usual mode of failure of rocks and concrete, but it can also appear in a wide range of metals when the temperature is low enough or when the strain rate is high enough, or, in a separate form, in metals which have been grain boundary embrittled.

The microcracks can appear and propagate in two ways: either trans-granularly or intergranularly. In the first case, referred to as cleavage fracture, the cracks are nucleated in a grain, and cross the boundaries to spread through the adjacent grains. In the second case, the cracks nucleate and propagate along the grain boundaries: this is the intergranular fracture.

In this section the two forms of brittle fracture will be reviewed briefly in order to see how they can be influenced by the stress state. The review will also include some information concerning the deformation and fracture of rocks.

II - 3 - 2   Intergranular Fracture

This mode involves the propagation of cracks along grain boundaries which have been weakened either by the accumulation of impurity elements or by the presence of a continuous film of a brittle phase. Another possibility is for the fracture to have an intergranular path, but to progress by the linkage of voids created around second phase particles existing on the grain boundaries: it is, therefore, a ductile fracture which follows the grain boundaries.

Intergranular fracture in steels and iron alloys has been reviewed by Briant and Banerji (1978). They have concluded that the fact that grain boundaries are the lowest energy paths for fracture is quite often related to their chemical composition. In some cases, the weakness of the grain boundaries is due to the presence of an extensive second phase precipitated at the boundary, such as AℓN in a slow cooled aluminum-killed steel (Wright and Quarrel, 1962), titanium carbonitrides in thermally embrittled maraging steels (Spaeder, 1970), or MnS precipitates in overheated steels (Brammer, 1963). Very often, the boundaries are weakened because of the segregation of certain solutes elements. Such a segregation has been widely studied in low alloy steels in which the most common grain boundary embrittling agents are from groups IV B to VI B in the periodic table of elements. The segregation is also strongly influenced by the presence of alloying elements in steels, such as Ni, Cr, Mo (Low et al., 1968; Marcus et al., 1972; Mulford et al., 1976; Dumoulin et al., 1980). Experimentally, the most widely used technique is   Auger electron spectroscopy. An example of this is given by Palmberg and Marcus (1969) who studied the segregation of Sb and P in pure iron. The degree of embrittlement is measured by the increase in the

ductile-brittle transition temperature, and/or in the appearance transition temperature. Theoretical treatments deal with the thermodynamics and the kinetics of segregation, and with the influence of segregated elements on the cohesive strength of grain boundaries.

McLean (1957) first derived an expression for the equilibrium segregation, with the help of statistical mechanics assuming that the grain boundary is a random ideal solid solution without any interactions between segregated elements and alloying ones. This last assumption was found to be wrong, and recently Guttman (1975, 1979, 1983) developed a model taking into account these interactions.

The kinetics of segregation has also been analyzed by McLean, assuming local equilibrium between a boundary layer and the neighbouring bulk material, and using a diffusional analysis. Tyson (1978) proposed a model using a computer simulation, and has obtained a faster segregation than that predicted by McLean.

The influence of segregation on fracture behaviour involves two concepts:

- first, the local modification of the bonding and subsequent energy to fracture;

- secondly, the modification of the local dislocations-boundary inter- actions, and hence the ability to spread plastic deformation at the grain boundary.

The ideal work of fracture per unit area of grain boundary is given by:

$$\gamma = 2\gamma_s - \gamma_b \qquad \text{(II - 60)}$$

where γ_s is the surface energy and γ_b is the grain boundary energy. This equation can only be used for the equilibrium process, as γ_s and γ_b refer to equilibrium values. As fracture is essentially an irreversible process, then equilibrium thermodynamics cannot be applied. However, Low (1954) obtained a value for γ of 3500 ergs/cm^2 in a decarburized low carbon steel containing oxygen, which agrees quite well with the value of 3120 ergs/cm^2 calculated from equation (III - 60) using γ_s = 1950 erg/cm^2 (Linford, 1973), and γ_b = 780 erg/cm^2 (Hirth and Lothe, 1968). This ideal work γ is, however, insufficient when explaining theoretically microcrack propagation (Knott, 1977). As proven experimentally, for example, by the broadening of X-ray lines in diffraction studies of fracture surfaces (Felbeck and Orowan, 1955), some plastic deformation, i.e. dislocation activity accompanies crack propagation. Therefore, another term, γ_p, or local plastic work, must be added to the ideal work γ to give the actual work at fracture. McMahon and Vitek (1979) have developed a qualitative model of microcrack propagation, arguing that the plastic work γ_p depends on the ideal work γ, and that a small change in γ, due to segregation, leads to a large change in γ_p. They have extended this model quantitatively later (Jokl et al., 1980). These later authors also propose some tentative ideas about the physical nature of the embrittlement phenomenon.

Other examples of intergranular fracture occur in aluminum alloys. Very often, they are of the type referred to earlier, in which fracture occurs by coalescence of voids formed at particles present at the boundaries. In this case, the fracture surface, which has a typical faceted appearance, shows on each facet many small dimples, proof of a ductile type of process, i.e. the existence of large local plastic deformations. This occurs quite often in high purity aluminum alloys, such as Al - Zn - Mg (Ryder

and Smale, 1963; Kawabata and Izumi, 1976), Al - Mg - Si (Evensen et al., 1975; Dowling and Martin, 1973), Al - Cu (Martin, 1982). The first cause of this type of failure is the existence of precipitate-free zones (PFZ) adjacent to the grain boundaries in aged alloys. These soft and ductile layers are prone to easy plastic flow, leading then to the nucleation, growth and coalescence of voids at the particles existing on the grain boundaries. Embury and Nes (1974) used a simple model of PFZ to derive a fracture strain as a function of the areal fraction of precipitates in the PFZ. Kawabata and Izumi (1976) have shown the importance of the width of the PFZ on the intergranular fracture of an Al - Zn - Mg alloy. Another important factor is the homogeneity of slip within grains; indeed, slip bands create stress concentrations capable of opening cracks at grain boundaries. Therefore, localization of slip will increase the tendency to intergranular failure. This also explains why commercial purity alloys are less likely to fail intergranularly: the existence of small dispersoids promotes both the spread or homogeneization of slip, and reduction in grain size. Assuming that fracture occurs at a grain boundary when a critical stress σ_c is reached, Evensen et al. (1975) express the influence of stress concentrations at the tip of a slip band in which precipitates exert a resistance σ_o to plastic flow by:

$$\sigma_{app} + \Phi (\sigma_{app} - \sigma_o) > \sigma_c \qquad (II - 61)$$

Here Φ is the stress concentration factor and can be approximated as $(L/W)^{\frac{1}{2}}$, where L is the length of the slip band and W its width. Equation (II - 61) gives then :

$$\sigma_{app} > \sigma_o + (\sigma_c W^{\frac{1}{2}})/L^{\frac{1}{2}} \qquad (II - 62)$$

This equation relates therefore the fracture stress to the grain size, equal to L, the length of the slip band.

As this type of intergranular failure is in fact a form of ductile fracture, it will be very sensitive to the stress state; any change in the hydrostatic stress component will affect subsequent damage development and may eventually change the fracture mode.

II - 3 - 3 Cleavage Fracture

In b.c.c. ferrous materials, at low temperatures, fracture occurs by transgranular cleavage on the {001} planes, involving the nucleation of a microcrack within a grain or a second phase particle and its propagation in the adjacent ferrite grain leading to catastrophic fracture.

Low (1954) has shown that the cleavage fracture stress in tension is always equal or greater than the yield stress, measured in compression, over a large range of grain sizes in a mild steel at 77^OK (fig. II - 11). It is, therefore, apparent that plastic flow is a necessary precursor to cleavage, and that yielding is involved in the nucleation of cleavage fracture.

Zener (1948) first suggested that the stress levels at the tip of a dislocation pile-up could be sufficient to nucleate a microcrack. Stroh (1954) developed this idea by proposing that the dislocations are squeezing together to give a crack nucleus. The critical stress for crack nucleation is:

$$\tau_{eff} = \tau_y - \tau_i \geq \left[\frac{12 \mu\gamma}{\pi (1 - \nu) d} \right]^{\frac{1}{2}} \quad (II - 63)$$

where τ_{eff} is the effective shear stress, τ_y is the shear yield stress, τ_i the lattice friction shear stress, μ the shear modulus, γ the surface energy, ν Poisson's ratio and d the slip band half-length. Stroh also argued that nucleation would be the most difficult stage, so that cleavage
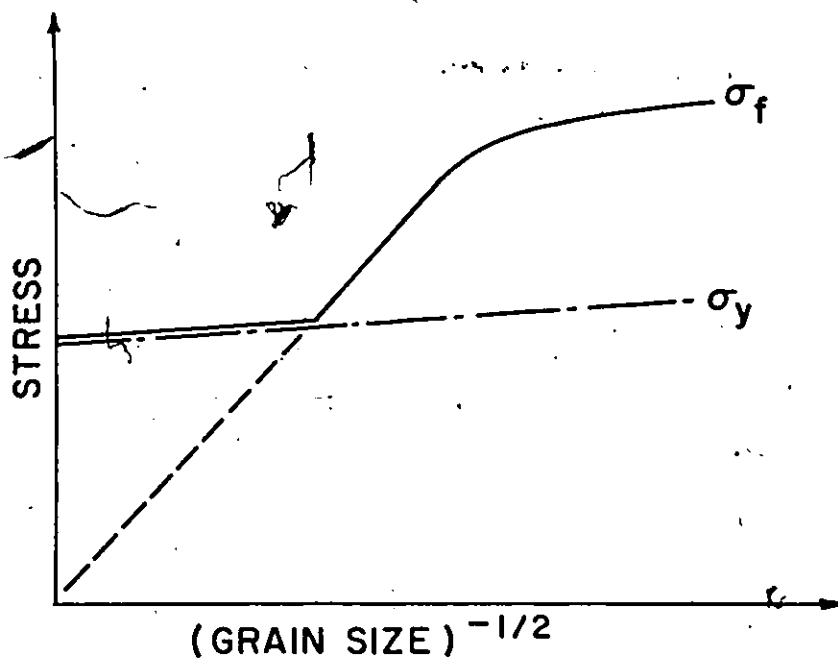
Fig. II-11 : Grain size dependence of the yield stress σ_y and fracture stress σ_f in mild steel at 77°K (after Low, 1954).

fracture is nucleation-controlled. However, Knott (1966) showed that cleavage fracture in mild steels follows a critical tensile stress criterion; since this stress governs the propagation of the microcrack, this means that cleavage fracture is propagation-controlled in mild steels. Cottrell (1958) proposed an alternative model for the nucleation of cleavage cracks in bcc metals. Two dislocations slipping on intersecting {101} planes interact to form a pure edge dislocation, whose large Burgers vector is normal to the cleavage plane. This reaction is accompanied by a reduction in dislocation energy so that nucleation is easier than with the previous Stroh's model. The cleavage fracture stress is:

$$\sigma_f = \frac{2 \mu \gamma}{k_y^s} \, d^{-\frac{1}{2}} \qquad (II - 64)$$

where d is the grain size and k_y^s is the shear Hall-Petch yielding constant. This model predicts a propagation-controlled cleavage fracture and explains the effect of grain size and yielding parameters on fracture. However, this model does not consider the effects of microstructural inhomogeneities such as the presence of second phase particles in grain boundaries, or alternative configurations for the dislocation pile-ups. McMahon and Cohen (1965) showed the influence of carbide size on fracture: coarse carbide particles promoted cleavage fracture whereas fine carbide particles allowed a ductile behaviour. Grain boundary carbides are cracked during plastic deformation, giving crack nuclei propagating into the surrounding ferrite as cleavage cracks, causing complete fracture. Smith (1966) proposed a model where crack nucleation within a grain boundary carbide of thickness C_o is created at the tip of a dislocation pile-up in the surrounding ferrite grain of diameter d. The change in energy required to spread the crack from the carbide into the

ferrite matrix gives the criterion for the growth-controlled cleavage fracture to occur at a stress σ_f:

$$(\frac{C_o}{d})\; \sigma_f^2 + \tau_{eff}^2 \left[\; \frac{1}{2} \; + \; \frac{2}{\pi} \; (\frac{C_o}{d})^{\frac{1}{2}} \; \frac{\tau_i}{\tau_{eff}} \; \right]^2 \; \geq \; \frac{4\, E\, \gamma_p}{\pi\, (1 - \nu)d} \quad \text{(II - 65)}$$

where E is the Young's modulus and γ_p is the effective surface energy of ferrite. Another mechanism is also possible to nucleate microcracks into second phase particles: Lindley et al. (1970) showed that a fibre loading mechanism could occur.

It can also be mentioned that cleavage fracture can be initiated by deformation twins produced at high strain rates and low temperatures (Hull, 1960; Knott and Cottrell, 1963).

Equation (II - 65) indicates that the only microstructural parameter to affect the fracture stress is the carbide thickness. Curry and Knott (1978) have, however, shown that it exists a relationship between ferrite grain size and the largest observed carbide thickness. Assuming that this carbide gives rise to fracture, the grain size can be introduced into equation (II - 65). Using typical values of yielding parameters, Knott (1977) has found a value of 14 J m^{-2} for the effective surface energy of ferrite γ_p. He also quoted an extension of this model to steels containing spheroidal carbides, done by Curry. Again, the critical step is the propagation of a crack nucleated in a spheroidal carbide into the adjacent ferrite grain. Ignoring the dislocation contribution, Curry found:

$$\sigma_f = (\frac{\pi\, E\, \gamma_p}{2\, C_o})^{\frac{1}{2}} \quad \text{(II - 66)}$$

where C_0 is the carbide diameter. Such a mechanism of fracture is consistent with the value of 14 J m^{-2} for γ_p if the carbide diameter is taken as the 95th percentile of the carbide size distribution. Finally, to explain that the effective surface energy γ_p is significantly larger than the elastic work to fracture, about 2 J m^{-2}, Knott (1977) suggested that it is necessary to consider a critical displacement of the crack tip as the full atomistic fracture criterion, so that some dislocations must be created and moved at the crack tip, thus raising the energy for fracture.

II - 3 - 4 Deformation and Fracture of Rocks

Rocks are very brittle materials, so that the easiest way to study their mechanisms of deformation and fracture is to perform a compression test with or without confining pressure.

In the former case, the typical stress-strain behaviour of rocks in compression is schematized in fig. II - 12 , and can be divided in four stages (Paterson, 1978):

- Stage I: the upward concavity of the curve is attributed to the closing of pre-existing cracks, which are intrinsic to the constitution of the rocks.

- Stage II: nearly perfect linear elastic behaviour. It involves the elastic deformation of the grains and pores. However, hysteresis has sometimes been detected, and attributed to some sliding of pre-existing cracks.

- Stage III: development of microfracturing and dilatancy. This occurs by the proliferation and stable propagation of microcracks distributed fairly uniformly throughout the material. They develop parallel to the maximum principal compressive stress. Very little is known about whether
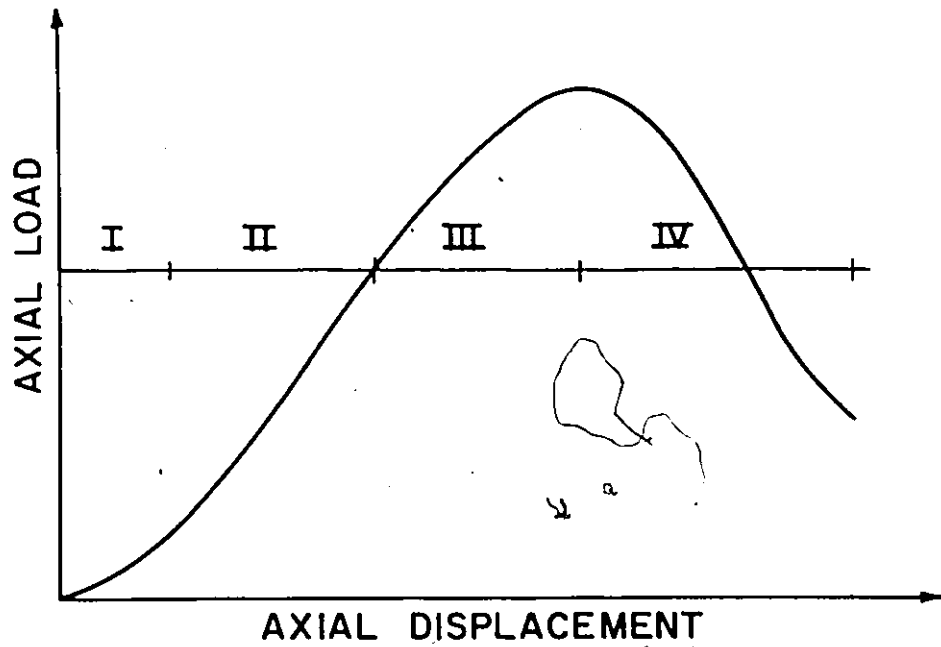
Fig. II-12 : Schematic representation of the load-displacement
curve of a rock in compression. The four stages are
also indicated (after Paterson, 1978).

microcracks mainly propagate from smaller ones initially present, or whether the nucleation of new cracks is important.

- Stage IV: localization of the microcracking development. In some cases, the microcracks remain predominantly axial in orientation, and their linkage leads to the axial splitting type of fracture. In other cases, an increasing proportion of microcracks comes to be of inclined orientation or shear character, and their linkage gives a shear type of fracture.

When the compression test is performed with a sufficiently high confining pressure, the material can become ductile i.e. can substantially change its shape without gross fracturing. The processes responsible for this transition to a ductile behaviour will be presented in the next section of this review. However, it is useful to recall here the deformation processes which can enter into the ductile behaviour of rocks. They are of three types, any combination of which is greatly dependent on the conditions of pressure, temperature and strain rate:

- Cataclastic Flow: this is the permanent deformation acheived by the combination of the distributed fracturing of the material into fragments, and the relative movement of the fragments. Two factors make this mechanism strongly pressure-dependent: a) the friction between the sliding parts, and b) the changes in volume associated with the re-arrangement of the fragments. The microscopic physical processes involved in this type of flow are very little understood.

- Crystal Plasticity: it covers the permanent deformation of crystalline material by slip and twinning within the grains.

- Diffusional Flow and Grain-Sliding Effects: these mechanisms are likely to appear when the temperature is high enough, as they involve thermally activated processes.

Finally, as ductile behaviour involves a change of shape without significant change of volume, some geometric constraints exist, in particular compatibility of strain between grains must be effective. When deformation takes place by slip within the grains, it is well known that five independent slip systems must be available (Von Mises, 1928; Groves and Kelly, 1963). However, in rocks, such a criterion is usually not fulfilled (Paterson, 1969). Therefore, the question arises to know how rocks can deform in a ductile manner by slip in the grains. Two possibilities exist. The first one is to take into account the heterogeneity existing at the scale of the grains: some grains may not deform, but behave as hard inclusions in a matrix of deforming grains. The second one is to consider that other types of deformation mechanisms can occur: twinning, kinking are two examples. However, these two possibilities are quite limited and generally the accommodation mechanisms will be cataclastic ones at low temperatures, and diffusional ones at higher temperatures.

II - 3 - 5 Conclusions

To conclude this review of brittle fracture, the main points can be recalled:
- Brittle fracture occurs as a sequence of nucleation, growth and propagation of microcracks, either transgranularly or intergranularly.
- The micromechanisms leading to the nucleation of microcracks generally involve local plastic deformation (slip or twinning).

- The work done in brittle fracture is always larger than the ideal
  elastic work. This shows that some kind of plastic deformation at the
  crack tip is associated with the crack propagation.
- As clearly shown in the case of rocks, but also for brittle metals,
  the hydrostatic stress component has a strong influence on the fracture
  process.

II - 4 Influence of the Stress State on the Tensile Fracture Mechanisms

As seen in the preceding reviews of the fracture modes, damage accumulation is a prerequisite for fracture. Unlike plastic flow, it is dependent on the hydrostatic component of the stress tensor. A great deal of experimental work has been carried out to investigate this dependence in different materials such as pure metals, alloys and rocks.

Two ways of changing the hydrostatic stress component have been used. The first one is to superimpose an hydrostatic pressure during the tensile deformation of a specimen. The second one is to create a triaxial state of stress by machining notches in axisymmetric tensile samples.

Quantitatively, the results of these studies have been expressed in terms of a relationship between the fracture strain ϵ_f and the superimposed pressure P. Some authors have also tried to find an analytical fracture criterion giving the fracture stress as a function of several parameters.

Qualitatively, some authors have tried to present an overview of the changes in fracture modes (Brandes, 1970; French and Weinrich, 1977; Francois, 1977).

The following review presents several features of the known experimental data for a particular type of material.

II - 4 - 1 Ductile Pure Metals

Investigations have been carried out on different pure metals such as Fe (Yajima et al., 1970), Aℓ (Yajima et al., 1970; French and Weinrich, 1975a) and Cu (Yajima et al. 1970; French and Weinrich, 1975b, 1976). These metals fail by the ductile "cup and cone" mechanism at atmospheric pressure, but develop other modes as the hydrostatic pressure is increased.

In copper, both authors obtain a linear increase of the fracture strain up to a pressure of 300 MPa. Above this value, Yajima et al. (1970) found a slower, but still linear increase, whereas French and Weinrich (1975b) indicate a fracture strain going to infinity as the fracture mode becomes the chisel-point mode.

In iron, Yajima et al. (1970) found a linear variation of ε_f with P up to 490 MPa, and a deviation from linearity above this pressure.

In aluminum, there are again contradictory results. Yajima et al. (1970) obtained a continuous, linear variation of ε_f with P up to 200 MPa, but French and Weinrich (1975a) observed a change to chisel-point fracture mode between 125 and 150 MPa. These differences may be attributed to the degree of purity of the materials studied.

However, the general picture which emerges from these works is that increasing pressure changes the fracture mode from a cup and cone one to a chisel-point type.

II - 4 - 2 Non-Ferrous Alloys

Two types of alloys have been studied.

The first group is composed of different Cu - Zn alloys (brasses). Beresnev et al. (1963) found a linear increase of ε_f with P up to 300 MPa,

and a constant value of ε_f above 400 MPa. Yajima et al. (1970) have

reported the same type of behaviour for brasses containing 30-40 wt% of

Zn. They suggest that this change in slope occurs because the fracture

might be dominated by the shear stress above a certain pressure in metals

with a low stacking fault energy. French and Weinrich (1973a, 1973b, 1974b,

1977) have studied in detail the variation of ε_f in different brasses.

The increase of ε_f with P is linear up to 300 to 400 MPa for all the brasses

tested, followed by a sharp decrease in ε_f around 400 MPa, and the achieve-

ment of an approximately constant value above 500 MPa. The authors relate

these variations to the changes occurring in the fracture mechanism. Below

300 or 400 MPa, the fracture is a cup and cone type, the fibrous part

decreasing as the pressure increases. At a critical pressure of 300 or

400 MPa, the mechanism of fracture changes into the shear mode, giving a

constant value of ε_f. Up to 1100 MPa, fracture occurs on a single shear

plane after a large amount of necking. At 1200 MPa, a chisel-point fracture

takes place by the operation of shear zones containing narrow bands of

intensive shear.

The second group of alloys is composed of some aluminum alloys.

French and Weinrich (1975a, 1977) have studied an Aℓ - 5.5 wt% Cu alloy

under pressures up to 1250 MPa. The fracture strain increases linearly

with pressure up to 300 MPa, and less rapidly at higher pressures. The

cup and cone fracture occurring at low pressures turns into a shear fracture

at about 350 MPa, and this mode exists up to 800 MPa. Above this pressure,

crossed shear zones, characteristic of chisel-point fracture, are developing.

Beresnev et al. (1963) reported a linear increase of ε_f with P up to 750 MPa,

for a heat-treated Aℓ - Cu alloy, but they could not measure ε_f at higher

pressures because of the distortion of the neck. Pugh and Green (1964-65) found similar results on an Aℓ - 1 wt% Si, a linear increase of ε_f up to 450 MPa, and a large distortion of the neck above 500 MPa. Finally, Auger and Francois (1974) have done some measurements of mechanical properties and fracture toughness under pressure up to 600 MPa in an 7075-T651 aluminum alloy. The fracture strain ε_f was found to increase linearly with P over the entire range of pressures investigated, and the fracture mode was the cup and cone one up to 600 MPa.

It can, therefore, be concluded that when the pressure is increased the fracture mode of non-ferrous alloys changes according to the following sequence: cup and cone → shear → chisel-point or plastic rupture.

II - 4 - 3   Steels and Ferrous Alloys

The first author to study the behaviour of steels under hydrostatic pressure was Bridgman (1952). He tested different grades of steel, and was able to outline the common features of their behaviour under hydrostatic pressure.

His first conclusion was that hydrostatic pressure affects slightly the plastic flow of steels, as seen when the strain hardening curves obtained under various pressures are plotted. Despite small increases of the yield strength and tensile strength when pressure is increased, Bridgman assumed that flow is independent of hydrostatic pressure when he derived his analysis of the stress distribution across the neck of a tensile specimen. Since then, Spitzig et al., (1975, 1976) found that yield and flow stresses were sensitive to hydrostatic pressure in several steels and polymers. Richmond and Spitzig (1980) showed that the flow stress can be written as :

$$\sigma = f(\varepsilon) \ (1 + 3 \alpha P) \qquad (II - 67)$$

where α is found to have an average value of 19×10^{-6} MPa^{-1} for all iron-based materials. This pressure sensitivity of the flow stress can be explained by the small pressure dependence of the elastic moduli which appear in most formulae in dislocation theories or, less directly, by the dilatancy around stacking faults or a slight pressure dependence of diffusion rates when dislocation motion is dependent on diffusion (climbing, jog-dragging).

The second result of Bridgman's work is related to fracture. He reported that ductility was increased by pressure, and he found a linear relationship between ε_f and P for all the steels he tested. He also noticed that the fibrous part of the fracture surface was decreasing as P was increased, and could even vanish at sufficiently high pressures.

Finally, he concluded that there is no universally valid criterion for fracture in terms of the stress only. This work has been followed by several studies on the behaviour of steel under pressure.

Davidson and Ansell (1968) studied a series of iron-carbon alloys in annealed and spheroidized conditions. They showed that the effect of pressure on ductility is highly structure-sensitive in terms of the amount, shape and distribution of cementite phase. They found a linear variation of ε_f with P in the spheroidized steels, and showed that the ratio of fibrous to total area of the fracture surface goes to zero at a pressure which increases with increasing tensile strength.

Yajima et al. (1970) tested three mild steels, and reported a linear relationship between ε_f and P. Using these results and those obtained for other materials, they showed that the slope of the linear relationship between ε_f and P is dependent upon the tensile strength σ_{TS} of

the material : the higher the strength, the smaller the slope. Finally, these authors proposed a fracture criterion based on the constancy of the hydrostatic stress component at fracture.

French and Weinrich (1974a) carried out the first quantitative study of the voiding mechanism in a spheroidized steel tested under hydrostatic pressure. The fracture strain was found to vary linearly with P; the results concerning nucleation have already been reported in the review of ductile fracture.

Other authors have used the triaxiality of the stress state created when machining a notch in axisymmetric tensile specimens. Alpaugh quoted by McClintock (1968b), Mackenzie et al. (1977), Hancock and Mackenzie (1976) have studied steels, and recently Sun Yao Quing et al. (1983) have investigated a spheroidal cast iron. The severity of the notch, i.e. the magnitude of the hydrostatic tension, increases as the ratio a/R increases, where a is the radius of the minimum cross section and R the radius of curvature of the notch root. Two principal conclusions can be drawn from these types of experiments:

- the ducility decreases as the severity of the notch increases.
- the damage is affected by the stress state (Sun Yao Quing et al., 1983): the volume fraction of voids found just at the onset of fracture is decreasing as the severity of the notch is increased.

II - 4 - 4 Brittle Materials

Superimposing an hydrostatic pressure during the deformation of a brittle material can have two main effects, both related to the extensive microcracking involved in brittle fracture. First, the pressure will have an influence on the amount of microcracking present in the sample, as it

opposes any dilatancy. The second effect is the influence of pressure on

the stability of existing microcracks, the pressure being able to delay

any form of unstable localization of flow. These effects have been studied

theoretically by Francois and Wilshaw (1968) for transgranular cleavage.

Considering dislocation models for the nucleation of microcracks, they

concluded that, as superimposed pressure is small compared with the local

stresses in the cores of dislocations, the stress for crack nucleation is

nearly independent of pressure. Two other steps, crack propagation across

a grain, and through a grain boundary, are, however, pressure-dependent.

Using energy balance calculations, Francois and Wilshaw showed that as the

pressure is increased, the stress to propagate cracks across grains is also

increased; but remains at first above the stress needed to cross a grain

boundary; then the cracks are still unstable. At higher pressures, the

propagation across a grain boundary becomes more difficult than the pro-

pagation in a grain, so that cracks are stabilized, and some arrested cracks

can be seen within the specimen. This type of calculation can be extended

to intergranular fracture due to weakening of the grain boundaries; however

the influence of pressure on the failure of aluminum alloys showing inter-

granular decohesion must be of the same nature as the influence it has

on ductile fracture, previously reviewed : pressure will delay damage

accumulation at the grain boundaries, eventually allowing another fracture

mode to take place.

Experiments have been performed in order to determine the increase

in ductility, which could be used for forming purposes, obtained by super-

imposing pressure. Two groups of materials have been investigated : h.c.p.

materials, such as beryllium (Bedere et al., 1971), zinc (Pugh and Green,

1964-65; Davidson et al., 1966; Carpentier and Francois, 1971), cobalt (Davidson et al., 1966; Carpentier and Francois, 1971), or magnesium (Pugh and Green, 1964-65; Davidson et al., 1966), b.c.c. materials such as tungsten (Davidson et al., 1966) and molybdenum (Galli and Gibbs, 1964), and also some brittle cast irons (Bridgman, 1952; Brandes, 1965,1967; Crossland and Dearden, 1958; Pugh and Green, 1964-65).

It has also been found that hydrostatic pressure has an influence on the ductile-brittle transition temperature. Galli and Gibbs (1964) have shown that this temperature could be lowered from $50^{\circ}C$ to $2^{\circ}C$ in molybdenum by the application of an hydrostatic pressure of about 140 MPa.

Finally, following the work of Von Karman (1911) on marble, several authors have studied the transition to a ductile behaviour which is achieved in brittle rocks when they are compressed with a sufficient confining pressure (Paterson, 1958; Heard, 1960). They have shown that ductile behaviour was characterized by a uniformly distributed deformation throughout the specimen. The brittle-ductile transition can be simply modelled in two ways as shown schematically in fig. II - 13, taken from Paterson (1978). Fig. II - 13 - a represents a transition to plastic flow; indeed, the fracture stress increases quicker than the yield stress as the pressure is increased. In practice, the transition will be less sharp because of local yielding effects occurring below the macroscopic yield stress. Fig. II - 13 - b represents a transition to a cataclastic flow : here it is assumed that the fracture stress is less dependent on pressure than the frictional sliding stress. These modes can occur because of the stabilization of microcracks, which cannot give rise to a localization into a shear band, for example.
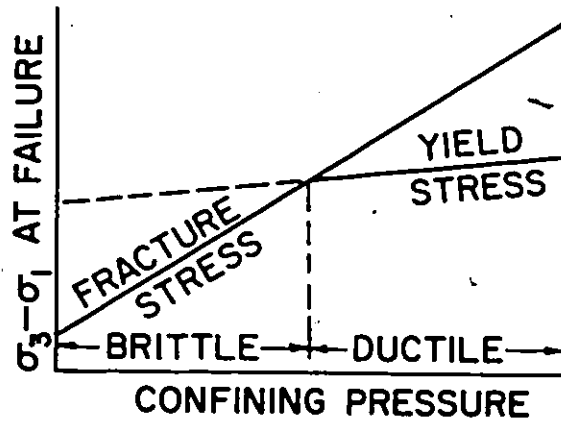
(a)
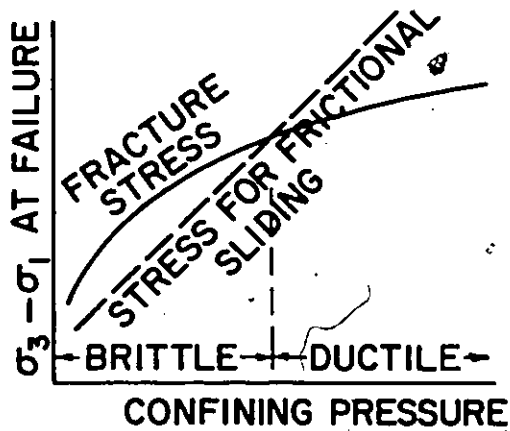
(b)

Fig. II-13 : Schematic models for the brittle-ductile transition
under confining pressure :
a) transition to plastic flow.
b) transition to cataclastic flow.
After Paterson (1978).

II - 5 Mapping of Competing Fracture Modes

Materials can fail by different mechanisms, the occurrence of
which depends on the values taken by a set of variables including the stress
state, the temperature, microstructural parameters, material properties
and the level of microstructural damage.

It appears that the determination and the presentation of maps in
an appropriate set of coordinates would be a convenient way of representing
the dominant mechanisms of deformation or fracture for a given material
under well-defined conditions.

In the section, three kinds of maps are considered, which correspond
to the main body of the mapping work to date: deformation mechanism maps,
fracture maps and formability maps.

II - 5 - 1 Deformation Mechanism Maps

Frost and Ashby (1982) have developed deformation mechanism maps
for a wide range of materials. They consider five possible deformation
mechanisms, each being characterized by a rate equation such as:

$$\dot{\gamma} = f(\tau, T, S_i, P_j) \qquad (II - 68)$$

where $\dot{\gamma}$ is the shear strain rate, τ the deviatoric part of the stress field,
T the absolute temperature, S_i a set of variables characterizing the micro-
structure, and P_j a set of variables giving the material properties. During
deformation, the state variables S_i are changing, so that another set of
equations giving their rate of change can be written:

$$\frac{d\,S_i}{dt} = g(\tau, T, S_i, P_j) \qquad (II - 69)$$

where t is time.

The coupled set of equations (II - 68) and (II - 69) are the constitutive laws for a mechanism. In order to simplify the equations (II - 69), two assumptions can be made:

- either assume a constant structure, i.e. $S_i = S_i^o$

- or assume a steady state, i.e. $dS_i/dt = 0$

With any of these assumptions, the constitutive law becomes:

$$\dot{\gamma} = f(\tau, T) \qquad (II - 70)$$

It is then possible to plot a deformation mechanism map, i.e. a diagram with normalized stress τ/μ, where μ is the shear modulus, on one axis, and normalized temperature T/T_M, where T_M is the melting temperature, on the other axis. It is divided into fields where a given mechanism is dominant. The boundaries between fields are the loci of points at which two mechanisms give the same contribution to the overall strain rate. Also, contours of constant strain rate are superimposed to the fields. An example of such maps is given in fig. II - 14 for pure aluminum of 10 μm grain size.

These maps have been plotted for all kinds of materials and have been proven to be useful for practical and pedagogical purposes. They are of course based on experimental data, as the parameters in the constitutive laws are best fitted to these data.

II - 5 - 2 Fracture Maps

Similar concepts can be applied to the different fracture mechanisms: a diagram showing the regions where a fracture mechanism is dominant can be plotted in a particular set of coordinates.

Ashby (1977), Ashby et al., (1979), Gandhi and Ashby (1979) proposed using available experimental data to plot some fracture mechanism
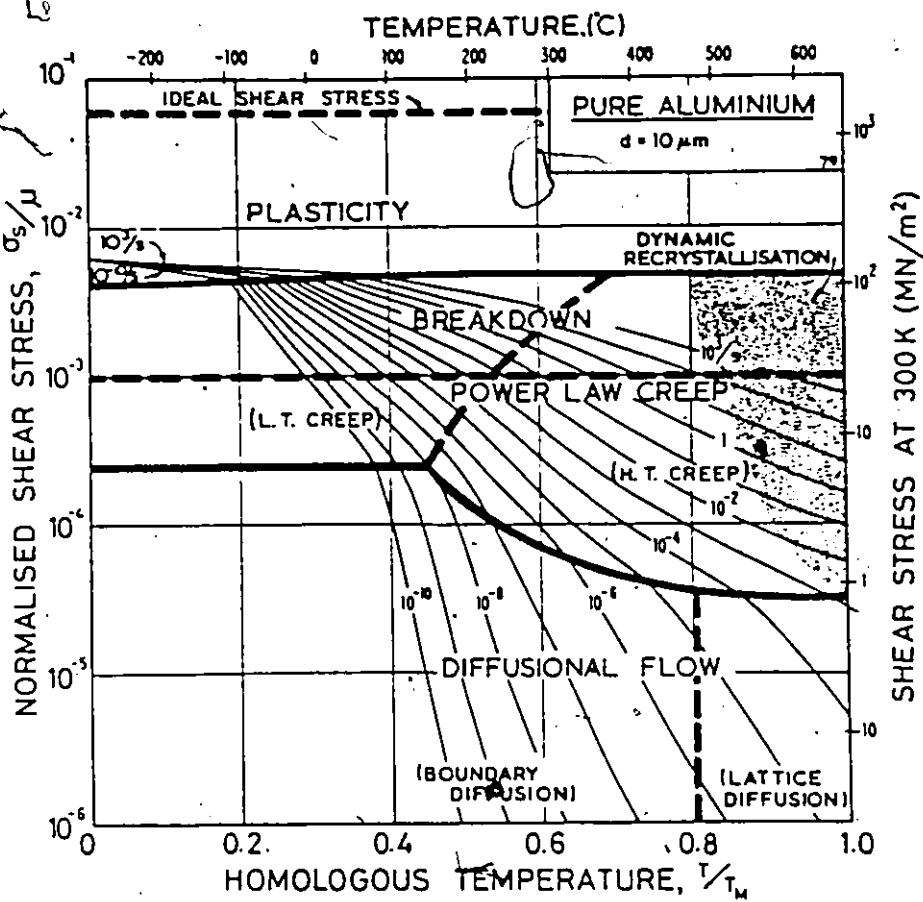
Fig. II-14 : Deformation-mechanism map for pure aluminum of grain
size d = 10 μm (after Frost and Ashby, 1982).

maps with the same coordinates as the deformation mechanism maps. They

determined the maps in a "botanical" way, without quantifying anything.

More recently, Ashby (1982) proposed a formalism similar to the one used

to describe deformation mechanisms. Here, the damage and its change with

time must be considered. This adds another equation to the previous set:

$$\frac{dD}{dt} = h(\tau, \sigma_N, P, T, S_i, P_j) \qquad (II - 71)$$

where D is the damage, σ_N the maximum normal stress and P the hydrostatic

pressure. Assuming either a steady state or a steady structure, the remaining

equations can be integrated to give the time t_f and the strain ε_f to fracture:

$$t_f = j(\tau, \sigma_N, P, T)$$
$$\varepsilon_f = k(\tau, \sigma_N, P, T) \qquad (II - 72)$$

However, as damage rate equations based on physical models are not yet

available, this approach is not practical, and the experimental one is

preferred. Some criticisms of the concept of fracture maps have been made

by Brandon (1980) who pointed out that some of the fracture mechanisms are

dependent on the volume and the geometry of the sample tested. Embury and

Duncan (1981) have also noticed that this concept may ignore important

history-dependent aspects of fracture modes.

Another important type of map has been previously developed by

McAdam (1945) and Nadai (1950). They are based on the notion of limiting

surface of rupture, given by a relationship such as $f(\sigma_1, \sigma_2, \sigma_3) = 0$,

where (σ_i) are the principal stress components. McAdam (1945) plotted

such surfaces on a 2-D diagram for axisymmetric testing where two stress

components are equal. This approach has also been used by Ashby and Embury (1981) for brittle solids such as rocks and cast irons. To describe cleavage fracture, they use the Murrell's model (1963) which gives the following fracture criterion :

$$(\sigma_1 - \sigma_2)^2 + (\sigma_2 - \sigma_3)^2 + (\sigma_3 - \sigma_1)^2$$
$$= 24 \, \sigma_f \, (\sigma_1 + \sigma_2 + \sigma_3) \qquad\qquad (II - 73)$$

where σ_f is the fracture stress in simple tension. Under axisymmetric conditions such as $\sigma_2 = \sigma_1$, this criterion becomes :

$$(\sigma_3 - \sigma_1)^2 = 12 \, \sigma_f \, (\sigma_3 + 2 \, \sigma_1) \qquad\qquad (II - 74)$$

The cleavage fracture locus described by equation (II - 74) is, on a plot with σ_1 and σ_3 as axes, a parabola truncated by the lines $\sigma_1 = \sigma_f$ and $\sigma_3 = \sigma_f$. Including the yield locus on this plot, and allowing it to move as temperature is changed, leads to a convenient way of describing the brittle-ductile transition occurring when temperature is raised, or when a stress component is altered. This type of map is shown in fig. II - 15 for an axisymmetric sample of molybdenum. Unfortunately, the other fracture modes, such as fibrous ductile fracture, or shear fracture, are not easy to characterize by a simple criterion such as equation (II - 74). However, Leroy (1978) developed a model for fibrous ductile, which has already been presented in a previous section. He plotted on a diagram with stress axes for both axisymmetric and plane stress deformation the loci of void nucleation and ductile fracture for a 1045 spheroidized steel.

Finally, Shimura and Saito (1980) have proposed several maps in 3-D space with negative pressure (or hydrostatic tension) - strain -
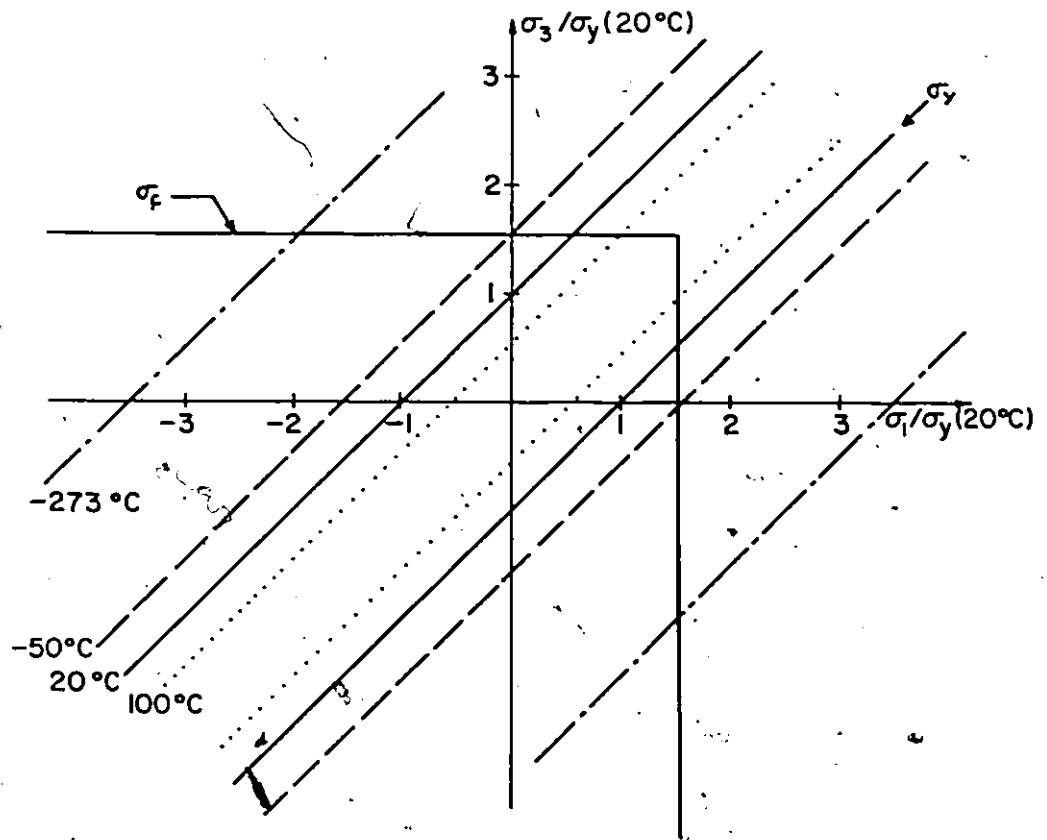
Fig. II-15: Fracture map for molybdenum under axisymmetric loading, showing the increase in ductility which can be achieved as the temperature is raised, therefore, decreasing the yield stress and setting the yield surface inside the brittle surface (after Ashby and Embury, 1981).

temperature axes, determined experimentally for different steels and one aluminum alloy, all these materials breaking by the fibrous ductile mode.

It must be, therefore, noticed that the fracture maps presented here are based on experimental data, with few exceptions. They cannot be used in a general way as they are dependent of the set of coordinates chosen.

II - - 3   Formability Maps

The purpose of these maps is to give the limiting response of a material to a particular forming operation. This response is dependent both on material characteristics (microstructure, geometry) and on the variables of the forming operation (deformation paths, loading paths). For sheet metal forming operations, two types of approach are found. The first one is the determination of a forming limit curve, for a technological purpose, showing in a diagram with the two principal strains in the plane of the sheet as axes, when failure occurs (Keeler and Backofen, 1963). The second approach deals with the modes of failure, either localized necking, or final fracture, represented in a stress space (Glover et al., 1977; Embury and Leroy, 1977; Leroy and Embury, 1978).

Embury and Duncan (1981) proposed drawing some formability maps for bulk forming process. These maps give the limiting strain components in a diagram with axial strain and hoop strain as axes for a given process. From them, it is possible to compare different friction conditions or different conditions of the surface (where failure generally occurs first) in cold-forged samples, to see the improvements which can be achieved (O'Reilly, 1983).

CHAPTER III

DUCTILE FRACTURE

III - 1 Introduction

The general purpose of this portion of the study is to quantify experimentally and to develop a theoretical model for the damage accumulation occurring prior to ductile fracture. In particular, emphasis is placed on the influence of changes in the stress state on one or more of the three stages occurring in the ductile fracture process, i.e. nucleation, growth and coalescence of voids.

The materials chosen for this study were spheroidized carbon steels, in which the distribution of carbide particle size and their volume fraction were well characterized.

Variations in the stress state were obtained by creating hydrostatic tension due to the presence of machined notches and/or pulling the samples under a high superimposed hydrostatic pressure.

After a description of the experimental procedures and of the materials used, their mechanical properties are presented and the damage accumulation data are given for a wide range of stress states. Finally, an attempt is made to develop a comprehensive model of the process of ductile fracture.

III - 2 Experimental Procedures

III - 2 - 1 Specimen Configuration and Testing Procedure

Tensile specimens with a reduced diameter of 5 mm and a gauge length

of 25 mm were machined from 19 mm diameter as-rolled bar stock. In some
specimens, circular notches whose geometry is given in fig. III - 1 were
machined.

Some of the tensile tests were performed in an Harwood hydrostatic
pressure unit (Spitzig, 1979). This rig is described in detail in Appendix
A. The fluid pressure P was controlled during the tests, and the additional
tensile force L was measured on a load cell in the pressure chamber. An
important feature of this apparatus is the ability to photograph specimens
during testing so that the neck diameter, 2a, and the radius of curvature,
R, can be recorded. This is accomplished by aligning the specimen between
two windows set into the pressure cylinder wall and using a high intensity
light source and mirror so that the silhouette of the specimen can be
recorded by a camera situated outside the pressure chamber. To ensure
that necking would initiate within the field of view of the windows, a
slight reduction in the specimen diameter at the midpoint of the gauge
length was made by polishing with fine SiC paper.

All tension tests were performed at a strain rate of 0.05 min.$^{-1}$,
and about 10 to 20 photographs were taken during the course of each test.

For both notched and unnotched samples, tests were made at three
or four pressures, namely one atmosphere or 0.1 MPa, 345, 690, and for
the unnotched samples only, 1100 MPa.

III - 2 - 2 Preparation of the Specimens for Fractography and Metallography

Fracture surfaces of broken specimens were mounted on a device to
be examined under a scanning electron microscope. Quantitative measurements

a[mm]	R[mm]	$[a/R]_o$
1.1	2.2	0.5
1.2	1	1.2
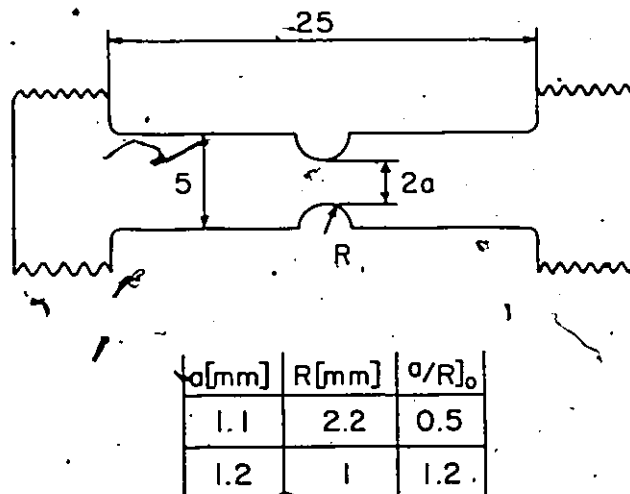
Fig. III-1 : Geometry and dimensions (in mm) of the notched samples.

$$\varepsilon_3 = 2\ln\frac{d_o}{d_z}$$
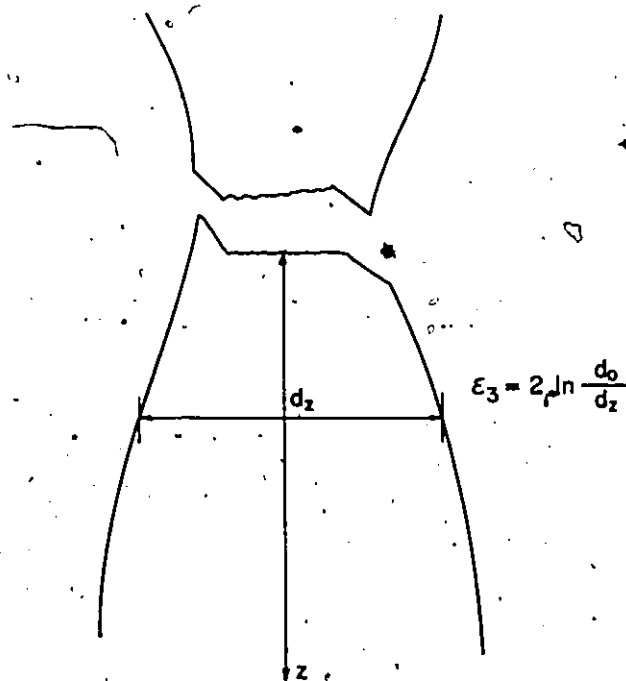
Fig. III-2 : Dimensions required for the calculation of the strain ε at a distance z from the fracture surface.

of dimple diameters were made on photographs taken in the centre of the fibrous part of the fracture surface. A minimum of four photographs at a magnification of 5000 were used. Dimple diameters were measured by the mean linear intercept of random lines method, and the results obtained by averaging the values obtained for each of the four photographs.

The damage was examined on longitudinal sections of broken specimens. The specimen was mounted in lucite after careful measurement of its diameter in the uniform region, d_A, and was afterwards polished down to the long-itudinal mid-plane with SiC papers. Just before reaching this plane, final polishing with diamond paste took place to prepare the polished surface for etching. The etching was done using nital 2%. The sample was finally coated with a thin film of gold to increase the contrast in the SEM.

The procedure during observation in the SEM was the following:
- first align correctly the sample under the beam.
- measure d_A and the diameter at fracture d_f.
- at different values of z (fig II - 2), from z = 0 cm to z = 1.5 cm, measure d_z, and move the beam on to the central longitudinal axis.
- take a photograph at a magnification of 2500 and 2 other ones at a magnification of 5000 on each side of the axis, but still at the same z value. If z is small, i.e. when examining near the fracture surface, up to 8 photographs at a magnification of 5000, and 3 at a magnification of 2500, were taken.

This procedure has been followed for all the samples investigated during this study.

The strain at a certain value of z is given by:

$$\varepsilon_3 = 2 \ln (d_o/d_z)$$

where d_o is the initial diameter of the sample.

At this strain level, the number of voids is counted from the photographs taken at a magnification of 2500, and the area fraction of voids is measured on all the pictures available by using a graphic tablet connected to an Apple II plus mini-computer, the final result being the average of the values obtained for all the measured pictures. This method gives therefore, a characterization of the damage as a function of the strain history.

The volume fraction of carbides, the mean carbide diameter, and the distribution of carbide sizes have been determined by using an automatic image analyser in a scanning electron microscope (Lee et al., 1981).

III - 3 Materials

Three different carbon steels were chosen. Their chemical composition is given in Table III - 1.

All the specimens were austenitized for 60 minutes at 900^oC and subsequently oil-quenched. They were then spheroidized at 700^oC for periods of 27, 51 and 79 hours for the 1080, 1045 and 1018 steels respectively. All the samples were sealed in glass tubes under vacuum during the spheroidization treatment to avoid any decarburization, and dummy specimens were sectioned to verify the consistency of spheroidization throughout the cross-section.

The microstructure of these steels consists of cementite particles dispersed in the ferrite matrix. The carbide size distributions shown in fig III - 3 were obtained from the analysis of about 1000 particles on sections perpendicular to the tensile axis of the specimen. When plotted

Table III-1 : Chemical compositions of the steels (wt%).

Material	C	Mn	S	Si
1018	0.192	0.688	0.015	0.008
1045	0.440	0.666	0.033	0.214
1080	0.770	0.718	0.025	0.643

Table III-2 : Parameters of the carbide size distributions.

Material	volume fraction of carbides (%)	50% fractile (μm)	84% fractile (μm)	mean diameter $\bar{d}$ (μm)
1018	3.14	0.41	0.66	0.46
1045	6.62	0.45	0.76	0.52
1080	15.75	0.72	1.12	0.79

The following relationships are used (Hald, 1952) :

ψ_g = 50% fractile

$\sigma_g = \dfrac{84\% \text{ fractile}}{50\% \text{ fractile}}$

$\log \bar{d} = \log \psi_g + 1.1513 \log^2 \sigma_g$
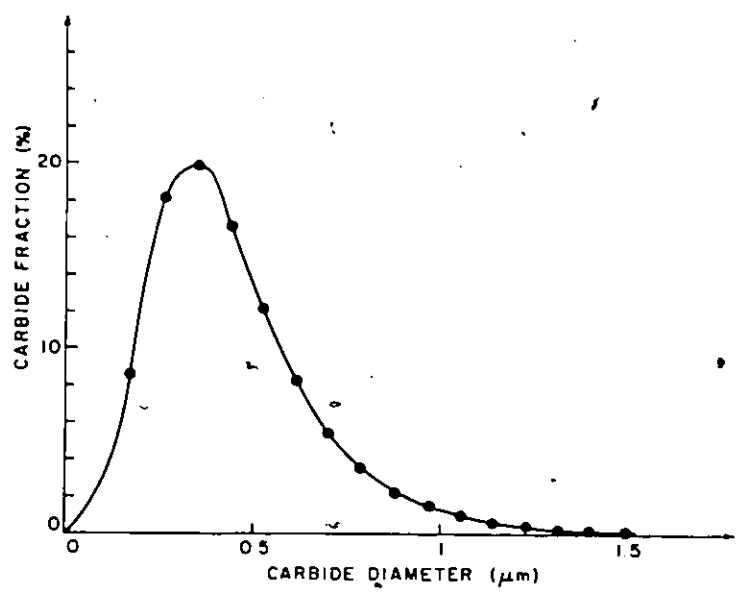
Fig. III-3-a
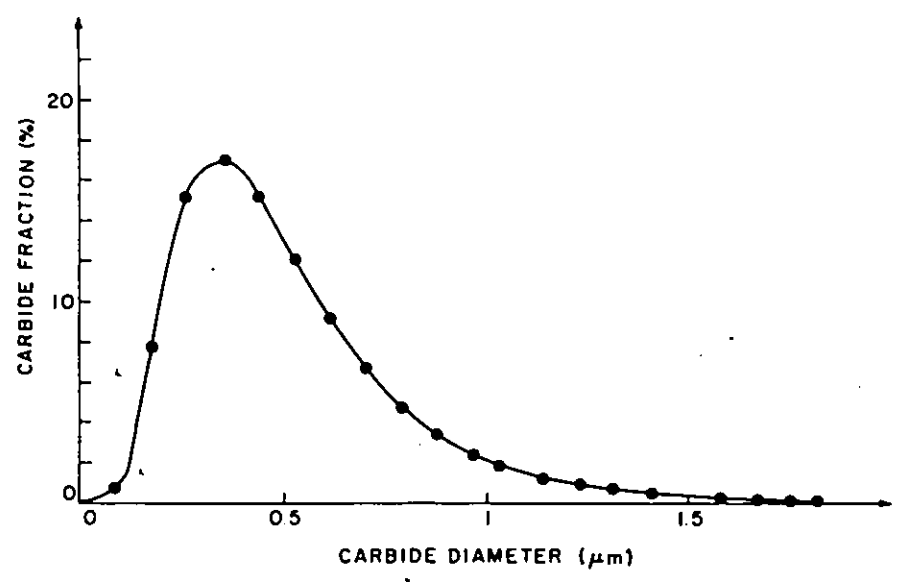
Fig. III-3-b
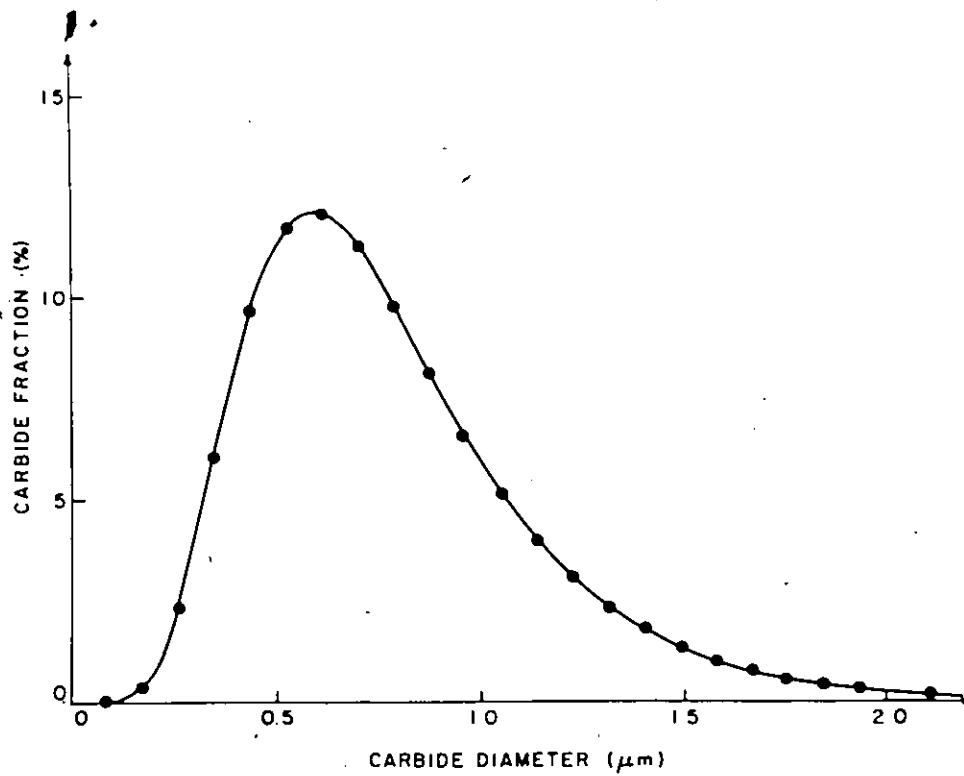
Fig. III-3-c

Fig. III-3 : Size distributions of carbide particles.
a) 1018 spheroidized steel
b) 1045 spheroidized steel
c) 1080 spheroidized steel
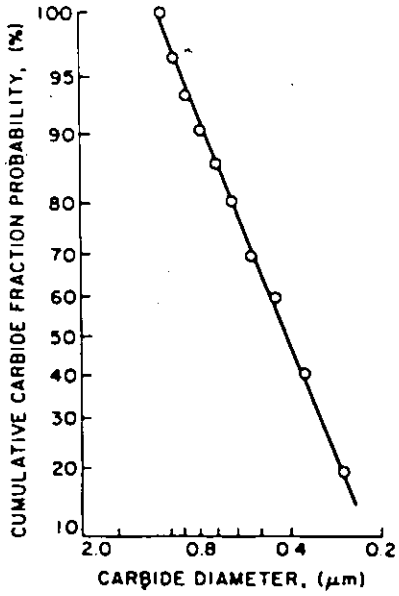
Fig. III-4-a
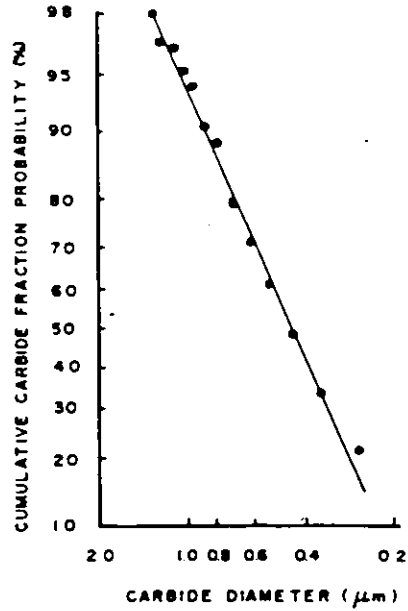
Fig. III-4-b
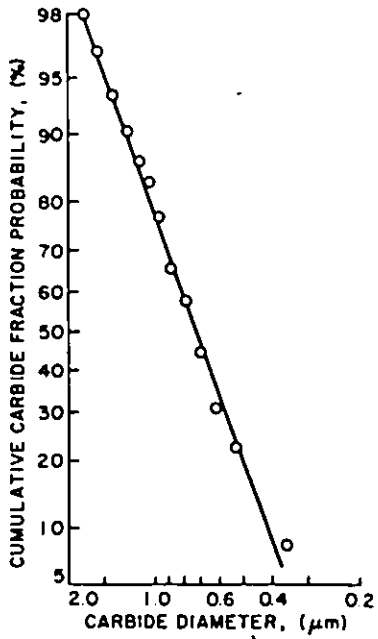
Fig. III-4-c

Fig. III-4 : Diagrams indicating
that the carbide size distri-
butions are log-normal :
a) 1018 spheroidized steel
b) 1045 spheroidized steel
c) 1080 spheroidized steel

on logarithmic probability paper, as in fig III - 4, the linear relation-
ships obtained indicate that the carbide diameter distributions obey a log-
normal law. The parameters of these distributions are given in Table III - 2.
The carbide diameters were obtained from quantitative metallography proce-
dures for determining the spatial diameter distribution of randomly dispersed
spherical particles from measurements on a plane using the chord-intercept
analysis (Cahn and Fullman, 1956; Underwood, 1970). The volume fraction was
obtained from analysis of about 5000 particles from different areas of the
section analyzed. The values are also given in Table III - 2.

III - 4 Mechanical Properties

III - 4 - 1 Deformation and Stresses

During the tensile test, the changing radius, a, of the minimum
section along with the applied fluid pressure P, and the applied axial load
L, are monitored. Thus, the average radial strain $\epsilon_{1_{av}}$ and the average
axial stress $\sigma_{3_{av}}$, on the minimum section, can be determined from :

$$\epsilon_1 = - \ln (a_o/a) \qquad\qquad (III - 1)$$

$$\sigma_3 = \frac{L}{\pi a^2} - P = T - P \qquad\qquad (III - 2)$$

where a_o is the initial radius.

Prior to the onset of necking, the stresses and strains are nearly
uniform; thus, if the volume change is assumed to be negligible and the
flow stress independent of hydrostatic pressure, then the effective strain,
$\bar{\epsilon}$, and the effective stress, $\bar{\sigma}$, can be determined from equations (III - 1)
and (III - 2) to give :

$$\bar{\epsilon} = 2 \ln (a_o/a) \qquad\qquad (III - 3)$$

$$\bar{\sigma} = \frac{L}{\pi a^2} = T \qquad\qquad (III - 4)$$
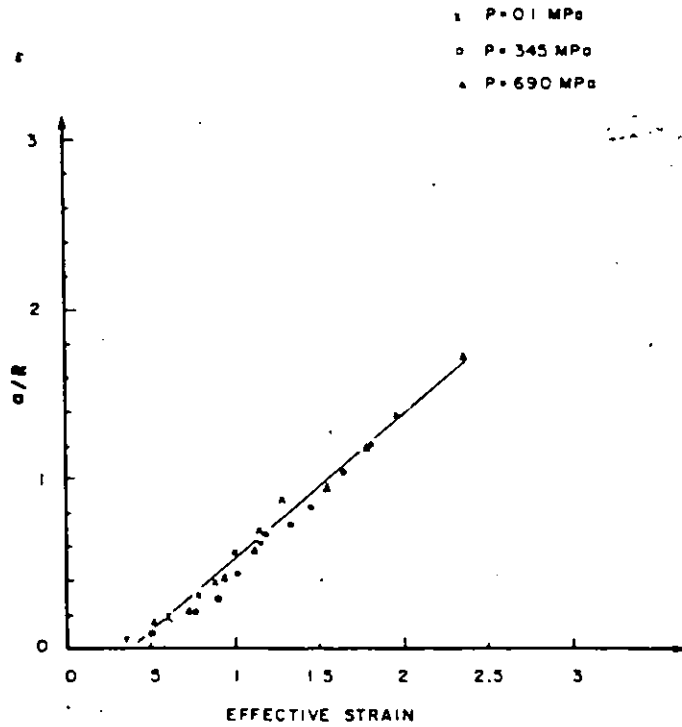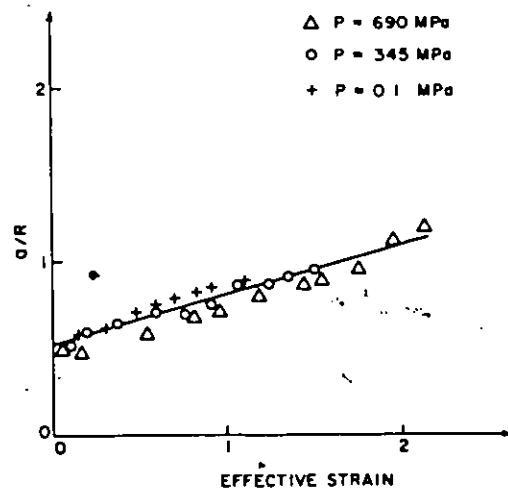
Fig. III-5 : Variation of the ratio a/R as a function of effective
strain for :
a) 1045 unnotched samples
b) 1045 a/R)$_0$ = .5 notched samples

After necking, according to Bridgman's classical analysis (Bridgman, 1952), the strains on the minimum section continue to be uniform so that equation (III - 3) still applies, but the stresses become non-uniform, and equation (III - 4) must be replaced by:

$$\bar{\sigma} = \frac{T}{(1 + 2R/a) \ \ln(1 + a/2R)} \qquad (III - 5)$$

where R is the radius of curvature of the neck at the minimum section. The principal stress components are then:

$$\sigma_1 = \sigma_2 = \bar{\sigma} \ \ln(1 + a/2R) - P \qquad (III - 6)$$

and

$$\sigma_3 = \bar{\sigma}(1 + \ln(1 + a/2R)) - P \qquad (III - 7)$$

In addition, the mean tensile stress, σ_m, is greatest in the center of the minimum section and is given by:

$$\sigma_m = \bar{\sigma}\left(\frac{1}{3} + \ln(1 + a/2R)\right) - P \qquad (III - 8)$$

Therefore, from a knowledge of the values of a/R during the test, the strain and stress components are completely determined with this analysis.

III - 4 - 2 Strain-Stress Relationships

The results are presented here for all the tests done i.e. for the unnotched samples of 1018, 1045 and 1080 steels, and the notched samples of 1045.

The values of a/R as determined from the photographs taken during testing at various pressures are shown in fig. III - 5 - a for the unnotched 1045 samples, and in fig. III - 5 - b for some notched 1045 samples, as a function of the effective strain. These values vary linearly with strain,

and are independent of hydrostatic pressure. The linear relationships

obtained for all the material tested are given in Table III - 3.

The calculated strain-stress curves ($\bar{\sigma}$, $\bar{\epsilon}$) using equations

(III - 3) and (III - 5) together with the measured values of a/R were

determined for all the materials, and are shown in fig. III - 6 - a to

fig. III - 6 - d for the 1018, 1045 and 1080 unnotched samples, and the

notched 1045 samples. The flow stresses are slightly increased by hydro-

static pressure, in accord with the previous work of Spitzig et al.,

(1975, 1976) mentioned in the literature review. It is also possible to

describe the flow curves according to the equation (II - 67), proposed by

Richmond and Spitzig (1980), using a Ludvik equation for the term independent

of pressure:

$$\bar{\sigma} = K \bar{\epsilon}^n (1 + 3\alpha P) \qquad\qquad (III - 9)$$

Here α was found to have an average value of 19×10^{-6} MPa^{-1} for all iron-

based alloys. The relationships obtained in this work are given in Table

III - 4 together with the yield stresses σ_Y and tensile strengths σ_{TS} for

each material. As expected, the flow stresses increase and the strain

hardening coefficient n decreases with increasing carbon content. It can

be seen from this table that the coefficient α suffers sensible departures

from the theoretical value, but these variations are small. It should be

noticed that Bridgman's analysis is strictly not applicable to pressure

dependent yielding. However, equation (III - 9) is considered to be a

reasonable representation of the flow behaviour of the spheroidized steels.

Finally, fig. III - 7 - a and III - 7 - b show for the unnotched

1045 and notched 1045 samples respectively that the mean stress σ_m + P in

Table III-3 : Relationships between the neck geometry and the

effective strain.

Assuming $a/R = \gamma\bar{\epsilon} + \delta$, the following values of γ and δ

are obtained :

Material	γ	δ
1018	0.643	-0.25
1045	0.865	-0.36
1080	1.028	-0.44
1045 $a/R)_o = 0.5$	0.285	+0.52
1045 $a/R)_o = 1.2$	0.720	+0.53

Table III-4 : Mechanical properties of the spheroidized steels.

Assuming $\bar{\sigma} = K\bar{\epsilon}^n (1 + 3 \alpha P)$, the following values of

K, n and α are obtained :

Material	σ_Y (MPa)	σ_{TS} (MPa)	K (MPa)	n	$\alpha \cdot (10^{-6}\text{MPa}^{-1})$
1018	247	410	769	.29	20
1045	382	510	920	.25	19
1080	465	615	1050	.24	31
1045 $a/R)_o = .5$	429	507	892	.20	33
1045 $a/R)_o = 1.2$	473	625	839	.23	32
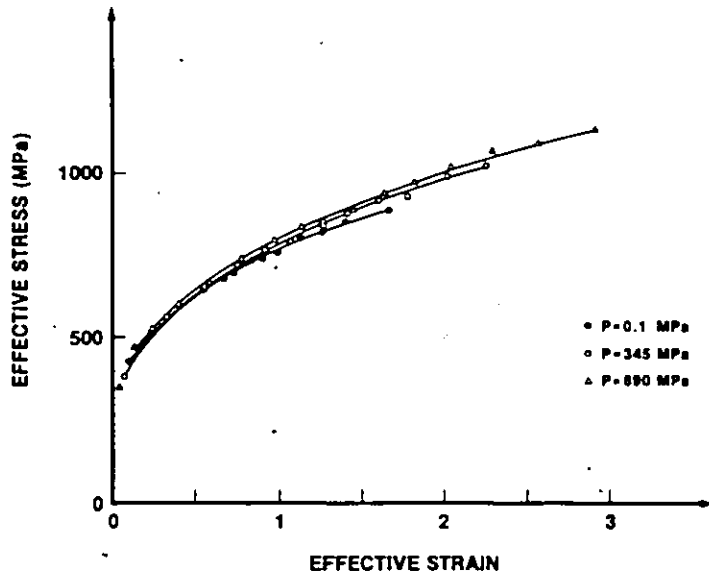
Fig. III-6-a
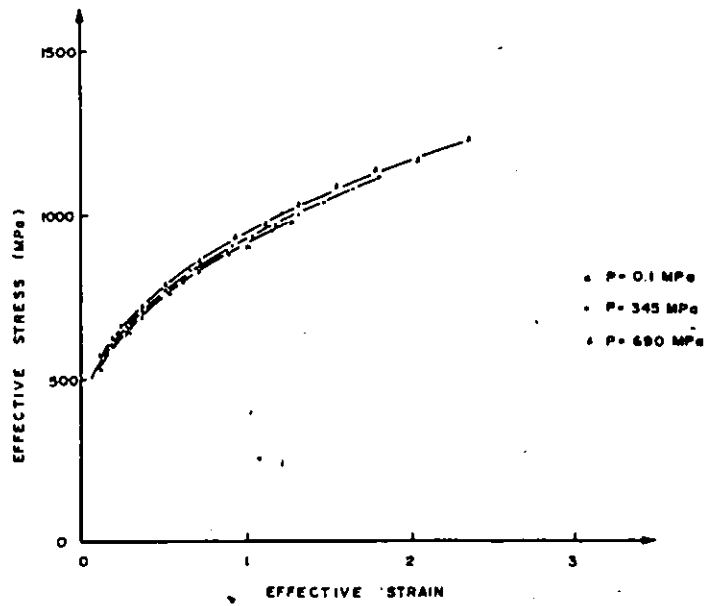
Fig. III-6-b
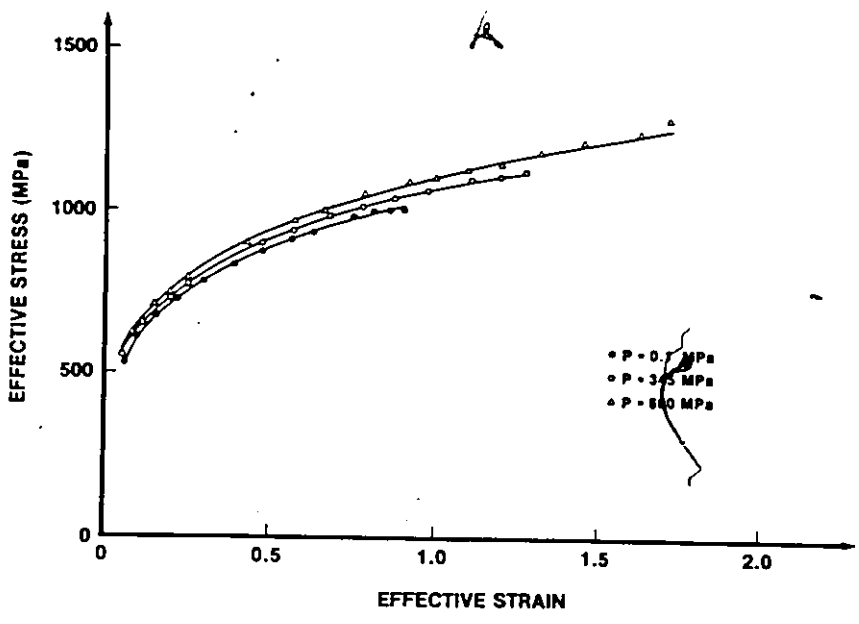
Fig. III-6-c
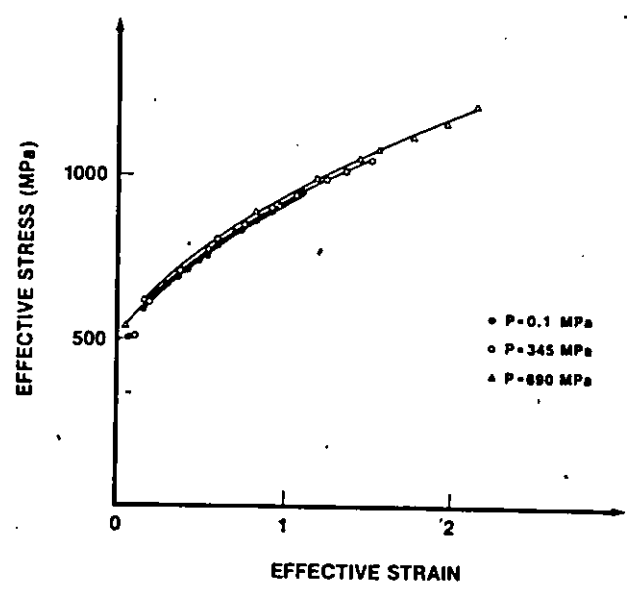
Fig. III-6-d

Fig. III-6 : Effeçtive strain-effective stress curves obtained at
various pressures for:
a) 1018 samples   b)1045 unnotched samples
c) 1080 samples   d)1045 a/R)$_o$= .5 notched samples

the center of the neck as calculated from equation (III - 8) increases

linearly with the strain from the beginning of necking to fracture.

According to Bridgman's analysis and the empirical finding that a/R is

essentially independent of pressure, so would be the values of σ_m + P.

However, the data show a slight pressure dependence, and the relationships

are well represented by an equation such as:

$$\sigma_m + P = A + B (1 + 3 \alpha P) \bar{\epsilon} \qquad \text{(III - 10)}$$

where α is the same coefficient as for the effective strain-effective

stress relationships. The values of the constants of equation (III - 10)

are given in Table III - 5 for all the materials.

III - 4 - 3   Fracture Strain and Fracture Appearance

The variations of the fracture strain ϵ_f defined by:

$$\epsilon_f = 2 \ln (d_0/d_f) \qquad \text{(III - 11)}$$

where d_f is the final diameter of the broken sample, are shown in

fig. III - 8 and fig. III - 9 as a function of superimposed hydrostatic

pressure. Fig. III - 8 compares the variation obtained for the unnotched

samples of different carbide content, whereas fig. III - 9 shows the effect

of a notch for the 1045 steel. Fracture strain generally decreases as

carbon content increases, and in all cases, the fracture strain increases

linearly with superimposed hydrostatic pressure, in accord with all the

previous works on steels quoted in the literature review. The linear

relationships obtained are given in Table III - 6.

The fracture surfaces of all the specimens were of the same type:

a fibrous central region consisting of equiaxed dimples, surrounded by an

outer rim of slant fracture containing shear dimples. The ratio of the

Table III-5 : Relationships between the mean stress component and

      the effective strain.

Assuming $\sigma_m + P = A + B (1 + 3 \alpha P) \bar{\varepsilon}$, the following values

of A, B and α are obtained :

Material	A (MPa)	B (MPa)	α (MPa^{-1})
1018	58	338	20
1045	68	463	20
1080	137	444	31
1045 a/R)$_o$=0.5	341	297	33
1045 a/R)$_o$=1.2	415	298	32

Table III-6 : Relationships between the fracture strain and the

      superimposed hydrostatic pressure.

Assuming $\varepsilon_f = \gamma P + \delta$, the following values of γ and δ are

obtained :

Material	γ (MPa^{-1})	δ
1018	$23.5 \; 10^{-4}$	1.59
1045	$17.65 \; 10^{-4}$	1.29
1080	$11.96 \; 10^{-4}$	0.89
1045 a/R)$_o$=0.5	$19.7 \; 10^{-4}$	1.12
1045 a/R)o=1.2	$19.3 \; 10^{-4}$	1.09

(a)

(b)
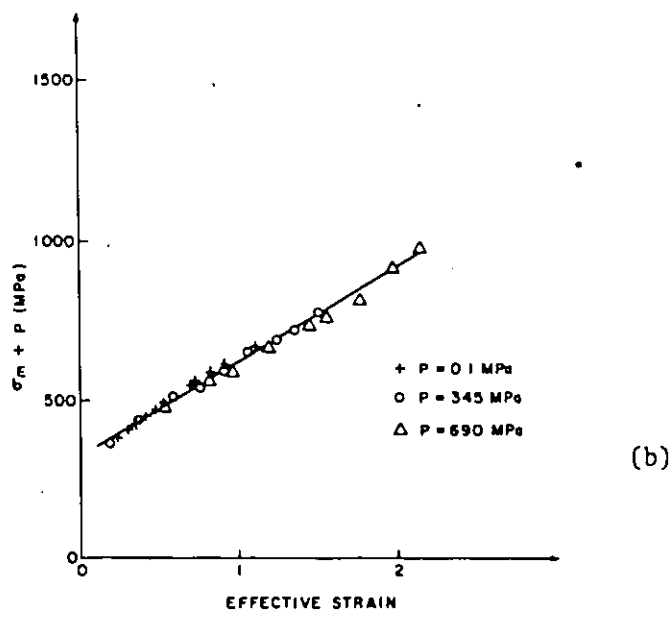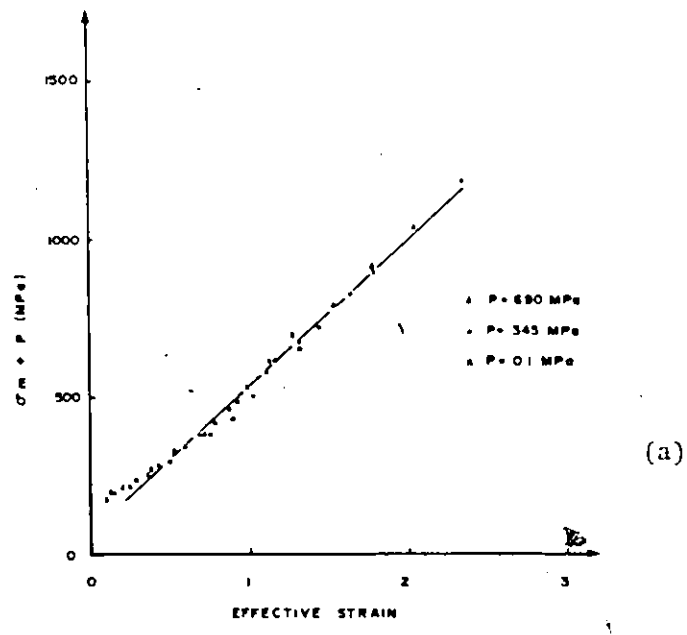
Fig. III-7 : Diagrams showing the variation of the mean stress
σ_m+P as a function of effective strain for :
a) 1045 unnotched samples
b) 1045 a/R)$_o$ = .5 notched samples
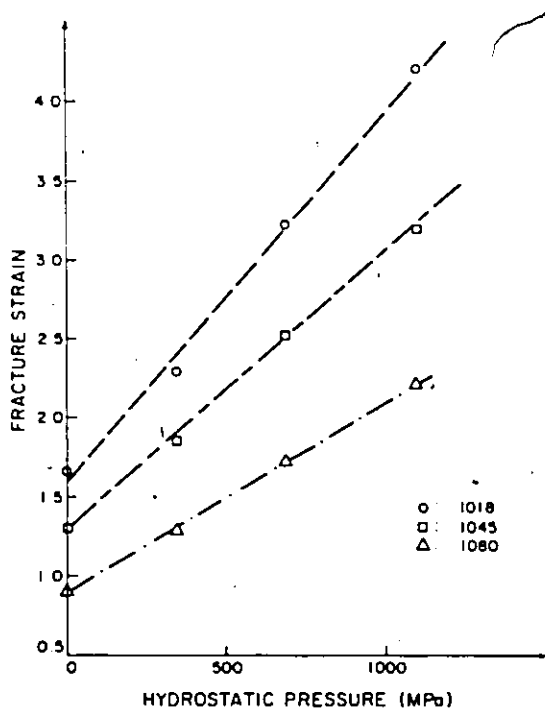
Fig. III-8 : Variation of the fracture strain as a function of hydro-
static pressure for the unnotched samples of 1018,1045,
and 1080 spheroidized steels.
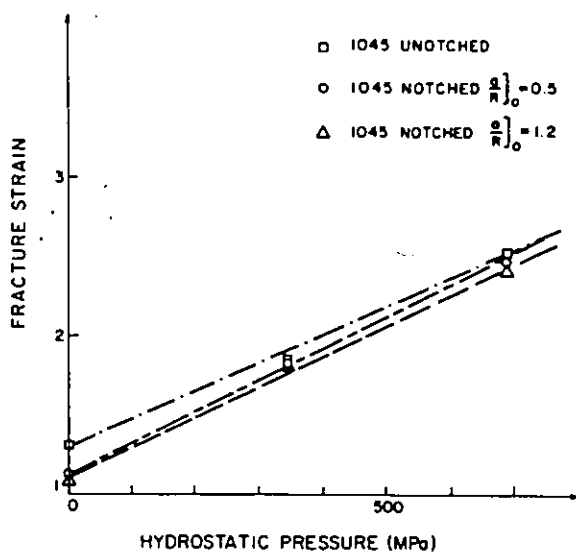
Fig. III-9 : Variation of the fracture strain as a function of
hydrostatic pressure for the notched and unnotched
samples of 1045 spheroidized steel.

central fibrous and total fracture areas decreases as the hydro-
static pressure increases (fig. III - 10 and fig. III - 11).

The equiaxed dimple size in the central region is also a
function of hydrostatic pressure. The dimple diameters, obtained
as described in Section III - 2 - 2 , are plotted as a function
of superimposed hydrostatic pressure in fig. III - 12 and III - 13.
In fig. III - 12, it can be seen that at a given pressure, the
dimple size decreases when carbon content increases. In all the
materials, the dimple size decreases linearly with pressure, and the
obtained relationships are given in Table III - 7. A composite
picture (fig. III - 14) shows the dramatic effect of superimposing
an hydrostatic pressure on the lateral growth of dimples in the
1045 steel, and fig. III - 15 shows the effect of pressure on the
macroscopic aspect of the fracture surfaces of the 1080 steel.

III - 5   Damage Measurements

III - 5 - 1   Number of Voids

Voids are created either by cracking of carbide particles
or by decohesion at the particle-matrix-interface, and it is not
possible to say which of these two mechanisms is dominant.

At a given level of strain, i.e. for a given value of z
(fig III - 2), there is a variation in the density of voids when
moving away from the central axis of the sample. The density
decreases slightly as the distance from the axis increases. However,
as the stress state is characterized along the sample axis, measure-
ments have been done only in this part of the samples.

Table III-7 : Relationships between the dimple diameter and the

superimposed pressure.

Assuming $D_f = \gamma P + \delta$, the following values of γ and δ
are obtained :

Material	γ (MPa^{1})	δ (μm)
1018	$-9.6 \ 10^{-4}$	2.52
1045	$-8.2 \ 10^{-4}$	2.16
1080	$-5.0 \ 10^{-4}$	1.69
1045 a/R)$_o$=0.5	$-8.0 \ 10^{-4}$	2.19
1045 a/R)$_o$=1.2	$-8.5 \ 10^{-4}$	2.29
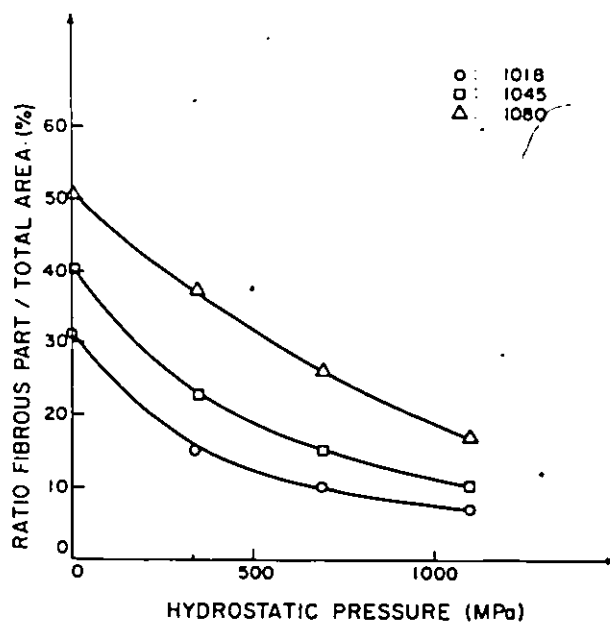
Fig. III-10 : Variation of the ratio of the central fibrous and total fracture areas as a function of hydrostatic pressure for the unnotched samples of 1018,1045 and 1080 steels.
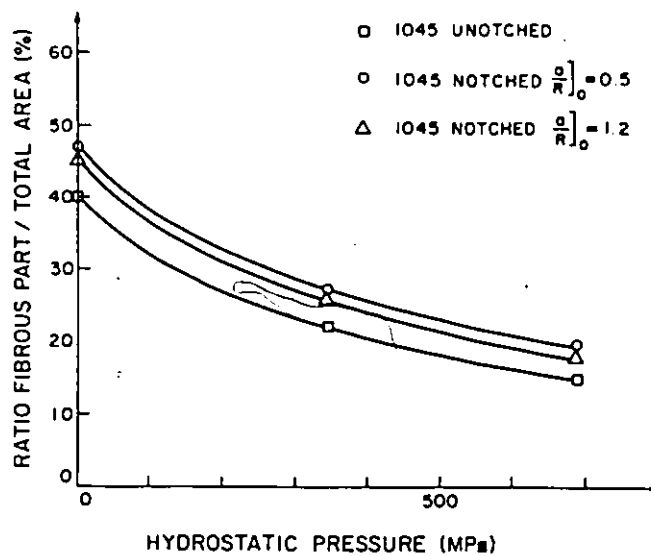
Fig. III-11 : Variation of the ratio of the central fibrous and total fracture areas as a function of hydrostatic pressure for the notched and unnotched samples of 1045 steel.
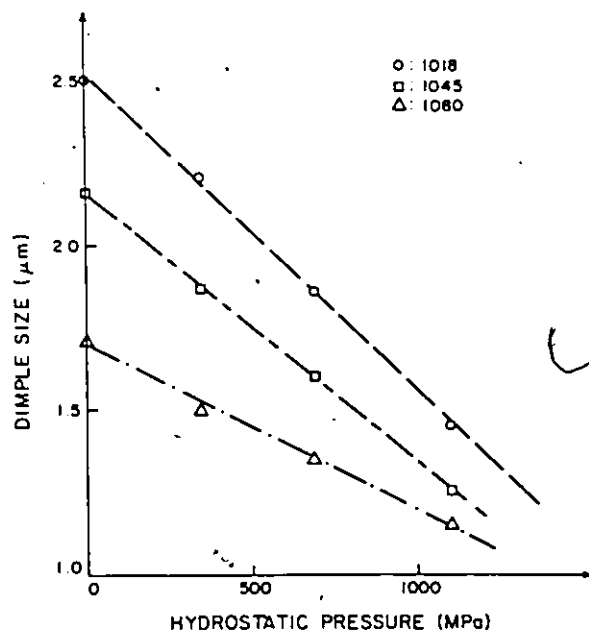
Fig. III-12 : Variation of the dimple size observed on the fracture
surface as a function of hydrostatic pressure for the
unnotched samples of 1018,1045 and 1080 steels.
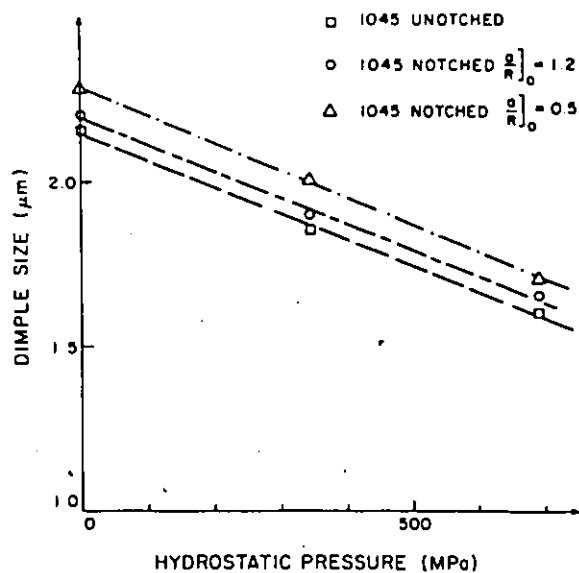
Fig. III-13 : Variation of the dimple size observed on the fracture
surface as a function of hydrostatic pressure for the
notched and unnotched samples of 1045 steel.

P = 0.1 MPA

P = 345 MPA

P = 690 MPA

P = 1100 MPA

10 μm
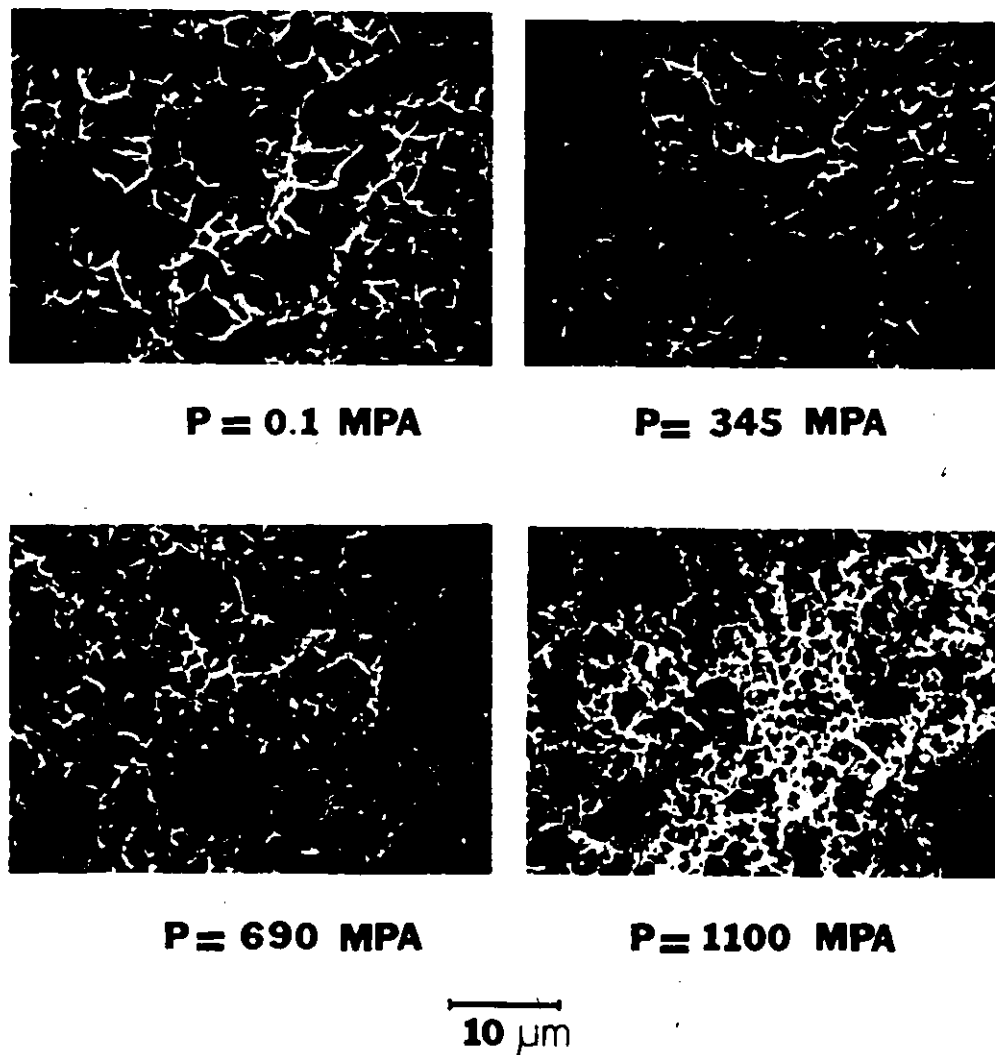
Fig. III-14 : Scanning electron micrographs of the central fibrous region of the fracture surface of the 1045 unnotched samples broken under various pressures.

P= 0.1 MPa   5.8x

P= 345 MPa   6.8x

P= 690 MPa   6.8x

P= 1100 MPa   6.8x

Fig. III-15 : Macroscopic aspect of the 1080 samples broken in
tension under various pressures.

For all the specimens examined, the larger particles have
been found to nucleate voids first. It was also observed that the
most irregularly shaped particles cavitated more readily.

The number of voids has been counted as a function of
strain and the results are shown in fig. III - 16 - a to III - 16 - e
for the 1018, 1045 and 1080 unnotched samples, and the 1045 a/R$]_o$=0.5,
1045 a/R$]_o$ = 1.2 notched samples, respectively. These curves show
similar trends which can be summarized as follows:

- the number of voids first increases linearly with strain, then
  increases more rapidly as the fracture surface is approached.
- the rate of increase of the number of voids per unit area with
  strain is reduced by superimposing hydrostatic pressure.
- for a given material, or specimen geometry, the number of voids
  at fracture increases as the superimposed hydrostatic pressure
  is increased.
- for the unnotched samples at a given pressure, the number of voids
  per unit area at fracture decreases as the volume fraction of
  carbide particles decreases.
- voids appear at lower strains when a notch is present in the
  specimen.

III - 5 - 2 Growth of Voids

Once nucleated, the voids grow most rapidly in the tensile
direction. For the specimens tested at atmospheric pressure, a
triaxial stress state is created in the neck, so that voids can
grow laterally after the onset of necking. A superimposed hydrostatic
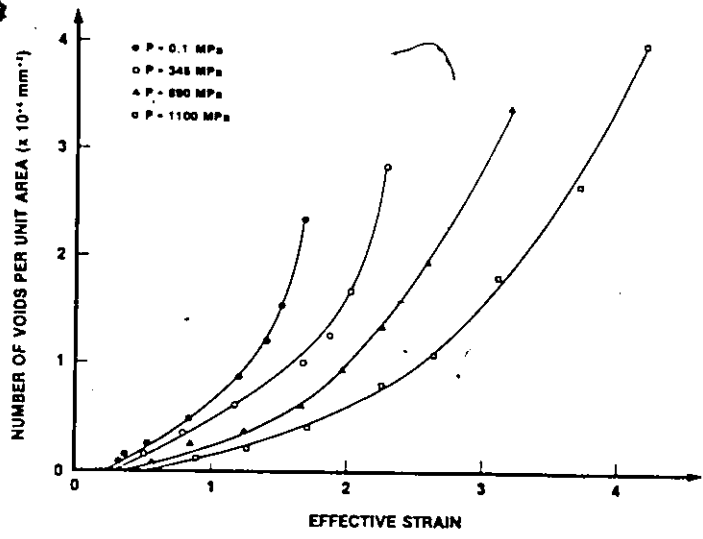
Fig. III-16-a
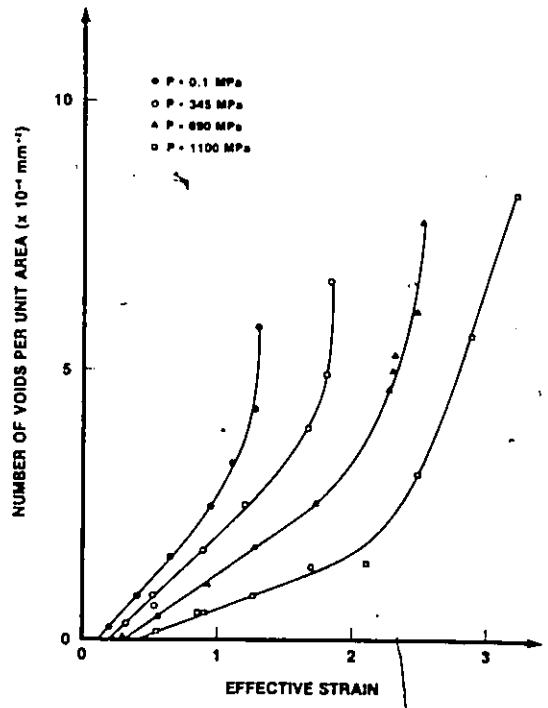
Fig. III-16-b
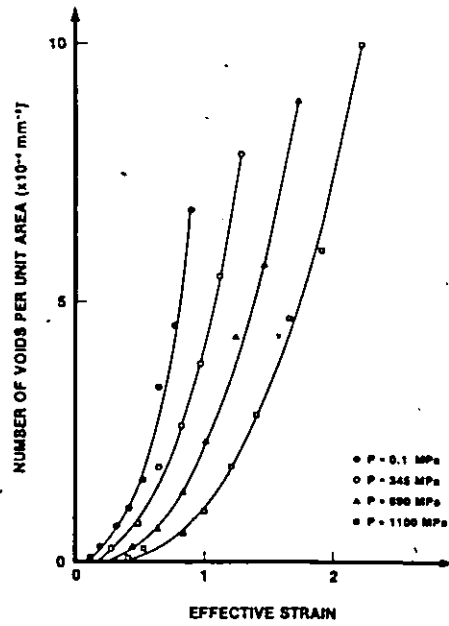
Fig. III-16-c
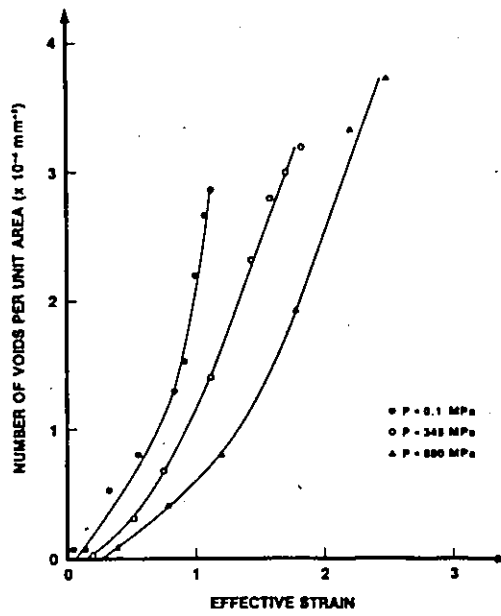
Fig. III-16-d
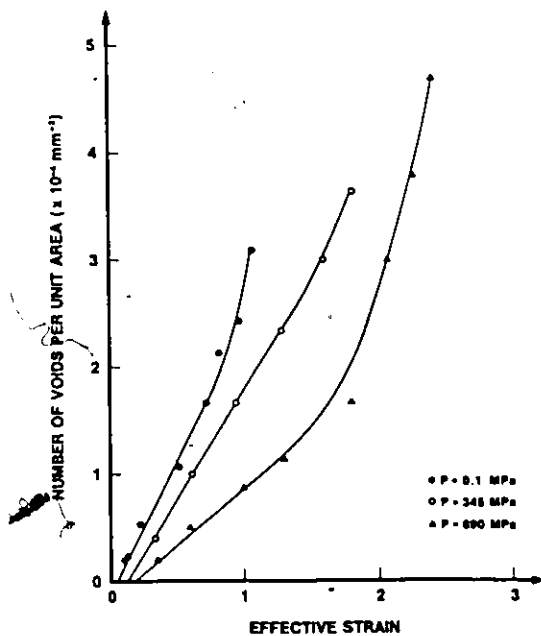
Fig. III-16-e

Fig. III-16 : Plot of the number of voids per unit area as a function
of effective strain for :
a) 1018 samples   b) 1045 unnotched samples
c) 1080 samples   d) 1045 a/R)$_o$= .5 notched samples
e) 1045 a/R)$_o$=1.2 notched samples

pressure will oppose this growth until a much higher degree of neck development; this results then in more extensive growth along the tensile axis, as shown from the comparison of the micrographs in fig. III - 17.

To provide a quantitative measure of microstructural damage, the area fraction of voids has been measured as a function of strain. This parameter is a global one, and it does not account for the drastic changes in the shape of the voids (fig. III - 17), but it allows a comparison from one stress state to another, or one material to another. The results are shown in fig. III - 18 - a to III - 18 - e for the 1018, 1045 and 1080 unnotched samples, and the 1045 a/R]$_o$ = 0.5, 1045 a/R]$_o$ = 1.2 notched samples, respectively. The following conclusions can be drawn from these curves:

- the rate of damage development is reduced by superimposed pressure.

- for a given material, or specimen geometry, the area fraction of voids at fracture is essentially independent of superimposed hydrostatic pressure. A similar result has been reported by Oyane (1972) for compression tests under pressure.

- for the 1045 steel, the area fraction of voids at fracture is decreased when a triaxiality is created by a notch.

- for the unnotched specimens, the critical value of area fraction of voids at fracture is increased as the volume fraction of carbide particles f_v is increased (fig. III - 19). After a rapid increase at low values of f_v, the critical amount of damage appears to increase very slowly at higher values of f_v; this may be
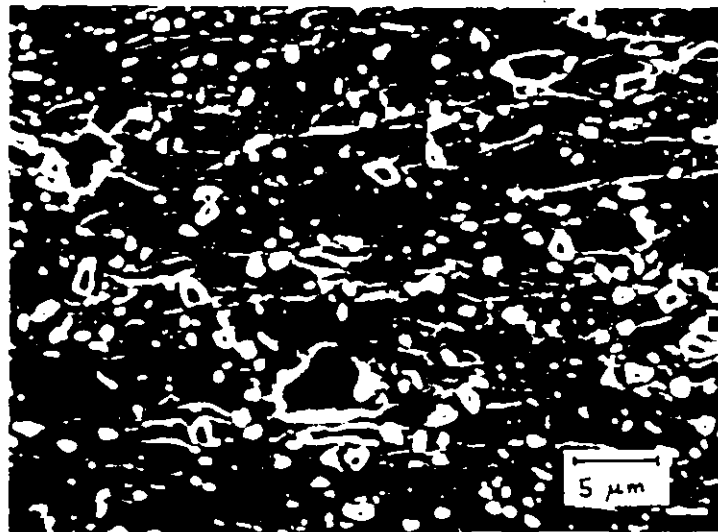
(a)
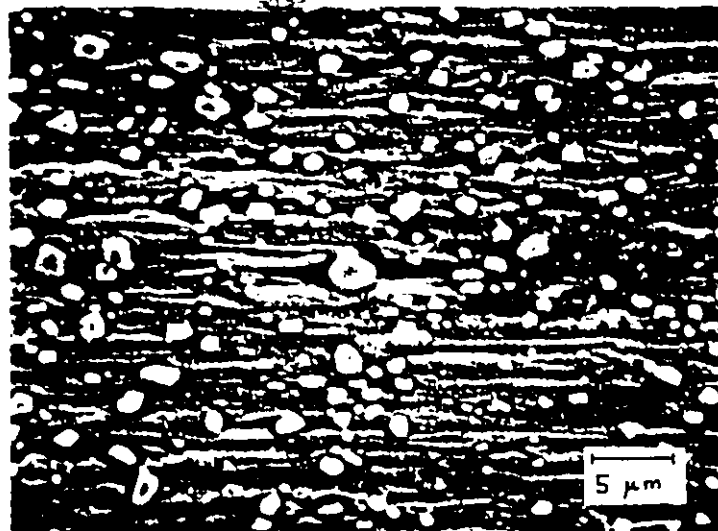
(b)

Fig. III-17 : Scanning electron micrographs showing the influence
of hydrostatic pressure on the shape of the voids in
the 1045 unnotched samples :
a) $\bar{\varepsilon} = 1.3$
b) $\bar{\varepsilon} = 3.2$
The tensile axis is horizontal.
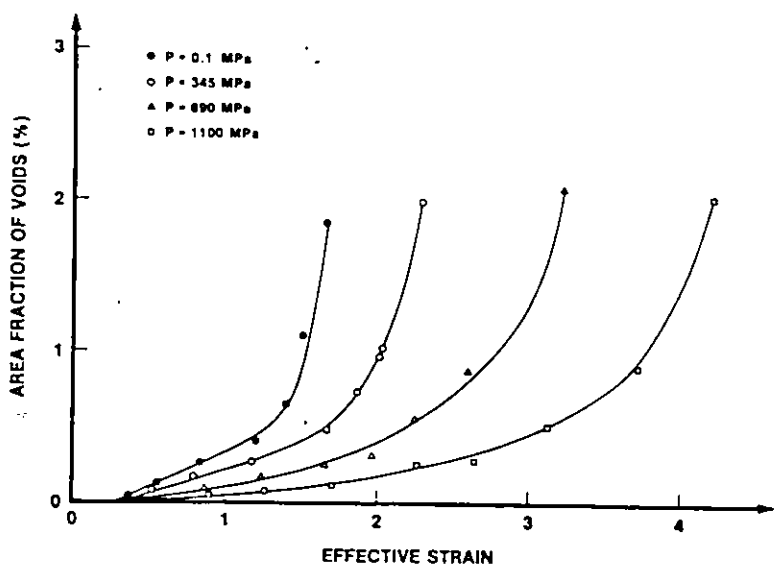
Fig. III-18-a
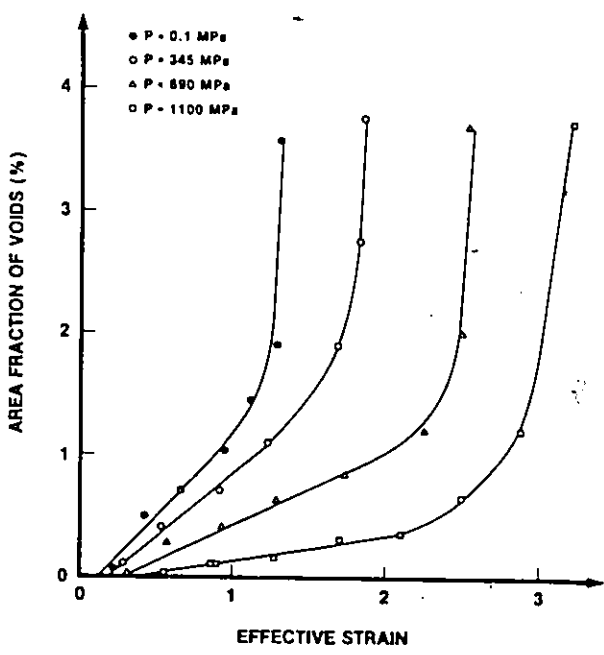
Fig. III-18-b
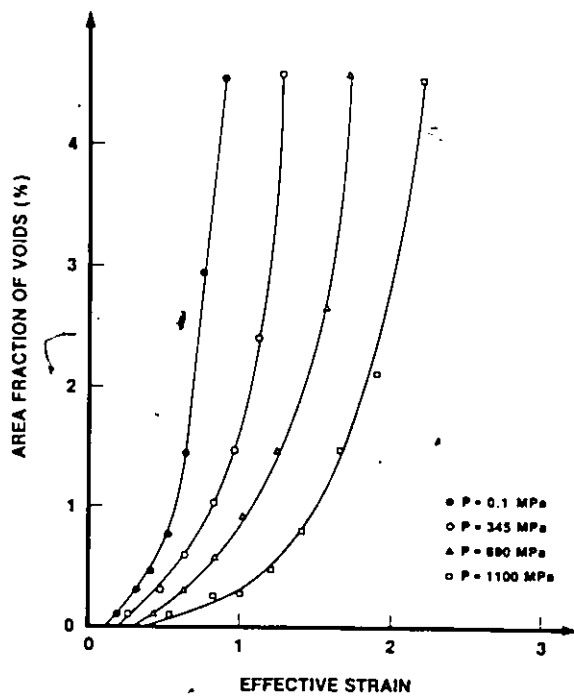
Fig. III-18-c
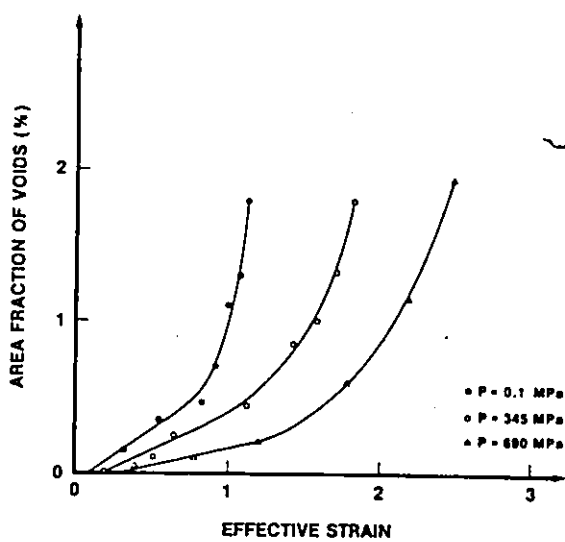
Fig. III-18-d
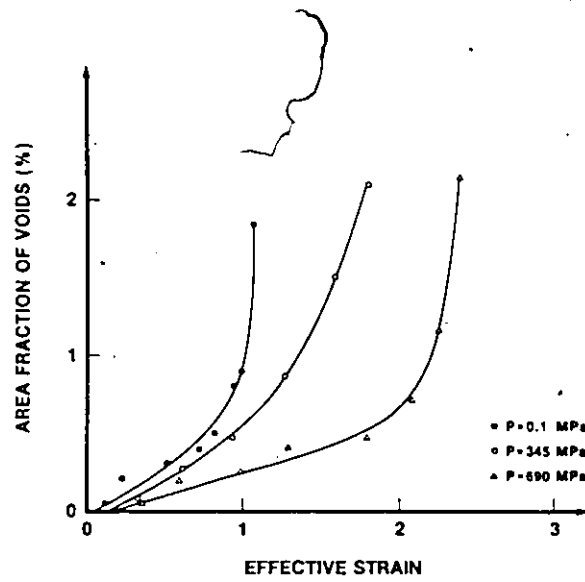
Fig. III-18-e

Fig. III-18 : Plot of the area fraction of voids as a function of
              effective strain for ;
              a) 1018 samples   b) 1045 unnotched samples
              c) 1080 samples   d) 1045 a/R)$_o$= .5 notched samples
              e) 1045 a/R)$_o$=1.2 notched samples
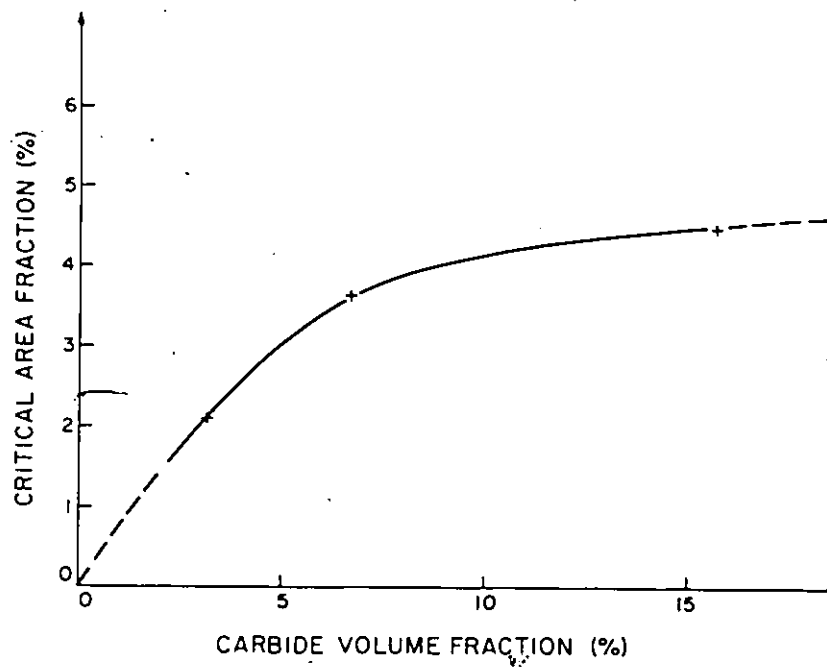
Fig. III-19 : Plot of the critical amount of damage for fracture
as a function of the carbide volume fraction.
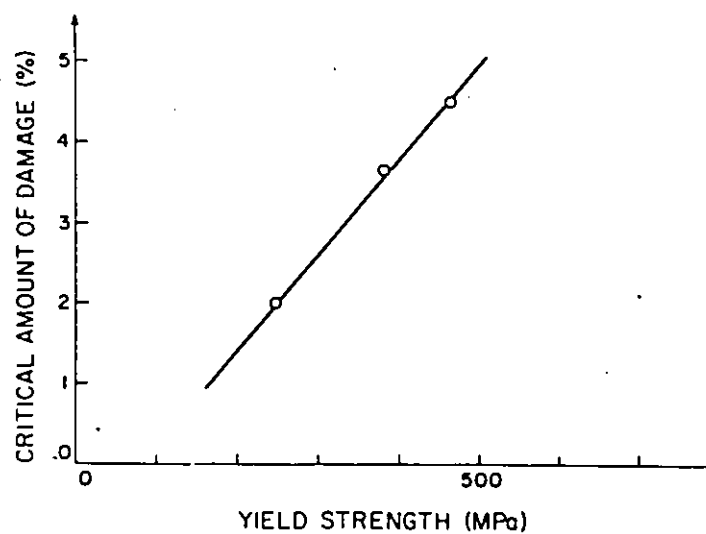
Fig. III-20 : Plot of the critical amount of damage for fracture
as a function of the yield stress of the corresponding
steel.

explained by the fact that the voids are interacting, and cannot develop too much without overlapping. The critical amount of damage is found to increase linearly with the yield stress of the corresponding spheroidized steel, as shown in fig. III - 20.

III - 5 - 3 Conclusions

The experimental work reported here allows the correlation between damage development and stress state during all the deformation of the sample.

It has also be emphasized that the nucleation of voids does not occur at a unique strain because it depends upon the particle size.

The next step is to attempt to model the nucleation and growth process to account for the experimental results and to comment on a criterion for fracture which is necessary to give an overall description of ductile fracture.

III - 6 Model and Discussion

III - 6 - 1 Nucleation

The experimental observations have shown the dependence of nucleation upon the size of second-phase particles. This suggests that the nucleation event can be considered as a reaction front scanning through the carbide size distribution at a rate which depends on both the stress state and the strain level. This is schematized in fig. III - 21. As a result of experimental observation, the "nucleation front" moves from the right to the left, i.e. from the largest to the smallest particles.

III - 6 - 1 - 1 Simplified Model

As seen in the literature review, the energy balance criterion is only a necessary condition and is fulfilled for large enough particles. The local stress criterion appears more realistic. The deformation of the plastic matrix around a hard particle produces dislocation tangles around the particle. This creates a stress on the interface, called σ_{loc}, such that:

$$\sigma_{loc} = 4.2 \; \sigma_\ell \qquad (III - 12)$$

according to Brown and Stobbs (1976). The flow stress σ_ℓ is directly related to the dislocation density around the particle ρ_ℓ in the following way (Nabarro et al., 1964):

$$\sigma_\ell = \alpha \; \mu b \sqrt{\rho_\ell} \qquad (III - 13)$$

where α is a constant equal to 1/7, μ is the shear modulus and b the Burgers vector.

The stress existing at the particle-matrix interface is:

$$\sigma = \sigma_{loc} + \sigma_m \qquad (III - 14)$$

where σ_m is the hydrostatic or mean stress component, and nucleation will take place when this stress σ will reach the interfacial strength σ_I, i.e.:

$$\sigma_I = \sigma_{loc} + \sigma_m \qquad (III - 15)$$

The next step is to relate the dislocation density to the strain, as, in fact, nucleation is a process dependent on both stress and
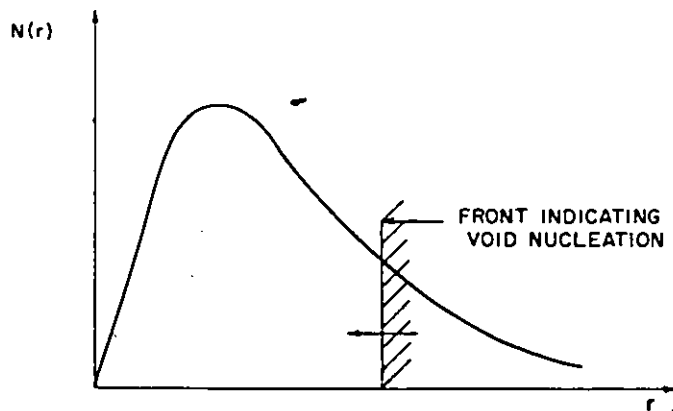
Fig. III-21 : Schematic diagram showing the passage of a void nucleation
front through the particle size distribution. The front
moves to the left with increasing effective strain at a
rate dependent on the superimposed pressure.
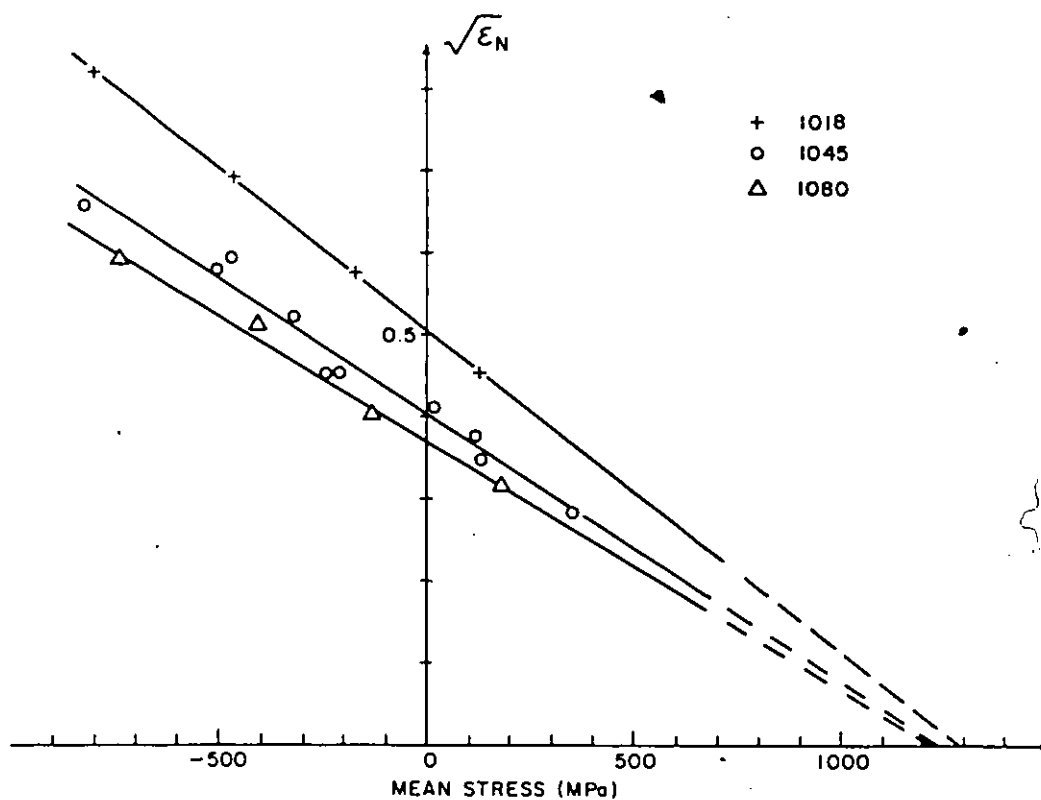
Fig. III-22 : Diagram showing the variation of the square root of the
nucleation strain with the mean stress σ_m obtained for
the 1018,1045 and 1080 spheroidized steels.

strain. This can be done by modelling the plastic zone around the particle. Assuming that there are no recovery processes occurring close to the particle, Brown and Stobbs (1976) have shown that ρ_ℓ is proporational to the strain ϵ. The coefficient of proportionality is subject to a variety of interpretations, and is not considered in detail in this simple model. Then:

$$\rho_\ell = \gamma \, \epsilon \qquad (III - 16)$$

combining equations (III - 12) to (III - 16), the nucleation is occurring when the following condition is fulfilled:

$$\sigma_I = \sigma_m + \delta\sqrt{\epsilon_N}$$

or:

$$\sqrt{\epsilon_N} = H(\sigma_I - \sigma_m) \qquad (III - 17)$$

where H is a constant for a given material and particle size, and ϵ_N is the nucleation strain. Therefore, according to equation (III - 17), a plot of $\sqrt{\epsilon_N}$ as a function of σ_m can give a value for the interfacial strength σ_I. In order to obtain this value for the iron-cementite system, the nucleation strains have been determined from the curves giving the number of voids per unit area vs strain, by extrapolating these curves down to N = 0. This provides, in fact, a very crude approximation of the nucleation strains, but it allows a comparison to be made with all the experiments. The data are plotted according to equation (III - 17) in fig. III - 22. Three curves are shown, each corresponding to one sort of steel. The curve for the 1045 steel includes the data obtained from the notched specimens. It can be seen that the curves are straight lines,

and that their intercepts with the stress axis, which give the value

of σ_I, are between 1200 and 1300 MPa, in good agreement with the value

of 1200 MPa obtained by Leroy (1978). The three relationships

obtained are:

for the 1018 steel $\quad \sqrt{\epsilon_N} = 3.95\ 10^{-4}(1280 - \sigma_m)$ (a)

for the 1045 steel $\quad \sqrt{\epsilon_N} = 3.27\ 10^{-4}(1230 - \sigma_m)$ (b) (III - 18)

for the 1080 steel $\quad \sqrt{\epsilon_N} = 3.05\ 10^{-4}(1215 - \sigma_m)$ (c)

This provides, therefore, a value of approximately 1200 MPa for the

interfacial strength of the Fe - Fe$_3$C system, which will be used in

further calculations.

III - 6 - 1 - 2 Complete Model

The model described here to calculate the number of voids

as a function of strain uses the distribution of particle sizes in

an analytical form. The nucleation starts at the strain ϵ_N deter-

mined above and goes on to the fracture strain ϵ_f. Each increment

of strain $d\epsilon$ leads to a change dr of the critical radius required

for a particle to nucleate a void. This change dr gives in turn an

increment dN of the number of voids, obtained from the particle size

distribution.

(a) The particle size distribution

It has been found to be a log-normal distribution, so that

the curves shown in fig. III - 3 can be described by a function of the

form:

$$f(r) = \frac{\beta}{r}\ \exp\left[- \frac{(\log r + \gamma)^2}{\delta}\right] \qquad (III - 19)$$

where β, γ and δ are constant for a given material.

(b) The critical radius of nucleation

In order to produce a more detailed model, the relationships existing between the local stress around the particles σ_{loc}, the dislocation density ρ_ℓ and the strain ε, must be expressed in such a way as to take into account the particle size dependence of the nucleation event. Indeed, the relationships used in the simplified model presented previously are assuming that dislocations are accumulating around the particles without any recovery taking place; therefore, they do not take into account the possibility of competition between local events such as accumulation of dislocations and recovery or recrystallization. Brown and Stobbs (1976) have proposed the following relationship:

$$\rho_\ell = \frac{8}{3} \frac{\varepsilon}{rb} \qquad (III - 20)$$

This equation gives a variation of the nucleation strain with particle radius (see equation II - 14) which is in disagreement with experimental observations. In the absence of any physical model describing the dislocation behaviour around a particle, an empirical relationship has been used in the present model:

$$\rho_\ell = \eta \frac{\varepsilon}{b} r^q \qquad (III - 21)$$

where q is a positive exponent which will have to be determined from experimental results, and η is a constant. Combining equations (III - 12), (III - 13), (III - 15) and (III - 21), the critical radius for nucleation r_c is given by:

$$r_c = \left[\frac{(\sigma_I - \sigma_m)^2}{K'} \right]^{1/q} \left[\frac{1}{b \, \epsilon} \right]^{1/q} \qquad \text{(III - 22)}$$

where K' is a constant.

From the experimental results presented before, the mean stress σ_m is a linear function of strain :

$$\sigma_m = A \, \epsilon + C$$

with, $\qquad A = \beta' \, (1 + 3 \, \alpha \, P) \qquad \text{(III - 23)}$

and $\qquad C = \gamma' - P$

where β' and γ' are constant and characterize a given material. Therefore, the critical radius for nucleation becomes :

$$r_c = \left[\frac{(\sigma_I - C - A \, \epsilon)^2}{K \, \epsilon} \right]^{1/q} \qquad \text{(III -24)}$$

The increment dr_c corresponding to an increment $d\epsilon$ of strain is then :

$$dr_c = \frac{d\epsilon}{q} \left[\frac{A^2 \epsilon^2 - (\sigma_I - C)^2}{K \, \epsilon^2} \right] \left[\frac{(\sigma_I - \sigma_m)^2}{K \, \epsilon} \right]^{\frac{1}{q} - 1} \qquad \text{(III - 25)}$$

In both equations (III - 24) and (III - 25), K is a constant including the shear modulus and the Burgers vector.

(d) The number of voids

If N_A is the number of particles per unit area of longitudinal surface, i.e. in a plane containing the tensile axis, the number of voids which nucleate at each strain increment is :

$$dN = N_A \, f(r_c) \, dr_c$$

Using a computer program, it is therefore possible to calculate incrementally the curves giving the number of voids N as a function of strain ϵ with the simple algorithm :

$$\varepsilon = \varepsilon + d\varepsilon$$

$$dN = N_A + f(r_c) \, dr_c$$

$$N = N + dN$$

(d) Comparison with the experiments

The model has one parameter, the exponent q, which must be
fitted from the experimental curves. For a given material, the fit
has been done by using the curve $N(\varepsilon)$ obtained at atmospheric pressure.
The value of q determined from this curve is then used to calculate
the curves at high superimposed pressures. Similarly, the number
of particles per unit area N_A has been calculated from metallographic
data. However, it has been adjusted to give the correct value of the
number of voids at fracture at atmospheric pressure. It has then been
used for the other curves.

For all the materials studied, i.e. the 1018, 1080 and
1045 (with and without notches) steels, the value of q has been found
to be q = 8, with minor variations from one material to another.
(from 7.75 to 8.25). The curves obtained from the model are compared
with the experimental ones in fig. III - 23 - a to III - 23 - e for
the 1018, 1045 and 1080 unnotched samples, and the 1045 a/R]$_0$ = .5,
1045 a/R]$_0$ = 1.2 notched samples, respectively. The agreement is
quite good, despite some discrepancies in the steep part of the
curves. This can be related to some possible errors in the way
the strain has been determined: if the surface under observation
is not exactly the mid-plane, the strain is, therefore, over-
estimated (see fig. III - 2). It should also be noticed that this
model accounts for the experimental observations that the number of

118

Fig. III-23-a

Fig. III-23-b

Fig. III-23-c

Fig. III-23-d

Fig. III-23-e

Fig. III-23 : Comparison of the calculated number of voids per unit
area vs effective strain curves with the experimental
ones for :
a) 1018 samples   b) 1045 unnotched samples
c) 1080 samples d) 1045 a/R)$_o$= .5 notched samples
e) 1045 a/R)$_o$=1.2 notched samples

voids at fracture increases as the superimposed pressure is increased.
It is, therefore, thought that the model gives a good description of
the nucleation of voids during tensile deformation.

III - 6 - 1 - 3 Discussion of the Model

The principal point to be made about the model is the signifi-
cance of the exponent q. Despite the fact that q has been found to
be equal to 8 for a wide range of materials, it is unlikely that
this value stems directly from a basic physical law.

In order to describe the experimental results, the particle
size distribution f(r) must be scanned slowly, i.e. the critical
radius of nucleation is varying slowly with strain, as shown in
fig. III - 24. This means that the local deformed state does not
allow the attainment of the interfacial strength σ_I to occur around
the small particles as quickly as around the large ones. Despite the
fact that the deformation structure at large strains around particles
is poorly understood (Humphreys, 1980), it is possible to argue that
around small particles, several plastic relaxation processes can
easily take place to relieve the dislocation accumulation and delay the
build-up of a local stress which is high enough to overcome σ_I. At
large strains, the matrix around a small particle can accomodate the
plastic heterogeneity by producing prismatic loops of either primary
Burgers vectors or secondary Burgers vectors. Around large particles,
the geometry of slip has been proven to be more complicated, and
processes involving the formation of large lattice rotations can
take place (Humphreys, 1979).

CRITICAL RADIUS FOR NUCLEATION (μm)

EFFECTIVE STRAIN

+ p = 0.1 MPa
o p = 345 MPa
△ p = 690 MPa
□ p = 1100 MPa
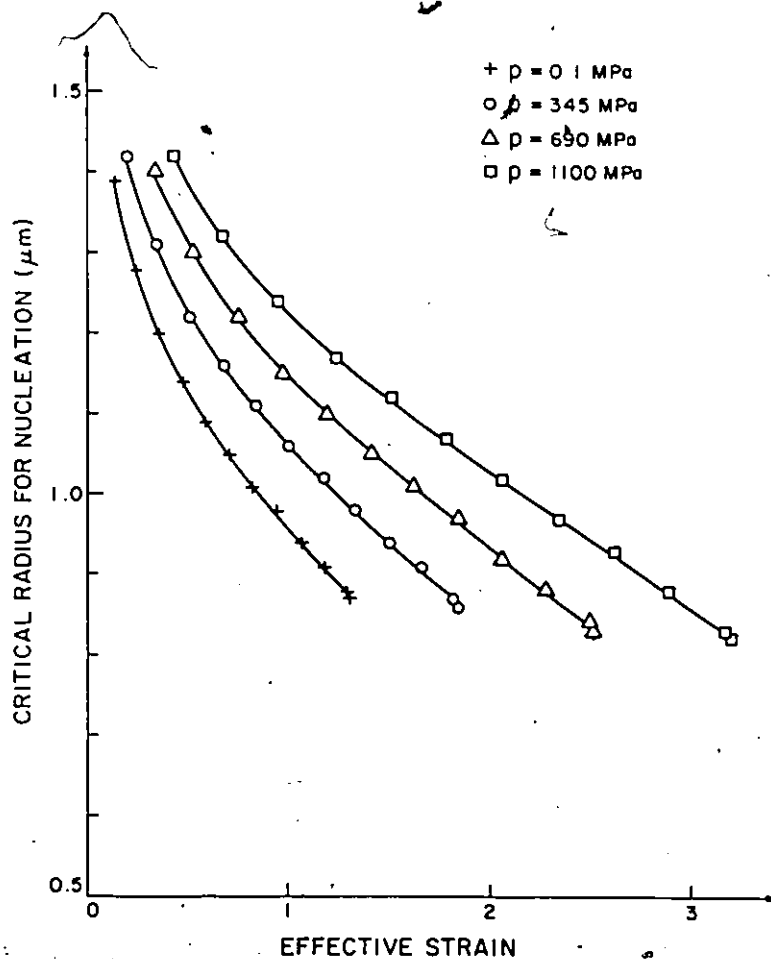
Fig. III-24 : Diagram showing the variation of the critical radius
for void nucleation as a function of effective strain
obtained at various pressures from the complete nucle-
ation model applied to the 1045 unnotched samples.

Therefore, it can be concluded that the existence of plastic relaxation processes occurring more easily around small particles can explain qualitatively the type of variation used empirically in equation (III - 21). Quantitatively, the completeness of the results available here indicates that the value of q is characteristic of the system iron-cementite. It must finally be emphasized that the dislocation density has been used here simply as a conceptional vehicle to get to the interfacial strength σ_I; a continuum plasticity treatment might have given the same type of results.

III - 6 - 2 Growth

The next step in the process of modelling damage accumulation is to make the voids grow once they have nucleated. The work presented here follows the treatment given by Rice and Tracey (1969) already presented in the literature review, of the growth of an isolated void in a plastic infinite matrix. It is the continuation of the previous incremental model used to describe the curves $N(\varepsilon)$.

Using the subscript 3 to designate the tensile axis, and the subscript 1 for the transverse direction, the growth rates of the void after its nucleation are given by (Rice and Tracey, 1969) :

$$dR_3 = R_3 \ (\gamma_a + D) \ d\varepsilon$$

$$dR_1 = R_1 \ (-\frac{\gamma_a}{2} + D) \ d\varepsilon$$

(III - 26)

where γ_a is an amplification factor describing the change in the shape of the voids, and is given by (Leroy, 1978) :

$$\gamma_a = 1 + \exp \ (-2.25 \ (\varepsilon - \varepsilon_N) \ ) \qquad (III - 27)$$

and D is a factor describing the volume change of the voids, and is given by:

$$D = 0.56 \; \sinh \left(\frac{3}{2} \; \frac{\sigma_m}{\bar{\sigma}} \right) \qquad \text{(III - 28)}$$

$\bar{\sigma}$ being the flow stress of the matrix.

It is, therefore, possible to complete the algorithm used to calculate the curves $N(\epsilon)$ and to determine the curves giving the area fraction of voids as a function of strain, $A(\epsilon)$. The dN voids created by the increment $d\epsilon$ of strain are made to grow incrementally as deformation proceeds: at every strain increment, their contribution to the area fraction is:

$$dA = \pi \; dN \; dR_1 \; dR_3 \qquad \text{(III - 29)}$$

The results obtained from this model are shown in fig. III - 25 - a to fig. III - 25 - e for the 1018, 1045 and 1080 unnotched specimens, and the 1045 a/R]$_o$ = 0 .5, 1045 a/R]$_o$ = 1.2 notched specimens, respectively. The main conclusions from this comparison are that the agreement is reasonable, with some expected discrepancies in the steep part of the curves, and that the area fractions of voids at fracture calculated from the model are, as the experimental values, essentially constant with respect to the superimposed pressure for a given material. This very important observation will be used later in the discussion of the coalescence process and of the fracture criterion.
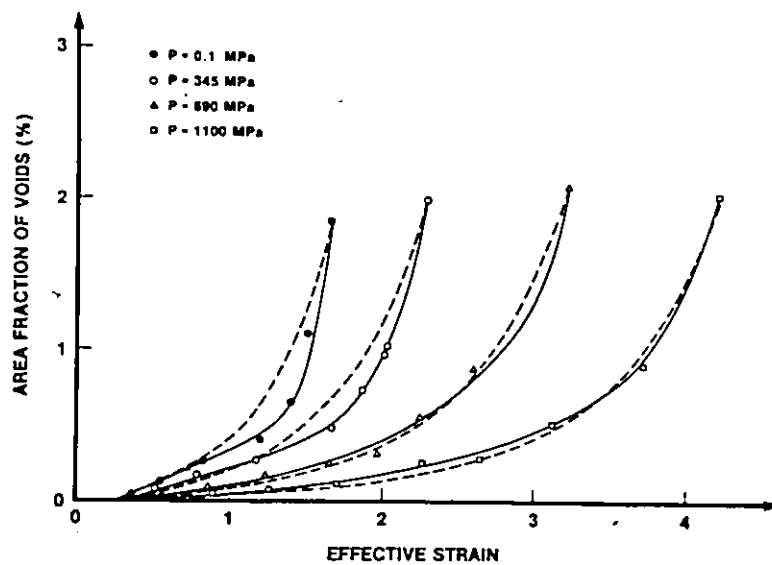
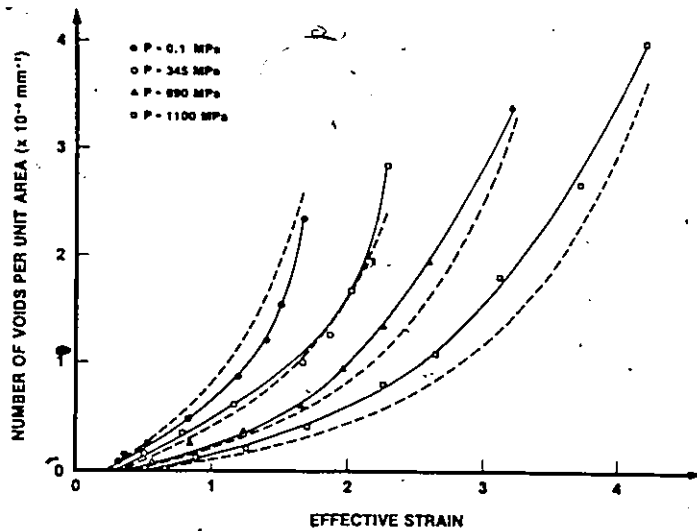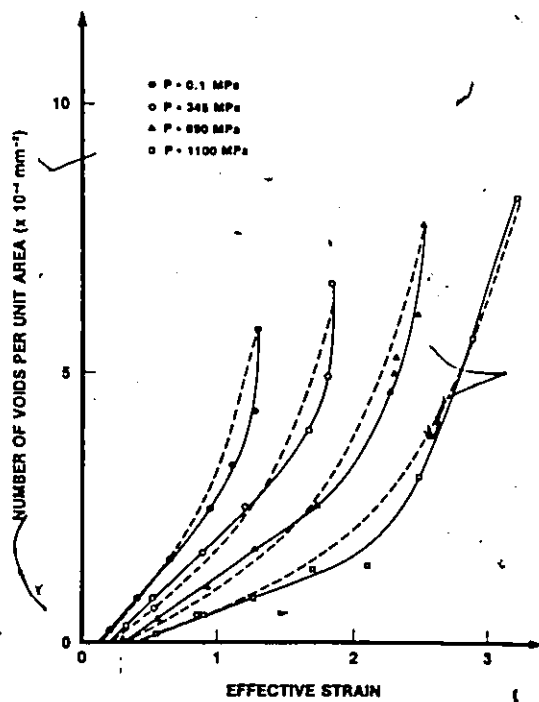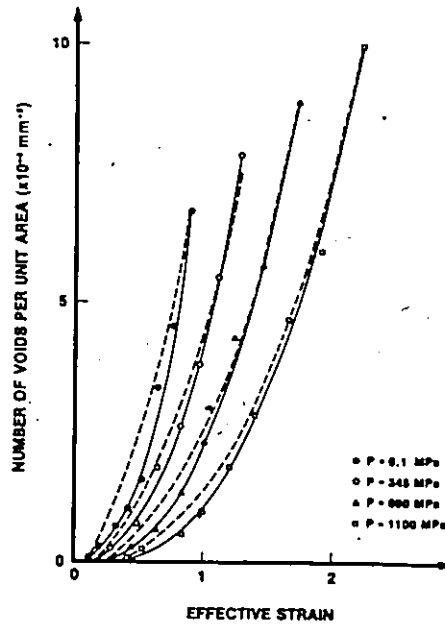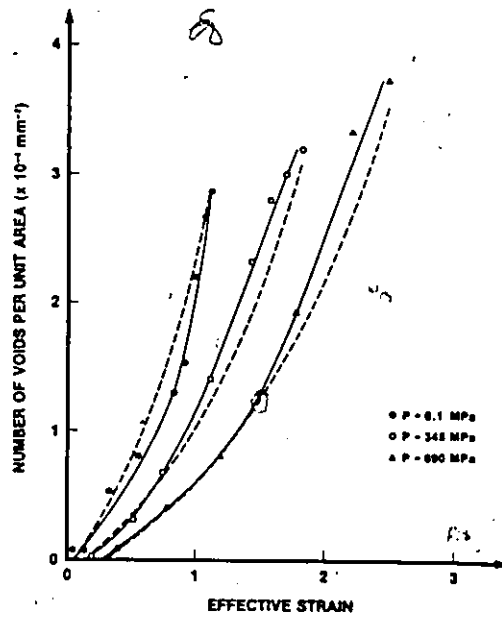Fig. III-25-a
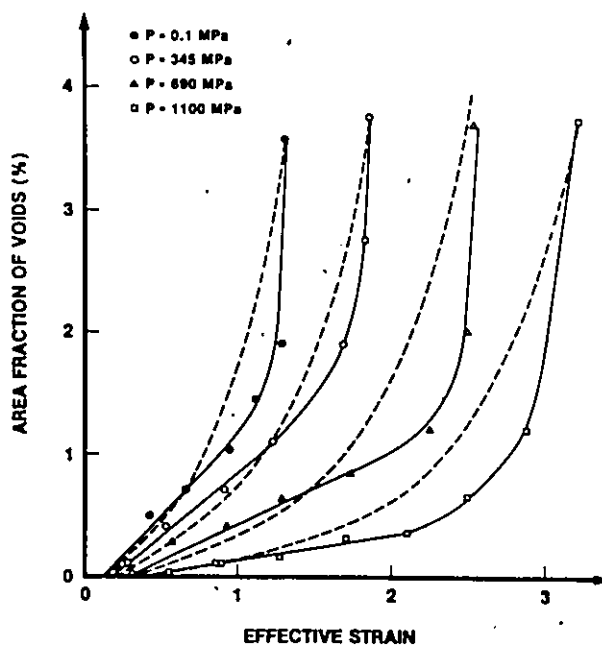
Fig. III-25-b
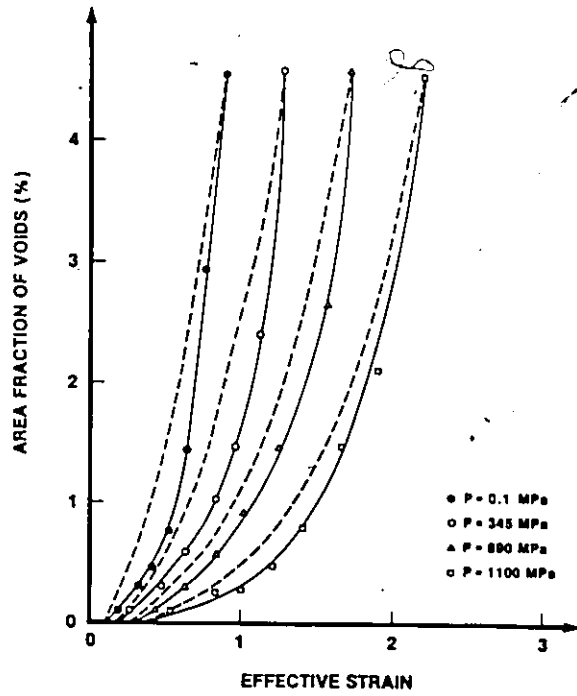
Fig. III-25-c
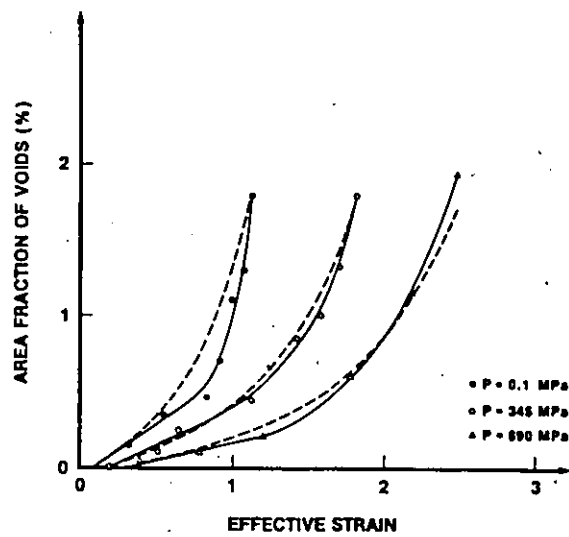
Fig. III-25-d
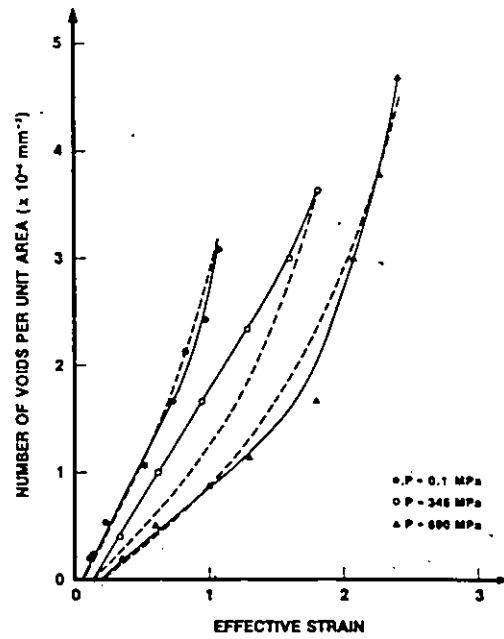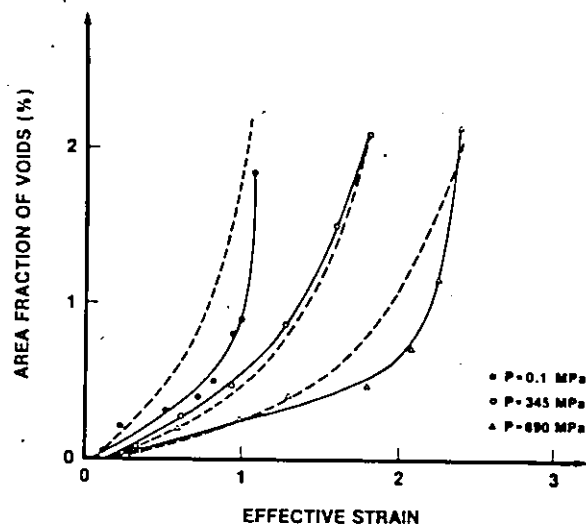
Fig. III-25-e

Fig. III-25 : Comparison of the calculated area fraction of voids vs
effective strain curves with the experimental ones for :
a) 1018 samples b) 1045 unnotched samples
c) 1080 samples d) 1045 a/R)$_o$= .5 notched samples
e) 1045 a/R)$_o$=1.2 notched samples

III - 6 - 3   Coalescence.Model of Ductile Fracture

The last part is concerned with the linkage of voids, leading to final failure. From this, it should be possible to propose a criterion for ductile fracture of the spheroidized steels.

The microstructural observations show different possibilities for the linkage of voids, according to the value of the applied pressure. At atmospheric pressure, voids can grow perpendicular to the tensile axis, and when two voids are impinging along this direction, by a process of local necking, they coalesce to form a larger void (fig. III - 26). Very few arrays of larger voids are seen below the fracture surface, and this emphasizes the highly localized and catastrophic character of final failure. When a pressure is applied, even for the smallest value (345 MPa), the lateral growth of the voids is almost suppressed. Instead, voids are joining along the tensile axis (fig. III - 27). No large or multiple voids have been seen at high pressures below the fracture surfaces, except in the 1080 steel, in which the high volume fraction of carbides makes the interparticle spacing quite small. It is worth noticing that these few multiple voids seem to be oriented like the shear lips of the fracture surface, i.e. at about 45° to the tensile axis, indicating that a localized shearing process between adjacent voids due to high superimposed pressure could be responsible for their coalescence (fig. III - 28).

From these observations, it is, therefore, difficult to propose a definitive mechanism of void linkage. However, a first attempt can be made by using the geometrical model of Brown and
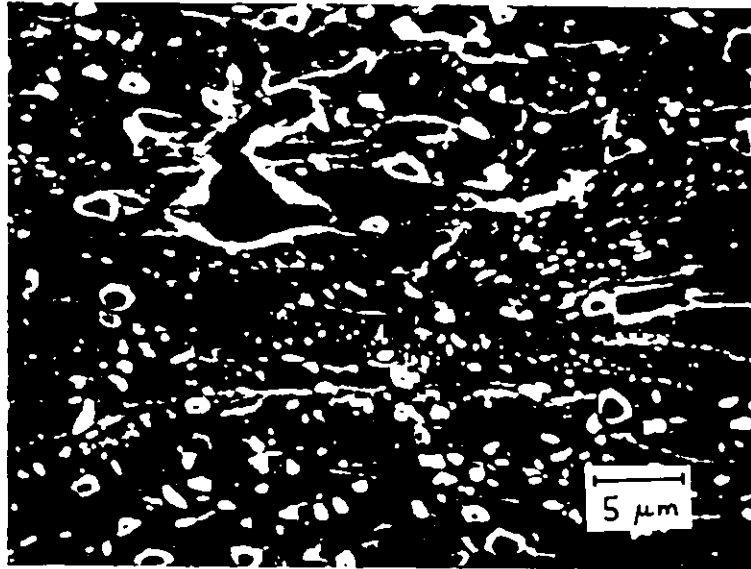
Fig. III-26 : Scanning electron micrograph showing a multiple void in the 1045 unnotched sample broken at atmospheric pressure. The tensile axis is horizontal.
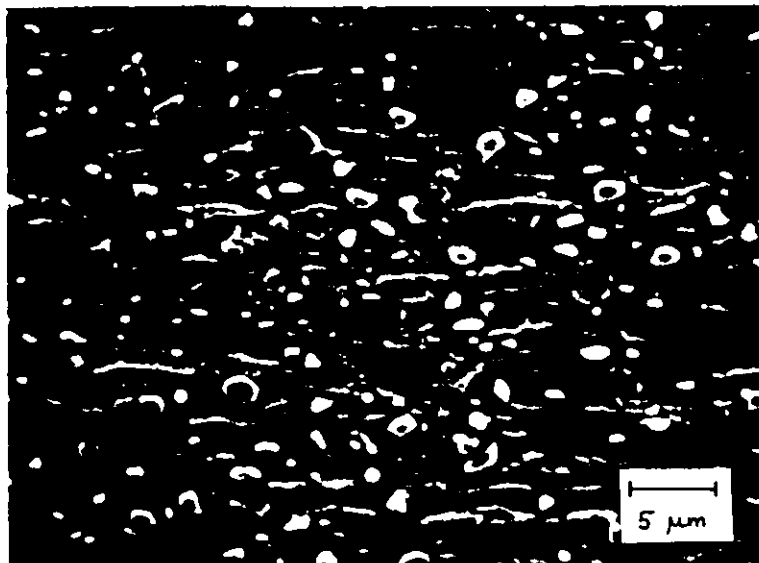
Fig. III-27 : Scanning electron micrograph showing the joining of voids along the tensile axis (horizontal) in the 1045 unnotched sample broken under 345 MPa.

10 μm
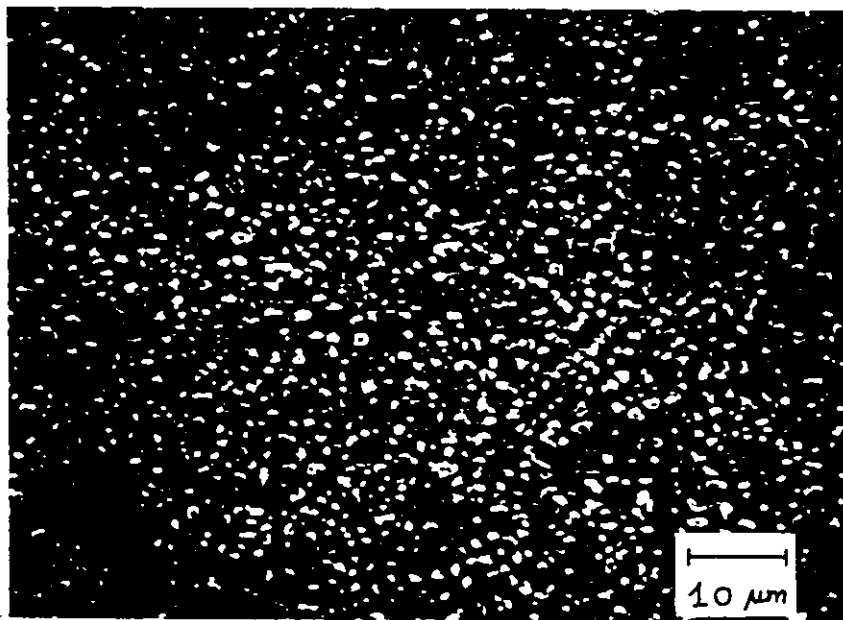
Fig. III-28 : Scanning electron micrograph showing the joining
of voids to form a shear crack in the 1080 sample
broken under 1100 MPa.

Embury (1973). The fracture criterion adopted is that fracture will occur when the void dimension in the principal tensile stress direction reaches a critical value which is determined by a micro-structural distance λ. With the notations previously used this can be written as:

$$2R_3^f = \lambda \qquad (III - 30)$$

where λ is assumed independent of any superimposed pressure. Therefore, if R_3^{f1} is the dimension of void when no pressure is applied, and if R_3^{f2} is the dimension when a pressure P is applied, this gives:

$$R_3^{f1} = R_3^{f2} = \lambda/2 \qquad (III - 31)$$

Using equation (II - 28) from Leroy et al., (1981) and letting the subscript 1 refer to a test without applied pressure and the subscript 2 to a test with an applied pressure P, this leads to:

$$\exp(D_1 \bar{\epsilon}_1) \; (2 \exp(\tfrac{3}{2} \bar{\epsilon}_1) - 1)^{2/3}$$
$$= \exp(D_2 \bar{\epsilon}_2) \; (2 \exp(\tfrac{3}{2} \bar{\epsilon}_2) - 1)^{2/3} \qquad (III - 32)$$

or:

$$D_1 \bar{\epsilon}_1 + \tfrac{2}{3} \ln(2 \exp(\tfrac{3}{2} \bar{\epsilon}_1) - 1) \qquad (III - 33)$$
$$= D_2 \bar{\epsilon}_2 + \tfrac{2}{3} \ln(2 \exp(\tfrac{3}{2} \bar{\epsilon}_2) - 1)$$

Typical values for the quantities involved are:

$$\bar{\epsilon}_1 = 1.2, \text{ thus } 2 \exp \tfrac{3}{2} \bar{\epsilon}_1 \simeq 15$$
$$\bar{\epsilon}_2 = 3 \quad, \text{ thus } 2 \exp \tfrac{3}{2} \bar{\epsilon}_2 \simeq 200$$

Therefore, in both cases:

$$2 \exp \left(\frac{3}{2} \bar{\epsilon}\right) \gg 1$$

Equation (III - 33) becomes:

$$D_1 \bar{\epsilon}_1 + \bar{\epsilon}_1 = D_2 \bar{\epsilon}_2 + \bar{\epsilon}_2$$

i.e.

$$\bar{\epsilon}_2 = \bar{\epsilon}_1 \left(\frac{1 + D_1}{1 + D_2}\right) \qquad \text{(III - 34)}$$

where $D = 0.56 \sinh \left(\frac{3}{2} \frac{\sigma_m}{\bar{\sigma}}\right)$

The term $\left(\frac{3}{2} \frac{\sigma_m}{\bar{\sigma}}\right)$ is small, so that the sinh term can be approximated to its argument:

$$D \simeq 0.56 \times \frac{3}{2} \frac{\sigma_m}{\bar{\sigma}}$$

which is still a small quantity.

Then, equation (III - 34) becomes:

$$\bar{\epsilon}_2 \simeq \bar{\epsilon}_1 (1 + D_1)(1 - D_2)$$

i.e.

$$\bar{\epsilon}_2 \simeq \bar{\epsilon}_1 (1 + D_1 - D_2)$$

and:

$$D_1 - D_2 = 0.56 \times \frac{3}{2} \left[\frac{\sigma_m (o)}{\bar{\sigma}} - \frac{\sigma_m (P)}{\bar{\sigma}}\right]$$

$$= \frac{1.68}{2} \left[\frac{\sigma_m (o)}{\bar{\sigma}} - \frac{\sigma_m (o)}{\bar{\sigma}} + \frac{P}{\bar{\sigma}}\right]$$

i.e.

$$D_1 - D_2 = \frac{1.68}{2} \frac{P}{\bar{\sigma}} \qquad \text{(III - 35)}$$

Therefore:

$$\epsilon_2 = \epsilon_1 \left[1 + \frac{1.68}{2} \frac{P}{\bar{\sigma}}\right] \qquad \text{(III - 36)}$$

This calculation, starting from a simple geometric argument, accounts, therefore, for the observed linear variation of the fracture strain with superimposed pressure.

This linear variation has been found in previous studies performed on steels and pure metals. The pressure dependence of the fracture strain varies from one material to another due to the variation in the strength parameter $\bar{\sigma}$ in equation (III -. 36). Yajima et al., (1970) reported such a variation and found that the slope of the curves $\varepsilon_f(P)$ was inversely proportional to the tensile strength of the material tested. A comparison of the experimental results with their theoretical values based on the tensile strength of various materials is given in Table (III - 8). This also includes the present work. The corresponding curves are shown in fig. III - 29. The agreement between calculated and experimental slopes is good, especially for the spheroidized steels. It should be noted that in deriving equation (III - 36), it has been assumed that the dominant effect is the influence of applied pressure on void growth; however, in other materials, other factors can be of importance. In particular, at large strains, both damage accumulation and a decrease in the rate of strain hardening occur simultaneously, so that other failure modes such as localized shear bands forming between adjacent voids or even complete suppression of damage leading to plastic rupture, can occur (Yajima et al., 1970; French and Weinrich, 1977).

As this geometrical model gives a good account of the variation of fracture strain with applied pressure, it is worth

+ : DAVIDSON ET AL (1969) 0.40 %C SPHER. STEEL
O : FRENCH ET AL (1974a) 0.51 %C SPHER. STEEL
▽ : YAJIMA ET AL (1970) PURE Cu
△ :   "   PURE Fe
□ :   "   0.49 %C STEEL
◇ :   "   0.27 %C STEEL
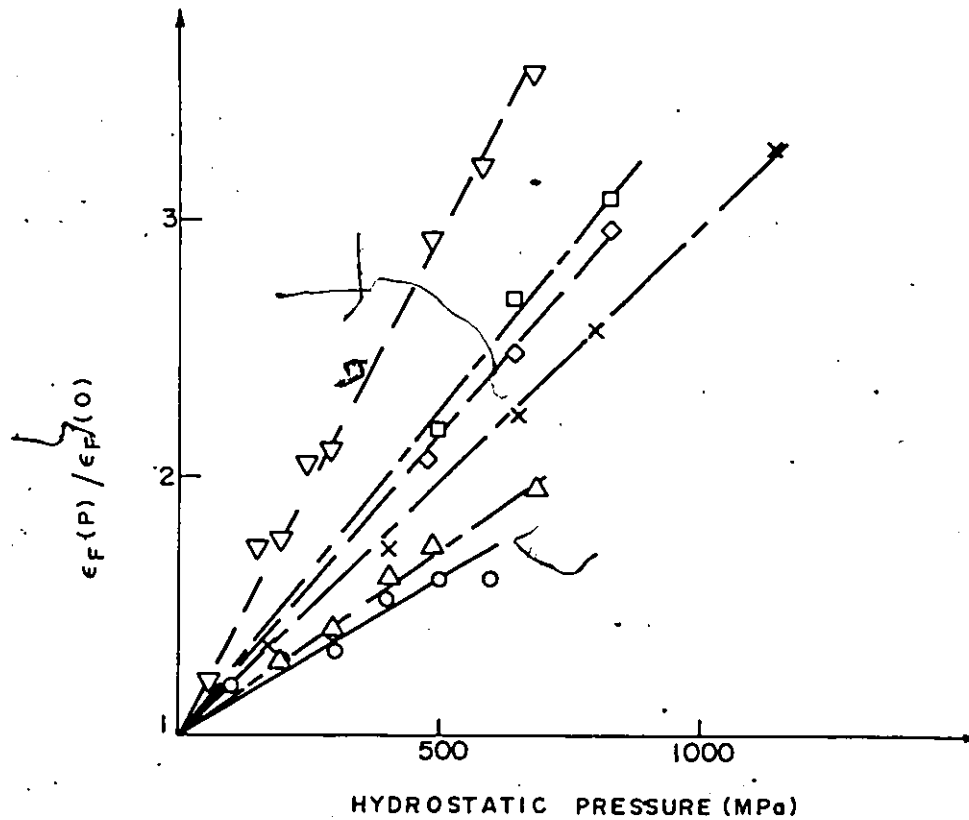
Fig. III-29 : Diagram showing the linear variation of the ratio of fracture strain under pressure $\varepsilon_f(P)$ to fracture strain at 0.1 MPa as a function of superimposed pressure, for a variety of materials (taken from the literature).

Table III-8 : Comparison of the calculated and measured values of the slopes of the linear relationships between fracture strain and superimposed hydrostatic pressure.

Material	Calculated slope ($MPa^{-1}x\ 10^3$)	Experimental slope ($MPa^{-1}x\ 10^3$)
1018 sph. steel (this work)	2.35	2.05
1045 " " " "	1.76	1.65
1080 " " " "	1.20	1.37
0.90% C sph. steel (Davidson et al., 1968)	2.13	1.97
0.51% C sph. steel (French and Weinrich, 1974a)	1.15	1.12
Pure Cu (Yajima et al., 1970)	2.60	3.71
Pure Fe (Yajima et al., 1970)	2.05	1.41
0.49% C steel (Yajima et al., 1970)	1.06	2.52
0.27% C steel (Yajima et al., 1970)	1.32	2.34

pursuing in order to calculate the lateral dimension of the voids at fracture, to compare it to the measured dimple size on the fracture surface.

Using the same notations than in the derivation of $\varepsilon_f(P)$, the lateral growth of voids is given by equation (II - 28) from Leroy et al., (1981):

$$\delta_1 = \delta_0 \ \exp(D_1 \ \bar{\varepsilon}_1) \ (2 \exp(\tfrac{3}{2} \bar{\varepsilon}_1) - 1)^{-1/3} \qquad (III - 37)$$

for a test without applied pressure, and:

$$\delta_2 = \delta_0 \ \exp(D_2 \ \bar{\varepsilon}_2) \ (2 \exp(\tfrac{3}{2} \bar{\varepsilon}_2) - 1)^{-1/3} \qquad (III - 38)$$

for a test under an applied pressure P.

Here again, in both cases:

$$2 \exp(\tfrac{3}{2} \bar{\varepsilon}) \gg 1$$

Therefore:

$$\ln(\delta_2/\delta_1) = (D_2 - \tfrac{1}{2}) \ \bar{\varepsilon}_2 - (D_1 - \tfrac{1}{2}) \ \bar{\varepsilon}_1 \qquad (III - 39)$$

From equation (III - 34):

$$\bar{\varepsilon}_2 = \bar{\varepsilon}_1 \ (\frac{1 + D_1}{1 + D_2})$$

then:

$$\ln(\delta_2/\delta_1) = \frac{3}{2} \ (\frac{D_2 - D_1}{1 + D_2}) \ \bar{\varepsilon}_1$$

$$\simeq \frac{3}{2} \ (D_2 - D_1) \ \bar{\varepsilon}_1$$

From equation (III - 35):

$$D_1 - D_2 = 0.84 \ \frac{P}{\bar{\sigma}}$$

then:

$$\ln(\delta_2/\delta_1) = -1.26 \ \frac{P}{\sigma} \ \bar{\varepsilon}_1 \qquad (III - 40)$$

i.e.

$$\delta_2 = \delta_1 \exp (-1.26 \frac{P}{\bar{\sigma}} \bar{\epsilon}_1) \qquad (III - 41)$$

or

$$\delta_2 \simeq \delta_1 (1 - 1.26 \frac{P}{\bar{\sigma}} \bar{\epsilon}_1) \qquad (III - 42)$$

Therefore, this model gives a linear relationship between the dimple diameter δ and the applied pressure P. In Table III - 9, a comparison is made between experiment and theory for the three tested spheroidized steels. It can be seen that at all pressures, the observed dimple size is larger than the calculated one. As the dimple size is the result of the process of void coalescence, this discrepancy means that the Rice and Tracey model of void growth and the geometrical model of void linkage become inappropriate in the final stage of void coalescence.

In all the materials tested, failure has occurred after the attainment of a critical amount of damage D independent of the super-imposed pressure. This observation can be used as a fracture criterion. However, the physical meaning of this critical level of damage is unclear. It could be considered in relation to the model of Melander (1980). This model states that crack initiation starts when the rate of energy consumptiom per unit of effective strain becomes constant, i.e. :

$$\frac{d^2W}{d\bar{\epsilon}^2} = 0 \qquad (III - 43)$$

with :

$$dW = \bar{\sigma}d\bar{\epsilon} - \sigma_m D \qquad (III - 44)$$

Therefore, equation (III - 43) is equivalent to :

$$\frac{d\bar{\sigma}}{d\bar{\epsilon}} - D \frac{d\sigma_m}{d\bar{\epsilon}} - \sigma_m \frac{dD}{d\bar{\epsilon}} = 0 \qquad (III - 45)$$

Table III-9 : Comparison of the calculated and the measured values

of dimple diameter for the unnotched samples of 1018,

1045 and 1080 spheroidized steels.

The data used in the calculation of the dimple diameters are :

Material	δ_1 (μm)	ε_1	$\bar{\sigma}$ (MPa)
1018	2.50	1.665	890
1045	2.20	1.30	990
1080	1.70	0.90	1030

Using these data in equation (III-41) leads to the following results:

Material	Pressure (MPa)	Calculated dimple diameter (μm)	Experimental dimple diameter (μm)
1018	345	1.11	2.21
	690	0.50	1.86
	1100	0.20	1.45
1045	345	1.24	1.87
	690	0.70	1.60
	1100	0.35	1.25
1080	345	1.16	1.50
	690	0.80	1.35
	1100	0.51	1.15

From fig. III - 7, it can be seen that $d\sigma_m/d\bar{\varepsilon}$ is essentially constant constant regardless of the applied pressure. The value of D at fracture also being constant, the criterion (III - 45) becomes:

$$\frac{d\bar{\sigma}}{d\bar{\varepsilon}} - \sigma_m \frac{dD}{d\varepsilon} = H \qquad (III - 46)$$

where H is a constant independent of applied pressure. This criterion has been tested with the results obtained for the 1045 unnotched samples, but does not seem to be correct, as the constant H varies from 125 MPa at atmospheric pressure to 70 MPa at 1100 MPa. Another possibility would be that, instead of occurring in a geometrical way, i.e. globally, the coalescence event could be a percolation process, triggered by the attainment of a critical amount of damage in the plane of the fracture surface.

Finally, it is possible to write the flow stress as:

$$\bar{\sigma} = \bar{\sigma} (\bar{\varepsilon}) (1 - D)$$

i.e.

$$\frac{d\bar{\sigma}}{d\bar{\varepsilon}} = \frac{\partial \bar{\sigma}}{\partial \bar{\varepsilon}} (1 - D) - \bar{\sigma}(\bar{\varepsilon}) \frac{\partial D}{\partial \bar{\varepsilon}} \qquad (III - 47)$$

The coalescence takes place when $d\bar{\sigma}/d\bar{\varepsilon} = 0$, i.e. the criterion is:

$$\frac{\partial \bar{\sigma}}{\partial \bar{\varepsilon}} (1 - D) = \bar{\sigma}(\bar{\varepsilon}) \frac{\partial D}{\partial \bar{\varepsilon}} \qquad (III - 48)$$

As the applied pressure increases, the strain hardening of the matrix $\partial \bar{\sigma}/\partial \bar{\varepsilon}$ decreases, the flow stress $\bar{\sigma}(\bar{\varepsilon})$ increases slightly, and the rate of damage development decreases. Therefore, the fact that D is constant could be consistent with the condition (III - 48). However, a test of this criterion shows that it is not fulfilled for the 1045 unnotched samples. This may be due to the fact that

the quantities used are global ones, including both the matrix and
the damage, whereas equation (III - 48) makes the distinction between
them.

To conclude this discussion, it can be noticed that the
localization of deformation which takes place at coalescence involves
the local spreading of damage. In fact, the macroscopic strain
occurring after the onset of this localization is negligible.
Therefore, despite the fact that the exact model of void coalescence
is not known, the present model of damage accumulation gives a
complete description of the ductile fracture process, because it
uses as a fracture criterion the attainment of a critical amount
of damage, the strain at which this occurs being the fracture strain.

III - 7   Conclusions

It is germane to restate the main features of the results
and model developed here.

a) The mechanical properties of different spheroidized steels
    tested in tension under various stress states have been
    recorded through the entire straining process.

b) A quantitative description of the damage accumulation
    during tensile deformation of the materials has been per-
    formed by measuring both the number of voids and their area
    fraction as a function of the effective strain. It has been
    found that the rate of damage development is decreased by
    superimposing an hydrostatic pressure, and that the number of
    voids participating at the final coalescence event is increasing

with superimposed pressure whereas the area fraction of voids just below the fracture surface is constant regardless of the superimposed pressure, for a given material.

c) A model has been developed to account for the damage accumulation process. It is based on the concept of a progressive nucleation event spreading through the particle size distribution at a rate dependent on the stress state and strain level. Once the voids are nucleated, their growth is calculated using the Rice and Tracey model. The agreement with the experiments is satisfactory, as the model gives the main features of the experimental curves.

d) The fracture criterion proposed is based on the experimental observation of a constant level of damage independent of the stress state. It is then proposed that failure occurs catastrophically by localization of the deformation occurring after a certain critical amount of damage has been reached.

CHAPTER IV

SHEAR FRACTURE

IV - 1 Introduction

In the Shear Fracture process, deformation becomes localized into narrow bands of material in which large strains are reached. Several continuum plasticity models describing localized shear failure have been presented in the literature review. However, the relationship between the microstructural events and the occurrence of macroscopic shear is not clear.

In particular, it has been suggested that the initiation of shear bands is related to some form of damage. This damage can be dilational, or it can take the form of a structural or geometrical softening. It is also not clear whether damage follows the occurrence of localization, or triggers it. If the damage is dilational, it should be possible to change the fracture behaviour of materials failing by shear fracture by superimposing an hydrostatic pressure during a tensile test. Thus, the initiation and growth of shear bands could be studied as a function of pressure.

For this purpose, some tensile tests under applied hydrostatic pressure have been performed on a 7075 aluminum alloy, which, with the appropriate aging treatment, fails by localized shear (Chung et al., 1977). The results of these experiments are presented in this chapter.

IV - 2 Material and Testing

IV - 2 - 1 Composition and Heat Treatment

The material chosen for this study of shear fracture is a 7075 aluminum alloy of commercial purity. Its composition is given in Table IV - 1. In addition to the three principal alloying elements Zn, Mg and Cu analysed in Table IV - 1, the alloy also contains Si, Fe, Mn, Cr, and Ti.

The axisymmetric tensile samples, 25 mm gauge length and 5 mm initial diameter, were machined from rods. They were heat-treated at 475°C for 30 minutes, followed by water quenching and natural aging at room temperature to a T4 condition (Polmear, 1981).

The microstructure of the final product is characteristic of the heat-treatable aluminum alloys. Several second phase particles are present in the material, and can be classified according to their size as following:

a) The constituents are the largest particles (from 1 to 20 μm). They form during casting and contain Fe and Si. They are plastic at high temperature so that they are elongated during extrusion or hot rolling to form stringers. At low temperatures they are brittle and are cracked as soon as deformation takes place. Fig. IV - 1 shows a scanning electron micrograph of these constituents, some of them being cracked.

b) The dispersoids are of intermediate size (500 Å to 0.5 μm). They form during ingot homogenization as intermetallic compounds of trace elements such as Cr, Zn, Mn or Cu. They are used to control the grain structure as they do not dissolve during further heat treatment.

Fig. IV-1 : Scanning electron micrograph of some constituents in the 7075 aluminum alloy used for axisymmetric tensile tests under pressure. The tensile axis is horizontal.
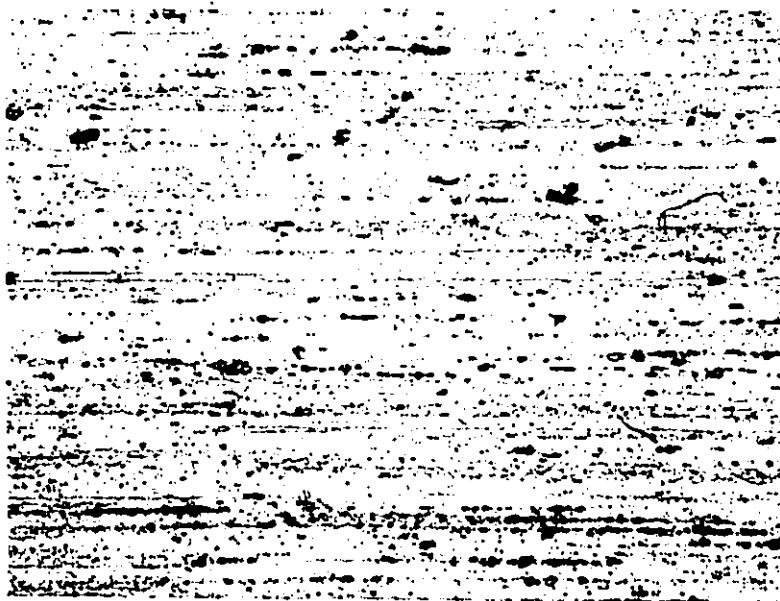
Fig. IV-2 : Optical micrograph of the grain structure of the 7075 axisymmetric tensile samples. The very small grains are elongated along the direction of the rod axis. Magnification : 160x

c) The precipitates are the finer second phase particles and are formed during aging treatments. They are coherent or semi-coherent precipitates involving Mg, Zn, Cu and Si. No detailed study has been done in the material considered here, but it is likely that the precipitates are an intermediate form of $MgZn_2$ (Van Stone et al., 1974). These precipitates are the main cause of strengthening obtained by heat treatment.

The grain structure is shown in fig. IV - 2. The grains are small and highly elongated in the extrusion direction.

In addition to the axisymmetric tensile tests, some plane strain tests have also been performed under superimposed hydrostatic pressure for metallographic observation purposes. The samples were machined to the geometry shown in fig. IV - 3 from a plate of 7075 alloy. The same heat treatment as for the round samples was used. The microstructure obtained is, however, slightly different. The grains are larger and elongated in the rolling direction (fig. IV - 4).

IV - 2 - 2 Testing. Preparation for Metallography

The tensile tests have been performed in the Harwood pressure unit, according to the procedure given in Chapter III. The pressures chosen were one atmosphere (0.1 MPa), 380, 690 and 1100 MPa. Some tests performed at 690 and 1100 MPa were interrupted prior to failure. The strain rate was for all the tests 0.04 min^{-1}.

The samples have been prepared for optical microscopic observations in the following manner. An aging treatment of 20 hours at

Table IV-1 : Chemical composition of the 7075 aluminum alloy (wt%).

Zn	Cu	Mg
5.02	1.34	2.06

Other elements (from commercial tolerances).

Si	Fe	Mn	Cr	Ti
0.40	0.50	0.30	0.18-0.28	0.20

Table IV-2 : Mechanical data for axisymmetric tensile tests of the 7075 aluminum alloy.

Pressure (MPa)	ϵ_u (or ϵ_f)	σ_u (or σ_f)(MPa)	ΔL (lbs)
0.1	.113	660	–
380	.123	670	–
690	.124	678	60
1100	.116	680	60
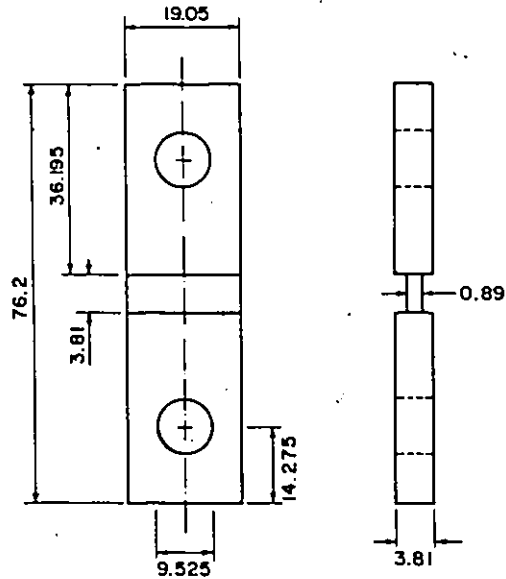
Fig. IV-3 : Geometry and dimensions (in mm) of the plane strain
samples for tensile tests under superimposed·pressure.
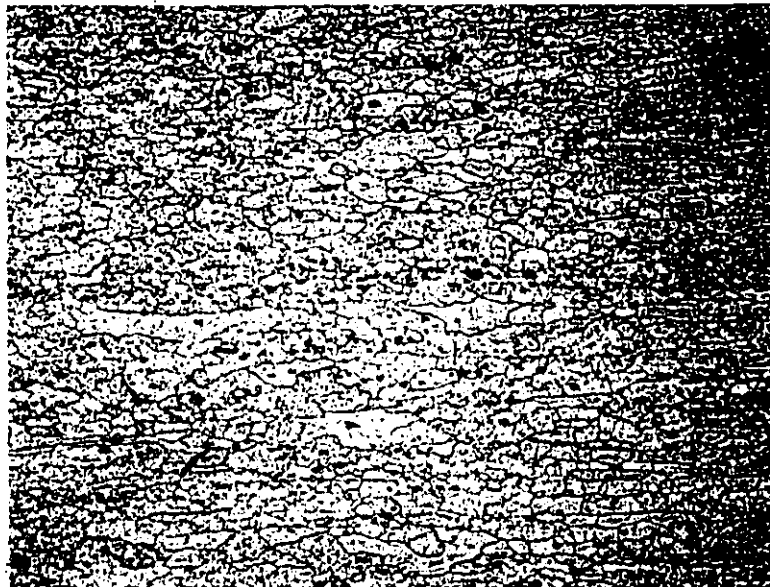
Fig. IV-4 : Optiçal micrograph of the grain structure of the
7075-T4 aluminum alloy used for the plane strain
tensile tests under superimposed pressure. The
grains are larger than in the material used for
the axisymmetric tests.

150°C was performed after testing, followed by mechanical polishing and etching with Keelers reagent. The purpose of this treatment was to decorate both the grain boundaries and the dislocation substructure, and to permit the shear bands to be revealed by etching.

In addition, some thin foils have been prepared from the samples pulled at 690 and 1100 MPa and examined in a transmission electron microscope (TEM) and a scanning transmission electron microscope (STEM).

IV - 3 Mechanical Properties

The values of yield stress (0.2% offset) and tensile strength obtained are:

$$\sigma_Y = 412 \text{ MPa}$$
$$\sigma_f = 670 \text{ MPa}$$

for the axisymmetric samples, and

$$\sigma_Y = 260 \text{ MPa}$$
$$\sigma_{TS} = 440 \text{ MPa}$$

for the plane strain samples.

For the axisymmetric samples, the tensile strength was never reached, the samples breaking or necking down at the stress called σ_f.

The differences between the two series of tests appear to reflect the different grain structures obtained in each case, because the plate and rod materials are of different purities.

The results presented below refer to the axisymmetric samples, as their behaviour is much affected by superimposed pressure.

However, qualitatively, the same trends are observed in the plane strain tests.

The load-extension curves obtained at low pressures (P < 500 MPa) and high pressures are depicted in fig. IV - 5 - a and IV - 5 - b respectively. It is seen that the material yields, strain hardens up to an effective strain of about 0.12 in both cases, and then a sharp decrease occurs in the load, down to zero at low pressures, i.e. the sample breaks, and to a defined value at high pressures. In the latter case, at a superimposed pressure of 1100 MPa, the load decreases continuously, step by step down to zero, as the specimen necks down to a chisel point. The values of the terms defined in fig. IV - 5 - b. are given in Table IV - 2.

The effective strain-effective stress curve obtained before the occurrence of necking is shown in fig. IV - 6. The hydrostatic pressure has a very slight influence on the flow behaviour, and the data can be analysed in the same way as for the spheroidized steels. Following equation (III - 9), the flow curve of the 7075 - T4 alloy is:

$$\bar{\sigma} = 1120 \; \bar{\varepsilon}^{.25} \; [1 + 63 \; 10^{-6} \; P] \qquad (IV - 1)$$

where all the stresses are in MPa.

Therefore, the mechanical behaviour can be summarized in the following way: the material, after yielding, undergoes strain hardening up to a strain of about 0.12, which corresponds to a ratio of strain hardening rate over flow stress $(1/\bar{\sigma})$ $(d\bar{\sigma}/d\bar{\varepsilon})$ equal to 0.75, at all the pressures considered. At this strain level, either the material fails catastrophically or its load-bearing capacity, after a sharp decrease (which is constant with respect to
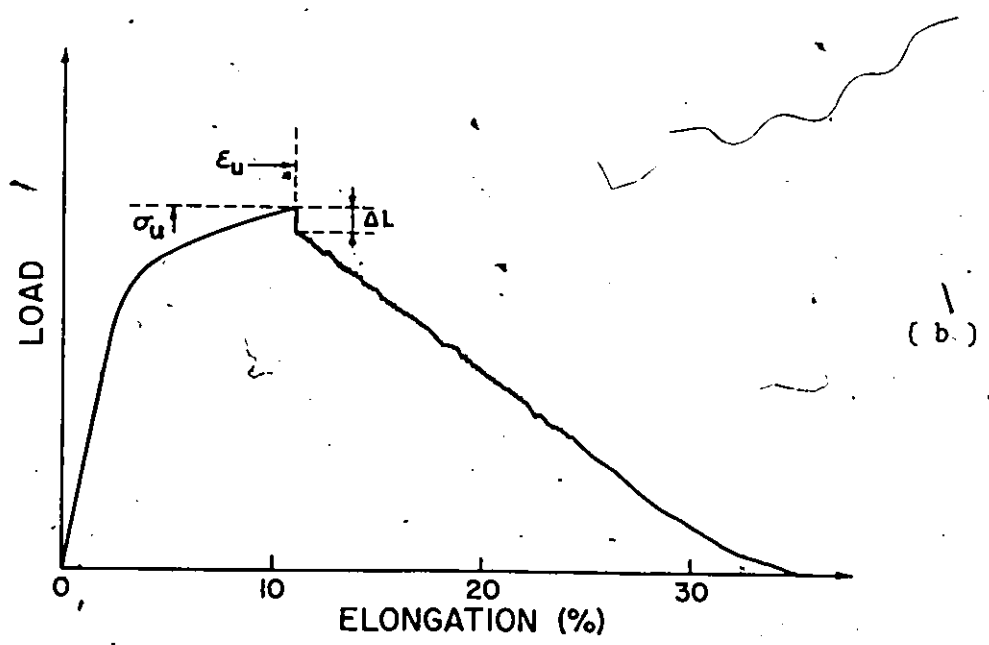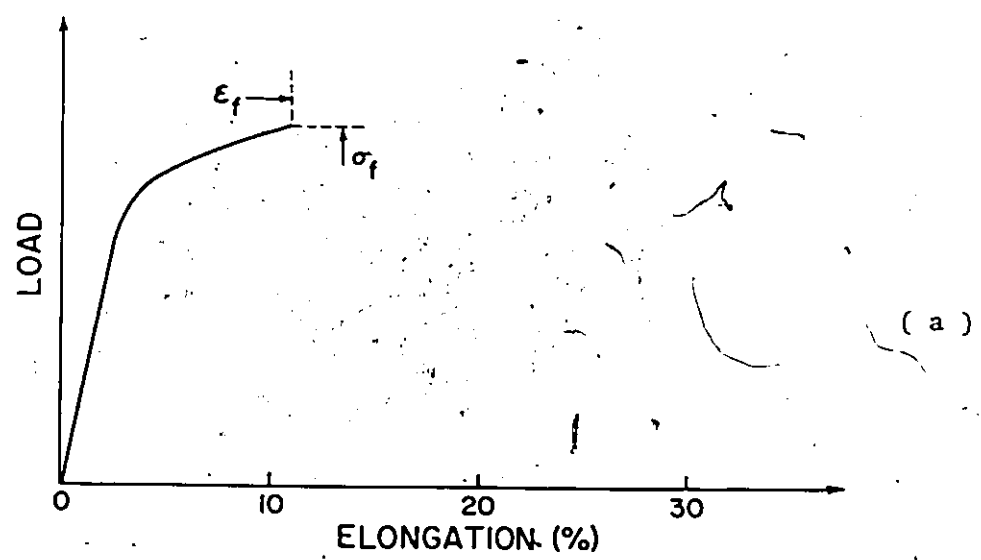
Fig. IV-5 : Schematic representation of the load-extension curves
obtained during the tensile tests of the 7075-T4 axi-
symmetric samples under superimposed pressures :
a)   below 500 MPa.
b)   above 500 MPa.
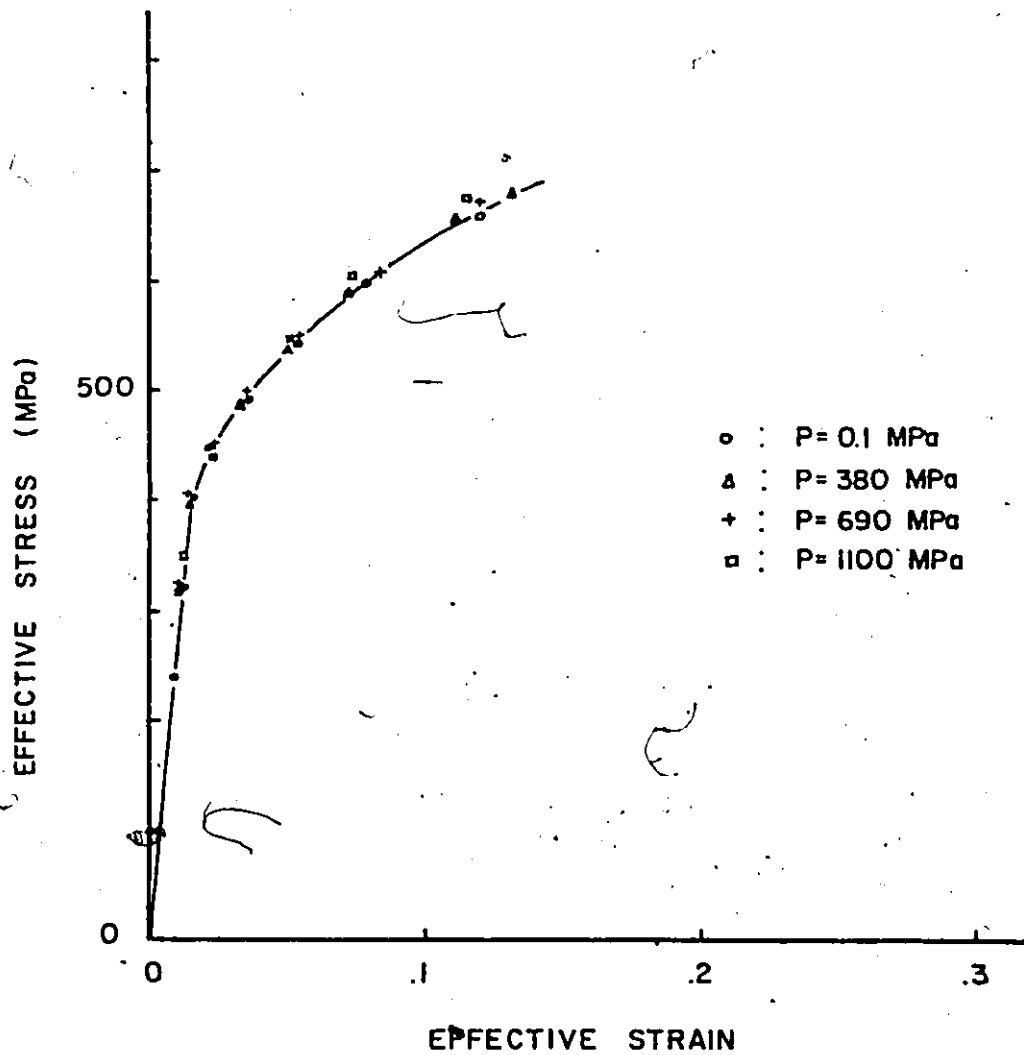
Fig. IV-6 : Effective strain-effective stress curves for the 7075 axisymmetric tensile samples tested under various pressures.

pressure), decreases slowly step by step up to final failure, due to necking.

The next paragraph presents the results of the metallographic observations.

IV - 4 Behaviour Under Pressure

IV - 4 - 1 Low Pressures

At 0.1 and 380 MPa, failure occurs catastrophically prior to necking along the first macroscopic shear band which is formed. The macroscopic appearance of the sample is shown in fig. IV - 7. After polishing the sample down to its mid-plane, the montage in fig. IV - 8 shows that the shear plane is oriented at 45° to the tensile axis. Careful examination also shows that some bands exist below the fracture surface. Such a band is shown in fig. IV - 9 - a for the axisymmetric sample tested at 0.1 MPa, and several bands can be seen in the plane strain sample pulled at 0.1 MPa (fig IV - 9 - b).

The fractographic examination of these fracture surfaces under a SEM reveals that a void sheet mechanism of failure is taking place, giving dimples elongated in the shear direction (fig. IV - 10).

IV - 4 - 2 High Pressures

At superimposed pressures of 690 and 1100 MPa, the first shear bands do not result in fracture. Instead, conjugate bands are formed on intersecting planes at 90°. This leads to the creation of a geometric neck in the sample, as shown in fig. IV - 11 for an interrupted test at 1100 MPa. Two subsequent patterns of deformation are observed:

Fig. IV-7 : Macrophotograph
of the 7075 axisymmetric
sample broken under
380 MPa.
Magnification :   10x
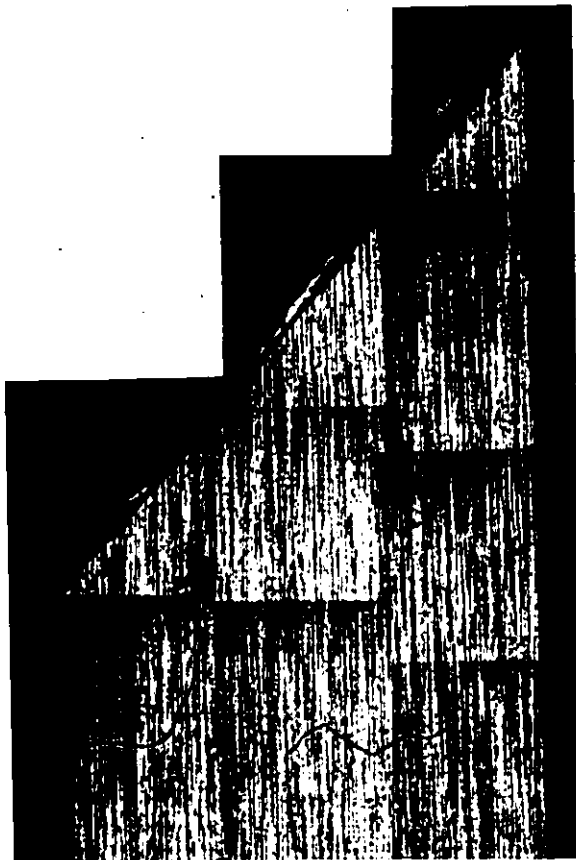
Fig. IV-8 : Montage showing
the occurrence of shear
fracture prior to
necking in the axisym-
metric sample broken
under 380 MPa.

Fig. IV-9-a : Optical micro-
graph showing a shear band
below the fracture surface
in the axisymmetric sample.
broken at 0.1 MPa.
Magnification : 160x.
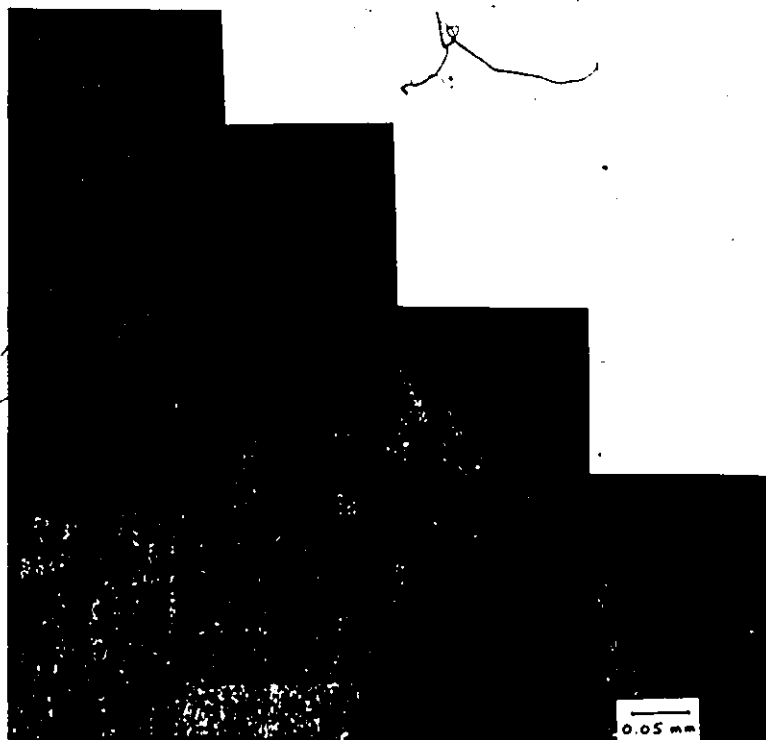
Fig. IV-9-b : Montage of the plane strain.sample broken at 0.1 MPa.
Several shear bands are seen below the shear fracture
surface.
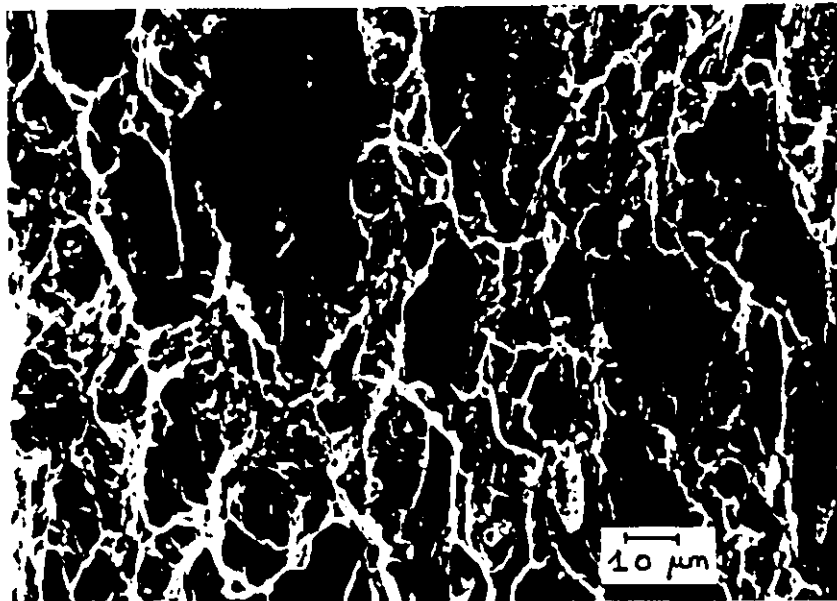
Fig IV-10 : Scanning electron micrograph showing the void sheet
mechanism on the fracture surface of the axisymmetric
sample broken under 380 MPa.

Fig. IV-11 : Macrophotographs of the 7075 axisymmetric.sample
tested under 1100 MPa showing the geometric neck
obtained when the test is interrupted prior to
failure.   Magnification :   6.5x

- at 690 MPa, the sample breaks while the neck is still sub-
  stantial. The two broken halves obtained are shown in
  fig. IV - 12;

- at 1100 MPa, the alternating shear process continues until
  the complete thinning of the cross-section of the sample;
  fig. IV - 13 shows the two halves obtained.

Similar process occur in the plane strain specimens.

The metallographic observation of the specimen reveals
the shear bands formed during deformation, each band corresponding
to a small drop or step in the load-extension curve. The montage
obtained on the polished and etched section is shown in fig. IV - 14
for the axisymmetric specimen pulled under 1100 MPa. In a montage
done at higher magnification (fig. IV - 15) it can be seen that the
shear bands are oriented at 45° to the tensile axis, and that they
cross through the grain structure without being deviated. However,
the offsets from each band are quite large and result in massive
reorientation of the existing grain structure. The bands also
create steps on the external surface of the sample, giving a
surface oriented at about 24° to the tensile axis. A high magni-
fication micrograph shows (fig IV - 16) that many bands are limited
to the grain diameter, whilst others cross a large number of grain
boundaries.

SEM observations of the surface perpendicular to the section
shown in fig. IV - 15 was performed in order to study the structure
of the offsets. Fig. IV - 17 shows the steps created on the surface
by the offsets. These macroscopic steps contain small, discontinuous
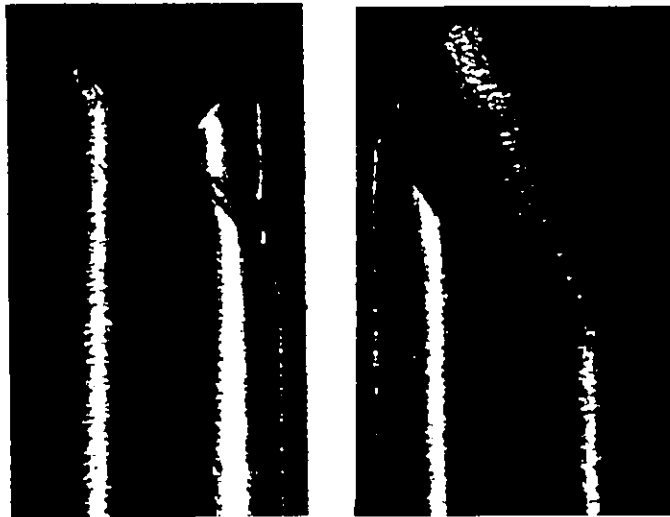
Fig. IV-12 : Macrophotographs of the 7075 axisymmetric sample
broken under 690 MPa.
Magnification : 9x

Fig. IV-13 : Macrophotograph of the 7075 axisymmetric sample
broken under 1100 MPa.
Magnification : 6.5x

Fig. IV-14 : Montage showing thinning of the axisymmetric sample by conjugate shear bands when broken under 1100 MPa.

Fig. IV-15 : High magnification montage of the axisymmetric sample broken under 1100 MPa. The details of shear bands and their effect on the grain structure are revealed.

250 μ
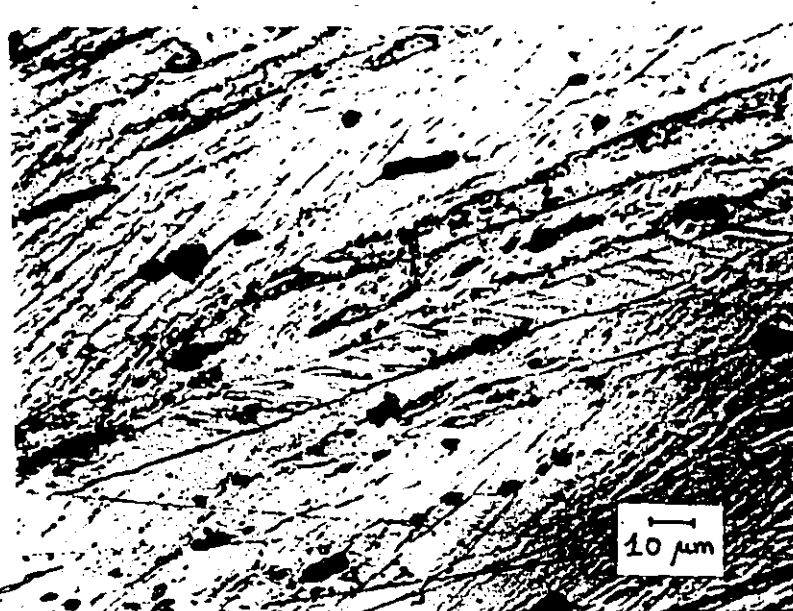
Fig. IV-16 : Micrograph showing the formation of shear bands
inside the grains in the axisymmetric sample
broken under 1100 MPa.
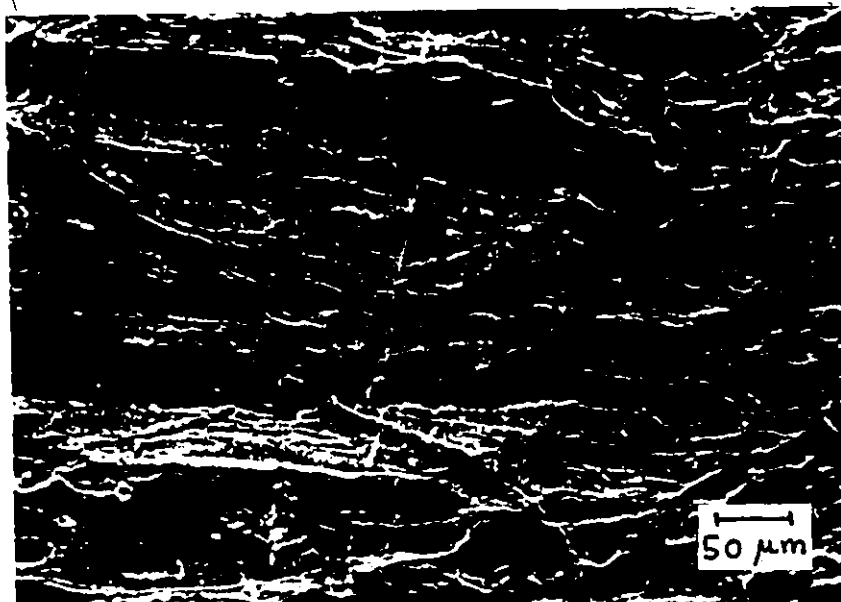
Fig. IV-17 : Scanning·electron micrograph showing the struc-
ture of macroscopic shear steps on the fracture
surface of the axisymmetric sample broken under
1100 MPa.

steps with traces approximately parallel to the plane of the step, which appear to be slip steps with a spacing of 2-5 μm, indicating then that the bands have an internal constitution due to some form of cooperative crystallographic slip events.

The montages of the unbroken axisymmetric and plane strain samples pulled under 1100 MPa are shown in fig. IV.- 18 and fig. IV - 19 respectively. In the former, it can be seen in the region X - Y that failure is initiated as a series of linked shear cracks lying in the bands of localized shear. SEM observations were performed to determine whether the shear bands contain dilational damage. This latter point is difficult to determine in an unambiguous sense because of the problem of local etching, and the possible loss of inclusions during the preparation of the sample. However, the observations reveal two types of damage associated with the shear bands. Fig. IV - 20 shows damage along the grain boundaries A - B, due to the large local strains associated with the shear bands X - Y. In other regions, the form of failure due to the linkage of elongated voids lying on the boundaries of the shear bands could be observed as in fig. IV - 21.

TEM and STEM observations have been performed on these samples by Raghunathan and Korbel (1983). A macroscopic shear band crossing several grains is shown in fig. IV - 22, in a sample broken under 1100 MPa. The position of the band is indicated by arrows. The foil in this case was approximately parallel to the fracture surface, and the shear bands are inclined to foil by about 22°. The tangled arrangement of dislocations tends to be
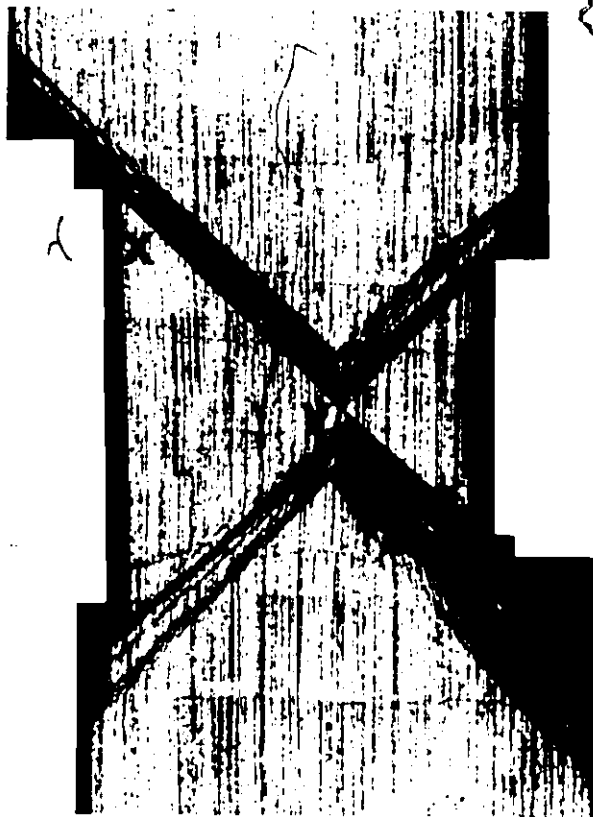
Fig. IV-18 : Montage of the
geometric neck obtained
in the 7075 axisymmetric
sample tested under
1100 MPa and interrupted
prior to failure.
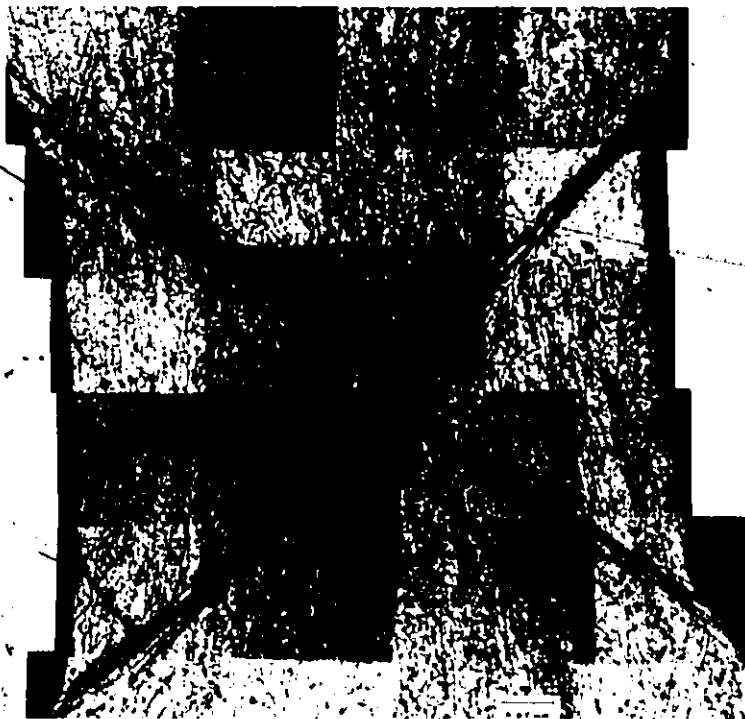
Fig. IV-19 : Montage of the
geometric neck obtained
in the 7075 plane strain
sample tested under
1100 MPa and interrupted
prior to failure.
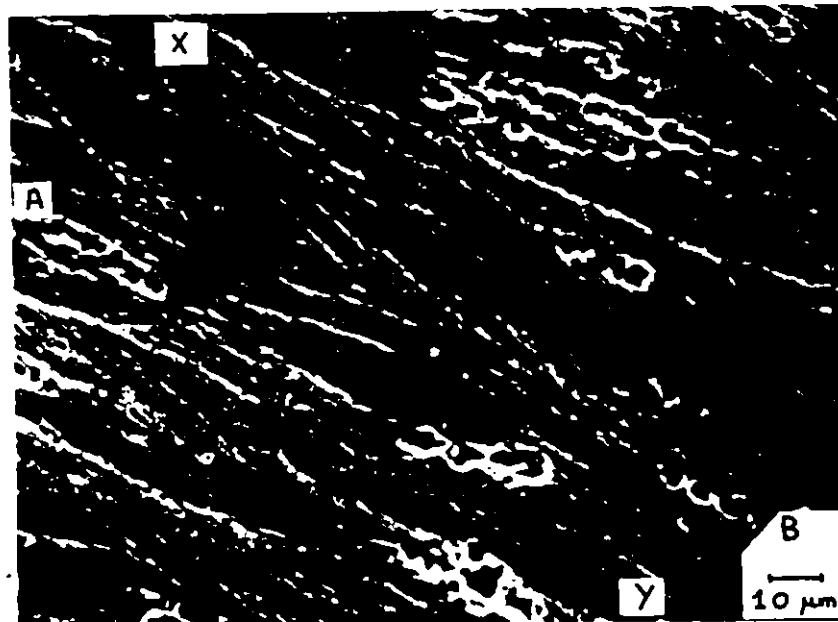
Fig. IV-20 : Scanning electron micrograph showing the damage
along the grain boundary A-B due to the shear
band X-Y, in the axisymmetric sample tested
under 1100 MPa.
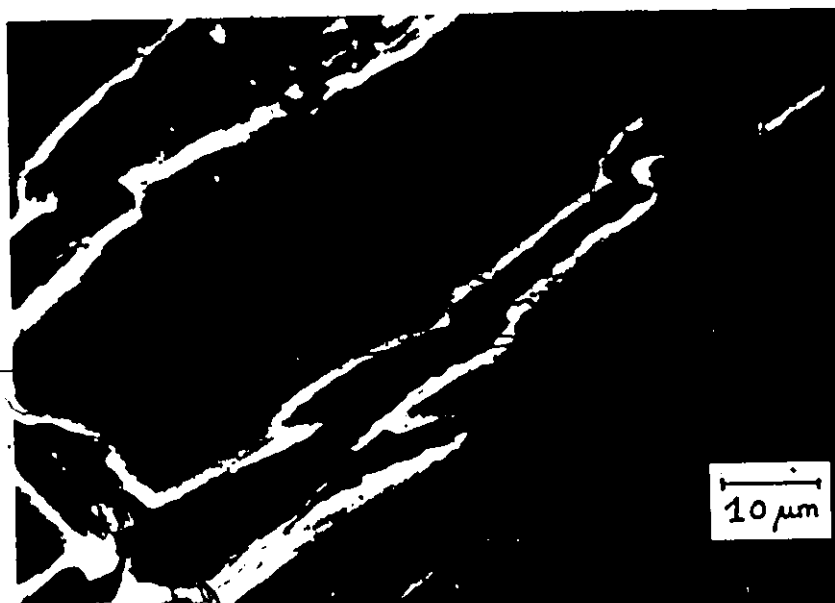
Fig. IV-21 : Scanning electron micrograph showing the linkage
of elongated voids on the boundary of shear bands
in the axisymmetric sample tested under 1100 MPa.

aligned along the length of the shear band. This can be seen more clearly in fig. IV - 23, where a shear band produces a step in the grain boundary separating grain A and grain B. The band keeps the same direction in the adjacent grains (noted B and C), in which the position of the band is not obviously crystallographic.

Within a band, the dislocation structure is not easily resolved: there is a large density of dislocations, whose cross-hatched appearance suggests operation of multiple slip systems within a shear band.

The plane strain samples show similar behaviour. In fig. IV - 24, a shear band can be seen to cross grain boundaries without deviation. The band produces a very pronounced step at the grain boundary. In one grain the band can be seen to correspond to a denuded zone without any precipitates: this feature is typical of coarse slip bands and is due to the shearing of the particles which reduce their size, resulting into their dissolution. Also shown are some dislocations on the sides of the band which have been decorated by precipitation during natural aging subsequent to the mechanical testing. It seems, therefore, that shear bands and coarse slip band have some common features. Another montage is shown in fig. IV - 25. In grain A, the trace of the shear band has a direction [325], coinciding with the direction of the intersection of the foil plane ($1\bar{4}1$) with the slip plane ($11\bar{1}$): therefore, deformation proceeds predominantly by single slip in this grain. The band then propagates into the adjacent grain by using a

Fig. IV-22 : Montage of electron micrographs of the neck region of
the axisymmetric sample tested under 1100 MPa. Micros-
copic shear bands are crossing several grains. An
accompanying sketch illustrates this.
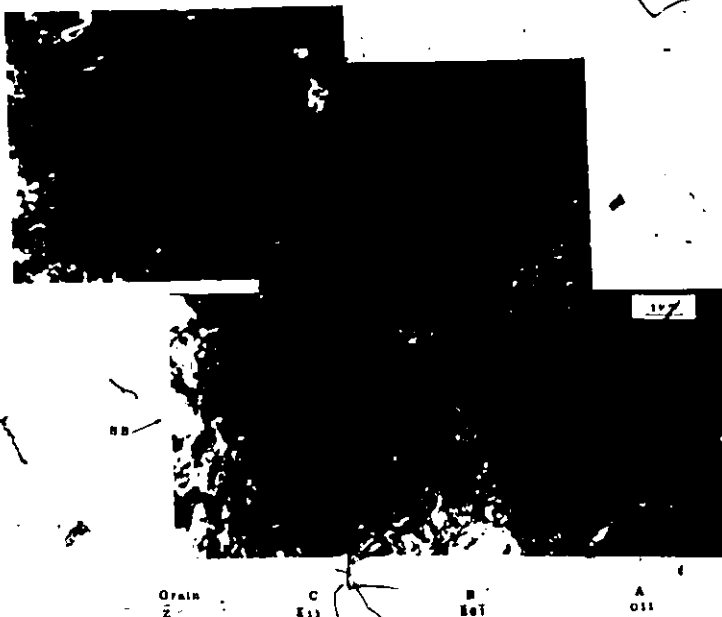
Fig IV-23 : TEM micrographs illustrating the crystallographic
nature of slip in the microscopic shear bands. The
step seen in the grain boundary separating A and B
is due to the propagation of shear band. Micrographs
are from the same sample as in fig. IV-22.
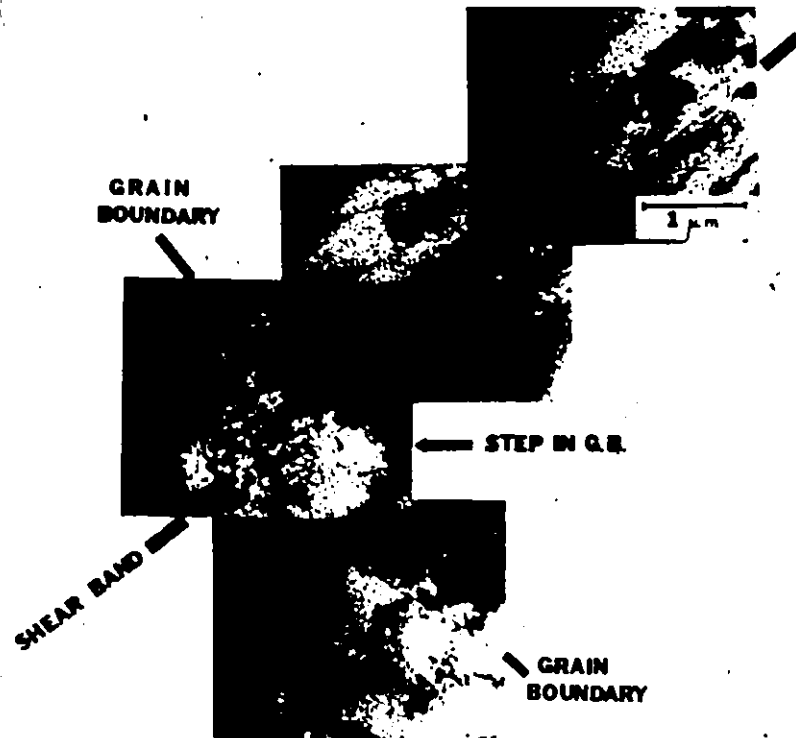
Fig. IV-24 : Montage of TEM micrographs of the plane strain sample
tested under 1100 MPa. The shear band creates a pro-
nounced step on the grain boundary.

multiplicity of slip systems. Indeed, the comparison of the selected
area diffraction patterns from the shear band in grains A and B of
fig. IV - 25, shows that in grain A, a relatively simple pattern
is produced due to the crystallographic nature of the shear band
explained by the slip on the $(11\bar{3})$ plane occurring in it; on the
other hand in grain B, the shear band region produces a well-
developed spotty ring pattern. This is clear evidence for operation
of multiple slip systems as this pattern could only be produced by
microscopic areas with large misorientations due to the operation
of multiple slips combined with large accumulated plastic strain
in the bands. It can then be concluded that in grain B, the shear
band is non-crystallographic in form. This indicates that in
spreading through the cross-section of the sample, the shear bands
involve a spatial distribution of regions of single slip similar
to coarse slip bands which are interspersed with regions of localized
multiple slip. Although the constitutive shear process involves
crystallographic slip, the overall macroscopic band can be non-
crystallographic in form.

IV - 5 Discussion

The main purpose of this study was to examine the occurrence
of shear bands. The experimental results from metallographic
observations give some important evidence concerning the nature
of the shear bands.

First, it was observed that the onset of band formation
occurs at the same stress level and strain level regardless of
the magnitude of the superimposed pressure. No evidence of any

Fig. IV-25 : Montage of TEM micrographs of the plane strain sample
tested under 1100 MPa. The direction of shear band
coincides with the crystallographic direction [325]
which is the trace of the slip plane (11$\bar{1}$) on the
foil in grain A.

dilational damage has been found below the fracture surface of the
samples tested at low pressures. This suggests, therefore, that
shear band formation does not depend on damage creation, but rather
on the state of the matrix. In all cases, the formation of the
first macroscopic band leads to a stress drop, whose magnitude
(60 lbs. or 17.5 MPa) must involve the response of the testing
system. This would be consistent with the occurrence of a structural
softening at this strain level. Before discussing the events
responsible for the softening, it is worth noting that the first
macroscopic shear band is occurring while the material is strain
hardening; this observation has been previously reported, as quoted
in the literature review. The ratio of the hardening rate to the
current flow stress is 0.75, which is within a factor 2 of the
ratio determined by Chang and Asaro (1980) in another aluminum
alloy, when account is taken of the Taylor factor, as the 7075
alloy is polycrystalline. These observations then eliminate any
possibility of geometric softening, or softening by damage accu-
mulation. The onset of localized deformation is due to structural
softening propagating in a cooperative manner. The question then is
to know what the possible mechanisms are for this softening.

The optical micrographs indicate that localization occurs
first on the scale of the grain diameter and then becomes spatially
organized into macroscopic bands at 45° to the tensile axis.
Examination of the bands shows that they contain a large density
of dislocations and that they are regions of highly localized

shear over a thickness less than a μm. This would indicate that

shear bands are due to crystallographic slip on a dominant slip system

within one grain in which a coarse slip band could be formed, and

then they penetrate into adjacent grains by cooperative slip events

which may involve several slip systems. Such cooperative phenomenon

may be assisted by stress concentrations leading to the overcoming

of obstacles such as the fine precipitates provided by natural aging,

and it involves the activation of coordinated slip in the region

ahead of the growing band. The reason for initial localized slip

events leading to the formation of shear bands is, therefore, a

structural softening event such as the destruction of zones of

fine precipitates, or the modification of the pre-existing dis-

location substructure.

In the experiments conducted under pressure, failure does

not occur after the formation of the first macroscopic band, but

a geometric neck is formed. The initial bands are at 45° to the

tensile axis and the angle between the outer surface of the

sample and the tensile axis is $22^{\circ} \pm 3^{\circ}$. This value can be cal-

culated by assuming a simple geometric situation depicted in

fig. IV - 26. If the unit of shear s of a band is taken equal

on the conjugate band, then with the notations of fig. IV - 26:

$$\tan \alpha = x/x + y$$

$$x = s \sqrt{2}/2$$

$$y = s \sqrt{2}$$

i.e. $\qquad \tan \alpha = 1/3$

or $\qquad \alpha = 19^{\circ}$
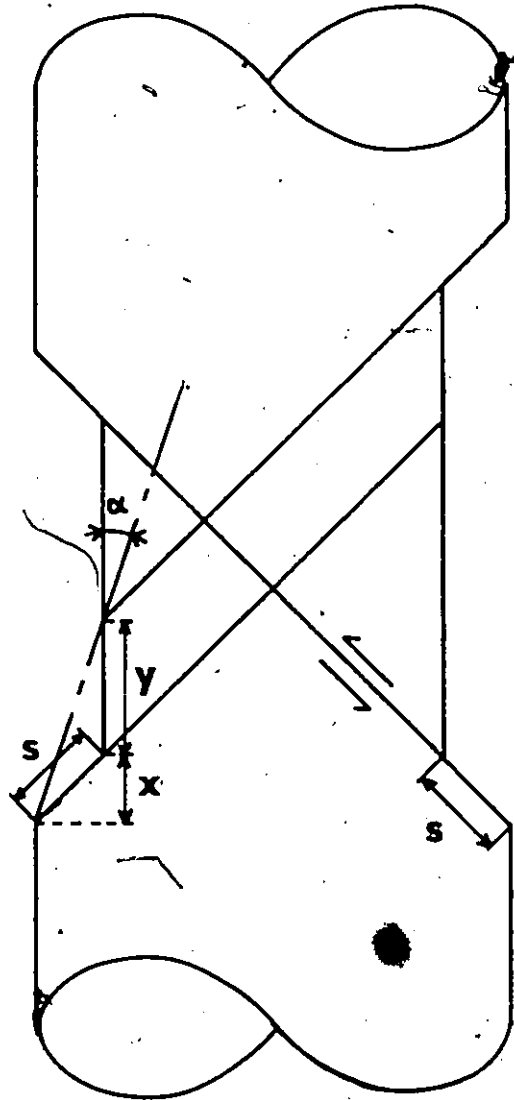
Fig. IV-26 : Schematic representation of the formation of the
geometric neck by conjugate shearing.

Therefore, the measured value of 22° falls between this calculated

value and the value of 26.5^{o} reported by Onat and Prager (1954)

for the case of a plane strain tensile test. Therefore, the simple

geometric description of conjugate bands appears to be in reasonable

accord with experiments. Thus it is clear that two forms of spatial

coordination occur in the shear process. The first one is a coordination

of crystallographic slip events in a number of systems which leads

to the spreading of a narrow shear band over the total cross-section

of the specimen. In addition, the lattice rotations due to the creation

of such a band triggers an equivalent process on the conjugate band

leading to the formation of the neck. Therefore, the events are

coordinated both in the macroscopic shear plane and longitudinally

along the specimen axis.

The last point to be examined is the pressure dependence

of the fracture behaviour. This must arise due to the creation

of damage within the shear bands. A void sheet mechanism where

voids are opened at the second phase particle-matrix interface or at

grain boundaries gives catastrophic failure, for the voids can grow

rapidly because of the large strain and strain rate within the

band. If a pressure is superimposed, the lateral growth of voids

is slowed, so that their coalescence is delayed. Thus, the hydro-

static pressure must either decrease the rate of damage accumulation

or even delay the onset of damage. It must also be recognized that

in examining the progress of a localized deformation band towards

fracture, both the work hardening of the material between the voids

and the accumulation of damage must be considered. Taking the

damage as a parameter D, the flow behaviour can be idealized by
(see equation III - 47) :

$$\bar{\sigma}\ (\bar{\varepsilon},\ D) = \bar{\sigma}(\bar{\varepsilon})\ (1 - D) \qquad (IV - 2)$$

i.e.
$$\frac{d\bar{\sigma}}{d\bar{\varepsilon}} = \frac{\partial\bar{\sigma}}{\partial\bar{\varepsilon}}\ (1 - D) - \bar{\sigma}(\bar{\varepsilon})\ \frac{\partial D}{\partial\bar{\varepsilon}} \qquad (IV - 3)$$

Assuming that failure corresponds to the vanishing of the global
rate of work hardening, the criterion for failure is then :

$$\frac{1}{\bar{\sigma}}\ \frac{\partial\bar{\sigma}}{\partial\bar{\varepsilon}} - \frac{1}{1 - D}\ \frac{\partial D}{\partial\bar{\varepsilon}} = 0. \qquad (IV - 4)$$

As the hydrostatic pressure P is increased, the term $(\partial D/\partial\bar{\varepsilon})$ $(1/1 - D)$
is decreasing so that the criterion (IV - 4) is not fulfilled unless
a large enough deformation takes place in order to lower the harde-
ning rate of the material between voids, $\partial\bar{\sigma}/\partial\bar{\varepsilon}$.

This very simplified model allows, therefore, a qualitative
understanding of the fact that below 500 MPa, failure occurs after
the formation of very few bands, whilst above 500 MPa, damage
accumulation is slowed so that a series of conjugate bands can be
formed leading to failure by geometric reduction of the cross-
section of the specimen.

IV - 6 Conclusions

This study has revealed some new features of macroscopic
shear fracture.

The first result is that the onset of localized shear is
independent of superimposed pressure. It is therefore not triggered
by dilational damage accumulation, but arises because of a structural
softening of the matrix.

The sequence of shear band formation appears to be the following :

- The bands are initiated by cooperative crystallographic slip within individual grains.

- These bands organize themselves into macroscopic regions traversing the entire cross-section and penetrating the grain boundaries, to form macroscopic bands at 45° to the tensile axis.

Together with this coordination along the macroscopic shear plane, there exists a coordination process along the longitudinal axis leading to the formation of a geometric neck at high super-imposed pressures.

Finally, the shear band formation is accompanied by creation of dilational damage which gives rise to the pressure dependence of the shear fracture process.

CHAPTER V

BRITTLE FRACTURE

V - 1 Introduction

Brittle fracture involves the creation and propagation of micro-
cracks. It has been found (Knott, 1977) that at atmospheric pressure,
crack propagation is the controlling step for the occurrence of failure,
so that the fracture criterion appears to be the attainment of a cri-
tical tensile stress. The effect of hydrostatic pressure is to raise
this critical stress, so that the controlling step becomes the deve-
lopment of microcracks into a critical defect leading to failure.
The purpose of the work reported in this chapter is to investigate
the mechanisms leading to the modifications in the fracture behaviour
of two materials : an aluminum-copper alloy which fails intergranu-
larly, and an iron-phosphorus alloy which fails by a mixture of
transgranular cleavage and intergranular fracture. Emphasis has been
given to the changes in fracture mode that these alloys exhibit as
a function of pressure, and to the stabilization of microcracks,
i.e. the separation of creation and propagation into two distinct
stages.

V - 2 Materials

The chemical compositions of the two alloys are given in
Tables V - 1 and V - 2.

The Aℓ-Cu alloy was received in the form of hot-rolled plate,

Table V-1 : Chemical composition of the aluminum-copper alloy (wt%).

Cu	Fe	Mg	Si	Al
3.62	0.002	<0.001	0.002	balance

Table V-2 : Chemical composition of the iron-phosphorus alloy (wt%).

P	C	N	O	Fe
1.2	0.005	0.0015	≃0.003	balance

25 cm wide and 1.4 cm thick. In order to break down the as-cast struc-
ture and provide a uniform grain size, the plate was reduced 22% in
thickness to 1.1 cm by rolling at room temperature prior to annealing.
Axisymmetric samples similar to the unnotched steel samples were
machined. They were then heat-treated at $540^{o}C$ for an hour, followed
by water quenching and storage in a freezer at $-10^{o}C$ prior to sub-
sequent ageing treatment. This assured a complete recrystallization to
a structure of equiaxed grains of average diameter equal to 0.23 mm,
so that the orientation of the test pieces relative to the initial
rolling direction was not considered. The ageing treatment was per-
formed at $130^{o}C$ for four days. This peak-aged condition results in
the formation of θ'' and θ' particles responsible for the strengthe-
ning (Kelly and Nicholson, 1963).

The iron-phosphorus alloy was obtained from the U.S. Steel
Research Laboratories. The elaboration of the alloy is described by
Spitzig (1972). The alloy was hot-rolled between $1093^{o}C$ and $899^{o}C$
and air cooled to a plate of 12.7 mm thickness. Rods were machined
from this plate, from which axisymmetric tensile samples similar to the
unnotched steel samples were obtained. The heat treatment was chosen
to give both a coarse grain size and optimum embrittlement of
grain boundaries by phosphorus segregation (Inman and Tipler, 1958;
Palmberg and Marcus, 1969). Following Spitzig (1972), the samples were
heat-treated in vacuum at $850^{o}C$ for 24 hours, followed by water
quenching. The equiaxed grains obtained had an average diameter of
0.20 mm. No TEM observations were performed to investigate the micro-
structure of the alloy.

V - 3 Mechanical properties

V - 3 - 1 Aluminum-copper alloy

Tensile tests were performed at 0.1, 100, 203, 300, 414, 503 and 690 MPa, at a strain rate of 0.04 min^{-1}. At atmospheric pressure, the alloy fails prior to necking, whereas at higher pressures, a neck is developed prior to failure.

The yield stress and tensile strength are approximately constant regardless of pressure and are :

$$\sigma_Y = 180 \text{ MPa}$$

$$\sigma_{TS} = 330 \text{ MPa}$$

The effective strain-effective stress curves plotted for the uniform part of the deformation were not affected by pressure (fig. V - 1). The flow behaviour is described by :

$$\bar{\sigma} = 645 \, \bar{\epsilon}^{.28} \qquad (V - 1)$$

where the stresses are in MPa.

The data at fracture are given in Table V - 3. Despite a distorsion of the neck, an attempt has been made to determine the stress state at fracture from the measurement of the ratio a/R on montages of the broken and polished longitudinal sections of the samples. This has however been possible only up to a superimposed pressure of 300 MPa, the neck becoming too asymmetric at higher pressures. The stresses have been calculated using equations (III - 2) to (III - 7) from Bridgman's analysis.

It was not possible to determine a fracture strain for all the samples. However, the influence of superimposed pressure on the ductility of this alloy can be seen by plotting the engineering strain at
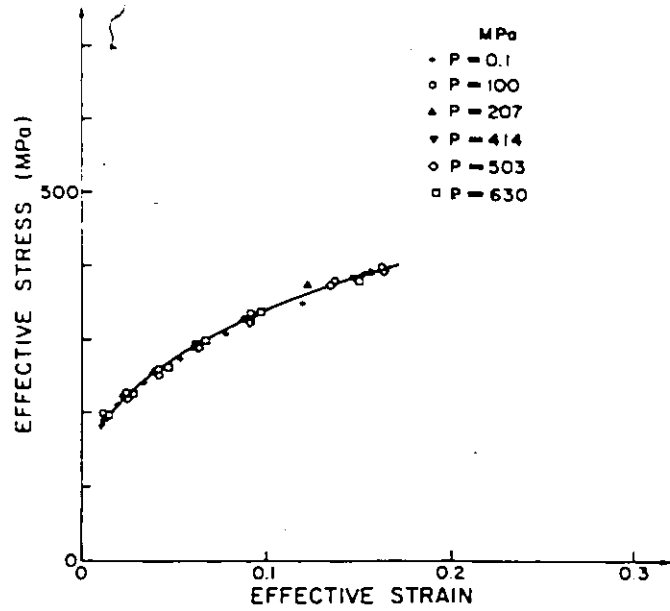
Fig. V-1 : Effective strain-effective stress curves for the Aℓ-Cu alloy tested in tension under various pressures.
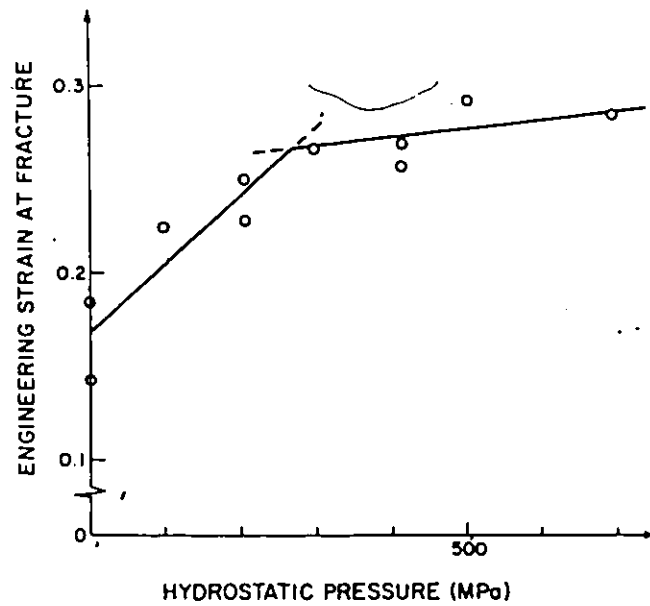
Fig. V-2 : Diagram showing the variation of the engineering strain to fracture for the Aℓ-Cu alloy broken under various pressures.

Table V-3 : Data at fracture for the tests under pressure performed
on the aluminum-copper alloy.

Pressure (MPa)	e_f	a (mm)	R (mm)	σ_f (MPa)	σ_1 (MPa)	σ_3 (MPa)
0.1	.1839	2.151	0	337	0	337
100	.2249	1.781	8.75	403	-61	343
207	.2387	1.624	6.87	415	-161	254
300	.2760	1.350	4	404	-237	167
414	.2630	-	-	-	-	-
503	.2929	-	-	-	-	-
690	.2848	-	-	-	-	-

Table V-4 : Data at fracture for the tensile tests under pressure
performed on the iron-phosphorus alloy.

Pressure (MPa)	e_f	ε_f	σ_f (MPa)	σ_1 (MPa)	σ_3 (MPa)
0.1	0.0219	0.0216	380	0	380
345	0.1062	0.1009	737	-345	392
517	0.2088	0.1896	853	-517	336
690	0.2330	-	-	-	-
869	0.2634	-	-	-	-
1100	0.2866	-	-	-	-

fracture e_f defined by :

$$e_f = \frac{l_f - l_o}{l_o} \qquad\qquad (V - 2)$$

as a function of pressure, as shown in fig. V - 2. It can be seen that after a rapid increase with pressure up to 300 MPa, e_f increases much less rapidly at higher pressures.

V - 3 - 2 Iron phosphorus alloy

Tensile tests have been performed at 0.1, 345, 517, 869 and 1100 MPa, at a strain rate of 0.1 min^{-1}. At atmospheric pressure, the sample breaks prior to general yielding; at 345 and 517 MPa, plastic yielding and strain hardening are occurring, but the samples break without necking. Above 517 MPa, a pronounced neck develops prior to failure.

In all the load-extension curves obtained at pressures above 0.1 MPa, several sharp drops could be seen, occurring at or after the onset of strain hardening. These drops are characteristic of extensive twinning, which was confirmed by subsequent metallographic examination.

The mechanical properties were determined from the tests at high pressures. The yield stress and tensile strength are :

$$\sigma_Y = 410 \text{ MPa}$$

$$\sigma_{TS} = 695 \text{ MPa}$$

The effective strain-effective stress curves for the tests at 0.1, 345 and 517 MPa are shown in fig. V - 3. The flow behaviour can be expressed using equation (III - 9) by :

$$\bar{\sigma} = 1270 \; \bar{\varepsilon}^{.245} \; (1 + 45 \; 10^{-6} \; P) \qquad\qquad (V - 3)$$

where all the stresses are in MPa. The value of the pressure coefficient, 15 10^{-6} MPa^{-1}, is in good agreement with its theoretical value
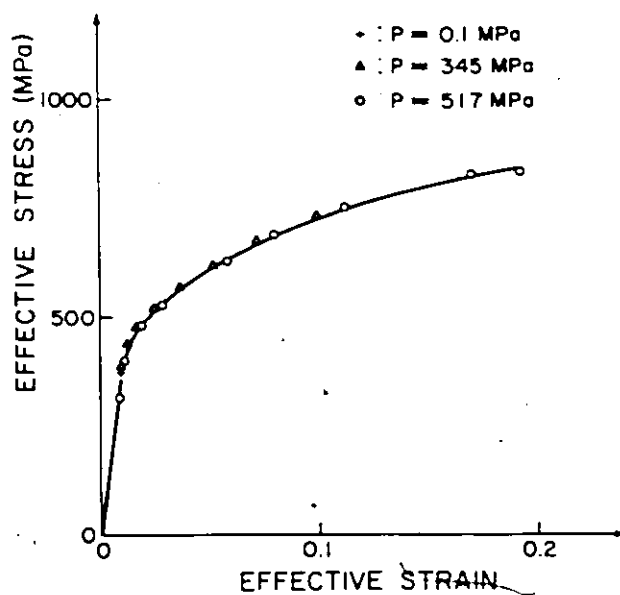
Fig. V-3 : Effective strain-effective stress curves for the Fe-P
alloy tested in tension under various pressures.
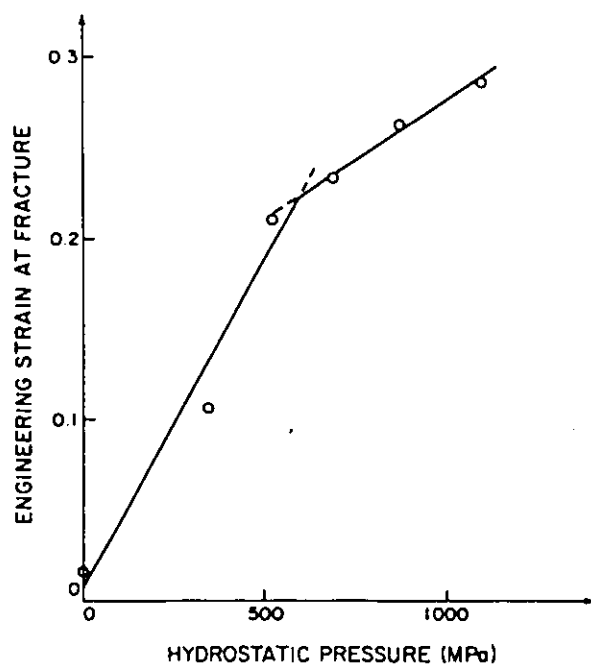
Fig. V-4 : Diagram showing the variation of the engineering strain
to fracture for the Fe-P alloy broken under various
pressures.

of 19 10^{-5} MPa^{-1} (Richmond and Spitzig, 1980).

The data at fracture are given in Table V - 4. The lower pressures allow calculations of the stress state to be made, as the samples deform uniformly. Above 517 MPa, it is not possible to determine the stress state because of the distorsion of the neck.

An attempt has been made to represent the effect of pressure on the ductility by plotting the engineering strain at fracture as a function of superimposed pressure. Fig. V - 4 shows that a rapid increase of e_f with P below 590 MPa is followed by a slower one above this value.

In order to investigate the mechanical behaviour of the alloy at atmospheric pressure, and in particular to determine its yield stress, compression tests have been performed by O'Reilly (1983). A first test on a cylindrical sample with h/d = 1.5, where h is the height of the sample and d its diameter, has been performed between smooth platens to reach almost homogeneous compression. The effective strain-effective stress curve obtained assuming incompressibility is :

$$\bar{\sigma} = 1305 \; \bar{\varepsilon}^{.23} \qquad \qquad (V - 4)$$

where the stresses are in MPa. It is worth noting that this expression is in good agreement with the one determined from the tests under pressure, equation (V - 3).

As the fracture stress in tension at atmospheric pressure is 380 MPa, and the yield stress determined from the tests under pressure is 410 MPa, it was thought useful to examine in more detail this small discrepancy by performing a compression test to obtain σ_Y (Low, 1954). During this test, two audible cracking noises could be heard and

corresponded to two sharp load drops on the load-compression curve.

After the first drop, the sample started to strain harden. The yield

stress was taken as the lower point of the drop and found to be equal

to 402 MPa. It was therefore concluded that, within the experimental

error, the yield stress and fracture stress in tension are coincident,

in accord with the previous work of Low (1954). In addition, another

test was interrupted in the elastic part of the deformation for further

metallographic observations.

V - 4 Behaviour under pressure

V - 4 - 1 Aluminum-copper alloy

V - 4 - 1 - 1 Specimen preparation

The samples were prepared similarly to the steel samples. They

were mounted in lucite, ground to their mid-plane and finally polished

and etched with Keeler's reagent.

V - 4 - 1 - 2 Macroscopic aspect. Fractography

A montage of the macrophotographs of the broken samples is shown

in fig. V - 5. While at the lower pressures, the samples are approximately

round, the asymmetry of the neck can be seen at higher pressures. There

is also a tendency for a macroscopic shear to take place : as the pres-

sure increases, the fracture plane appears to be one of shear. At the

highest pressures, the samples have a chisel-point appearance.

To investigate this in more detail, fractographic examinations

have been carried out using a scanning electron microscope (SEM). At

atmospheric pressure, the fracture surface is mainly composed of grain

facets, despite the presence of some dimples (fig. V - 6 - a). At

P = 0.1 MPa
8x

P = 100 MPa
8x

P = 203 MPa
9x

P = 300 MPa
8x

P = 414 MPa
8x

P = 503 MPa
8x

P = 690 MPa
9x
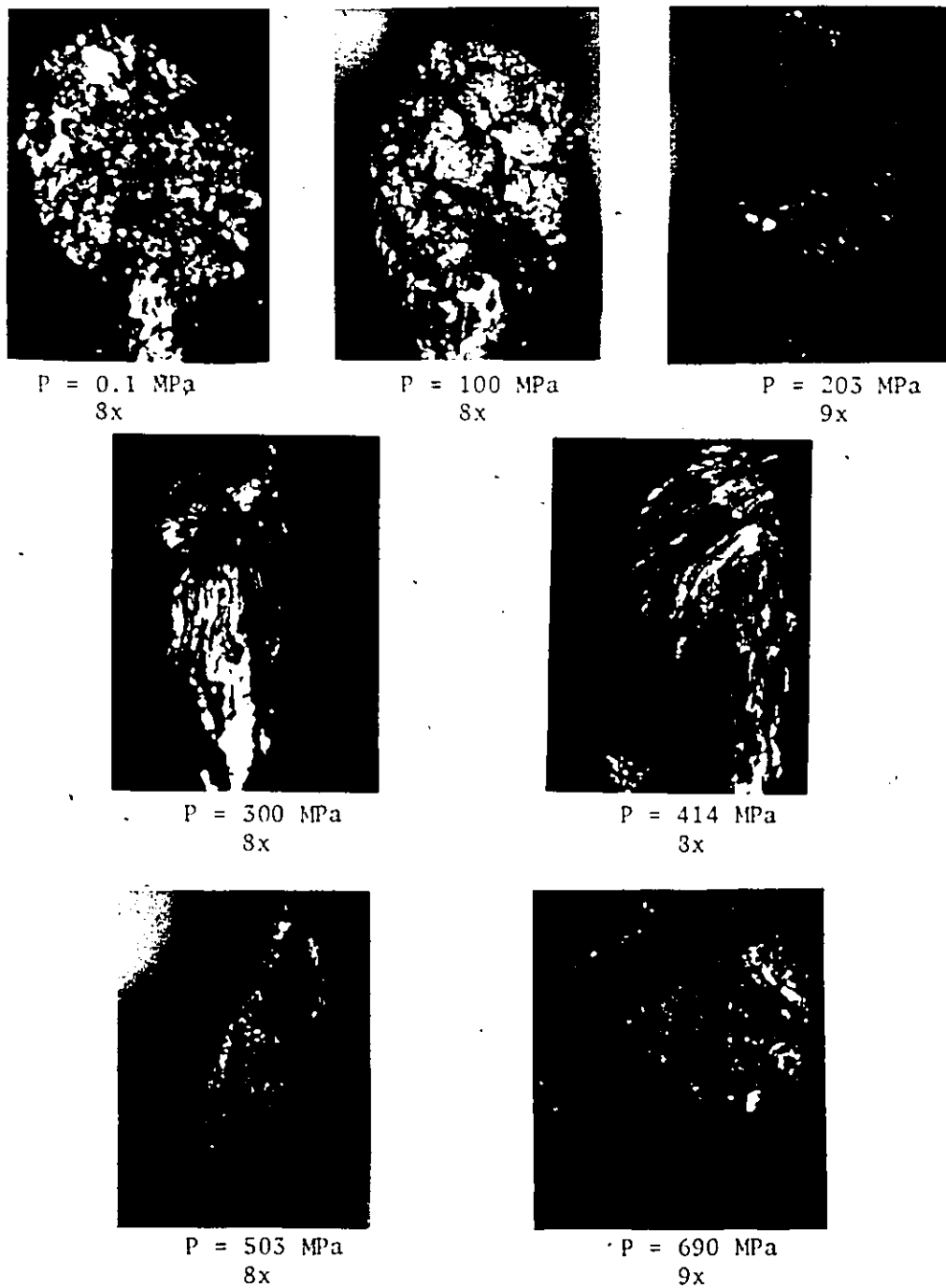
Fig. V-5 : Macrophotographs of the Al-Cu tensile samples
broken under various pressures.

(a)   160 x
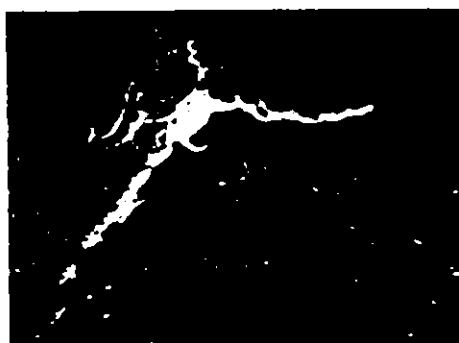
(b)   2500 x
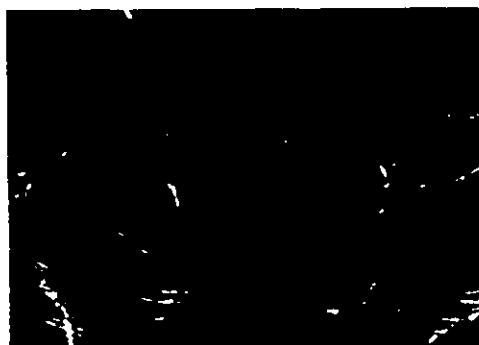
(c)   80 x

Fig. V-6 : Scanning electron micrographs of the Al-Cu sample
broken at atmospheric pressure :
a) general view of the fracture surface
b) dimples on the grain boundary facets
c) intergranular cracks on the outer surface

higher magnification, the facets reveal a dimple structure (fig.
V - 6 - b) characteristic of fibrous intergranular fracture. On the
outer surface of the sample, some microcracks can be seen (fig.
V - 6 - c), together with very pronounced slip line traces. The micro-
cracks have an intergranular appearance, and the slip lines indicate
the coarse nature of the slip in this alloy, due to the absence of
dispersoids which could homogenize it. These slip line traces can be
seen on the outer surface of all the samples regardless of applied
pressure. When the pressure in increased to 100 MPa, the fracture sur-
face still shows some grain facets (fig. V - 7 - a) but the grains
seem to have been highly elongated. The dimples present a shear
character (fig V - 7 - b). The same features are found on the frac-
ture surface of the sample pulled under 207 MPa. There is still some
evidence of grain boundary decohesion, and the number of shear dim-
ples has increased (fig. V - 8). At 300 MPa, no facets are present on
the surface (fig. V - 9 - a); instead, the surface is composed of
shear dimples (fig. V - 9 - b). A similar situation is found at 414
MPa (fig. V - 10). At the highest pressures, no evidence of damage has
been found on the fracture surface of the sample pulled under 503 MPa
(fig. V - 11) or under 690 MPa (fig. V - 12). Extensive slip lines
which create surface steps can be seen on the outer surfaces of both
specimens (fig. V - 13 - a and V - 13 - b).

It appears that the fracture mode is changing when the applied
pressure is increased. This was confirmed by metallographic exami-
nation.

(a)   160 x   (b)   640 x
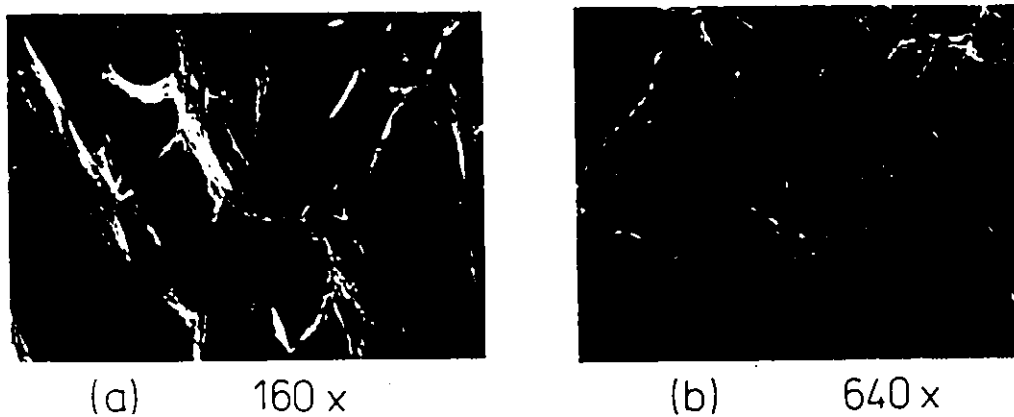
Fig. V-7 : Scanning electron micrographs of the Al-Cu sample
           broken under 100 MPa :
           a) general view of the fracture surface
           b) elongated dimples on the fracture surface

Fig. V-8. : Scanning electron micrograph of the fracture surface
            of the Al-Cu sample broken under 207 MPa.

(a)   40 x   (b)   320 x
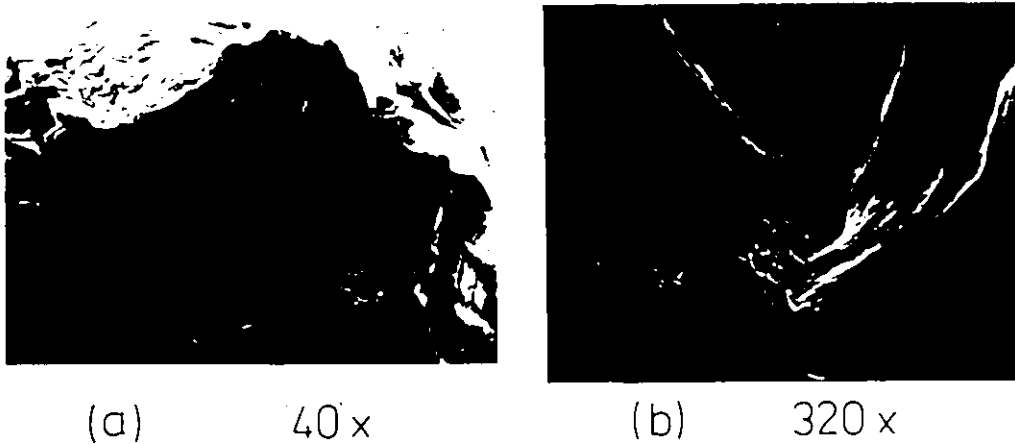
Fig. V-9 : Scanning electron micrographs of the Al-Cu sample
           broken under 300 MPa :
           a) general view of the fracture surface
           b) detailed micrograph of the shear dimples

Fig. V-10 : Scanning electron micrograph of the fracture
            surface of the Al-Cu sample broken under 414 MPa.
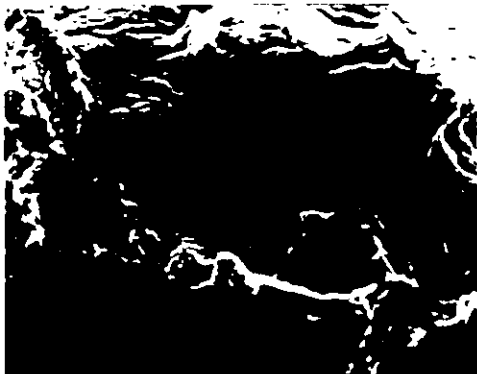
Fig. V-11 : Scanning electron
micrograph of the fracture
surface of the Al-Cu sample
broken under 503 MPa.

Fig. V-12 : Scanning electron micro-
graph of the fracture surface
of the Al-Cu sample broken
under 690 MPa.

(a)   80 x

(b)   1250 x

Fig. V-13 : Scanning electron micrographs of the slip steps
created on the surfaces of the Al-Cu samples broken
under :
a) 503 MPa   b) 690 MPa

V - 4 - 1 - 3   Metallography

For each sample, a montage of the polished broken half has been made.

At atmospheric pressure, the intergranular path of the failure appears clearly (fig.V - 14 - a), and virtually no microcracks exist below the fracture surface; slip lines can be seen within individual grains, which have been slightly elongated. At 100 and 207 MPa, the shear character is developing; at 100 MPa, the failure path is partly inter-granular (fig. V - 14 - b), this being less obvious at 207 MPa (fig. V - 14 - c); in both cases, some stabilized microcracks exist in the bulk of the sample, more of them being present at 100 MPa; the grains are extensively elongated, and within each of them slip has taken place. At 300 and 414 MPa, the fracture has a fully shear character, and no microcracks are present (fig. V - 14 - d and V - 14 - e); the organization of slip into a macroscopic shear band is clearly seen near the fracture surface of both samples. At higher pressures, the fracture has a chisel-point appearance; grains have been highly elonga-ted; some macroscopic bands crossing several grains can be seen below the fracture surface in both the sample pulled under 503 MPa (fig. V - 14 - f) and under 690 MPa (fig. V - 14 - g); in the latter, these bands have created steps on the external surface of the sample.

In addition, a montage of an unbroken sample deformed under a pressure of 503 MPa is shown in fig. V - 15. It can be seen that grains are undergoing large deformations when the macroscopic shear band is developed; despite the large strains involved, no evidence of damage is seen, possibly because of the superimposed pressure which could be
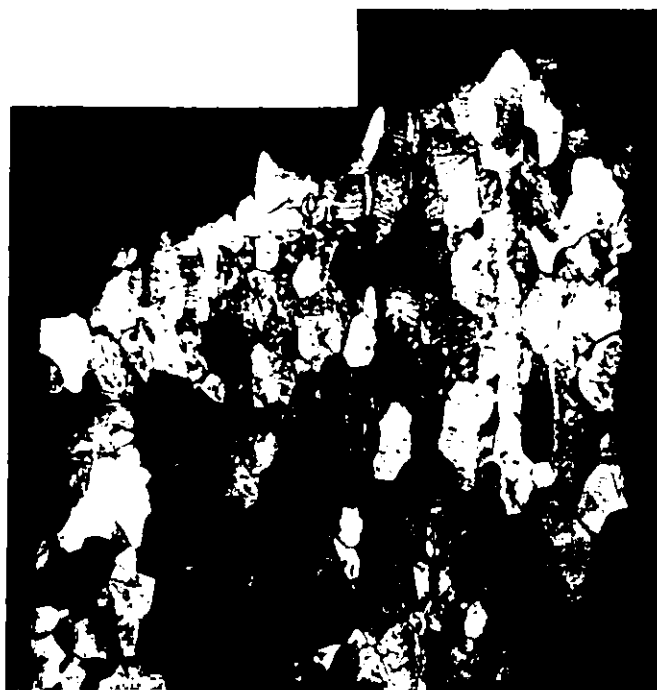
Fig. V-14-a

Fig. V-14-b

Fig. V-14-c

Fig. V-14-d

Fig. V-14-e

Fig. V-14-f

Fig. V-14-g

Fig. V-14 : Montages of the Al-Cu samples tested in tension
under various pressures :
a) 0.1 MPa   b) 100 MPa   c) 207 MPa
d) 300 MPa   e) 414 MPa   f) 503 MPa
g) 690 MPa

Fig. V-15 : Montage of the Al-Cu sample tested in tension
under 503 MPa and interrupted prior to failure.

sufficient to suppress totally any crack or void development.

To conclude this metallographic and fractographic study, it can be said that pressure has a strong influence on the fracture mode of the aluminum-copper alloy. The mode changes according to a sequence which is in agreement with the one found in previous works (French and Weinrich, 1977) and is the following :

$P < 50$ MPa : fibrous intergranular

$50 < P < 250$ MPa : fibrous intergranular + shear

$250 < P < 480$ MPa : shear

$480 < P$: chisel-point

V - 4 - 2   Iron-phosphorus alloy

V - 4 - 2 - 1   Specimen preparation

After being mounted in lucite, the broken halves of the tensile samples have been polished down to their mid-plane. For each of the two compression samples, both a section parallel to the compression axis and a section perpendicular to it have been mounted and polished. The etching has been performed in two steps :

- a light preliminary etching with nital 2%,

- a subsequent etching with a solution of 10 gr. of potassium meta-bisulfite $K_2 S_2 O_5$ in 100 ml. of distilled water (Petzow, 1978).

This etchant colours the grains and reveals the twins present in them.

V - 4 - 2 - 2   Macroscopic aspect. Fractography

The macroscopic aspect of the samples broken under various pressures is shown in fig. V - 16. It can be seen that despite the appearance of a distorted neck above 517 MPa, the fracture surface has bright facets at all pressures.
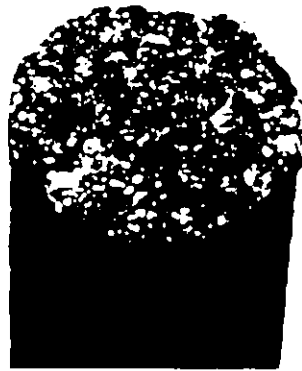
P = 0.1 MPa   P = 345 MPa

P = 517 MPa   P = 690 MPa

P = 869 MPa   P = 1100 MPa

Fig. V-16 : Macrophotographs of the Fe-P tensile samples
            broken under various pressures.
            Magnification : 7.5x

The fractography performed with the SEM revealed the details of these surfaces. At atmospheric pressure, the fracture surface is composed (fig. V - 17 - a) of both cleavage facets (fig. V - 17 - b) and grain boundary facets with no evidence of dimples on them (fig. V - 17 - c). The relative proportion of cleavage and grain facets is not easily determined. A similar situation is found at 345 MPa (fig. V - 18) and 517 MPa (fig. V - 19 - a). It is worth noting the presence of lines on the grain boundary facets, which could be the emergence of twins. At 517 MPa, as the strain increases, cracks appear on the outer surface of the sample (fig. V - 19 - b). At 690 MPa, a neck is observed. The cross-section takes an elliptical shape (fig. V - 20 - a); large cracks parallel to the major axis of this ellipse develop inside the grains or on their boundaries (fig. V - 20 - b); the fracture surface is itself a mixture of cleavage facets and grain boundaries (fig. V - 20 - c); on the outer surface, large cracks are opened, in general perpendicular to the tensile axis, but a few are parallel to it (fig. V - 20 - d and V - 20 - e). Similar observations can be made at higher pressures. At 869 MPa, both cleavage facets and grain boundaries are seen on the fracture surface (fig. V - 21 - a) together with large cracks (fig. V - 21 - b). At 1100 MPa, a very large crack is extending parallel to the tensile axis on the outer surface of the sample (fig. V - 22 - a); details of this crack are shown in fig. V - 22 - b; the fracture surface is again a mixture of cleavage and grain facets (fig. V - 22 - c).

It can therefore be concluded that at all pressures the fracture mode is a mixture of intergranular and transgranular cleavage. The pressure appears to alter the development of microcracks and to allow ex-

(a) 80 x   (b) 640 x

(c) 640 x
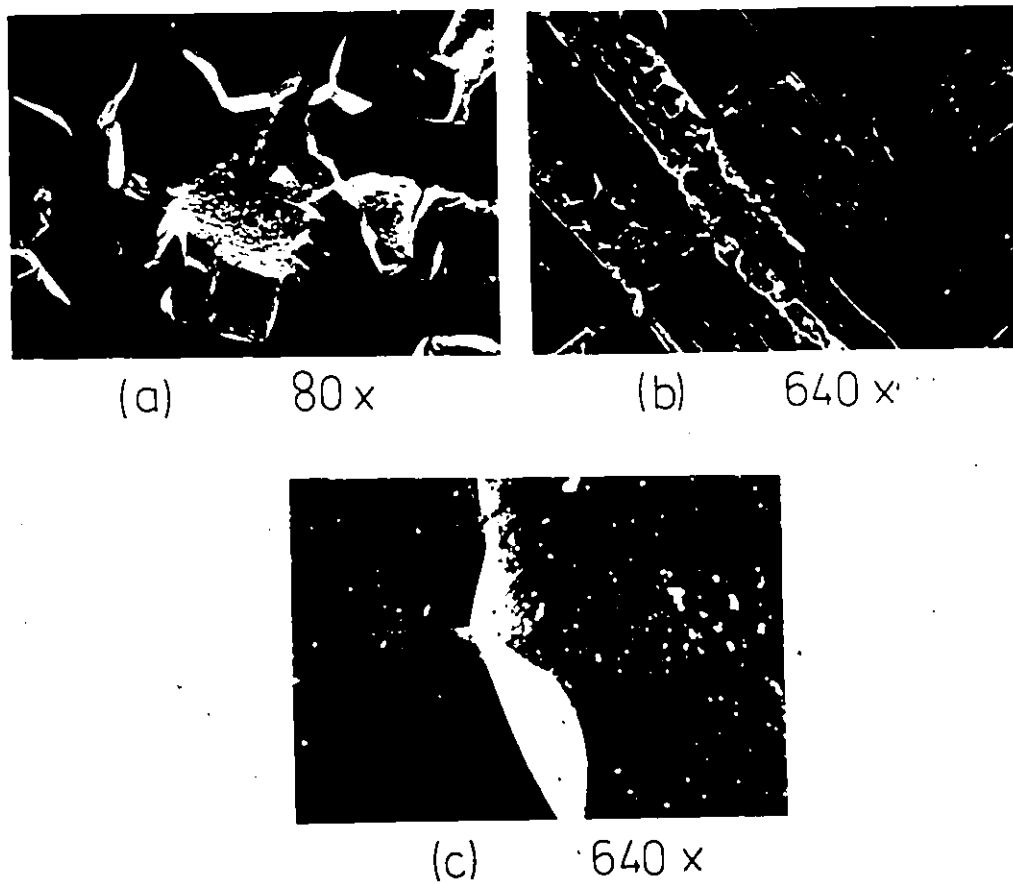
Fig. V-17 : Scanning electron micrographs of the Fe-P tensile
sample broken at atmospheric pressure :
a) general view of the fracture surface
b) details of the cleavage facets
.c) grain boundary facet showing no evidence of dimples

Fig. V-18 : Scanning electron micrograph of the fracture surface
of the Fe-P tensile sample broken under 345 MPa.
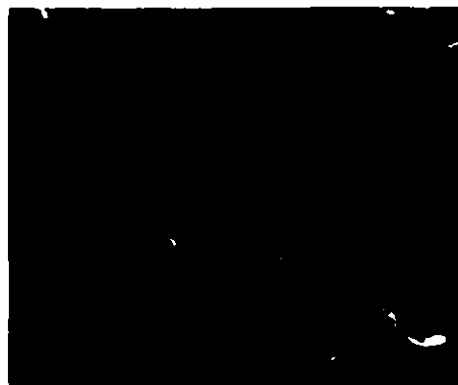
(a)　　　320 x　　　　　(b)　　　320 x
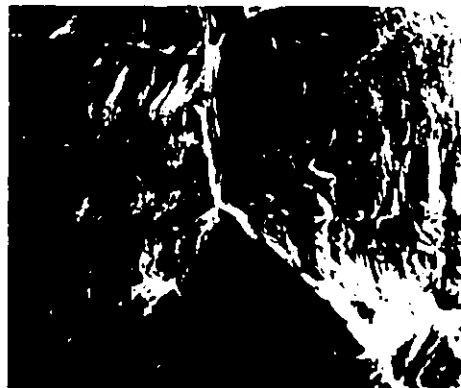
Fig. V-19 : Scanning electron micrographs of the Fe-P tensile
sample broken under 517 MPa :
a)general view of the fracture surface
b)cracks on the outer surface of the sample
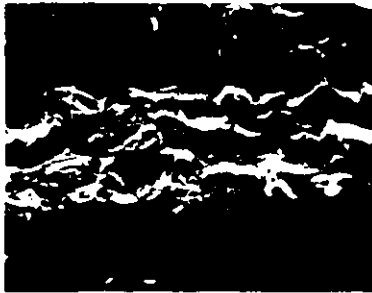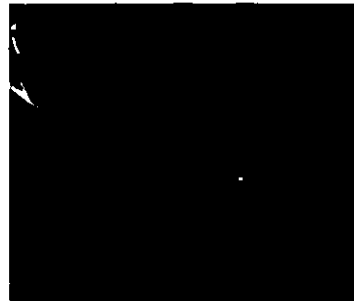
Fig. V-20 : Scanning electron micrographs of the Fe-P tensile
sample broken under 690 MPa :
a) general view of the fracture surface
b) large cracks on the fracture surface
c) detailed view of the fracture surface
d) cracks on the outer surface
e) high magnification of the cracks on the outer
surface.
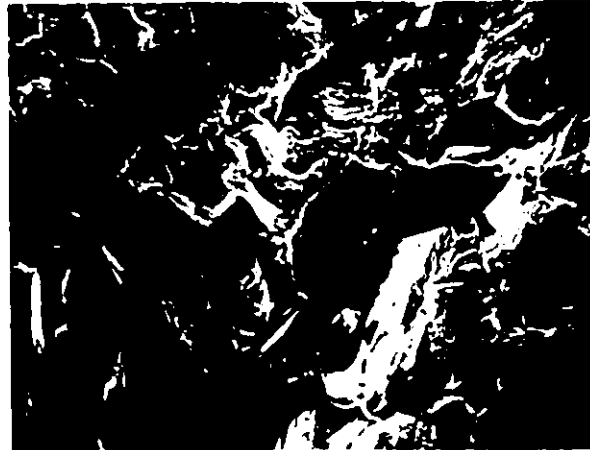
(a) 160 x
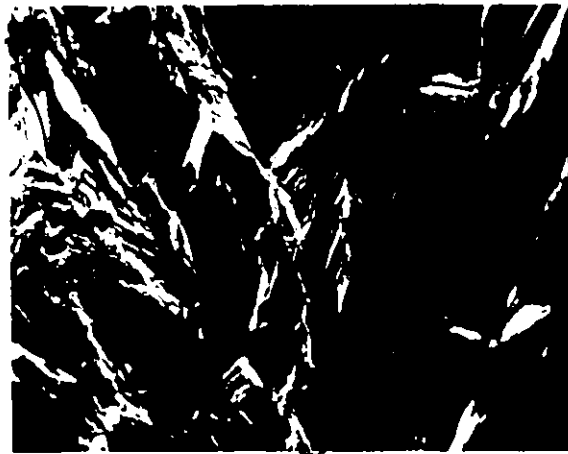
(b) 80 x

Fig. V-21 : Scanning electron micrographs of the Fe-P tensile
sample broken under 869 MPa :
a) general view of the fracture surface
b) cracks on the fracture surface

(a) 40 x

(b) 640 x

(c) 160 x
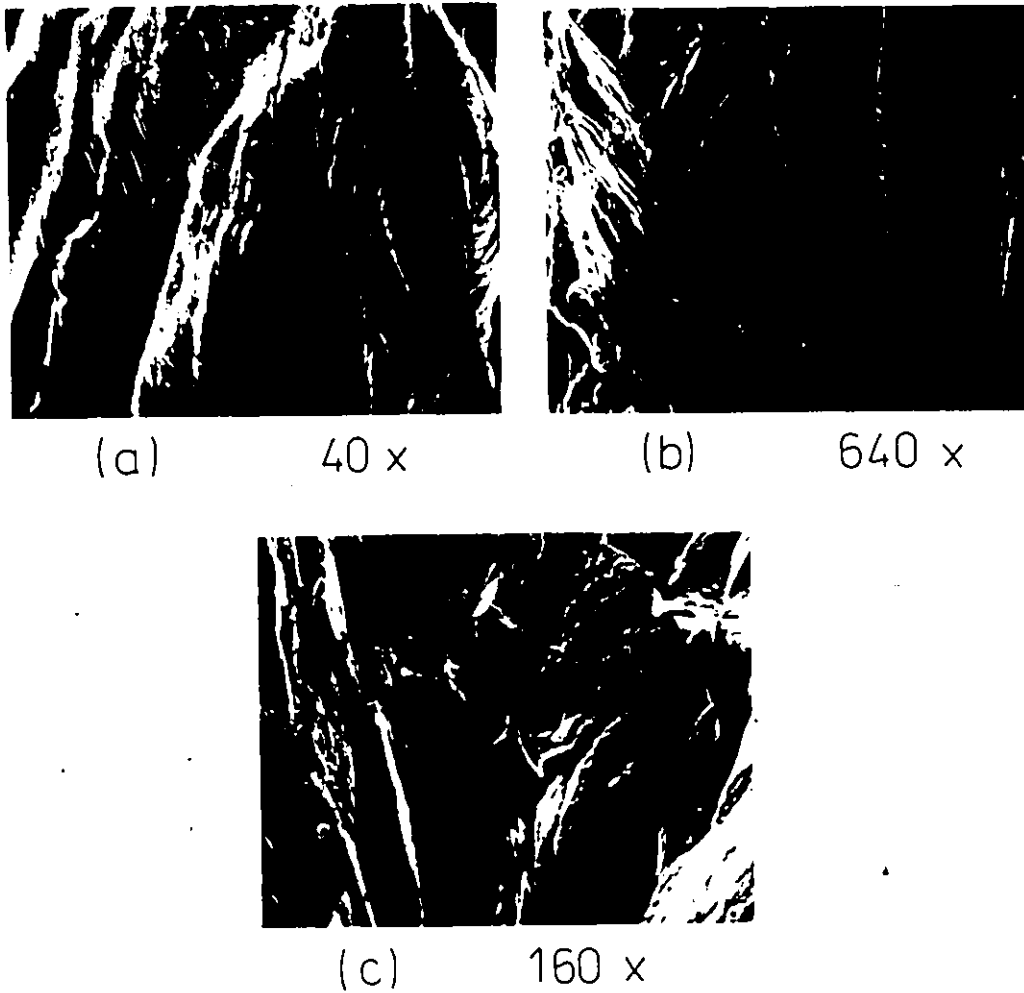
Fig. V-22 : Scanning electron micrographs of the Fe-P tensile
sample broken under 1100 MPa :
a) cracks on the outer surface
b) detail of a crack on the outer surface
c) general view of the fracture surface

tensive deformation of the grains.

V - 4 - 2 - 3 Metallography

At atmospheric pressure (fig. V - 23 - a), the outer surface of the sample is straight; the fracture path is both transgranular and in-tergranular; no cracks are seen below the fracture surface, and there is no evidence of twinning or slip in the grains, except in the ones adjacent to the fracture surface : these twins can be formed during the propagation of the crack, because of the high strain rate existing then at its tip. At 345 and 517 MPa (fig. V - 23 - b and V - 23 -c), almost all the grains show twins, and some microcracks are present well below the fracture surface. At 345 MPa, the cracks are perpendicular to the tensile axis and are either intergranular or transgranular. At 517 MPa, some cracks parallel to the tensile axis are found. At 690 MPa, the distorted shape of the sample is clearly apparent (fig. V - 23 - d), and there are no cracks perpendicular to the tensile axis; the fracture surface is slightly inclined to the tensile axis, similar to a macroscopic shear plane. At 869 and 1100 MPa, the neck is more pronounced and appears to consist of two shear planes at 90° (fig. V - 23 - e and V - 23 - f); very long cracks are running along the tensile axis, intergranularly or transgranularly. Extensive twinning has taken place in all the grains.

Fig. V - 24 - a shows a section of the sample tested in compression and interrupted before the occurrence of the first twin burst on the load-compression curve, and fig. V - 24 - b a section of the sample which has been compressed up to the occurrence of strain hardening. Both sections are perpendicular to the compressive axis. In the former

Fig. V-23-a

Fig. V-23-c
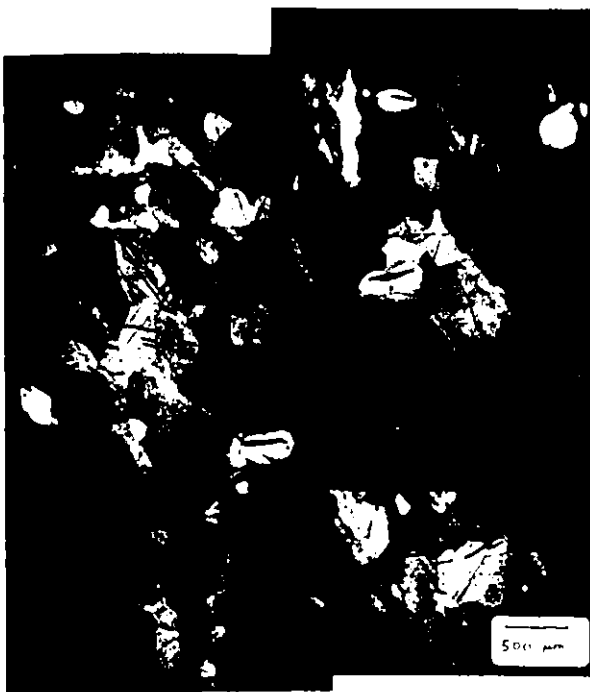
Fig. V-23-b

Fig. V-23-d

Fig. V-23-e   Fig. V-23-f

Fig. V-23 : Montages of the Fe-P samples tested in tension
under various pressures :
a) 0.1 MPa   b) 345 MPa   c) 517 MPa
d) 690 MPa   e) 869 MPa   f) 1100 MPa

Fig. V-24-a   Fig. V-24-b

Fig. V-24 : Montages of sections perpendicular to the compressive
            axis of the Fe-P samples tested in compression at
            atmospheric pressure interrupted :
            a) before general yielding throughout the sample
            b) after general yielding throughout the sample.

one, almost no twinning has taken place, whereas in the latter one, extensive twinning is seen in almost all the grains. In both specimens, a large crack is running through the section, following a mainly intergranular path with,however,some transgranular terminations.

In summary,   pressure appears to affect crack propagation, allowing their stabilization in the bulk of the material. The large deformations obtained under superimposed pressures are due to extensive twinning within the grains which are elongated. Some cracks parallel to the tensile axis have also been observed at the highest pressures tested.

V - 5   Discussion

V - 5 - 1   Aluminum-copper alloy

At atmospheric pressure, once a microcrack is created at a grain boundary by a process involving the nucleation, growth and coalescence of voids appearing at the second phase particles existing along this boundary, the stress concentration at its tip is sufficient to insure   fast propagation along an intergranular path. This explains the absence of cracks below the fracture surface : crack nucleation is the critical event at atmospheric pressure, and the measured fracture stress is the one needed for this nucleation, which is in fact the stress at which coalescence of voids occurs along a boundary.

When a pressure is superimposed, the stress concentration at the tip of an intergranular crack can be insufficient to make it propagate rapidly; then, some stable microcracks can be seen in the

bulk of the sample, arrested at obstacles such as boundaries which are almost perpendicular to the tensile axis.

It has been concluded from the metallographic investigation that the fracture mode is changing as the superimposed pressure is increasing. From intergranular, the mode goes to a shear one and finally to a chisel-point one. This sequence involves the occurrence of a localization of the deformation, which can have several causes.

The first one is related to the damage created at particle-matrix interfaces. The superimposed pressure delays the lateral growth of the voids, and therefore, their coalescence into a microcrack. Instead, the growth of voids in the direction of the tensile axis can be sufficient to trigger a void-sheeting mechanism such as described in section II - 2 - 3. This would then explain the shear character of the fracture surface of the samples broken under 300 and 414 MPa.

Another possibility is related to the large strains which are obtained when the samples are tested under pressure. The grains are highly elongated, so that a texture softening could occur (Dillamore et al., 1979) leading to a localization of the deformation.

Finally, it has been seen that the slip in this alloy is highly heterogeneous. At large strains, the slip lines can organize themselves into microbands, and softening effects such as cutting of precipitates and their susequent dissolution can occur (Hornbogen and Zum Gahr, 1975).

Thus, the occurrence of shear fracture in the aluminum-copper alloy can be explained by different softening events related to the microstructure. When the pressure is sufficiently high, it can suppress

any dilational damage, so that the sample fails by plastic rupture,
necking down to almost zero cross-section and giving the chisel-point
appearance obtained in the samples broken under 503 and 690 MPa.

V - 5 - 2 Iron-phosphorus alloy

It has been seen in the literature review that brittle fracture
involves three stages :

    - the nucleation of a microcrack

    - its initial growth

    - the traversing of the first strong barrier (e.g. grain boundary)

      that the crack encounters.

The measured fracture stress is the stress at which the most difficult
of these stages is overcome. At atmospheric pressure, no arrested micro-
cracks are present below the fracture surface; it can thus be concluded
that the initial growth of a crack is the critical step in this case.
This growth occurs either along a grain boundary or within a grain. From
the mechanical testing and the metallography, a crack appears after the
onset of plastic deformation, at least locally, which is assured by
twinning in this alloy. It has not been possible to observe the detailed
mechanism of crack initiation which could occur either at the intersec-
tion of twins (Hull, 1960) or, more likely, because of the stress con-
centration at the tip of a twin line.

As there is no second phase susceptible to play a role in the
crack initiation and initial growth, a mechanism such as the one pro-
posed by Cottrell (1958) may be used to obtain a value of the plastic
work γ_p associated with the fracture. The fracture stress is :

$$\sigma_f = \frac{2 \mu \gamma_p}{k_y^s} \, d^{-\frac{1}{2}} \qquad\qquad (V - 5)$$

Spitzig (1972) has reported values of k_y measured in tension for a similar Fe-P alloy. At room temperature, he found :

$$k_y = 0.12 \text{ MN/m}^{3/2}$$

so that $\qquad\qquad k_y^s = 0.06 \text{ MN/m}^{3/2}.$

Using this value in equation (V - 5) gives :

$$\gamma_p = 2.5 \text{ Jm}^{-2}$$

This value is sensibly lower than the one of 14 Jm^{-2} obtained by Knott (1977) for the plastic work for crack propagation in a ferrite grain. A possible explanation of this difference is that in this alloy, fracture occurs along a mixture of transgranular and intergranular paths, so that the plastic work for fracture can be considered as a weighed sum of γ_p(ferrite) and γ(boundary), the latter being very low due to embrittlement of the boundary by phosphorus segregation.

In the literature review, the theoretical treatment of the influence of hydrostatic pressure on cleavage fracture proposed by Francois and Wilshaw (1968) has been presented. In accord with their predictions, some arrested microcracks are present in the samples tested under high pressures. The critical step has become the traversing of the strong barrier encountered by the microcrack. When the crack reaches the barrier, it has a length equal to the grain size, so that the stress needed to propagate it through the barrier is given by the Griffith formula :

$$\sigma_b - P = \left(\frac{4 E \gamma_b}{\pi(1-\nu^2)d} \right)^{\frac{1}{2}} \qquad\qquad (V - 6)$$

where γ_b is the plastic work associated with the crossing of the barrier.

Bedere et al. (1971) have also reported some arrested cracks in samples
of beryllium pulled under pressure. Assuming that the fracture stress
which is measured corresponds to the stress required to cross the barrier,
they proposed to use equation (V - 6) to calculate γ_b by extrapolating
the relationship giving the fracture stress as a function of the super-
imposed pressure down to P = 0. However Tetelman and McEvily (1967)
have argued that the two stresses could be different, as the measured
fracture stress is in fact the stress needed to create a new, unstable
microcrack in the plastic zone near the tip of the arrested one. There-
fore, the extrapolation was not attempted here.

Finally, the presence of large cracks running parallel to the
tensile axis in the samples pulled under the highest pressures can be
explained by considering the large deformations reached in these tests,
and also the production of a neck in the samples. Indeed, if a crack is
created at an angle less than 90° to the tensile axis and then stabili-
zed, the subsequent tensile deformation can rotate it towards the direc-
tion of the tensile axis. When a neck is formed, the hydrostatic tension
created perpendicular to the tensile axis can counterbalance the super-
imposed pressure, if the neck is sufficiently pronounced. In this case,
a tensile stress exists at the tip of the crack parallel to the tensile
axis, so that it can open and propagate according to a mode I opening
along the direction of the tensile axis. This would explain the presence
of very long cracks observed in the samples tested under 869 and 1100 MPa.

V - 6   Conclusions

It has been seen in this chapter that, as brittle fracture invol-

ves a form of damage accumulation, it is markedly influenced by a superimposed hydrostatic pressure.

The experiments performed on two different alloys have led to two conclusions :

a) it is possible to separate the nucleation of a microcrack from its propagation leading to final failure, by superimposing a sufficient pressure.

b) when the pressure is increased, two alternatives have been found :

- the fracture mode changes quite drastically, or

- the microcracking pattern is modified.

These two possibilities have been related to the existence of damage in the material. In both cases, the superimposed pressure delays damage accumulation, allowing the occurrence of softening events leading to shear fracture, or changing the orientation of stabilized microcracks and their mode of opening. This leads to the attainment of substantial ductility in the two alloys tested under superimposed pressure.

CHAPTER VI

FRACTURE - MECHANISM DIAGRAMS IN STRESS SPACE

VI - 1 Introduction

The results discussed in the previous three chapters indicate
that the stress state is of prime importance in determining which frac-
ture mode is operative in a material. In both this study and previous
work reported in the literature, the fracture modes have been found to
change according to the magnitude of the superimposed hydrostatic
stress.

Following the previous work on mapping reviewed in Section
II - 5, it was decided to express the results as fracture maps in
stress space. The loading path has been chosen to be an axisymmetric
one, in which the principal stress in the tensile direction is called
σ_3 and the two equal principal stresses in the transverse directions
are called σ_1 and σ_2. The effective stress $\bar{\sigma}$ is given by :

$$\bar{\sigma} = [\frac{1}{2} ((\sigma_1 - \sigma_2)^2 + (\sigma_2 - \sigma_3)^2 + (\sigma_3 - \sigma_1)^2)]^{\frac{1}{2}} \qquad (VI - 1)$$

It has been emphasized in Section II - 5 that in order to
determine the locus for a given fracture mechanism, a knowledge of the
process of damage accumulation leading to this type of fracture is
necessary, together with a fracture criterion. Therefore, two alter-
natives exist :

- the first one is to use the quantitative model developed in Chapter III

to describe the ductile fracture and by extension, the shear fracture by a void-sheet mechanism. This provides maps with σ_3 and σ_1 as coordinates for the spheroidized steels studied in this work.

- the second possibility is to use simplified models of damage accumulation and fracture criteria, to produce analytical expressions and utilise them in order to rationalize available data from the literature for a wide range of materials. This alternative has been developed here to produce maps with $\bar{\sigma}$ and P as coordinates, where P is the superimposed pressure.

These two forms of maps are presented in this chapter, together with their applications. The detailed calculations related to the maps have been treated separately in Appendices B and C.

VI - 2   Maps in $\sigma_1 - \sigma_3$ space

The purpose of these maps is to determine, for a given axisymmetric loading path, the sequence of events undergone by a spheroidized steel.

The following events have to be considered :

- the onset of plastic yielding, when $\bar{\sigma}$ exceeds the yield strength σ_Y.
- the nucleation of voids, which starts at a given strain ε_N.
- the growth of voids and their eventual coalescence to give fibrous ductile fracture, or alternatively shear fracture by a void-sheet mechanism.
- if the temperature and/or the strain rate are adjusted correctly, the occurrence of cleavage fracture.

On the map, each of these events will be represented by a

line, the determination of which is now presented.

VI - 2 - 1 Plastic yielding

It occurs when $\bar{\sigma} = \sigma_Y$, i.e. using equation (VI - 1) for axisymmetric loading :

$$\sigma_3 - \sigma_1 = \sigma_Y \qquad (VI - 2)$$

VI - 2 - 2 Void nucleation

According to the simplified model presented in Section III - 6 - 1 - 1, the nucleation strain is given by :

$$\sqrt{\varepsilon_N} = H (\sigma_I - \sigma_m) \qquad (VI - 3)$$

Also, the mean stress component σ_m is a linear function of strain which has the general form :

$$\sigma_m = A (1 + 3 \alpha P) \varepsilon_N + B - P \qquad (VI - 4)$$

Using equations (VI - 3) and (VI - 4), it is possible to calculate ε_N at different pressures P. This value corresponds to a neck geometry or ratio a/R which is known from the linear relationships given in Table III - 3; therefore, it is possible to calculate the corresponding stresses σ_3 and σ_1 using equations (III - 6) and (III - 7) from Bridgman's analysis.

VI - 2 - 3 Fibrous ductile fracture

The fracture criterion used here is the one determined in Chapter III, i.e. the attainment of a critical amount of damage independent of the applied pressure. The fibrous ductile fracture line is determined point by point, calculating at various pressures P the strain at which this critical amount of damage is reached (using the computer program developed in Chapter III), and converting this strain into a value of the ratio a/R and further into stress components as

for the void nucleation line.

This method gives correct results over a wide range of super-
imposed pressures (P> 0) or tensions (P <0), but becomes inadequate
as the stress state is approaching pure hydrostatic tension, i.e.
$\sigma_3 = \sigma_1 = \sigma_2$.

VI - 2 - 4 Shear fracture

It has been seen in Section II - 4 - 3 that when the super-
imposed pressure is sufficiently high, the fracture of spheroidized
steels can occur by the creation of a band of localized deformation
between adjacent voids. McClintock (1968b) has proposed an analysis
of the instability leading to this event, and the criterion found for
the spheroidized steels is (see Appendix B) :

$$\frac{n}{\varepsilon} = H \, N_T \, R_3^2 \qquad\qquad (VI - 5)$$

Here, a power law hardening has been assumed, and the coefficient of
hardening n is assumed to be constant over the entire range of strains
considered. N_T is the number of voids per unit area provided by the
model of damage accumulation of Chapter III; R_3 is the void dimension
in the direction of the tensile axis, and H is a constant to be
determined from an experimental point.

The shear fracture line is then determined point by point
using the computer model of damage accumulation to calculate the
strain at which the condition (VI - 5) is fulfilled, and converting
this value into stress components as for the void nucleation line.

VI - 2 - 5 Cleavage fracture

Gurrell (1963) has proposed that the locus for brittle frac-

ture of materials is a parabola represented by :

$$(\sigma_3 - \sigma_1)^2 = 12 \; \sigma_f^o \; (2 \; \sigma_1 + \sigma_3) \qquad\qquad \text{(VI - 6)}$$

truncated by the two lines :

$$\sigma_3 = \sigma_f^o$$
$$\sigma_1 = \sigma_f^o \qquad\qquad\qquad\qquad \text{(VI - 7)}$$

for axisymmetric loading, where σ_f^o is the cleavage fracture stress in a tensile test performed at atmospheric pressure.

The value of σ_f^o can be estimated from the particle size distribution by (Knott, 1977) :

$$\sigma_f^o = \left(\frac{\pi \; E \; \gamma_p}{2 \; C_o} \right)^{\frac{1}{2}} \qquad\qquad \text{(VI - 8)}$$

where C_o is the 95th percentile of the distribution, and γ_p is equal to 14 J m^{-2}.

However, Cheng Jian-Hua (1981) has performed tensile tests at -196°C on spheroidized steels similar to those considered here. The steels were found to break by cleavage fracture. Accounting for the variation of the Young's modulus with temperature, an increase of 20% has been made to the values of σ_f^o found at -196°C; the values so obtained are :

$$\text{1018 steel} : \sigma_f^o = 2000 \text{ MPa}$$
$$\text{1045 steel} : \sigma_f^o = 1600 \text{ MPa}$$
$$\text{1080 steel} : \sigma_f^o = 1400 \text{ MPa}$$

It can be noted that these values can be found from equation (VI - 8) if the 99th percentile is used instead of the 95th one for the value of C_o. This latter value was taken arbitrarily by Knott (1977) to account for the fact that cleavage fracture occurs by the fast propa-

gation of a microcrack created in the largest carbide particle present

in the distribution. Therefore, it is physically reasonable to obtain

the 99th percentile for the critical carbide diameter to give cleavage

fracture.

VI - 2 - 6 Maps for the spheroidized steels

The maps are shown in fig. VI - 1 to fig. VI - 4 for the 1018,

1045, 1080 and 1045 a/R)$_o$=0.5 spheroidized steels, respectively.

It can be seen that the cleavage line is above all the other

lines, meaning that cleavage fracture cannot occur at room temperature,

and that only at very high superimposed pressures, i.e. at transverse

stress sufficiently negative, is the shear locus below the ductile one,

so that shear fracture is occurring. On the upper-right quadrant of the

maps, both the ductile fracture and the void nucleation lines tend to

a single point on the hydrostatic axis where $\sigma_1 = \sigma_2 = \sigma_3 \simeq 1200$ MPa,

which is of the order of the interfacial strength of the iron-cementite

system : under these critical conditions, nucleation, growth and

coalescence of a void are simultaneous, the situation being effectively

the catastrophic expansion of voids formed in a field of pure hydro-

static tension.

In addition to the fracture events, some lines of constant

damage can be superimposed on the maps presented above, expressing

in essence damage contour maps. Fig. VI - 5 shows such a map obtained

for the 1045 unnotched spheroidized steel. The lines corresponding to

0.5, 1 and 2% of damage, expressed in terms of the area fraction of

voids, have been drawn. They give a quantitative account of the damage

development during straining. It can be seen that at small super-
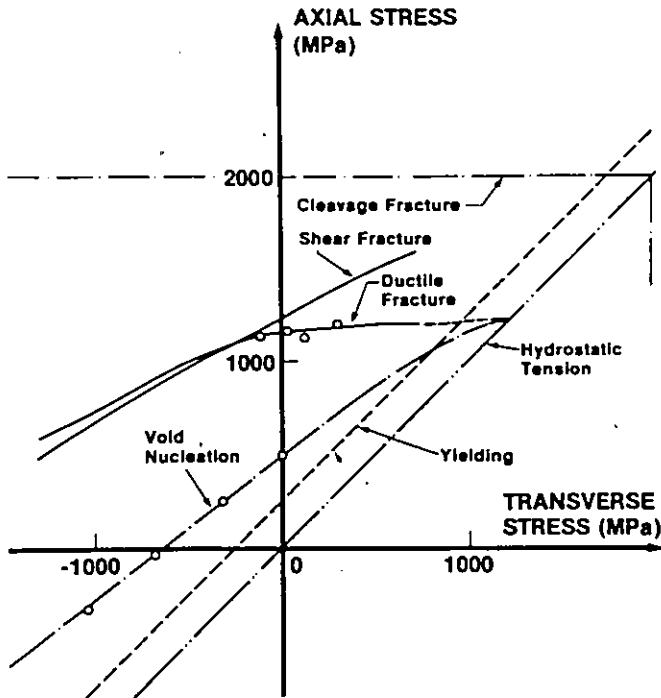
Fig. VI-1 : Fracture map in σ_1 - σ_3 coordinates for the 1018 spheroidized steel.

Fig. VI-2 : Fracture map in σ_1 - σ_3 coordinates for the 1045 unnotched spheroidized steel.

Fig. VI-3 : Fracture map in σ_1 - σ_3 coordinates for the 1080 spheroidized steel.

Fig. VI-4 : Fracture map in σ_1 - σ_3 coordinates for the 1045 a/R)$_o$ =0.5 notched spheroidized steel.

Fig. VI-5 : Fracture map in $\sigma_1 - \sigma_3$ coordinates showing both
fracture loci and contours of constant damage for
the 1045 unnotched spheroidized steel.

imposed pressures, damage develops fairly uniformly throughout defor-
mation. On the contrary, for the high superimposed pressures, the lines
of constant damage are close to the ductile fracture line. In this
case, nucleation starts early, but the material can be deformed quite
·extensively before reaching a substantial amount of damage. When this
occurs, final failure occurs after only a small amount of subsequent
deformation. This indicates therefore that the initial rate of damage
accumulation is slowed by high superimposed pressure, i.e. that its
pressure dependence is higher than the one of the onset of void
nucleation.

VI - 3 Maps in $\bar{\sigma}$ - P space

The purpose of these maps is to present a rational description
of the experimental results concerning the influence of a superimposed
pressure P on the fracture mechanisms. The stress coordinates chosen
are the effective stress $\bar{\sigma}$ and the superimposed pressure P itself.
The·fracture mechanism occurring at a given value of P will be the one
corresponding to the lowest value of $\bar{\sigma}$.

In this section, simplified analytical relationships between
$\bar{\sigma}$ and P are presented for the same mechanisms as in the preceding
paragraph. However, as seen from the review of previous experimental
work, and because these maps are to be drawn for several types of
materials, the plastic failure mode, where the specimen necks down to
zero cross-section, has been added.

VI - 3 - 1 Plastic yielding. Necking. Plastic failure

·It has been seen in Section II - 4 - 3 that the flow behaviour

of materials is slightly pressure dependent. This dependence can be written as :

$$\bar{\sigma} = A \bar{\epsilon}^{\dot{n}} \left(1 + \frac{10 \, P}{K} \right) \qquad \text{(VI - 9)}$$

where K is the bulk modulus of a particular material.

Plastic flow starts when $\bar{\sigma}$ exceeds the yield strength σ_Y. If the yield strength at P = 0 is σ_Y^o, the relationship between $\bar{\sigma}$ and P for plastic yielding is :

$$\bar{\sigma} = \sigma_Y^o \left(1 + \frac{10 \, P}{K} \right) \qquad \text{(VI - 10)}$$

Similarly, if σ_n^o is the stress at which necking starts at P = 0, the effective stress for necking is given by :

$$\bar{\sigma} = \sigma_n^o \left(1 + \frac{10 \, P}{K} \right) \qquad \text{(VI - 11)}$$

and σ_n^o is given by :

$$\sigma_n^o = A \, n^n \qquad \text{(VI - 12)}$$

If no other fracture mechanism intervenes, then necking leads to plastic failure : once the neck is created, flow is localized within the neck, and after a further strain of order 1, the cross-section is reduced to zero. The effective stress for plastic failure is therefore :

$$\bar{\sigma} = A \, (1 + n)^n \left(1 + \frac{10 \, P}{K} \right) \qquad \text{(VI - 13)}$$

Alternatively, if the rupture stress $\bar{\sigma}*$ is known at some pressure P*, then :

$$\bar{\sigma} = \bar{\sigma}* \left(\frac{1 + 10 \, P/K}{1 + 10 \, P*/K} \right) \qquad \text{(VI - 14)}$$

VI - 3 - 2 Ductile fracture

An approximate relationship between $\bar{\sigma}$ and P can be derived (see

Appendix C) by using the growth model of Rice and Tracey (1969) and Leroy et al. (1981) with the geometrical criterion for fracture of Brown and Embury (1973). In its simplest form, the result is :

$$\bar{\sigma} = \bar{\sigma}^o \left[\frac{C}{1 + 0.56 \sinh \{ \frac{1}{2} - \frac{3}{2} \frac{P}{\bar{\sigma}^o} \}} \right]^n \left(1 + \frac{10\ P}{K} \right) \qquad (VI - 15)$$

where C is a constant (roughly 2.5) and $\bar{\sigma}^o$ the effective stress for ductile fracture when P = 0.

VI – 3 – 3 Shear fracture

The occurrence of a band of localized deformation leading to shear fracture can be analysed by using the instability criterion of McClintock (1968b) and a simplified void nucleation model (see Appendix C). The relationship between $\bar{\sigma}$ and P which is obtained is :

$$\bar{\sigma} \left(\bar{\sigma}^{1/n} - C \left(1 + \frac{P}{\sigma_I} \right)^2 \right) = \bar{\sigma}^o \left(\bar{\sigma}^{o\ 1/n} - C \right) \qquad (VI - 16)$$

where $\bar{\sigma}^o$ is the fracture stress by shear failure when P = 0, C is a constant and σ_I is the strength of the particle-matrix interface.

VI – 3 – 4 Cleavage and brittle intergranular fracture

Murrell's criterion (1963) gives the relationship between $\bar{\sigma}$ and $\sigma_m = \frac{1}{3} \left(\sigma_1 + \sigma_2 + \sigma_3 \right)$ which causes fracture as :

$$\bar{\sigma} = 24\ \sigma_m\ \bar{\sigma}^o$$

truncated by the line :

$$\bar{\sigma} = \bar{\sigma}^o + \sigma_m$$

where $\bar{\sigma}^o$ is the fracture stress by cleavage in simple tension with no confining pressure. As no neck is created in this type of fracture, σ_m can be approximated to the superimposed hydrostatic pressure. The effective stress for brittle fracture is then :

$$\bar{\sigma} = \bar{\sigma}^\circ + P \qquad\qquad\qquad (VI - 17)$$

VI - 3 - 5 Construction of the maps

The results provided by the various relationships presented above are plotted by stepping through values of P, evaluating $\bar{\sigma}$ at each step. To do so, data are needed for a number of material properties. These data are presented in Table VI - 1 for different spheroidized steels, and in Table VI - 2 for other materials. Their origins are discussed below.

The procedure to draw the maps is the following. First, the yield, necking and void nucleation lines are constructed using the equations given above. The fracture mechanism at P = 0 is then identified; for most considered alloys, it is ductile fracture. Thus, the ductile fracture line is constructed using the value of $\bar{\sigma}$ at P = 0 as a normalizing stress. The value of $\bar{\sigma}$ given by this line at the pressure P* corresponding to the first change of mechanism can then be read off as $\bar{\sigma}*$, and the pair ($\bar{\sigma}*$, P*) can be used as the normalizing stress and pressure for the new mechanism. This is then repeated for each change of mechanism.

The next two sections present the maps so obtained and discuss the data used in their determination, together with the applications of the maps.

VI - 3 - 6 Maps obtained for the spheroidized steels

The data used are given in Table VI - 1. The maps shown in fig. VI - 6 to fig. VI - 9 for the 1018, 1045, 1080 and 1045 a/R)$_o$=0.5 spheroidized steels respectively, give the fracture modes taking place

MATERIAL	1018	1080	1045 $(a/R)_o = .5$	1045	1045 at $-196°C$	1045 Coarse Grains
Bulk Modulus K (MPa)	$1.93 \ 10^5$	$1.93 \ 10^5$	$1.93 \ 10^5$	$1.93 \ 10^5$	$1.93 \ 10^5$	$1.93 \ 10^5$
Yield Strength σ_y^o (MPa)	246	463	430	380	825	300
Tensile Strength σ_{TS}^o (MPa)	410	614	577	515	1013	412
Power Hardening Constant A (MPa)	769	1050	892.5	920	1393	735
Power Hardening Exponent n	.29	.24	.20	.25	.095	.25
Fracture Strain at 1 atm. ε_f^o	1.665	.90	1.115	1.3	9.3	1.3
Fracture Stress at 1 atm. σ_f (MPa)	891	1024	912	980	1430	785
Void Nucleation Stress at 1 atm. σ_{vn}^o (MPa)	486	622	539	562	1155	445
Interfacial Strength σ_I (MPa)	1200	1200	1200	1200	1200	1200
Cleavage Stress at 1 atm. (MPa)	2000	1400	1600	1600	1290	650

TABLE VI – 1: Data for the Spheroidized Steels
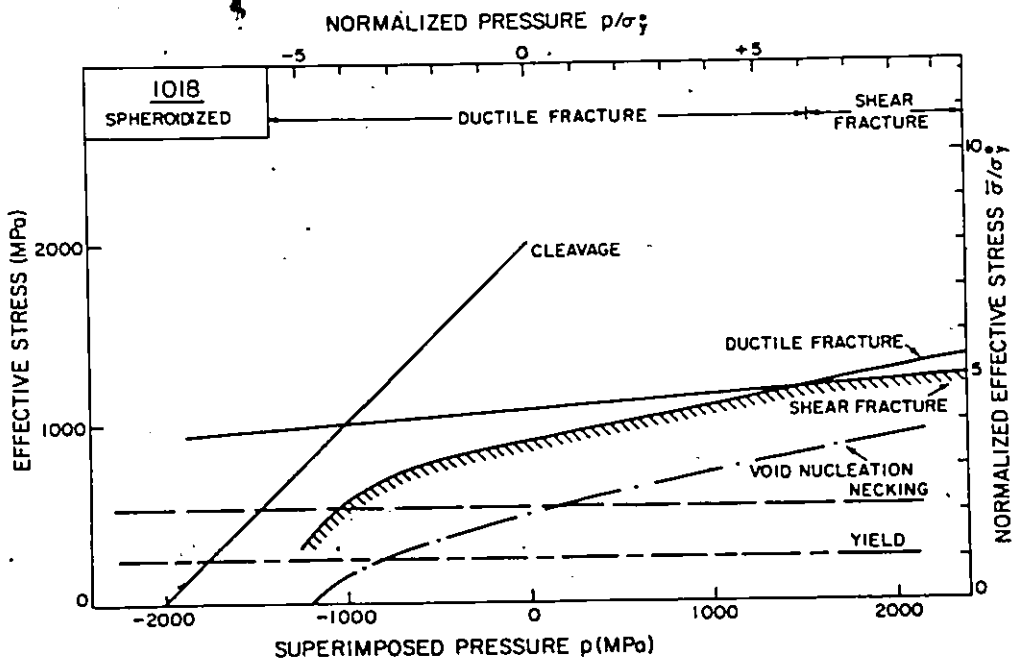
Fig. VI-6 : Fracture map in $\bar{\sigma}$ - P coordinates for the 1018
spheroidized steel.

Fig. VI-7 : Fracture map in $\bar{\sigma}$ - P coordinates for the 1045
unnotched spheroidized steel.
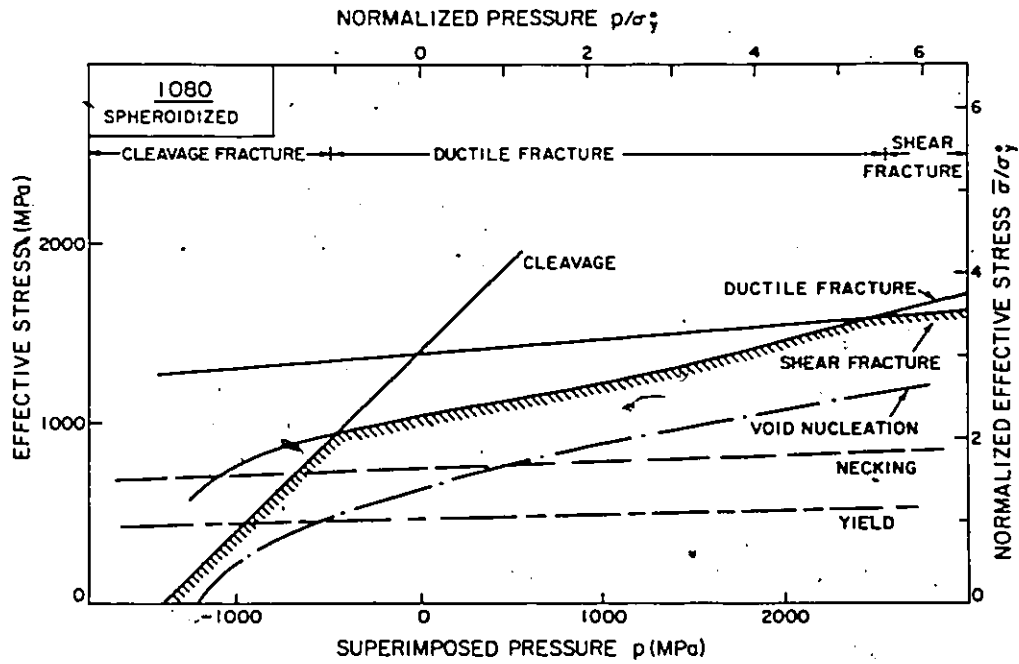
Fig. VI-8 : Fracture map in $\bar{\sigma}$ - P coordinates for the 1080 spheroidized steel.
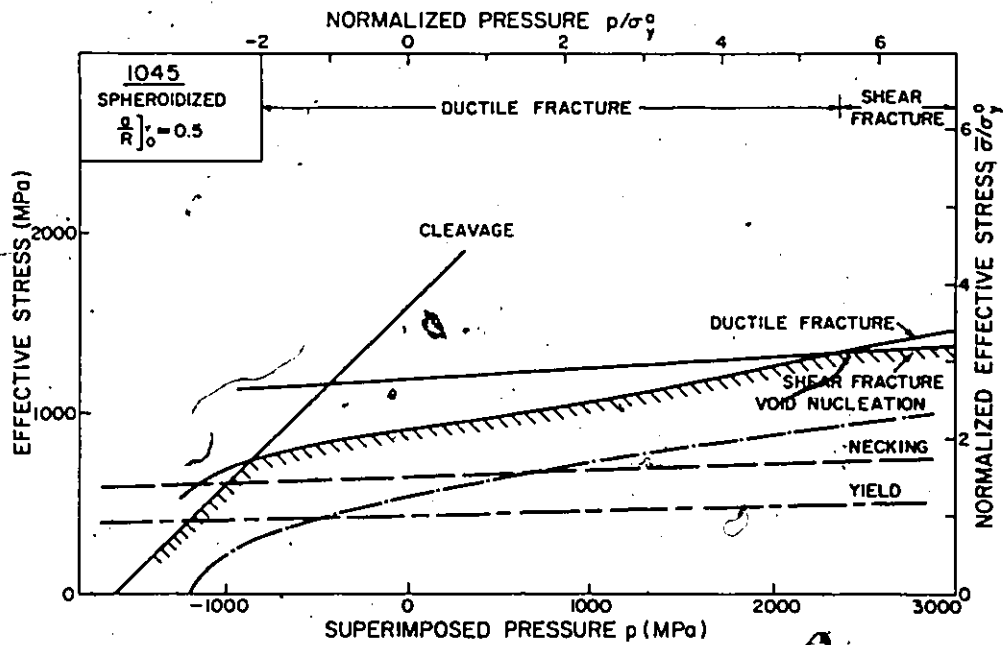
Fig. VI-9 : Fracture map in $\bar{\sigma}$ - P coordinates for the 1045 a/R)$_o$=0.5 notched spheroidized steel.

at room temperature under various superimposed pressures. Each fracture mechanism is represented by a full line, while broken lines are used for the yield surface, the onset of necking and the onset of void nucleation. The inner envelope of the fracture surfaces (cross-hatched) defines failure. The fracture mode is defined across the top of the diagram. The data in Table VI - 1 are the ones obtained in this study and presented in Chapter III. It can be seen that the ductile fracture mode is operating at atmospheric pressure up to high superimposed pressures whose values are given in Table B - 1 of Appendix B. Above these pressures, the shear mode takes place, as it corresponds to a lower value of $\bar{\sigma}$. Cleavage fracture is never found except if an hydrostatic tension is created (P < 0).

It is possible, for a given material, to change either the testing temperature, or some microstructural parameters such as ferrite grain size, and to draw the corresponding new maps to compare them with the previous maps. This has been done for the 1045 steel. Fig. VI - 10 shows the map which could be obtained if the tensile tests had been performed at -196°C. The corresponding experimental data are given in Table VI - 1, and are taken from Cheng Jian-Hua (1981). The yield stress is raised to a higher value, and so are all the events involving plastic flow. Therefore, at P = 0, the cleavage stress is smaller than the ductile fracture stress : the operative fracture mode is cleavage, up to a superimposed pressure of about 200 MPa, where the fracture mode changes to a ductile fracture one.

If the carbide particles are inside the ferrite grains, Anand
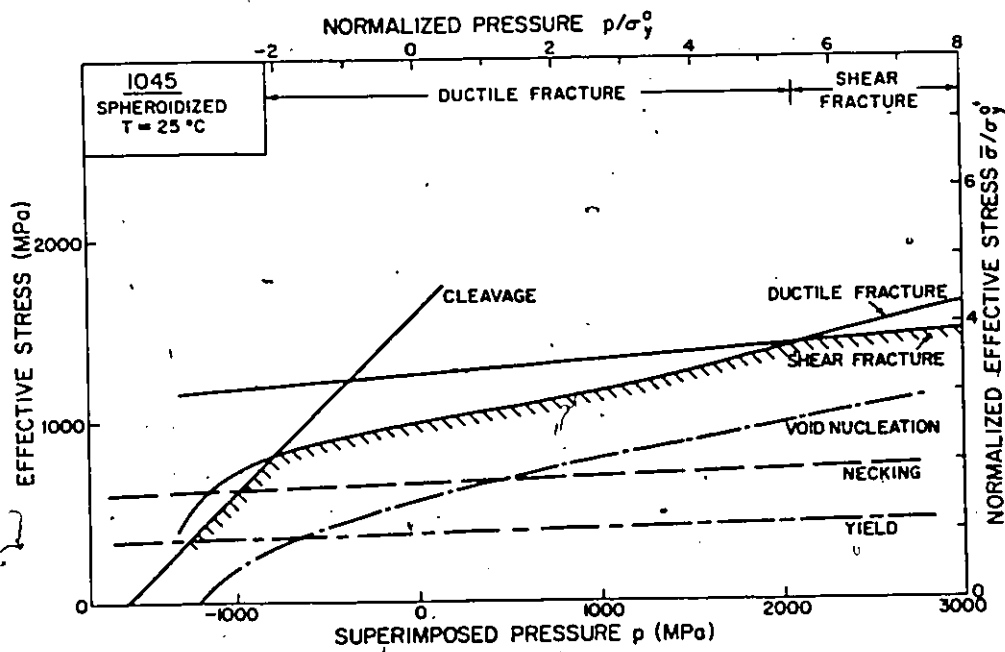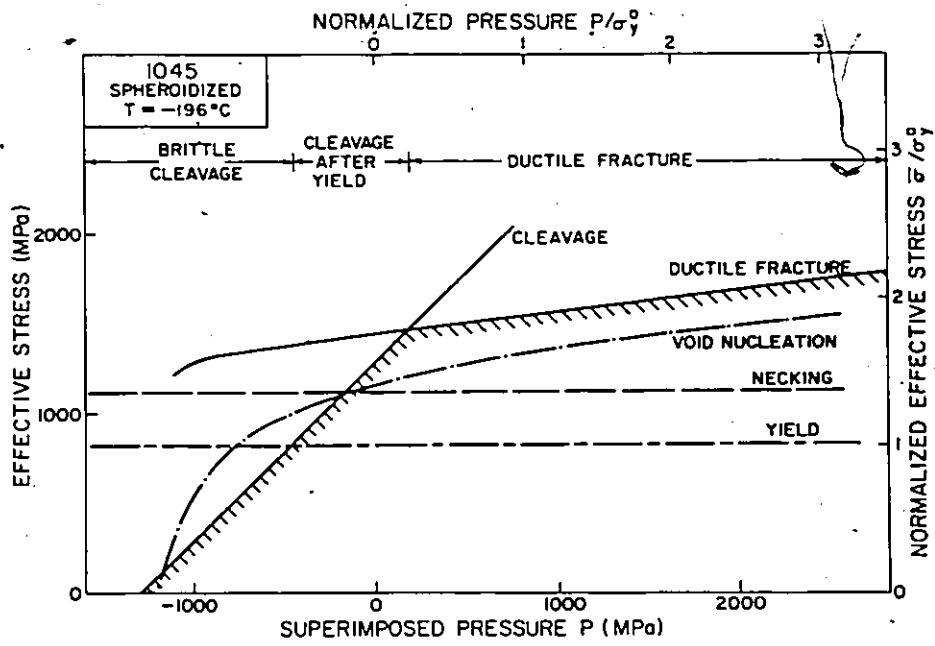
Fig. VI-10 : Fracture map in $\bar{\sigma}$ - P coordinates for the 1045 unnotched spheroidized steel tested at -196°C.
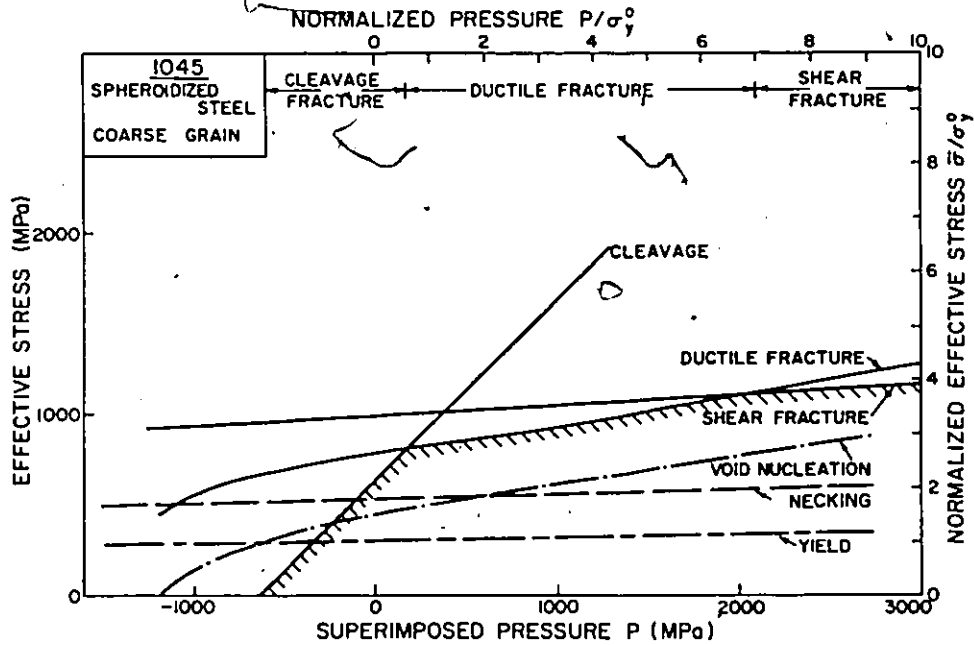
Fig. VI-11 : Fracture map in $\bar{\sigma}$ - P coordinates for the 1045 unnotched spheroidized steel with a coarse ferrite grain size.

and Gurland (1976) have shown that the yield strength of such spheroi-
dized steels is controlled by the ferrite grain size. If an appropriate
heat treatment is used to alter this size without changing the carbide
distribution, then the yield strength is decreased, together with the
cleavage stress, the latter by a larger amount than the former (see
fig. II - 11). The brittle-ductile transition temperature can be raised
and become eventually higher than room temperature. An arbitrary
increase of 100% in the grain size (from 5 to 10 μm) gives a decrease
of 20% in the stresses involving plastic flow, together with à decrease
of 50% of the cleavage fracture stress (see data in Table VI - 1).
The corresponding map in fig. VI - 11 shows that cleavage fracture is
operating at atmospheric pressure, and up to about 200 MPa, where
ductile fracture takes place.

These last two maps show therefore qualitatively the influence
of the testing temperature and of some microstructural parameters on
the fracture modes occurring under various pressures.

VI - 3 - 7 Maps for other materials

The purpose of this section is to show the generality of the
representation of fracture events presented in this chapter. Maps are
shown for all the other materials investigated in this study, and for
three typical materials taken from the literature.

The first three maps are shown in fig. VI - 12 to fig. VI - 14
·for the 7075-T4 aluminum alloy, the Aℓ-Cu alloy and the Fe-P alloy,
respectively. In fig. VI - 12, a transition occurs around 600 MPa :
pressure is sufficiently high to suppress damage development, and to
allow the chisel-point or plastic failure mode to occur (see Chapter IV).

MATERIAL	COPPER ETP	α BRASS	Aℓ - 3.6%Cu	Fe - 1.2%P	7075 T4	4340 EMBRIT.
Bulk Modulus K (MPa)	$1.15 \ 10^5$	$1.08 \ 10^5$	$7 \ 10^4$	$1.93 \ 10^5$	$7 \ 10^4$	$1.99 \ 10^5$
Yield Strength σ_y^o (MPa)	72	105	180	400	413	1412
Tensile Strength σ_{TS}^o (MPa)	223	310	330	695	-	1528
Power Hardening Constant A (MPa)	480	800	645	1270	1130	1930
Power Hardening Exponent n	.54	.82	.28	.245	.25	.05
Fracture Strain at 1 atm. ε_f^o	1.5	1.7	.15	.02	.12	.29
Fracture Stress at 1 atm. σ_f^o (MPa)	597	1230	350	400	660	1810
Void Nucleation Stress at 1 atm. σ_{vn}^o (MPa)	1	680	300	-	458	1415
Interfacial Strength σ_I (MPa)	1	5000	3500	-	3000	1415
Cleavage Stress at 1 atm. (MPa)	-	-	-	400	-	1000
Strain After Necking to Cause Plastic Failure ε_R	1.35	1.12	.02	1.0	-	-

TABLE VI - 2: Data for Other Materials

NORMALIZED PRESSURE p/σ_y^o

Fig. VI-12 : Fracture map in $\bar{\sigma}$ - P coordinates for the 7075-T4
aluminum alloy.

NORMALIZED PRESSURE p/σ_y^o
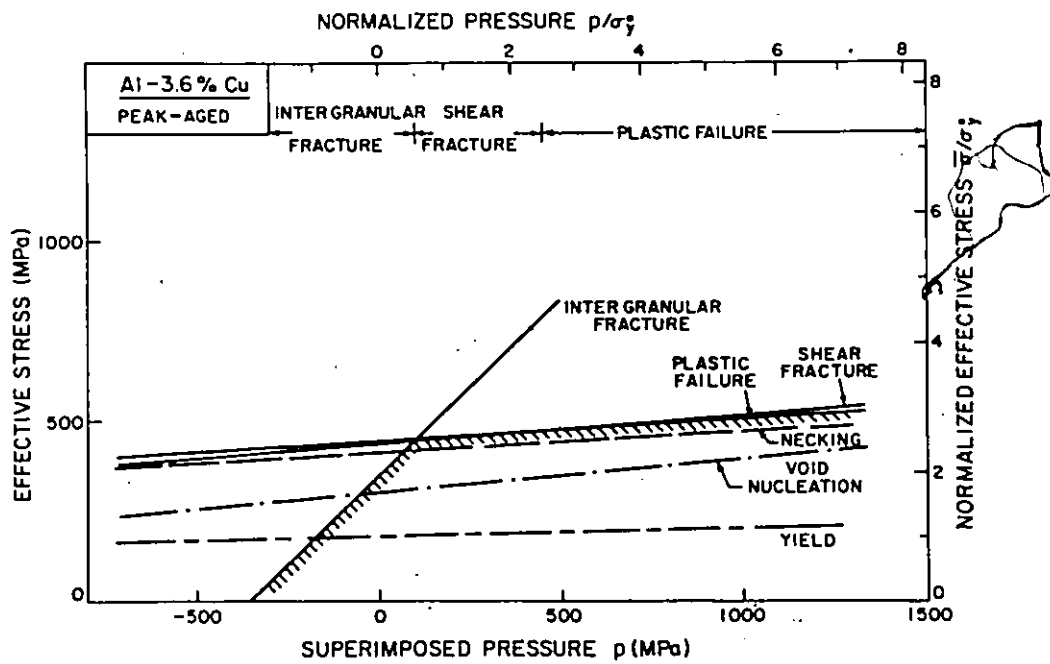
Fig. VI-13 : Fracture map in $\bar{\sigma}$ - P coordinates for the Aℓ-Cu alloy.

The Aℓ-Cu alloy undergoes two transitions as the pressure is increased (fig. VI - 13); the corresponding values of superimposed pressure are given in Section V - 4 - 1 - 3. For the Fe-P alloy, it is found that necking precedes cleavage fracture when the superimposed pressure is larger then 540 MPa (fig. VI - 14), in good agreement with the experimental observations, and, using equation (VI - 13), a transition from cleavage fracture to plastic failure is found at a pressure close to the highest one investigated in this work, i.e. 1100 MPa. The data used in the determination of these maps are given in Table VI - 2, and have been reported throughout this study(see Chapter IV and Chapter V).

The last three maps are showing the behaviour under various stress states of alloys and metals taken from the literature. The data for E.T.P. copper are taken from Yajima et al. (1970) and French and Weinrich (1975b). This material contains some inclusions of Cu_2O which are responsible for the occurrence of ductile fracture at atmospheric pressure. These inclusions are cracked in the as-received material, so that the interfacial strength and the void nucleation stress at P = 0 are taken very small (see Table VI - 2). The map obtained is shown in fig. VI - 15. Above 400 MPa, the plastic failure mode takes place. This material is typical of the pure metals when tested under superimposed pressure. Similarly for the non-ferrous alloys, α-brass can be considered as a good representative of these materials. The map for α-brass, shown in fig. VI - 16, has been determined using data from French and Weinrich (1973, 1974, 1976, 1977) given in Table VI - 2. The overall observations of fracture mode are adequately described by taking σ_I = 5000 MPa for the interfacial strength of the ZnS-α brass
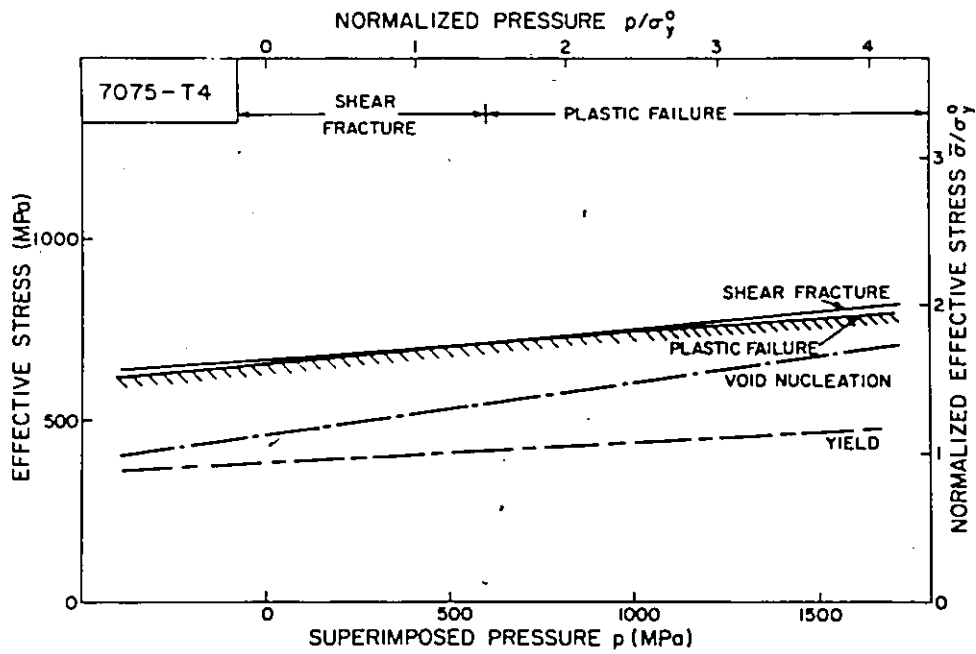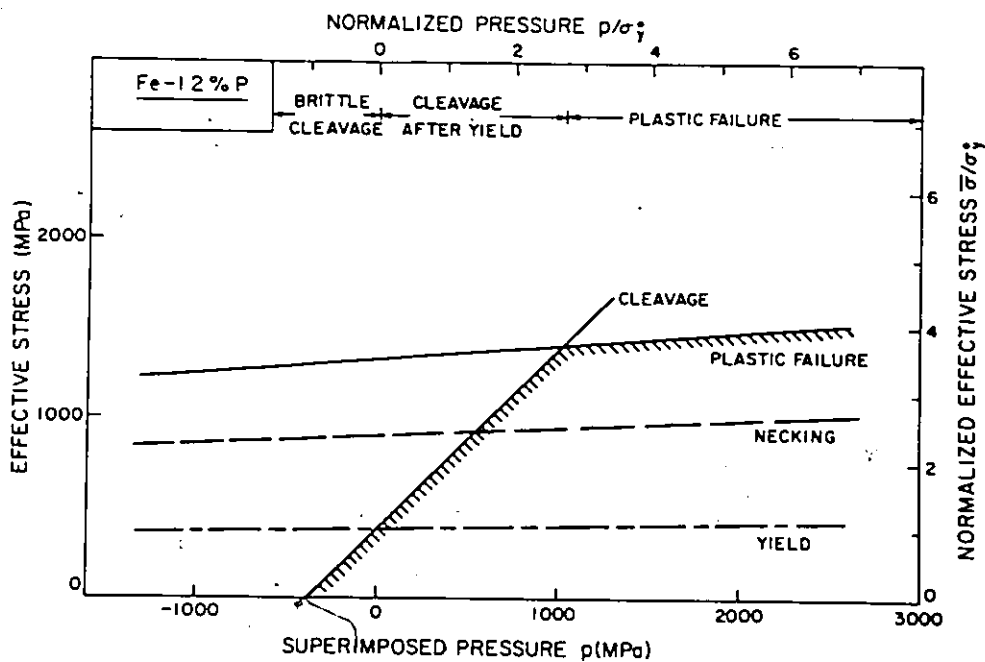
Fig. VI-14 : Fracture map in $\bar{\sigma}$ - P coordinates for the Fe-P alloy.
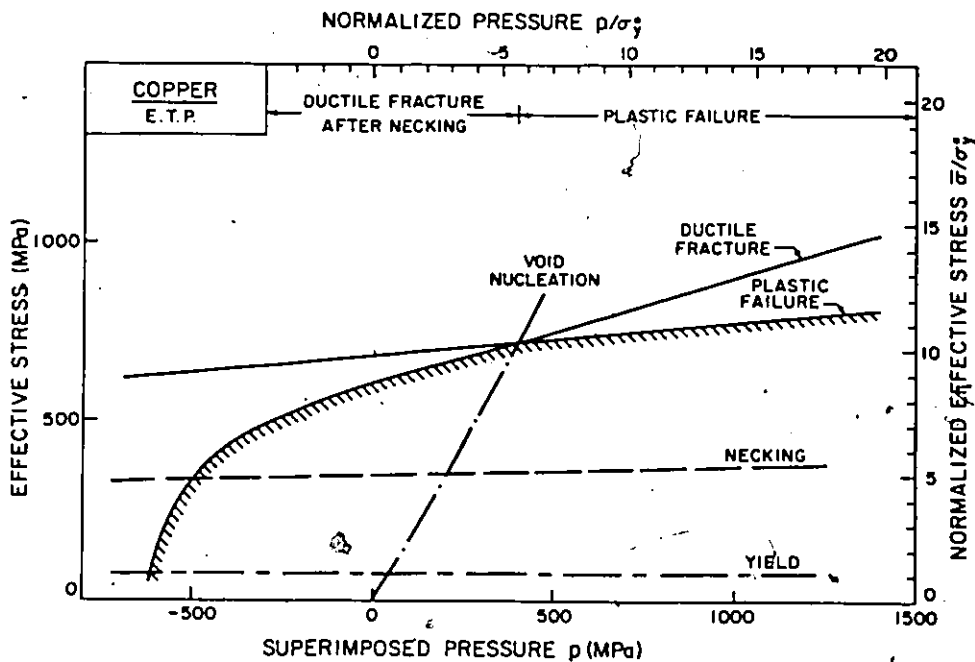
Fig. VI-15 : Fracture map in $\bar{\sigma}$ - P coordinates for E.T.P. copper.
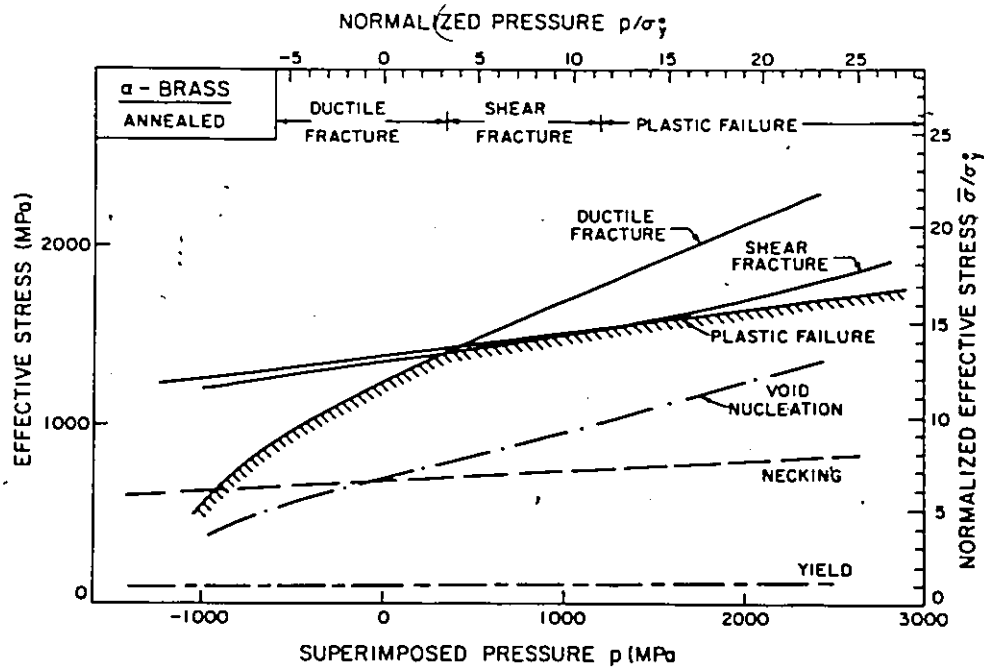
Fig. VI-16 : Fracture map in $\bar{\sigma}$ - P coordinates for α-brass.
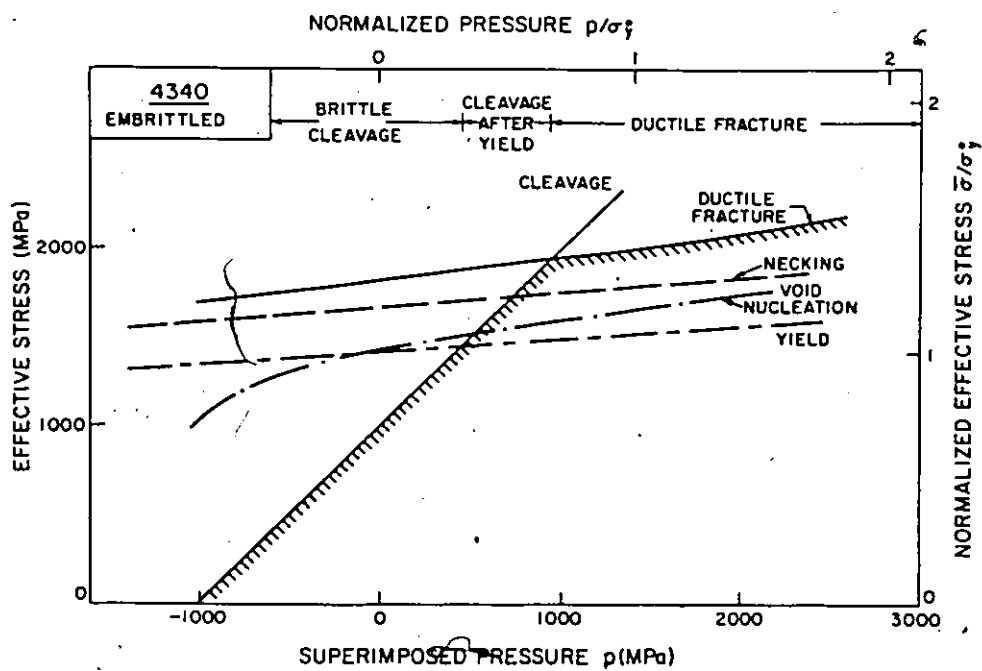
Fig. VI-17 : Fracture map in $\bar{\sigma}$ - P coordinates for a 4340
embrittled steel.

system. This alloy undergoes two transitions, first from a ductile
fracture mode to a shear fracture mode, followed at higher pressure by
a change to plastic failure mode. This sequence is typical of non-
ferrous alloys. Finally, the influence of a temper embrittlement on the
behaviour of a high strength steel is shown in fig. VI - 17. The map
has been determined for a 4340 steel embrittled such as its fracture
stress at P = 0 is equal to 1000 MPa. The data are taken from Cox and
Low (1974), and the nucleation of voids at MnS particles is assumed to
occur as soon as the material yields plastically, so that at atmospheric
pressure, $\sigma_I = \sigma_Y^o = \sigma_{vn}^o = 1415$ MPa. The brittle intergranular fracture
is found to be replaced by ductile fracture at a superimposed pressure
of about 900 MPa.

VI - 4 Conclusions

The basic fracture mechanisms of engineering alloys (plastic
failure, ductile fracture, shear fracture and brittle fracture) can be
modelled and described by a set of lines in stress spaces. These lines
have been obtained either point by point using the model of damage
accumulation developed in Chapter III for the fracture of spheroidized
steels, or they have been calculated from approximate equations des-
cribing each fracture mode. When the loading is axisymmetric, these
equations take simple forms relating the effective stress $\bar{\sigma}$ to the
superimposed pressure P. Although they do not give in general an exact
description of the data, they correctly describe the relationships
between mechanisms, and the diagrams so obtained have a number of
applications :

a) they reveal in a simple way the complex interaction between competing fracture mechanisms, and the underlying physical origins.

b) they show how the stress state may be used in processing to change the fracture mechanism.

c) they help show how processing variables which change the material properties (yield strength, work hardening exponent, inclusion content etc.) change the fracture mode of the material.

CHAPTER VII

CONCLUSIONS

This study has emphasized the influence of superimposed hydro-static stress on fracture processes, and has delineated the process of cumulative damage for a variety of fracture modes.

The salient features of the study can be summarized as follows.

a) Ductile fracture

It is well known that ductile fracture can be represented by a sequence of nucleation of voids at heterogeneities in the micro-structure of a material, and their growth and coalescence. The existing models generally deal with global quantities such as f_v, the volume frac-tion of second phase particles. However, this study has indicated the complexity of the nucleation process : it does not occur at a unique strain ϵ_N ; instead, the nucleation of a void at a particle will occur at a strain which depends on the particle size. A model has then be developed to account for this size dependence. This has enabled the exami-nation of the influence of the shape of the particle size distri-bution on the occurrence of void nucleation and therefore, on ductile fracture.

The growth of voids, which takes place simultaneously with the nucleation of new ones, has been treated as an extension of the Rice and Tracey model (1969) applied to a wide range of stress states and volume fractions of carbides.

240

The study has also indicated a new criterion for ductile fracture, namely the attainment of a critical value of damage in terms of the area fraction of voids, which seems to apply for a range of superimposed pressures. This implies that some form of localization of the deformation should occur at this damage level. Therefore, it would be of interest to explore other temperature ranges, or strain rate sensitivity regimes to investigate the process of localization. In particular, the concept of critical amount of damage could be used to explore the fracture behaviour of superplastic materials, and also the grain boundary damage created during high temperature creep in other materials.

The present study gives an experimental basis for the investigation of damage accumulation. The data fit quite well with the model developed here based on the simultaneous nucleation and growth of voids.

b) Localized shear fracture

This study has not dealt with the plasticity formulation of localization based on bifurcation theories, but has concentrated on the pressure dependence of flow localization and on a microstructural study of the geometry of shear bands and the damage associated with them.

It has indicated that for materials such as a naturally aged Aℓ-Zn-Mg alloy, the onset of macroscopic bands is independent of superimposed pressure. The macroscopic bands involve the linkage of crystallographic shear bands and their spatial correlation over the entire cross-section. The local softening event triggering the

occurrence of crystallographic bands appears to be the modification of the precipitate structure by the applied strain. It should be emphasized that the local softening event is not unique, but that the spatial correlation of crystallographic slip events may be quite general.

Although the onset of macroscopic bands is not pressure dependent, their growth and distribution is pressure sensitive. A dilational damage is created in the bands during their propagation through the cross-section. The growth of this damage is retarded by superimposed pressure, and this allows the plasticity process to occur by further band formation, and this results at higher pressures in a change of the fracture mode.

c) Brittle fracture

The experimental evidence has shown that for both cleavage and intergranular fracture, a high superimposed pressure allows the separation of the nucleation of microcracks from their critical coalescence leading to failure. It can therefore be concluded that at high pressure, brittle fracture becomes a cumulative damage process which depends not only on the criterion for crack nucleation, involving local plastic flow, but mainly on the attainment of a critical density of microcracks whose correlation leads to final fracture.

In an attempt to generalize the informations concerning the damage accumulation process for various fracture modes outlined above, two types of failure maps have been developed. They have been determined in stress coordinates for axisymmetric deformation using either σ_3 vs $\sigma_1 = \sigma_2$ or $\bar{\sigma}$ vs P coordinates. The maps can be constructed by

using criteria to describe the competitive fracture modes, which appear as separate loci on the maps. The position of the loci and the manner they are intersected by a given trajectory for stress history determine the mode of failure. These maps can also be used as contour maps displaying the degree of cumulative damage as a function of stress history. Such diagrams enable quantification of both plastic history and damage accumulation to be considered simultaneously. In addition, the maps can be used in a semi-quantitative manner to discuss the influence of changes in testing temperature, grain size or flow stress level on the occurrence of the various possible fracture modes.

In conclusion, it should be emphasized that the results and fracture maps reported in this study relate to a limited range of stress states and materials, and are almost all developed for ambient temperature. However, the basic experimental approach and the formulation of the dependence of damage accumulation and fracture mode on super-imposed pressure could be applied to other temperature regimes and a. wide range of materials, both metallic and non-metallic.

APPENDIX A

DESCRIPTION OF THE HARWOOD HIGH PRESSURE UNIT

The Harwood high pressure chamber is shown in fig. A - 1. It is comprised of a liner and a jacket. The upper major bore of the liner is fitted with a 17 cm long pressurization piston and the lower minor bore with a 26 cm long retraction piston. The upper or pressurization piston contains a well in its tip for the pressure-sensing manganin coil. Force is applied to this piston via a 500-ton jack. A 125-ton lower jack provides the means for loading the specimen at a desired rate by bleeding hydraulic fluid from the lower jack, thereby allowing the retraction piston, connected with the specimen, to withdraw from the pressurized chamber. The chamber has been cross-bored at midheight to provide the capability of photographing specimen configuration during deformation via windows inserted in the cross-bore plugs (fig. A - 2).

The cavity between the upper and lower pistons contains the test specimen and a load cell for measuring loads applied to the specimen.

The retraction piston is coupled to the specimen via a free-floating connector, such that the piston may be elevated a short distance prior to testing without disturbing the support column, load cell or specimen. Then, as the retraction piston is withdrawn, sufficient time is available to establish a constant "crosshead" rate when the specimen is loaded.
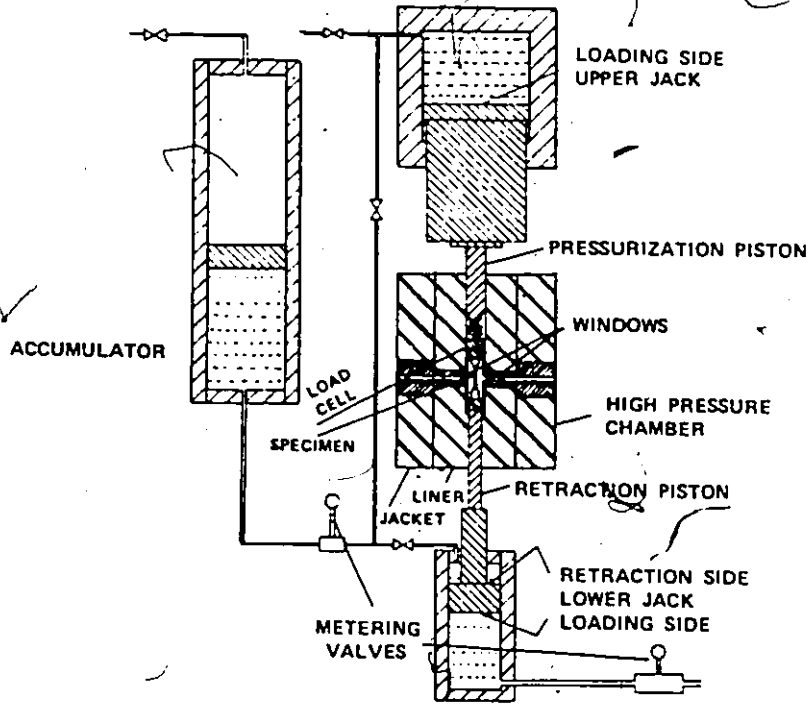
Fig. A-1 : Schematic drawing of the high pressure apparatus with accumulator.
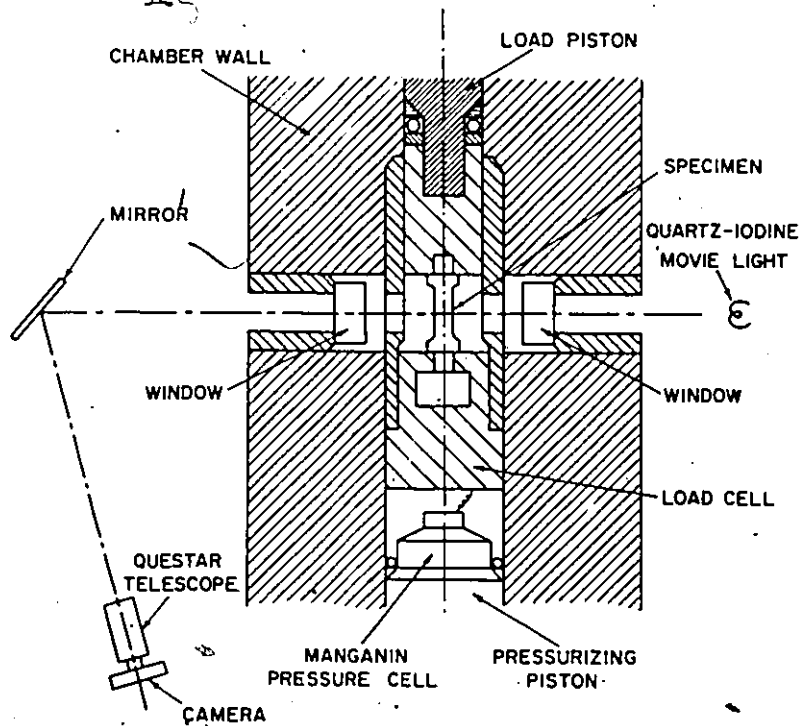
Fig. A-2 : Diagram of the high pressure chamber with the photographic setup.

A 10 : 2 mixture of castor oil and methanol is used as a pressurization fluid for pressures up to 1100 MPa.

The elongation is measured from the retraction piston motion via a linear potentiometer with a sensitivity of 8 mV / 0.1 mm. Machine stiffness measurements have been made by the staff of the U.S. Steel Research Laboratories through all the pressure range used, and this effect is taken into account when plotting strain-stress curves.

To minimize the fluctuations in pressure, a 11471 cm^3 accumulator has been added to the apparatus. After the desired pressure is developed within the high pressure unit, the accumulator is allowed to discharge at a controlled rate into the loading side of the pressurization jack, forcing the pressurization piston down at a rate that just maintains the desired hydrostatic pressure as the retraction piston is withdrawn to effect specimen deformation. The constancy of chamber pressure is then ± 0.5 MPa.

Fig. A - 2 shows the photographic setup used during the tests performed below 700 MPa.

APPENDIX B

DERIVATION OF THE INSTABILITY CRITERION LEADING TO A VOID-SHEET

FRACTURE MECHANISM -

The geometry of the problem is depicted in fig. B - 1, and the void in a shear band is schematized in fig. B - 2.

The displacement du is related to the shear strain by :

$$du = t \ d\gamma \qquad (B - 1)$$

where t is the thickness of the band and is given by :

$$t = 2R_3 \cos\theta$$

The shear strain $d\gamma$ can be related to the effective strain $d\bar{\epsilon}$ as :

$$d\gamma = \sqrt{3} \ d\bar{\epsilon}$$

Then, equation (B - 1) becomes :

$$du = 2\sqrt{3} \ R_3 \cos\theta \ d\bar{\epsilon} \qquad (B - 2)$$

When a void is sheared by a displacement du, the loss of cross-sectional area is, from fig. B - 2 :

$$da = - 2R_1 \ du \qquad (B - 3)$$

The total loss of cross-sectional area is, therefore :

$$\frac{dA}{A} = - N_A \ 2R_1 \ du \qquad (B - 4)$$

where N_A is the number of voids per unit area of the shear plane. Using equation (B - 2), this becomes :

$$\frac{dA}{A} = - 4\sqrt{3} \ N_A \ R_1 R_3 \cos\theta \ d\bar{\epsilon} \qquad (B - 5)$$

The shear stress acting on the band is :

$$\tau = F_s \ / \ A$$

247
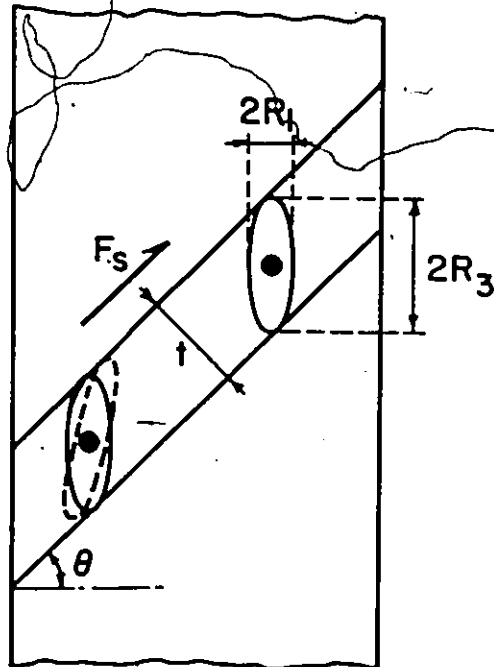
Fig. B-1 : Schematic diagram representing the creation of a shear band between adjacent voids leading to shear fracture by a void-sheet mechanism.
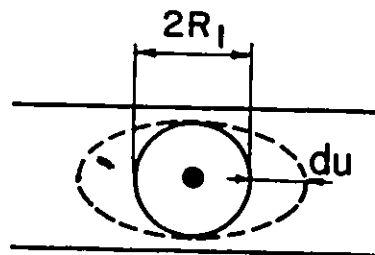
Fig. B-2 : Schematic representation of a void in a shear band.

Therefore :

$$d\tau / \tau = - dA / A = d\bar{\sigma} / \bar{\sigma} \qquad (B - 6)$$

The criterion for shear colescence is then :

$$\frac{1}{\bar{\sigma}} \frac{d\bar{\sigma}}{d\bar{\varepsilon}} = 4\sqrt{3} \ N_A \ R_1 R_3 \ \cos\theta \qquad (B - 7)$$

The band being oriented at 45° to the tensile axis, equation (B - 7)

is , therefore :

$$\frac{1}{\bar{\sigma}} \frac{d\bar{\sigma}}{d\bar{\varepsilon}} = 2\sqrt{6} \ N_A \ R_1 R_3 \qquad (B - 8)$$

The next step is to relate N_A to the quantity provided by the model

of damage accumulation, namely the number of voids per unit area of

section parallel to the tensile axis, N_T.

If N_V is the number of voids per unit volume, N_T is given by :

$$N_T = N_V \ 2R_1 \qquad (B - 9)$$

Assuming that the normal to the shear plane is at an angle θ to the

tensile axis, N_A is given by :

$$N_A = N_V \ 2R_3 \ \cos\theta \qquad (B - 10)$$

Combining equations (B - 9) and (B - 10) leads to

$$N_A = N_T \ \frac{R_3}{R_1} \ \cos\theta \qquad (B - 11)$$

Introducing equation (B - 11) into the criterion (B - 8) gives :

$$\frac{1}{\bar{\sigma}} \frac{d^-}{d\bar{\varepsilon}} = H \ N_T \ R_3^{\ 2} \qquad (B - 12)$$

or, using equation (VI - 9) :

$$\frac{n}{\bar{\varepsilon}} = H \ N_T \ R_3^{\ 2} \qquad (B - 13)$$

where H is a constant to be determined from experimental data concer-

ning the occurrence of shear fracture in ductile materials deformed

under pressure.

Following Davidson and Ansell (1968), the pressure P* at which the fibrous part of the fracture surface disappears varies with the tensile strength of the spheroidized steel as follows :

$$P^* = 4.95 \, \sigma_{TS} - 470 \qquad\qquad (B - 14)$$

where all the stresses are in MPa.

The values of P* obtained for the steels investigated are given in Table B - 1. It is also possible to calculate N_T and R_3 at this pressure P* from empirical extrapolations of the data provided by the model of damage accumulation at lower pressures. The constant H can be calculated for each steel and used to determine the shear fracture locus. The values of H are also given in Table B- 1.

Table B - 1 : Parameters used in the determination of the shear fracture locus.

Material	P* (MPa)	H
1018	1560	0.059
1045	2100	0.024
1080	2570	0.104
1045 $a/R)_o = 0.5$	2385	0.013

APPENDIX C

DERIVATION OF THE EQUATIONS RELATING $\bar{\sigma}$ AND P FOR DUCTILE FRACTURE

AND SHEAR FRACTURE

1 - Ductile fracture

1 - 1 Nucleation

The model used here is the simplified analytical model presented in Section III - 6 - 1 - 1. Neglecting the hydrostatic component of the flow stress, the nucleation strain ε_N is :

$$\varepsilon_N = C \left(\frac{\sigma_I + P}{G} \right)^2 \qquad (C - 1)$$

where C is a constant and G the shear modulus. Then, using equation (VI - 9), the void nucleation stress is :

$$\sigma_{vn} = A \left(C \left(\frac{\sigma_I + P}{G} \right)^2 \right)^n \left(1 + \frac{10 \, P}{K} \right) \qquad (C - 2)$$

ong introducing the void nucleation stress at P = 0 :

$$\sigma_{vn} = \sigma_{vn}^o \left(1 + \frac{P}{\sigma_I} \right)^{2n} \left(1 + \frac{10 \, P}{K} \right) \qquad (C - 3)$$

1 - 2 Growth and coalescence

The starting point is the equation (II - 28) taken from Leroy et al. (1981) together with the geometrical criterion for fracture of Brown and Embury (1973) which can be expressed as :

$$\left(\frac{R_3}{R_o} \right)_f = \ell n \left(\sqrt{\frac{\pi}{6 \, f_v}} - \sqrt{2/3} \right) \qquad (C - 4)$$

Using this criterion and equation (II - 28) leads to the fracture strain :

251

$$\varepsilon_f = \frac{K}{1 + 0.56 \sinh \left\{ \frac{3}{2} \left(\ln \left(1 + \frac{a}{2R}\right) + \frac{1}{3} - \frac{P}{\bar{\sigma}} \right) \right\}} \qquad (C - 5)$$

where K is a constant including the initial value of R_3/R_o.

When P is large, the argument of the sinh is small, and it can be approximated by the argument itself :

$$\varepsilon_f = \frac{K}{1 + 0.84 \ln \left(1 + \frac{a}{2R}\right) + 0.28 - 0.84 \frac{P}{\bar{\sigma}}} \qquad (C - 6)$$

Introducing the fracture strain ε_f^o at P = 0 gives :

$$\varepsilon_f = \varepsilon_f^o \left[\frac{1.5 + \ln \left(1 + \frac{a}{2R}\right)^o}{1.5 + \ln \left(1 + \frac{a}{2R}\right) - \frac{P}{\bar{\sigma}}} \right] \qquad (C - 7)$$

Using equation (VI - 9) and introducing the fracture stress $\bar{\sigma}^o$ at

P = 0 gives the effective stress for ductile fracture :

$$\bar{\sigma} = \bar{\sigma}^o \left[\frac{1.5 + \ln \left(1 + \frac{a}{2R}\right)^o}{1.5 + \ln \left(1 + \frac{a}{2R}\right) - \frac{P}{\bar{\sigma}}} \right]^n \left(1 + \frac{10\ P}{K} \right) \qquad (C - 8)$$

When P is near zero, the sinh must be retained. Thus :

$$\bar{\sigma} = \bar{\sigma}^o \left[\frac{1 + 0.56 \sinh \left\{ 0.5 + 1.5 \ln \left(1 + \frac{a}{2R}\right)^o \right\}}{1 + 0.56 \sinh \left\{ 0.5 + 1.5 \ln \left(1 + \frac{a}{2R}\right) - 1.5 \frac{P}{\bar{\sigma}} \right\}} \right]^n (1 + \frac{10P}{K}) \quad (C - 9)$$

When P is sufficiently negative, fracture occurs before necking

begins, and in this case, the $\ln$ terms disappear; but the hyperbolic

sin must still be retained. Proceeding as before gives :

$$\bar{\sigma} = \bar{\sigma}^o \left[\frac{1 + 0.56 \sinh \left\{ 0.5 + 1.5 \ln \left(1 + \frac{a}{2R}\right)^o \right\}}{1 + 0.56 \sinh \left\{ \frac{3}{2} \left(\frac{1}{3} - \frac{P}{\bar{\sigma}} \right) \right\}} \right]^n (1 + \frac{10P}{K}) \quad (C - 10)$$

In order to make this treatment general, the neck geometry

a/R has to be found. In his extensive study, Bridgman (1952) has

demonstrated that, at all pressures, the development of the neck in

tensile samples follows a master curve; the ratio a/2R at fracture is given by : .

$$\frac{a}{2R} = 0.38 \ (\ \epsilon_f - n) \qquad\qquad (C - 11)$$

where ϵ_f is the fracture strain given by equation (C - 6). To an adequate approximation for the purpose of this work, equation (C - 6) can be simplified to :

$$\epsilon_f = \frac{\epsilon_f^o}{(1 - P/\bar{\sigma})} \qquad\qquad (C - 12)$$

This gives :

$$\frac{a}{2R} = 0.38 \ \epsilon_f^o \ \{ \ \frac{1}{(1 - P/\bar{\sigma})} \ - \ \frac{n}{\epsilon_f^o} \ \} \qquad\qquad (C - 13)$$

The combination of equations (C - 13) and (C - 8) or (C - 9) allows the effective stress $\bar{\sigma}$ to be calculated for positive values of P.

2 - Shear fracture

The instability leading to the creation of a shear band between adjacent voids has been analyzed in Appendix B. The criterion is :

$$\frac{1}{\bar{\sigma}} \frac{d\bar{\sigma}}{d\bar{\epsilon}} \ \leq \ V \ N_V \qquad\qquad (C - 14)$$

where V is the volume of a void and N_V the number of voids per unit volume. Using equation (VI - 9), the criterion becomes :

$$n \ (\frac{A}{\sigma})^{1/n} \ \leq \ V \ N_V \qquad\qquad (C - 15)$$

Shear coalescence becomes increasingly important as the pressure increases. At high pressures, voids do not grow much, so that the most important term on the right hand side of equation (C - 15) is N_V. This number is taken to increase proportionally to the plastic

strain ϵ after the nucleation strain ϵ_N has been reached. From equation (C - 3) :

$$\sigma_{vn} = \sigma_{vn}^{o} \left(1 + \frac{P}{\sigma_I} \right)^{2n}$$

Then :

$$N_V = \frac{C}{A^{1/n}} \left(\bar{\sigma}^{1/n} - \sigma_{vn}^{1/n} \right) \qquad (C - 16)$$

provided $\bar{\sigma} > \sigma_{vn}$, where C is a constant. The criterion (C - 15) becomes :

$$n^n A^2 \leq C' \bar{\sigma} \left(\bar{\sigma}^{1/n} - \sigma_{vn}^{1/n} \right)^n \qquad (C - 17)$$

The constant C' is removed by using the information that void coalescence by shear is observed at a stress $\bar{\sigma}*$ when the pressure is P*. This gives :

$$\left(\frac{\bar{\sigma}*}{\bar{\sigma}} \right)^{1/n} = \frac{\bar{\sigma}^{1/n} - \sigma_{vn}^{1/n}}{\bar{\sigma}*^{1/n} - \sigma_{vn}*^{1/n}} \qquad \text{for } \bar{\sigma} > \sigma_{vn} \qquad (C - 18)$$

REFERENCES

Anand, L. and Gurland, J. (1976) Met. Trans. 7A , 191.

Anand, L. and Spitzig, W.A. (1982) Acta Met. 30 , 553.

Argon, A.S. and Im, J. (1975) Met. Trans. 6A , 839)

Argon, A.S., Im, J. and Safoglu, R. (1975) Met. Trans. 6A , 839.

Asaro, R.J. and Rice, J.R. (1977) J. Mech. Phys. Solids 25 , 309.

Asaro, R.J. (1979) Acta Met. 27 , 445.

Ashby, M.F. (1966) Phil. Mag. 14 , 1157.

Ashby, M.F. (1970) Phil. Mag. 21 , 399.

Ashby, M.F. (1977) Proc. 4th Int. Conf. on Fract., ed. D.M.R. Taplin,
    Pergamon Press, 1 , 1.

Ashby, M.F., Gandhi, C. and Taplin, D.M.R. (1979) Acta Met. 27 , 699.

Ashby, M.F. and Embury, J.D. (1981) C.U.E.D. Report.

Ashby, M.F. (1982) C.U.E.D. Report, T.R. 92.

Atkinson, J.D. (1973) Ph.D. Thesis, Cambridge University, England.

Auger, J.P. and Francois, D. (1974) Rev. Phys. Appl. 9 , 637.

Baker, T.J. and Charles, J.A. (1971) in "Effects of second phase
    particles on the mechanical properties of steel" I.S.I. Conf.,
    Scarborough, England, 68.

Bedere, D., Jamard, C., Jarland, A. and Francois, D. (1971) Acta Met.
    19 , 973.

Beresnev, B.I., Vereshchagin, L.F., Ryabinin, Yu.N. and Livshits,
    L.D. (1963) in "Some problems of large plastic deformation of
    metals at high pressures", Oxford, Pergamon Press, 1.

Berg, C.A. (1962) Proc 4th Nat. Congr. Appl. Mech., 2 , 885.

Blum, J.I. and Morrisey, R.J. (1966) Proc. 1st Int. Conf. on Fract.,
    Sendai, Japan, 3 , 1739.

Brammer, I.S. (1963) J. Iron Steel Inst. 201 , 752.

Brandes, M.A. (1965) Int. J. of Fract. Mech. 1 , 56.

Brandes, M.A. (1967) Int. J. of Fract. Mech. 3 , 175.

Brandes, M.A. (1970) in "The mechanical behaviour of materials under pressure", ed. H.Ll.D. Pugh, Elsevier, London, 236.

Brandon, D.G. (1980) Scripta Met. 14 , 555.

Briant, C.L. and Banerji, S.K. (1978) Int. Met. Rev. 4 , 164.

Bridgman, P.W. (1952) "Studies in large plastic flow and fracture", McGraw-Hill, New York.

Brown, L.M. and Stobbs, W.M. (1971) Phil. Mag. 23 , 1201.

Brown, L.M. and Embury, J.D. (1973) Proc. 3rd Int. Conf. Strength Metals and Alloys, Cambridge, England, 164.

Brown, L.M. (1976) Proc. Conf. on Mech. and Phys. of Fracture, Cambridge, England, paper 10.

Brown, L.M. and Stobbs, W.M. (1976) Phil. Mag. 34 , 351.

Brownrigg, A. (1982) private communication.

Cahn, J.W. and Fullman, L.Y. (1956) Trans. AIME 206 , 610.

Carpentier, D. and Francois, D. (1971) Proc. 3rd Conf. on High Pressure, "Engineering Solids under Pressure", ed. H.Ll.D. Pugh, Inst. of Mech. Eng., London, 61.

Chandra-Holm, H. and Embury, J.D. (1982) Department of Metallurgy Report, McMaster University, Hamilton, Canada.

Chang, J.W. and Asaro, R.J. (1980) Arch. Mech. 32 , 369.

Cheng Jian-Hua (1981) private communication.

Chin, G.Y., Hosford, W.F. and Backofen, W.A. (1964) Trans. AIME 230 , 437.

Chung, N., Embury, J.D., Evensen, J.D., Hoagland, R.C. and Sargent, C.M. (1977) Acta Met. 25 , 377.

Cottrell, A.H. (1958) Trans. AIME 212 , 192.

Cox, T.B. and Low, J.R. (1974) Met. Trans. 5 , 1457.

Crossland, B. and Dearden, W.H. (1958) Proc. Inst. Mech. Engrs
172 , 805.

Curry, D.A. and Knott, J.F. (1978) Met. Sci. 12 , 511.

Davidson, T.E., Uy, J.C. and Lee, A.P. (1966) Acta Met. 14 , 937.

Davidson, T.E. and Ansell, G.S. (1968) Trans. ASM 61 , 242.

Dillamore, I.L., Roberts, J.G. and Bush, A.C. (1979) Met. Sci.
13 , 73.

Dodd, B. and Atkins, A.G. (1983) Acta Met. 31 , 9.

Dowling, J.M. and Martin, J.W. (1973) Proc. 3rd Int. Conf. Strength
of Metals and Alloys, Cambridge, England, 170.

Dumoulin, P. and Guttman, M. (1980) Mat. Sci. Eng. 42 , 249.

Embury, J.D. and Nes, E. (1974) Z. Metalkunde 65 , 45.

Embury, J.D. and LeRoy, G.H. (1977) Proc 4th Int. Conf. on Fract.,
ed. D.M.R. Taplin, Pergamon Press, 1 , 15.

Embury, J.D. and Duncan, J.L. (1981) Ann. Rev. Mat. Sci. 11 , 505.

Evensen, J.D., Ryum, N. and Embury, J.D. (1975) Mat. Sci. Eng.
18 , 221.

Feldbeck, D.K. and Orowan, E. (1955) Welding J. Res. Suppl.
34 , 570S.

Fisher, J.R. and Gurland, J. (1981) Met. Sci. 15 , 185.

Francois, D. and Wilshaw, T.R. (1968) J. Appl. Phys. 39 , 4170.

Francois, D. (1977) Proc. 4th Int. Conf. on Fract., ed. D.M.R.
. Taplin, Pergamon Press, 1 , 805.

French, I.E., Weinrich, P.F. and Weaver, C.W. (1973a) Acta Met.
21 , 1045.

French, I.E. and Weinrich, P.F. (1973b) Acta Met. 21 , 1533.

French, I.E. and Weinrich, P.F. (1974a) Scripta Met. 8 , 87.

French, I.E. and Weinrich, P.F. (1974b) Scripta Met. 8 , 7.

French, I.E. and Weinrich, P.F. (1975a) Met. Trans. 6A , 1165.

French, I.E. and Weinrich, P.F. (1975b) Met. Trans. 6A , 785.

French, I.E. and Weinrich, P.F. (1976) Acta Met. 24 , 317.

French, I.E. and Weinrich, P.F. (1977) J. Austr. Inst. Metals 22 , 40.

French, I.E. and Weinrich, P.F. (1979) Met. Trans. 10A , 297.

Frost, H.J. and Ashby, M.F. (1982) "Deformation Mechanism Maps. The plasticity and creep of metals and ceramics", Pergamon press, Oxford.

Galli, J.R. and Gibbs, P. (1964) Acta Met. 12 , 775.

Gandhi, C. and Ashby, M.F. (1979) Acta Met. 27 , 1565.

Gil-Sevillano, J., Van Houtte, P. and Aernoudt, E. (1980) Progress in Materials Science 25 , 69.

Glover, G., Duncan, J.L. and Embury, J.D. (1977) Metals Technology, March, 153.

Goods, S.H. and Brown, L.M. (1979) Acta Met. 27 , 1.

Groves, G.W. and Kelly, A. (1963) Phil. Mag. 8 , 877.

Gurland, J. and Plateau, J. (1963) Trans. ASM 56 , 442.

Gurland, J. (1972) Acta Met. 20 , 735.

Gurson, A.L. (1977a) J. Engng. Mat. and Tech., Trans. ASME 99 , 2.

Gurson, A.L. (1977b) Proc. 4th Int. Conf. on Fract. ed. D.M.R. Taplin, Pergamon Press, 2 , 357.

Guttman, M. (1975) Surf. Sci. 53 , 213.

Guttman, M. and McLean, D. (1979) in "Interfacial Segregation", ed. W.C. Johnson and J.M. Blakely, ASM, Metals Park, Ohio.

Guttman, M. (1983) in "Atomistics of Fracture", ed. R.M. Latanision and J.R. Pickens, Plenum Press, New York, 465.

Hald, A. (1952) "Statistical theory with engineering applications", J. Wiley and Sons, New York.

Hancock, J.W. and Mackenzie, A.C. (1976) J. Mech. Phys. Solids 24 , 147.

Hatherly, M. (1982) Proc. 6th Int. Conf. Strength of Metals and Alloys, Melbourne, Australia, ed. R.C. Gifkins, Pergamon Press,

Heard, H.C. (1960) in "Rocks Deformation", eds D. Griggs and J.
    Handin, Geol. Soc. Am., memoir 79 , 193.

Hill, R. (1967) J. Mech. Phys. Solids 15 , 79.

Hill, R. and Hutchinson, J.W. (1975) J. Mech. Phys. Solids 23 , 239.

Hippsley, C.A. and Druce, S.G. (1983) accepted for publication in
    Acta Met.

Hirth, J.P. and Lothe, J. (1968) "Theory of dislocations",McGraw-
    Hill, New York, 764.

Hornbogen, E. and Zum Gahr, K.H. (1975) Metallography 8 , 181.

Hull, D. (1960) Acta Met. 8 , 11.

Humphreys, F.J. (1979) Acta Met. 27 , 1801.

Humphreys, F.J. (1980) in "Risø Conf. on recrystallization and grain
    growth of multi-phase and particles containing materials", eds.
    N. Hansen, A.R. Jones and T. Leffers, Risø Nat. Lab., 35.

Lyman, M.C. and Tipler, H.R. (1958) Acta Met. 6 , 73.

Jokl, M.L., Vitek, V. and McMahon, C.J. (1980) Acta Met. 28 ,1479.

Karman, T., von (1911) Z. Verein. Dtsch. Ing. 55 , 1749.

Kawabata, T. and Izumi, O. (1976) Acta Met. 24 , 817.

Keeler, S.P. and Backofen, W.A. (1963) Trans. ASM 56 , 25.

Kelly, A. and Nicholson, R.B. (1963) Progress in Materials Science
    10 , 149.

Knott, J.F. and Cottrell, A.H. (1963) J. Iron Steel Inst. 201 , 249.

Knott, J.F. (1966) J. Iron Steel Inst. 204 ,104.

Knott, J.F. Proc. 4th Int. Conf. on Fract., ed. D.M.R. Taplin,
    Pergamon Press, 1 , 61.

Korbel, A., Dobrzanski, F. and Richert, M. (1983) Acta Met. 31 , 293.

Lee, R.J., Spitzig, W.A., Kelly,J.F. and Fisher, R.M. (1981) J.
    Metals 33 , 20.

LeRoy, G.H. (1978) Ph.D. Thesis, McMaster University, Hamilton, Canada.

LeRoy, G.H. and Embury, J.D. (1978) in "Formability analysis model-
    ling and experiment", ed. S.S. Hecker, AIME

LeRoy, G.H., Embury, J.D., Edward, G. and Ashby, M.F. (1981) Acta
     Met. 29 , 1509.

Lindley, T.C., Oates, T. and Richards, C.E. (1970) Acta Met. 18 , 1127.

Linford, R.G. (1973) "Solid state surface science", Mercer Dekker,
     New York, 2 , 85.

Lloyd, D.J. (1982) private communication.

Low, J.R. (1954) Symposium on Relation of Properties to Microstruc-
     ture, ASM, Metals Park, Ohio, 163.

Low, J.R., Stein, D.F., Turkalo, A.M. and Laforce, R.P. (1968)
     Trans. TSM-AIME 242 , 14.

Mackenzie, A.C., Hancock, J.W. and Brown, D.K. (1977) Eng. Fract.
     Mech. 9 , 167.

Marcus, H.L., Hackett, L.H. and Palmberg, P.W. (1972) in "Temper
     embrittlement of low alloy steels", ASTM-STP 499, 91.

Martin, N. (1982) Master of Engineering Thesis, McMaster University,
     Hamilton, Canada.

McAdam, D.J. (1945) in Fracture of metals under combined stresses",
     ASM.

McClintock, F.A., Kaplan, S.M. and Berg, C.A. (1966) Int. J. of
     Fract. Mech. 2 , 614.

McClintock, F.A. (1968a) J. Appl. Mech. 35 , 363.

McClintock, F.A. (1968b) in "Ductility", ASM, Metals Park, Ohio, 255.

McLean D. (1957) "Grain boundaries in metals", Oxford University
     Press, 116.

McMahon, C.J. and Cohen, M. (1965) Acta Met. 13 , 591.

McMahon, C.J. and Vitek, V. (1979) Acta Met. 27 , 507.

Melander, A. (1980) Acta Met. 28 , 1799.

Mises, R., von (1928) Z. Angew. Math. Mech. 8 , 161.

Mulford, R.A., McMahon, C.J., Pope, D.P. and Feng, H.C. (1976)
     Met. Trans. 7A , 1183.

Murrell, S.A.F. (1963) in "Rocks Mechanics", Proc. 5th Symp. Rocks
     Mech., ed. C. Fairhurst, Pergamon Press, 563.

Nabarro, F.R.N., Bazinski, Z.S. and Holt, D.B. (1964) Adv. in Phys $\underline{13}$, 193.

Nadai, A. (1950) "Theory of flow and fracture", 2nd ed., McGraw-Hill, New York, 175.

Needleman, A. and Rice, J.R. (1978) in "Mechanics of sheet metal forming", eds. D.P. Koistinen and N.M. Wang, Plenum Press, 237.

Onat, E.T. and Prager, W. (1954) J. Appl. Phys. $\underline{25}$, 491.

O'Reilly, I. (1983) Master of engineering Thesis, McMaster University, Hamilton, Canada.

Oyane, M. (1972) Bull. JSME. $\underline{15}$, 1507.

Palmberg, P.W. and Marcus, H.L. (1969) Trans. ASM $\underline{62}$, 1016.

Palmer, I.G. and Smith, G.C. (1966) in "Oxide dispersion strengthening", Gordon and Breach, New York, 253.

Paterson, M.S. (1958) Bull. Geol. Soc. Am. $\underline{69}$, 465.

Paterson, M.S. (1969) in "Physics of Strength and Pasticity", ed. A.S. Argon, M.I.T. Press, Cambridge, Mass., 377.

Paterson, M.S. (1978) "Experimental rock deformation-The brittle field", Springer-Verlag, Berlin.

Petzow, G. (1978) in "Metallographic etching", ASM, Metals Park, Ohio, 67.

Pierce, D., Asaro, R.J. and Needleman, A. (1982) Acta Met. $\underline{30}$, 1087.

Polmear, I.J. (1981) "Metallurgy of the light metals", Edward Arnold, London.

Price, R.J. and Kelly, A. (1964) Acta Met. $\underline{12}$, 979.

Pugh, H.Ll.D. and Green, D. (1964-65) Proc. Inst. Mech. Engrs $\underline{179}$, 415.

Puttick, K.E. (1959) Phil. Mag. $\underline{4}$, 964.

Raghunathan, W.S. and Korbel, A. (1983) private communication.

Rice, J.R and Tracey, D.M. (1969) J. Mech. Phys. Solids $\underline{17}$, 201.

Rice, J.R. (1976) Proc. 14th IUTAM Congress, ed. W.T. Koiter, North Holland, $\underline{1}$, 207.

Richmond, O. and Spitzig, W.A. (1980) Proc. 15th IUTAM Congress, Toronto, Canada.

Rogers, H.C. (1960) Trans. AIME 218. , 498.

Rogers, H.C. (1968) in "Ductility, ASM, Metals Park, Ohio, 31.

Rosenfield A.R. (1968) Met. Rev. 13 , 29.

Rudnicki, J.W. and Rice, J.R. (1975) J. Mech. Phys Solids 23 , 371.

Ryder, R.A. and Smale, A.C. (1963) in "Fracture of solids", eds.
    D.C. Drucker and J.J. Gilman, Interscience, New York, 237.

Saje, M., Pan, J. and Needleman, A. (1982) Int. J. Fract. 19 , 163.

Schmitt, J.H. and Jalinier, J.M. (1982) Acta Met. 30 , 1789.

Shimura, M. and Saito, S. (1980) Sci. Rep. RITU 29 , 50.

Smith ,E. (1966) Proc. Conf. Physical Basis of Yield and Fracture,
    Inst. Phys. and Phys. Soc., Oxford, 36.

Spaeder, G.J. (1970) Met. Trans. 1 , 2011.

Spitzig, W.A. (1972) Met. Trans. 3 , 1183.

Spitzig, W.A., Sober, R.J. and Richmond, O. (1975) Acta Met. 23 , 885.

Spitzig, W.A., Sober, R.J. and Richmond, O. (1976) Met. Trans. 7A , 1703.

Spitzig, W.A. (1979) Acta Met. 27 , 523.

Spitzig, W.A. (1981) Acta Met. 29 , 1359.

Stroh, A.N. (1954) Proc. R. Soc. A223 , 404.

Sun Yao Quing, Detraux, J.M., Touzot, G. and Francois, D. (1983)
    Memoires et etudes scientifiques, Rev. Met., Avril, 183.

Tanaka, K, Mori, T. and Nakamura, T. (1970) Phil. Mag. 21 , 267.

Tanaka, K. and Spretnak, J.W. (1973) Met. Trans. 4 , 443.

Tetelman, A.S. and McEvily, A.J. (1967) "Fracture of structural
    materials", J. Wiley and Sons, New York, 262.

Thomason, P.F. (1968) J.Inst. Metals 98 , 360.

Thomason, P.F. (1971) Met. Sci. Journal 5 , 64.

Tyson, W.R. (1978) Acta Met. 26 , 1471.

Underwood, E.E. (1970) "Quantitative stereology", Addison-Wesley, Reading, Mass.

Van Stone, R.H., Merchant, R.H. and Low, J.R. (1974) in "Fatigue and fracture toughness-Cryogenic behaviour", ASTM-STP 556, 93.

Wright, J.A. and Quarrel, A.G. (1962) J. Iron Steel Inst. $\underline{195}$, 409.

Yajima, M., Ishii, M. and Kobayashi, M. (1970) Int. J. of Fract. Mech. $\underline{6}$, 139.

Yamamoto, H. (1978) Int. J. Fract. $\underline{14}$, 347.

Zener, C. (1948) Trans. ASM $\underline{40A}$, 3.

ERRATUM

The model presented in the bottom of p. 169 and the situation depicted in Fig. IV - 26 are incorrect.

Conservation of volume requires that, with the notations of Fig. IV - 26:

$$x = \dot{y}$$

so that:

$$\tan \alpha = x/(x + y)$$

$$= \tfrac{1}{2}$$

i.e.

$$\alpha = 26.5^{o}$$

This is in fact the results obtained by Onat and Prager. (1954).